Étude de décharges Ar-NH3 en simple et double fréquence à la pression atmosphérique

Raphaël Robert

▶ **To cite this version:**

Raphaël Robert. Étude de décharges Ar-NH3 en simple et double fréquence à la pression atmosphérique. Physique [physics]. Université de Perpignan; Université de Montréal (1978-..), 2023. Français. NNT : 2023PERP0043 . tel-04485847

HAL Id: tel-04485847
https://theses.hal.science/tel-04485847

Submitted on 1 Mar 2024

HAL is a multi-disciplinary open access archive for the deposit and dissemination of scientific research documents, whether they are published or not. The documents may come from teaching and research institutions in France or abroad, or from public or private research centers.

L'archive ouverte pluridisciplinaire **HAL**, est destinée au dépôt et à la diffusion de documents scientifiques de niveau recherche, publiés ou non, émanant des établissements d'enseignement et de recherche français ou étrangers, des laboratoires publics ou privés.

Université de Montréal

Et

Université de Perpignan

Étude de décharges Ar-NH_3 en simple et double fréquence à la pression atmosphérique

Par

Raphaël ROBERT

Thèse présentée

En vue de l'obtention du

Doctorat de l'université de Perpignan

Et du grade de

Philosophiae doctor (Ph.D.) en physique

Aout 2023

© Raphaël ROBERT, 2023

Université de Montréal et Université de Perpignan

Cette thèse intitulée

Étude de décharges Ar-NH_3 en simple et double fréquence à la pression atmosphérique

Présentée par

Raphaël ROBERT

A été évaluée par un jury composé des personnes suivantes

Joëlle Margot et Laurent Thomas
Président-rapporteur

Françoise Massines et Luc Stafford
Directeurs de recherche

Gerjan Hagelaar et Ahmad Hamdan
Membre du jury

Jean-Paul Booth et David B. Graves
Examinateur externe (pour une thèse)

Résumé

L'objectif de cette thèse est d'acquérir une meilleure connaissance des décharges à barrières diélectriques basse fréquence et double fréquence BF-RF (50 kHz – 5 MHz), en Ar-NH_3 à la pression atmosphérique, notamment à travers l'étude de leurs propriétés spatio-temporelles. Dans ce contexte, des mesures d'émission et d'absorption spectroscopiques, résolues dans l'espace et /ou le temps, incluant des cartographies sur un cycle BF (20 µs) résolues à l'échelle de la RF (7 ns) ainsi que des mesures électriques ont été confrontées avec un modèle fluide 1D. Dans un premier temps, la comparaison de l'évolution de la densité d'argon métastable entre le modèle et la mesure a mis en évidence l'influence des photons VUV sur l'émission secondaire et donc sur l'auto-entretien de la décharge basse fréquence et double fréquence. En double fréquence, l'étude de l'effet de l'amplitude de la tension RF démontre l'influence du niveau d'ionisation RF sur le claquage γ. Plus l'amplitude de la tension RF est importante, plus la densité du plasma RF α est élevée et plus la tension appliquée au gaz nécessaire pour obtenir le mode γ diminue. Ainsi, la densité d'électrons augmente, alors que la densité des espèces formées par des électrons de haute énergie (Ar(1s) et Ar(2p)) décroit. Ensuite, la dissymétrie du courant à l'échelle RF est expliquée par la présence continue d'une gaine cathodique oscillante à l'échelle de la fréquence RF. Ainsi, nous avons montré que le transport des charges est contrôlé par la tension BF dans la gaine et par la tension RF dans le volume. Enfin, la physico-chimie de ces décharges en mélange Penning Ar-NH_3 a été explorée à travers la caractérisation des produits de décomposition de NH_3 visibles en spectroscopie d'émission optique, et en particulier, l'émission liée à la désexcitation du $H_2(a)$ observée à autour de 200 nm. En couplant expérience et modélisation, un nouveau mécanisme de formation de $H_2(a)$ en post-décharge a été proposé. En s'appuyant sur le modèle 1D, le degré de dissociation de NH_3 a été estimé et les mesures en fonction du temps de résidence de NH_3 dans le plasma ont, en particulier, montrées que la décharge homogène peut se propager le long des lignes de flux sans changer de régime.

Mots-clés : DBD, pression atmosphérique, mélange Penning, diagnostics spectroscopiques, double fréquence, Ar-NH_3.

Abstract

The aim of this thesis is to gain a better understanding of low-frequency and dual-frequency LF-RF (50 kHz - 5 MHz) dielectric barrier discharges in Ar-NH_3 at atmospheric pressure, in particular by studying their spatio-temporal properties. In this context, spectroscopic emission and absorption measurements, space and/or time resolved, including mappings on an LF cycle (20 µs) resolved on the RF scale (7 ns), as well as electrical measurements, were compared with a 1D fluid model. Firstly, a comparison of the evolution of the metastable argon density between the model and the measurement highlighted the influence of VUV photons on secondary emission and therefore on the self-maintenance of the low-frequency and dual-frequency discharge. In dual frequency discharges, the study of the effect of the amplitude of the RF voltage demonstrates the influence of the level of RF ionisation on γ breakdown. The higher the amplitude of the RF voltage, the higher the density of the RF α plasma and the lower the gas voltage required to obtain the γ mode. As a result, the electron density increases, while the density of species formed by high-energy electrons (Ar(1s) and Ar(2p)) decreases. Secondly, the current asymmetry at the RF scale is explained by the continuous presence of an oscillating cathode sheath at the RF frequency scale. Thus, it is shown that charge transport is controlled by the LF voltage in the cathodic and by the RF voltage in the bulk. Finally, the physico-chemistry of these Ar-NH_3 Penning discharges is explored through the characterization of NH_3 by-products, visible in optical emission spectroscopy, especially the emission of H_2(a) around 200 nm. By coupling experiments and modelling, a new mechanism of H_2(a) formation is proposed in the post-discharge. Based on the 1D model, a degree of NH_3 dissociation has been estimated and measurements as a function of the residence time of NH_3 in the plasma have, in particular, shown that the homogeneous discharge can propagate along the lines of flow without changing regime.

Keywords: DBD, atmospheric pressure, Penning mixture, spectroscopic diagnostics, dual frequency, Ar-NH_3.

Table des matières

Liste des tableaux

Liste des figures

Remerciements

Je tiens tout d'abord à remercier Françoise Massines et Luc Stafford pour m'avoir offert l'opportunité d'effectuer cette thèse. Je les remercie aussi pour la liberté d'action qu'ils m'ont accordée ainsi que leur soutien constant au cours de ces 4 années. Mon appréciation de la thèse y est grandement liée.

Je remercie aussi tout particulièrement Gerjan Hagelaar pour son aide précieuse sur le modèle fluide utilisé ainsi que concernant des réflexions sur la physique des décharges.

Je remercie également Nader Sadeghi, sans qui, les mesures présentes dans les articles 1 à 3 n'auraient pu exister.

Je remercie mes collèges de bureaux (et amis) de Perpignan et Montréal pour l'ambiance générale permettant de venir au laboratoire avec envie chaque matin. Mes pensées vont aussi au personnels technique de Perpignan et de Montréal qui ont permis de réaliser les différents montages expérimentaux présentés dans ces travaux de doctorat.

Enfin, merci à l'ensemble de mon entourage pour leur soutien pendant ces 4 années.

Introduction générale

La décharge à barrière diélectrique (DBD) produite dans un espace gazeux entre deux électrodes métalliques associées à un diélectrique est un type de décharge utilisée principalement à la pression atmosphérique pour éviter le passage à l'arc électrique [1]. En effet, lorsque le produit de la pression du gaz et de la distance interélectrodes devient important, la multiplication électronique, liée aux collisions ionisantes dans la phase gazeuse, devient très rapide et engendre la formation d'un canal conducteur fortement localisé dans l'espace [2]. Lorsque non désirée, cette décharge localisée (associé à de fortes densités de particules chargées et de hautes températures) peut grandement endommager les électrodes. De plus, ces aspects (localisation, forte température) peuvent être problématiques pour des applications en traitement de surfaces, particulièrement pour des matériaux thermosensibles comme les polymères [3], [4].

Pour éviter cette transition vers l'arc électrique, W. Siemens a proposé en 1857 d'introduire une couche de diélectrique sur la surface des électrodes excitatrices [5]. La DBD obtenue devient ainsi constituée d'un ensemble de micro-décharges. Dans ce régime de décharges dites filamentaires, l'intérêt des diélectriques est de collecter les charges à leur surface et de créer un champ électrique qui s'oppose au champ électrique issus de la tension appliquée, de manière à entrainer une extinction prématurée de la décharge avant le passage à l'arc [6].]. L'intérêt de la DBD est donc de produire une décharge hors régime d'arc à la pression atmosphérique afin de viser des applications nécessitant un plasma froid, c'est-à-dire un plasma hors équilibre thermodynamique, caractérisé par un faible degré d'ionisation et une température électronique largement supérieure à celle des lourds (ions et neutres). À partir de 1933, selon un choix judicieux des conditions opératoires, il a aussi été montré qu'il était possible d'obtenir un régime de décharge homogène sur toute la surface des électrodes (plutôt que filamentaire) [7]–[10], ouvrant ainsi la voie à de nouvelles possibilités au niveau des applications. À la pression atmosphérique, on pourra par ailleurs se libérer de la contrainte du traitement par lots souvent liée à la mise sous vide des systèmes [11].

Les travaux de cette thèse de doctorat se concentrent sur les différents régimes de décharge pertinents pour la synthèse de couches minces nanocomposites formées à partir d'inclusions de nanoparticules dans une matrice. Par la combinaison de deux matériaux différents couplée aux propriétés spécifiques liées à la composition et la structure cristalline des nanoparticules [12], [13], il devient ainsi possible d'envisager la production de surfaces dites multifonctionnelles. L'avantage principal de ces nouveaux nanomatériaux est de répondre à plusieurs besoins d'une application donnée en un seul et unique système. Par exemple, le recours à des nanoparticules de TiO_2 dispersées dans une matrice de SiO_2 ouvre la voie à la formation de surfaces autonettoyantes et antibuée [14]. Le recours aux DBDs pour ce type d'applications soulève toutefois plusieurs défis scientifiques et technologiques. En particulier, les DBDs offrant la possibilité d'obtenir des décharges homogènes (plutôt que filamentaires) sont traditionnellement produites par des champs électriques oscillants à de basses fréquences (BF, de l'ordre du kHz à la centaine de kHz). Des DBD homogènes sont en particulier obtenues à la pression atmosphérique en mélange Penning [2], [15]–[17]. Cette notion est décrite plus en détails dans le chapitre suivant ; il faut ici retenir que ce système repose sur un gaz vecteur principal (par exemple l'argon) et un gaz adjuvant (par exemple NH_3). Ainsi, avec l'allumage de la décharge, il est possible d'observer des variations de la composition chimique du gaz en fonction de l'éloignement par rapport à l'entrée de la décharge [18]. De plus, dans ces conditions de basses fréquences avec ou sans mélange Penning, les densités de puissance s'avèrent modestes de sorte que les vitesses de dépôt des couches minces demeurent relativement faibles [19], [20]. Pour contourner ce problème, des études récentes ont proposé d'augmenter la fréquence d'oscillation du champ électrique du kHz vers le MHz [21]–[25]. Bien qu'elles offrent de plus fortes densités de puissance, et donc des vitesses de dépôt plus élevées [26], [27], dans ces décharges, les nanoparticules, qui se chargent en contact avec le plasma, demeurent piégées dans l'espace interélectrodes du fait de la haute fréquence et ne se déposent donc plus à la surface [28], [29]. Il en est de même des ions qui participent à la densification du dépôt. Plusieurs groupes ont ainsi proposé de recourir à des alimentations électriques modulées [29], [30], ce qui semble très prometteur pour obtenir un fin contrôle des propriétés physico-chimiques des couches minces [31], [32]. Dans des travaux récents [33], les nanoparticules sont formées dans le plasma afin d'éviter leur agrégation. Dans

ce cadre, il est intéressant d'appliquer continument la basse fréquence pour les déposer dès qu'elles sont suffisamment chargées pour dériver vers la surface. Cette approche conduit à utiliser une décharge double fréquence RF-BF. La physique de la décharge devient évidemment plus complexe que dans les DBDs habituelles, surtout en présence d'espèces réactives utilisées pour le mélange Penning ou pour le dépôt [34].

Cette thèse vise donc à caractériser et à mieux appréhender la physique des DBDs doubles fréquences produites dans des mélange Penning. Les travaux sont menés dans le cas particulier de la DBD produite dans un gaz principal d'argon avec NH_3 comme gaz adjuvant. De plus, nous avons sélectionné le cas d'une double fréquence 50 kHz – 5 MHz. Dans ce contexte, nous avons mis au point plusieurs moyens de caractérisation couplés à de la modélisation. Ceci inclut des diagnostics électriques et optiques, notamment ceux basés sur la spectroscopie d'absorption et d'émission résolues dans le temps et dans l'espace. Pour les simulations, nous avons eu recours à un modèle fluide (présenté plus en détail en Annexe) [35].

Dans le premier chapitre, nous présentons un portrait de l'état des connaissances de la physique des DBDs produites sur une gamme étendue de conditions opératoires. En particulier, nous présentons un survol des travaux liés à l'augmentation de la fréquence d'excitation, du kHz jusqu'au MHz. Par la suite, nous abordons les verrous scientifiques du régime hybride couplant des signaux de basse et de haute fréquence.

Suite à cette revue critique de la littérature scientifique, nous exposons les principales contributions à la recherche de cette thèse de doctorat réalisée en cotutelle entre l'Université de Perpignan, laboratoire PROcédés Matériaux et Énergie Solaire - PROMES et l'Université de Montréal, département de physique. Les travaux sont présentés sous la forme de publications dans des journaux scientifiques. Pour l'ensemble de ces travaux, Raphaël Robert a participé à

l'idéation, au développement des outils de caractérisation, à la prise de mesure, et à l'analyse et l'interprétation des données issues des expériences et du modèle. Dans certains cas, il a été appuyé par Nader Sadeghi pour la mise au point des diagnostics optiques, et par Gerjan Hagelaar pour le développement du modèle fluide. Les travaux étaient sous la supervision de Luc Stafford et Françoise Massines. Plus spécifiquement, en lien avec l'objectif général de cette thèse de doctorat, les contributions concernent :

- Au chapitre 2, la mise en évidence d'un mécanisme rapide de création d'électrons dans les DBDs d'argon par photoémission aux électrodes (via la production de photons VUV issus de niveaux radiatifs Ar_2^* peuplés par conversion des atomes d'argon dans un niveau métastable (Ar(1s)) ;
- Au chapitre 3, le recours à des cartographies spatio-temporelles de certaines propriétés fondamentales des DBDs, dont la densité d'Ar(1s), la population d'électrons énergétiques et la densité totale d'électrons pour mieux comprendre l'influence de l'amplitude de la tension RF dans les DBDs double fréquence ;
- Au chapitre 4, l'analyse du transport électronique et ionique en présence d'une gaine cathodique à basse fréquence dans une décharge double fréquence RF-BF ;
- Au chapitre 5, les premières bases d'une étude spectroscopique des produits de réaction de l'adjuvant NH_3 dans les DBDs à base d'argon produites dans des mélanges Penning Ar-NH_3. Ici, les travaux concernent d'abord la cinétique de l'état $H_2(a)$ et les processus de recombinaison entre les ions et les électrons dans la création de ce niveau. Puis, nous examinons l'évolution de la chimie de la DBD Ar-NH_3 en fonction du temps de résidence ainsi que son influence sur ses propriétés fondamentales.
- Enfin nous allons conclure et présenter quelques perspectives de ce travail de recherche.

Chapitre 1 – Revue de littérature : Les décharges à barrière diélectrique homogènes à la pression atmosphérique

Régimes de décharges homogènes en fonction de la fréquence dans les gaz nobles

Afin d'éviter la transition au régime filamentaire, tout en maintenant un transfert de puissance à la décharge important, nous allons nous intéresser dans cette partie à l'influence de la fréquence d'excitation du champ électrique sur les différents comportements des DBDs. Pour recentrer le sujet d'étude, nous examinerons plus particulièrement le cas des gaz nobles qui sont des gaz non réactifs qui conviennent bien à l'étude de la physique des décharges. Les fréquences étudiées vont de quelques kHz à quelques MHz, fréquences pour lesquelles la DBD se montre utile. Au-delà, la température du gaz devient trop élevée pour l'activation de surface de matériaux thermosensibles comme les polymères ou la synthèse de couche minces nanocomposites sur ces mêmes substrats.

Régimes de décharges homogènes en simple fréquence

Rappel sur les mécanismes régissant le claquage électrique

Pour appréhender les notions de décharge, il est nécessaire d'aborder les différents modes de claquage du gaz et leurs conséquences. De manière générale, le claquage est la rupture diélectrique d'un milieu ; lorsqu'un diélectrique est soumis à une tension assez élevée, celui-ci devient conducteur et permet alors le passage d'un courant électrique. Dans une configuration constituée d'un gaz entre deux électrodes, le claquage est communément caractérisé par 2 coefficients : α et γ. Le premier, α, définit le nombre d'électrons produits par unité de longueur

pour un électron incident tandis que le second, **γ**, définit le nombre d'électrons secondaires émis par bombardement de la cathode par un ion positif ou toute espèce énergétique. Le claquage de type *streamer* est un claquage rapide et localisé dans l'espace, lié à une avalanche électronique importante [36], c'est-à-dire une forte ionisation dans le gaz définie par le coefficient **α**. La contribution des processus de surface liés au coefficient **γ** est dans ce cas petite par rapport à ceux du **α**. Quant au claquage de Townsend, il a lieu lorsque 1 électron initialement à la cathode produit au moins 1 électron secondaire à la cathode. Illustré à la Figure 1. – , ce critère se traduit par l'équation d'auto-entretien de la décharge [37]:

$$\gamma(e^{\alpha d} - 1) = 1, \qquad 1$$

Où *d* est la distance interélectrodes. Dans cette formule, il faut noter que seuls les ions positifs sont considérés comme responsables de l'émission secondaire ; en réalité, les espèces métastables ou encore certains photons énergétiques peuvent aussi y participer [38]. Nous reviendrons sur ce point au chapitre 2.

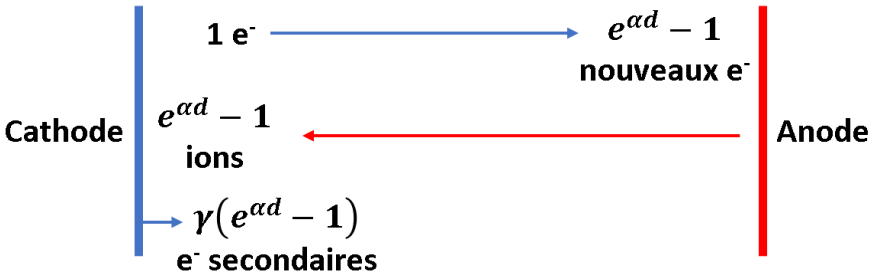

Figure 1. – Schéma de principe du claquage de Townsend.

Pour obtenir une décharge homogène (plutôt que filamentaire), il est nécessaire d'obtenir un claquage de Townsend (contrôlé par **α** et **γ**) plutôt qu'un claquage de *streamer* (contrôlé par **α** seulement). Pour y arriver, il faut donc diminuer la contribution de l'ionisation en volume **α** et/ou augmenter la création d'électrons en surface **γ**. Ainsi, il est possible : (i) d'ajouter un matériau diélectrique pour augmenter le nombre d'électrons secondaires crées par un ion positif (les

électrons adsorbés à la paroi seront des électrons secondaires facilement émis à la cathode) ou (ii) de diminuer la contribution de l'ionisation **α** en obtenant un claquage du gaz sous faible champ électrique. Pour ce deuxième critère, une solution couramment utilisée consiste à ajouter des impuretés dans le gaz pouvant être ionisées par les atomes ou molécules excités du gaz (par exemple des métastables) ; on parle alors de décharges dans un mélange Penning [39]. Dans l'hélium, les impuretés présentes dans la bouteille sont typiquement suffisantes (effet perçu à partir de 0.5 ppm d'impuretés [17], [40]). Dans l'argon, quelques dizaines de ppm d'un gaz comme l'ammoniac doivent être rajoutés afin de favoriser l'ionisation Penning :

$$Ar^* + NH_3 \Rightarrow Ar + NH_3^+ + e^-. \qquad 2$$

Cette ionisation Penning est possible lorsque l'adjuvant ou les impuretés ont un seuil d'ionisation inférieur au niveau d'excitation des métastables du gaz atomique. Dans le cas de l'argon, comme le montre la Figure 2. – , les états métastables ont une énergie de 11.71 eV pour l'état $1s_3$ et 11.55 eV pour l'état $1s_5$ alors que l'énergie d'ionisation de la molécule d'ammoniac est de 10.07 eV. L'ionisation Penning possède ainsi un double effet sur l'ionisation dans le volume du gaz (liée au coefficient **α**) : en plus de directement abaisser la tension nécessaire pour le claquage, elle vient également promouvoir un processus d'ionisation par étape qui ralentit d'autant plus le processus d'ionisation [11], [41]. Dans ces conditions, en plus des électrons et des ions, il faut toutefois noter que la population des métastables du gaz vecteur a aussi un rôle clé sur la physique de la décharge.

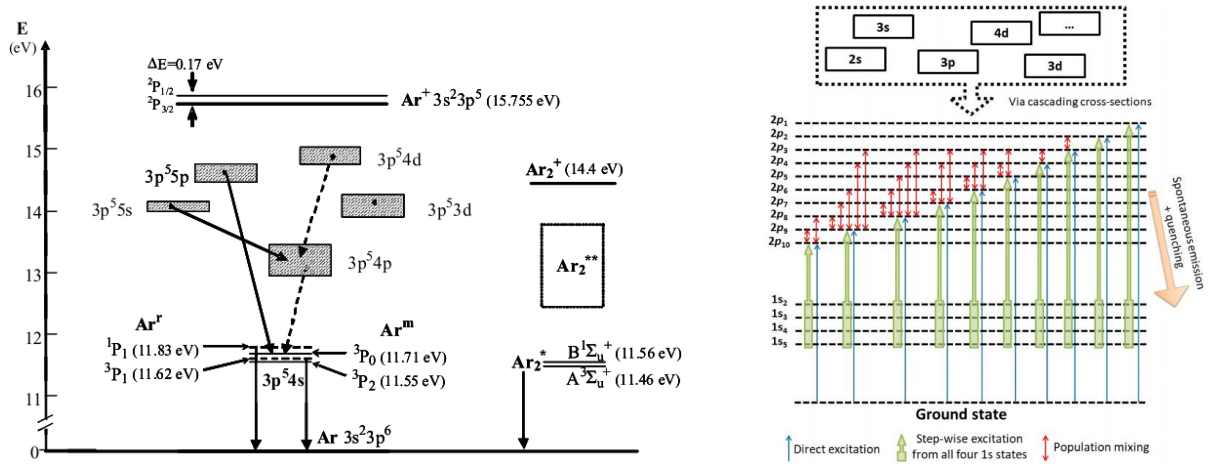

Figure 2. – Diagramme énergétique de l'argon [42]–[44].

Les mélanges Penning obtenus avec des espèces moléculaires comme l'ammoniaque présentent cependant un inconvénient majeur qui va se matérialiser sous la forme de la dissociation des molécules et la formation de nouvelles espèces [45], [46]. Par exemple, les produits de dissociation du NH_3 incluent NH, NH_2, H_2, etc. [47]. De plus, le degré de dissociation de l'adjuvant et la cinétique de la formation des produits de réaction sont susceptibles de varier fortement en fonction des conditions opératoires. Par exemple, plus le temps passé dans la décharge est important, plus la probabilité de dissociation d'une molécule suivant son interaction avec les espèces énergétiques est élevée.

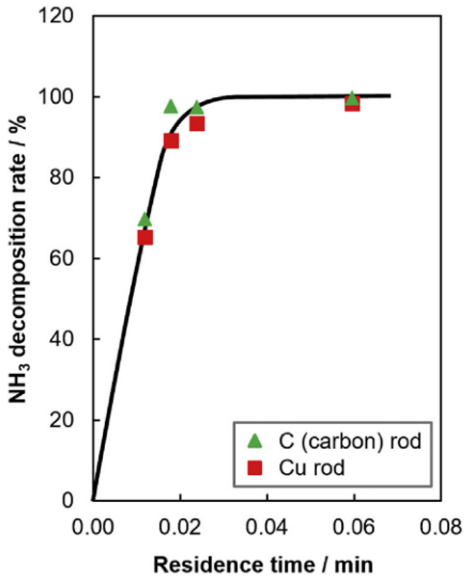

Figure 3. – Degré de dissociation du NH_3 en fonction du temps de résidence et de la composition de l'électrode dans une DBD N_2-NH_3 à la pression atmosphérique [48].

À titre d'illustration, la Figure 3. – présente le degré de dissociation du NH_3 dans une DBD en régime filamentaire en fonction du temps de résidence. Ici, le degré de dissociation augmente d'environ 65% à quasiment 100% lorsque le temps de résidence du NH_3 passe de 0.01 à 0.06 min. Notons que la littérature est peu abondante sur le sujet puisqu'il est souvent difficile de mesurer la dissociation et la nature des fragments, en particulier dans les mélanges Penning pour lesquels les concentrations relatives des adjuvants nécessaires à l'obtention de la décharge homogène sont typiquement de 10 – 500 ppm [21], [49], [50]. En fonction du temps de résidence du gaz dans la décharge (et donc de l'éloignement à l'entrée de la décharge dans une configuration plan-plan), la chimie de la décharge est donc susceptible d'évoluer fortement. Par conséquent, plus on s'éloigne de l'entrée de la décharge, plus sa physique risque de dévier de celle d'une décharge en mélange Penning. Le flux de gaz et la longueur de l'électrode sont donc des paramètres importants dans l'étude des DBDs en mélange Penning pour minimiser le gradient de composition du mélange entre l'entrée et la sortie de la décharge. La décomposition des précurseurs de dépôt en fonction de l'énergie du plasma vu par la molécule soit le produit temps de résidence de la molécule dans le plasma par la puissance de la décharge a été largement étudiée pour différents

précurseurs de dépôt [19]. En revanche, l'évolution du mélange Penning en tant que tel a peu été étudié car la concentration du précurseur est ajustée de façon à être toujours assez importante pour avoir le même mode de claquage quelle que soit la position dans le plasma. Nous reviendrons sur ce point dans le chapitre 5.

Survol des régimes de décharge selon la fréquence du champ électrique

Comme on peut le voir sur la Figure 4. – , il existe entre le kHz et la dizaine de MHz 5 régimes de décharge habituellement observés dans les DBDs produites dans des gaz nobles [21], [23]. En commençant par les plus basses fréquences, jusqu'à environ 10 kHz, on retrouve le régime filamentaire typiquement inapproprié pour le traitement de surfaces. En augmentant la fréquence d'excitation ou en diminuant l'amplitude de la tension appliquée à la décharge, il est possible de transiter vers une décharge dite luminescente (régime *glow*) pouvant être considérée comme homogène sur toute la surface des électrodes. Entre 250 kHz et 500 kHz, la décharge n'est plus luminescente et montre plutôt un régime analogue à un régime dit de Townsend ; c'est le dernier régime où les ions suivent encore les variations temporelles du champ électrique [51]. Enfin, entre 2 et 40 MHz, on retrouve 2 modes du régime radio fréquence (RF). En fonction de l'amplitude de la tension RF appliquée, on pourra passer d'un mode dit **α** à un mode dit **γ**. Entre ces principaux régimes, on rencontre des zones de transitions, par exemple entre 200 et 250 kHz et entre 500 kHz et 2 MHz. Dans ces zones de fréquence, la décharge n'est pas vraiment caractérisée par un comportement lié à un régime de décharge précis, mais on retrouve des caractéristiques appartenant aux deux régimes jouxtant la transition et très largement définies par la taille du gap [23].

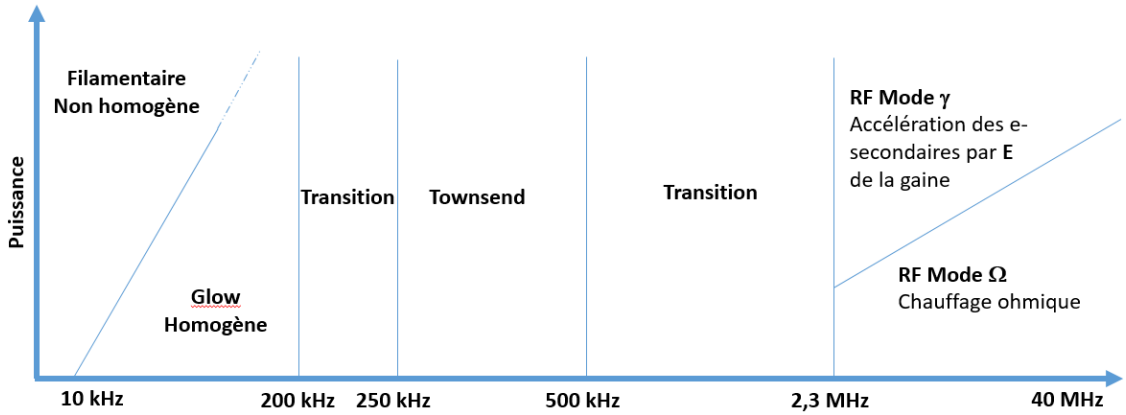

Figure 4. – Régimes de décharges en fonction de la tension appliquée et de la fréquence d'excitation observés pour un gap de 2 mm dans un gaz noble.

Décharge luminescente ou *glow*

Les premières DBDs homogènes à la pression atmosphérique ont été observées par Engel et al. [7] puis par Bartnikas [8] et Kanazawa et al. [9]. Elles seront par la suite fortement étudiées à partir des années 1990 notamment au Japon par Okazaki et al. [9], [52] aux États-Unis par Roth et al. [53], [54] et en France par Massines et al. [4], [6], [55]. En augmentant la fréquence entre 10 et 200 kHz, le premier régime de décharge homogène que l'on atteint est la décharge luminescente ; c'est le régime fréquemment observé dans les mélanges Penning à la pression atmosphérique. Cette décharge est issue d'un claquage de Townsend (plutôt que *streamer*) de sorte que les densités d'espèces seront, dans un premier temps, importantes à l'anode [56] (là où la densité ionique et électronique est la plus importante suite à l'avalanche électronique). Les espèces chargées vont ensuite se déplacer vers les électrodes de signes opposés à leur charge et vont ainsi déformer le champ électrique géométrique. Ce transport engendre un champ électrique fort proche de la cathode ; c'est la chute cathodique. Comme le montre la Figure 5. – , la décharge luminescente est donc reconnaissable par sa forte intensité lumineuse près de la cathode.

Figure 5. – Photographie du gap gazeux d'une glow DBD en hélium (la cathode est en bas et l'anode est en haut), temps d'exposition 10 ns [11].

La décharge luminescente à la pression atmosphérique a donc le même comportement que la décharge luminescente produite par des courants continus à basse pression [37] ; c'est d'ailleurs de là qu'elle tient son nom. Du fait de la pression importante, le gap se retrouve néanmoins bien inférieur à celui des décharges à basse pression. Ainsi, les zones présentes à la pression atmosphérique ne seront pas la totalité de celles observées à basse pression : on verra uniquement la chute cathodique, la lueur négative, l'espace sombre de Faraday et la colonne positive (seul endroit de la décharge où l'on observe un plasma, i.e. Ne ≈ Ni). De plus, comme le montre les caractéristiques courant-tension de la Figure 6. – , ce type de décharge est allumé pendant environ 1/10 de la période du champ électrique appliqué. Dans ces conditions, la décharge reste dans un régime homogène malgré la haute pression via ce qu'on appelle communément l'effet mémoire [11] lié au piégeage des particules chargées dans l'espace interélectrodes d'un demi-cycle de la tension appliquée à l'autre [6].

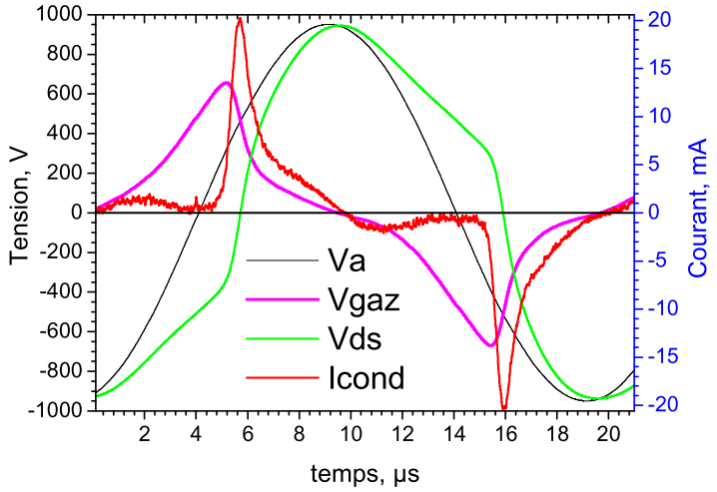

Figure 6. – Tension appliquée entre les électrodes (Va), tension dans le gap gazeux (Vg), tension appliquée au diélectrique (Vds) et courant de conduction en fonction du temps (Icond), calculé à partir des mesures du courant et de la tension Va par un modèle électrique [57].

Décharge de Townsend

Dans le reste de ce chapitre, une décharge analogue aux décharges de Townsend observée à des faibles fréquences d'excitation est observée. Malgré certaines différences, notamment concernant les mécanismes d'effet mémoire à l'œuvre, les deux types de décharges seront définies par le terme décharge de Townsend dans ce chapitre.

En augmentant la fréquence d'oscillation du champ électrique, la transition de la décharge luminescente à une décharge de Townsend basse fréquence s'explique par une diminution de l'excursion des ions dans l'espace interélectrodes [21], [23]. En effet, à partir de l'équation du mouvement des ions de masse m_i et de charge q_i dans un champ électrique sinusoïdale de pulsation ω et d'amplitude E_0, on peut écrire, en négligeant les processus collisionels :

$$m_i \frac{d^2 \boldsymbol{x_i}}{dt^2} = q_i[\boldsymbol{E_0}\, cos(\omega t)]. \qquad 3$$

De ceci, on peut aisément remonter à une excursion maximale $\boldsymbol{x_i}$ des ions pendant une demi-période du champ électrique :

$$|x_i| = \frac{q_i E_0}{m_i \omega^2}. \qquad 4$$

Lorsque la fréquence d'excitation du champ électrique augmente, on peut imaginer un régime dans lequel l'excursion maximale des ions devient inférieure à l'espace interélectrodes. Ou encore, en admettant une vitesse des ions $\boldsymbol{v_i}$ uniquement liée à leur mobilité μ_i dans le champ électrique oscillant $\boldsymbol{E_0}\, cos(\omega t)$, on peut imaginer des conditions dans lesquelles le temps que mettent les ions pour traverser le gap gazeux devient inférieur à la demi-période du champ électrique appliqué. Pour des ions NH_3^+ dans une DBD Ar + 133 ppm de NH_3 produite dans un gap de 1 mm [21], la Figure 7. – montre que cette transition s'effectue à partir de 200 kHz.

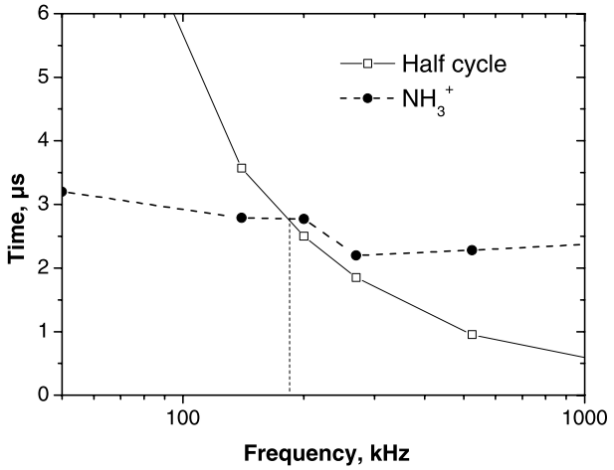

Figure 7. – Comparaison du temps de demi-période de la tension appliquée avec le temps que mettent les ions pour traverser le gap gazeux (en pointillé) en fonction de la fréquence d'excitation [21].

Par ailleurs, si l'excursion des ions devient trop faible pour atteindre les parois alors que celle des électrons demeure supérieure à l'espace interélectrodes, $n_i \gg n_e$ en tout point de l'espace. Dans ces conditions, on obtient une décharge de Townsend similaire à celle des décharges en courant continu à très faibles courants [37]. Si le niveau d'ionisation et faible, le champ électrique géométrique n'est que très peu déformé par la charge d'espace et l'émission optique est

maximum au voisinage de l'anode (voir Figure 8. –) [58]. Contrairement à la décharge luminescente, il est important de noter que la décharge de Townsend demeure allumée sur un temps relativement long, environ la moitié de l'alternance de la tension appliquée. De plus, comme le montre la Figure 8. – , il n'y a aucune chute de la tension du gaz après le claquage ; le gaz reste capacitif et le courant s'ajuste de façon à compenser la variation de la tension appliquée, il s'agit du plateau de Townsend [37].

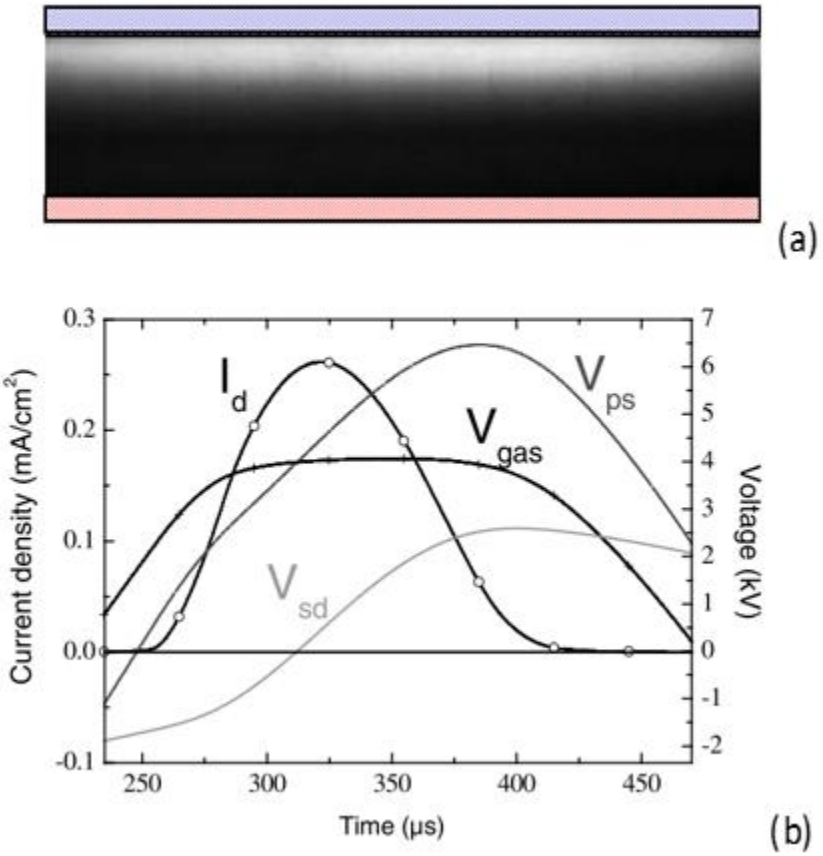

Figure 8. – (a) Photographie du gap gazeux d'une DBD dans un régime de Townsend (la cathode est en bas et l'anode est en haut), temps d'exposition 10 ns et (b) tension appliquée (V_{ps}), tension gaz (V_{gaz}), tension dans les diélectriques solides (V_{sd}) et courant de décharge (I_d), en fonction du temps, sur une demi période dans une décharge de Townsend [58].

Décharge radiofréquence en régime α (ou Ω)

Lors de l'augmentation de la fréquence à partir de la décharge de Townsend, il se passe un phénomène analogue à celui qui a entrainé la transition luminescent-Townsend, mais cette fois concernant les électrons. En admettant une vitesse des électrons $\boldsymbol{v_e}$ uniquement liée à leur mobilité μ_e dans le champ électrique oscillant $\boldsymbol{E_0}\, cos(\omega t)$, on peut en effet imaginer des conditions dans lesquelles le temps que mettent les électrons pour traverser le gap gazeux devient inférieur à la demi-période du champ électrique appliqué. Dans une DBD dans Ar-NH_3 et un gap de 1 mm [21], en supposant une mobilité électronique de 340 $cm^2V^{-1}s^{-1}$ [59], la Figure 9. – montre que cette transition s'effectue à partir de quelques MHz. Dans ce régime, les électrons produits par la multiplication électronique sont moins perdus aux parois, entrainant une augmentation de la densité électronique dans le temps et permettant à la décharge de rester allumée entre deux alternance [60] ; c'est la décharge radio fréquence (RF). Comme le montre la Figure 9. – , les électrons commencent à être piégés dans le gap avec des excursions, dans le champ électrique oscillant, inférieures à l'espace interélectrodes.

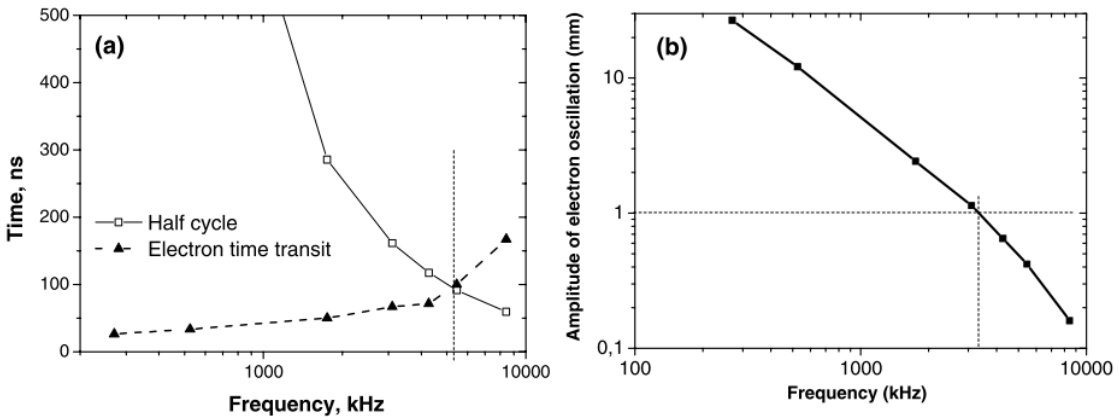

Figure 9. – (a) Comparaison entre le temps de demi-période et le temps de transit des électrons pour traverser le gap de 1 mm dans un mélange Ar + 133 ppm de NH_3, (b) Amplitude de l'oscillation des électrons en fonction de la fréquence d'excitation. La tension considérée ici est la tension maximum permettant de rester dans une DBD homogène [21].

Dans la littérature, ce régime est communément nommé régime RF **α** suite à l'observation de similitudes avec les plasmas RF à basse pression. Cependant, cette appellation est critiquée et on voit de plus en plus le terme de régime **Ω** [61]–[63]. En effet, la RF **α** à basse pression est souvent associée à un chauffage stochastique des électrons (lié au transfert de quantité de mouvement issu des variations de longueur de la gaine) [37] alors qu'à la pression atmosphérique, ce chauffage est purement ohmique (du aux collisions électrons-neutre), d'où le **Ω** [64], [65].

Pour mieux illustrer les différences entre la décharge luminescente, la décharge de Townsend et la décharge **α**, la Figure 10. – compare les distributions spatiales des émissions lumineuses à 50 kHz (glow), 250 kHz (Townsend) et 1,3 MHz (**α**). Lorsque le maximum d'intensité lumineuse est à la cathode (à droite sur la Figure 10. –), c'est le régime luminescent. Avec l'augmentation de la fréquence, l'émission se trouve majoritairement à l'anode (à gauche sur la Figure 10. –), caractéristique des décharges de Townsend. Enfin, en RF, l'émission lumineuse devient globalement répartie dans le gap, ce qui est conforme avec une multiplication électronique dominée dans le volume.

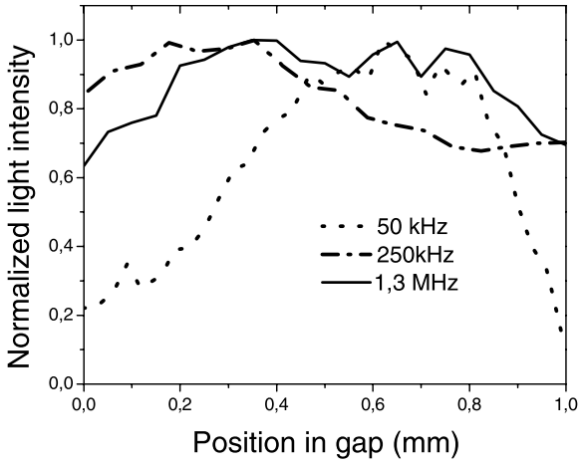

Figure 10. – Profil normalisé de la distribution spatiale de la lumière émise entre l'anode (à gauche) et la cathode (à droite) quand l'intensité lumineuse est maximale pour plusieurs fréquences d'excitation [21].

Décharge radiofréquence en régime γ

Avec l'augmentation de la puissance fournie à une décharge RF **α** (ou **Ω**), et donc avec l'augmentation de l'amplitude de la tension RF, la répartition de lumière est largement modifiée, suggérant un changement de régime. Comme le montre la Figure 11. – , l'émission lumineuse qui était principalement située dans le volume en lisière de gaine en RF **α** (ou **Ω**) se décale progressivement dans la gaine au voisinage des électrodes avec l'augmentation de la puissance appliquée à la décharge. Ce phénomène est observé en hélium comme en argon. Il est d'autant plus visible en hélium, où la puissance maximum fournie à la décharge tout en restant en régime homogène est plus importante qu'en argon [63].

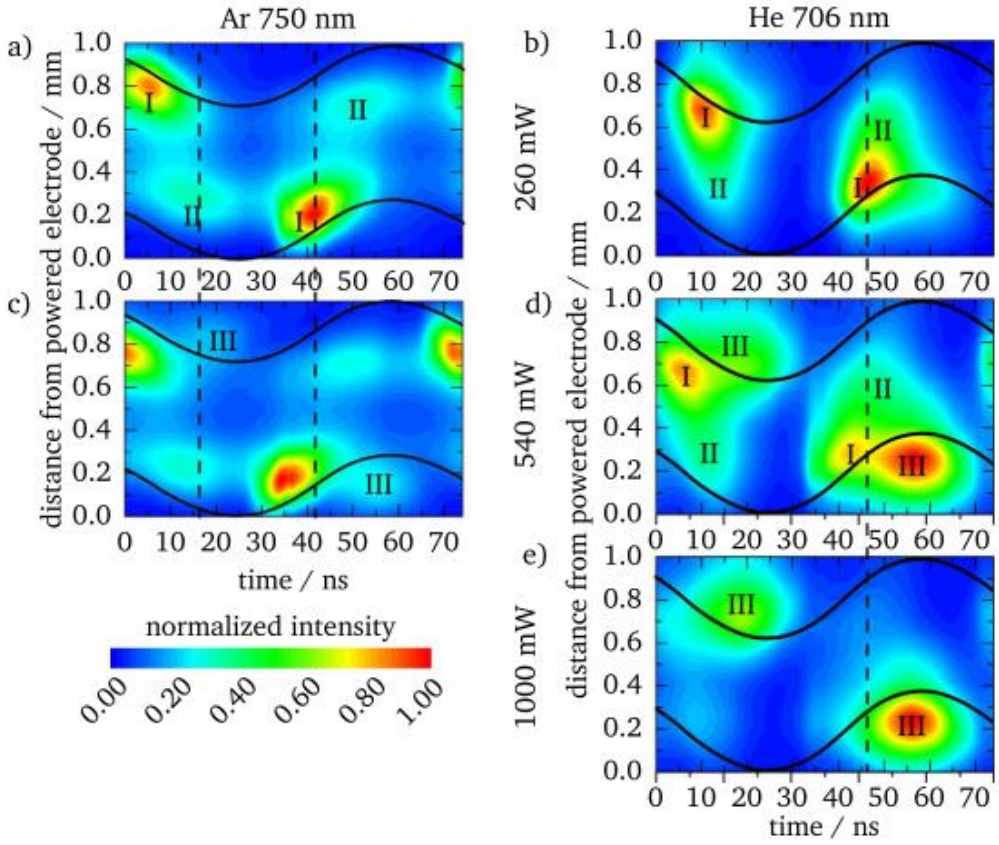

Figure 11. – Émission lumineuse résolue dans l'espace et dans le temps sur une période RF de la tension appliquée en fonction de la puissance appliquée à la décharge pour l'argon à 750 nm à gauche, pour l'hélium à 706 nm à droite : (a), (b) 260 mW, (c), (d) 540 mW et (e) 1000 mW.

Cette transition entre RF **α** (ou **Ω**) et RF **γ** survient lorsque l'intensité du champ électrique (majoritairement localisé dans la gaine) augmente. Ce phénomène permet aux électrons secondaires crées à la paroi d'être fortement repoussés vers le plasma par la chute cathodique et ainsi pouvoir créer des avalanches électroniques dans la gaine suffisamment importantes pour permettre le critère d'auto-entretien d'un claquage de Townsend (voir Équation (1)). On est alors en présence d'une décharge dont la majorité des électrons sont créés dans la gaine, plutôt que dans le volume du plasma [66]. Le passage en régime **γ** est donc non seulement dépendant de la valeur du coefficient d'émission secondaire éponyme et donc de la nature du matériau diélectrique [66]–[68], mais aussi du coefficient d'ionisation effectif du gaz, **α**. Ainsi, dans une décharge dans l'argon, le régime **γ** n'est typiquement pas atteint car la décharge se localise et chauffe l'électrode. En revanche, dans un mélange Penning Ar + NH_3, il devient observable lorsque l'amplitude de la tension RF est suffisamment élevée. D'après Dünnbier et al. [69], l'énergie électrique nécessaire pour observer la transition de **α** à **γ** est une fonction de la fréquence à la puissance 3/2.

Pour résumer, les différents régimes d'opération des DBDs en fonction de la fréquence d'excitation sont majoritairement contrôlés par l'excursion des particules chargées dans le champ électrique oscillant (voir Figure 12. –). Or, dans ces conditions dites de haute fréquence, les nanoparticules pertinentes pour la synthèse de couches minces nanocomposites sont confinées dans l'espace interélectrodes : de plus basses fréquences sont requises pour les déposer à la surface du substrat [28], [30], [31]. Pour ce type d'applications, les décharges dites hybrides combinant des signaux électriques de basse et de haute fréquence semblent beaucoup plus appropriées [29]–[32].

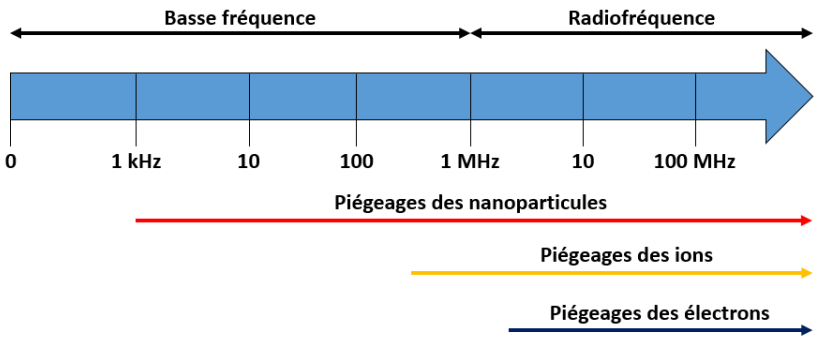

Figure 12. – Transport des espèces chargées en fonction de la fréquence dans un gap millimétrique d'une DBD d'Ar-NH_3.

Régimes de décharges homogènes en double fréquence dans les gaz nobles

En lien avec les objectifs de cette thèse de doctorat, il est judicieux d'approfondir la physique des DBDs reposant sur des combinaisons de fréquences. Plus spécifiquement, inspirés des travaux publiés dans la littérature, on va se pencher sur l'association de 2 basses fréquences ainsi que sur la combinaison d'une basse fréquence avec une radio fréquence. La double fréquence RF-RF n'étant pas adaptée pour les applications visées, elle ne sera pas abordée dans ce travail.

Double fréquence BF-BF

Ce cas particulier de double fréquence est très peu étudié dans la littérature, uniquement deux publications mentionnent son utilisation [70], [71]. On s'aperçoit que l'ajout d'une fréquence de polarisation de 1 kHz à une décharge luminescente d'Ar-NH_3 à 50 kHz ne provoque pas de changement significatif de la décharge initiale. Ces résultats sont notamment visibles par des données de calculs qui indiquent que la puissance absorbée et dissipée par les électrons et les densités de particules chargées ne varient que peu avec l'amplitude de la tension de basse fréquence [70]. De plus, comme le montre la Figure 13. – , la tension appliquée au gaz demeure constante malgré l'ajout du signal à 1 kHz. Dans ces conditions, la charge du diélectrique par la décharge 50 kHz compense les variations engendrées par la tension de 1 kHz.

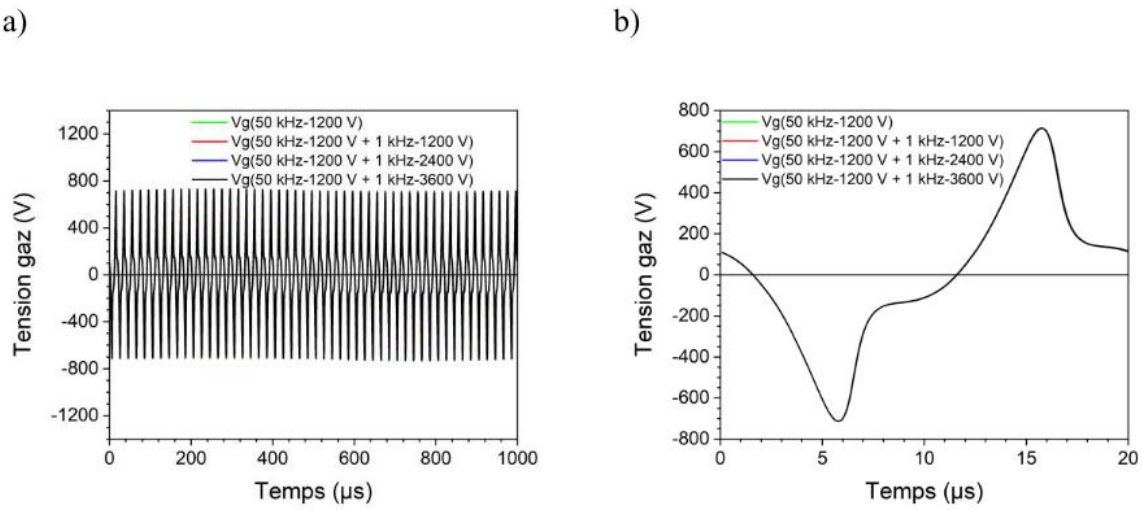

Figure 13. – Variation de la tension gaz pour quatre décharges (50 kHz-1200 V ; 50 kHz-1200 V + 1 kHz-1200 V ; 50 kHz-1200 V + 1 kHz-2400 V ; 50 kHz-1200 V + 1 kHz-3600 V) au cours d'un cycle (a) 1 kHz et (b) 50 kHz [70].

Cet effet de compensation via la charge du diélectrique est due au rapport de la fréquence haute sur la fréquence basse : en ayant assez de périodes 50 kHz, il devient en effet possible de compenser l'effet de la 1 kHz [72]. On retrouve ce concept avec les émissions de l'argon à 696 nm et de NH à 324 et 335 nm. Lors de l'application d'une tension 1 kHz sur une décharge homogène à 188 kHz, aucun changement d'émission pour les 3 longueurs d'onde n'est observable, et ce, quelle que soit l'amplitude de la tension de 1 kHz [71]. Par contre, dès que les deux fréquences BF deviennent plus proches, ici 50 kHz – 188 kHz ou 100 kHz – 188 kHz, l'augmentation de la tension de la plus basse fréquence va augmenter les émissions pour les 3 fréquences comme le montre la Figure 14. – .

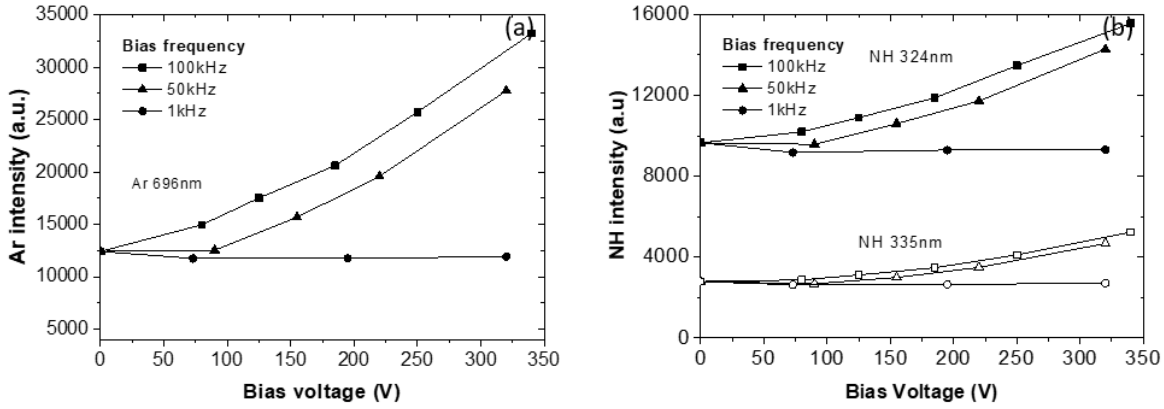

Figure 14. – Intensité des émissions en fonction de la tension V_l appliquée à une fréquence f_l = 1 kHz, 50 kHz ou 100 kHz, pour (a) la raie d'Ar à 696 nm, (b) les bandes des NH à 324 et 336 nm [71].

Ces résultats montrent les limites de tels régimes lorsque les deux fréquences BF sont éloignées, la plus basse fréquence est alors compensée par la plus haute du fait de la charge du diélectrique. Lorsque les deux fréquences sont du même ordre de grandeur, un effet est ressenti sur les émissions lumineuses. Le peu de littérature concernant ce type de décharges nous empêche néanmoins de pousser les analyses physiques plus loin.

Double fréquence BF-RF

Une alternative à l'utilisation d'une décharge double fréquence BF-BF est de remplacer une des basses fréquences par une radiofréquence. Lors de l'ajout d'une RF à la BF, plusieurs comportements ont été observés en fonction de l'amplitude de la tension BF [50], [71]. En supposant la tension RF suffisamment élevée pour pouvoir engendrer une décharge à elle seule, mais pas assez pour passer en RF **γ**, on peut identifier 3 régimes distincts :

- Lorsque la tension BF est très faible, voire nulle, comme on peut s'y attendre, on est en présence d'une RF en mode **α** (ou **Ω**).

- Avec une tension BF plus élevée (ce critère dépend du gaz, du gap et de la fréquence de la RF), la décharge reste en mode **α** (ou **Ω**). Néanmoins l'intensité de la décharge est modulée. Plus la tension BF est forte plus la décharge RF est atténuée.
- Avec une tension BF encore plus élevée, on va pouvoir rentrer dans un régime d'alternance entre une RF **α** (ou **Ω**) et un mode RF **γ**, c'est dans ce mode que la puissance la plus élevée pour une décharge homogène est atteinte. Il est donc d'un grand intérêt pour les applications. [50].

La Figure 15. – aide à mieux comprendre ces aspects. Celle-ci présente la mesure de la tension appliquée sur les électrodes, du courant et de l'émission lumineuse entre 200 et 900 nm sur une demi-période BF pour les 3 différents régimes de décharge. En (a), la tension BF est nulle, on est dans le cas d'une RF **α** (ou **Ω**) avec le maximum d'émission lumineuse au centre du gap, comme dans la Figure 10. – . En (b), lorsque la tension BF augmente, l'émission lumineuse reste maximum près du centre du gap, ce qui est caractéristique du régime RF **α**. Cependant, une variation est observée en fonction du temps. Plus spécifiquement, le maximum d'intensité lumineuse correspondant au régime RF **α** apparaît un peu avant que la tension BF appliquée passe par zéro, c'est à dire lorsque la tension appliquée sur le gaz (ou tension gaz) correspondante est nulle ou très faible. La zone où l'intensité lumineuse est la plus faible est le moment où la tension gaz BF est maximum. Dans ce dernier cas, les ions présents dans le gap dérivent vers la cathode BF où ils sont « perdus » par recombinaison. L'effet de la tension BF est alors d'augmenter la perte d'espèces énergétiques à la paroi et donc de diminuer la puissance absorbée ou dissipée par les électrons de la décharge ; c'est le régime **α** (ou **Ω**) atténué.

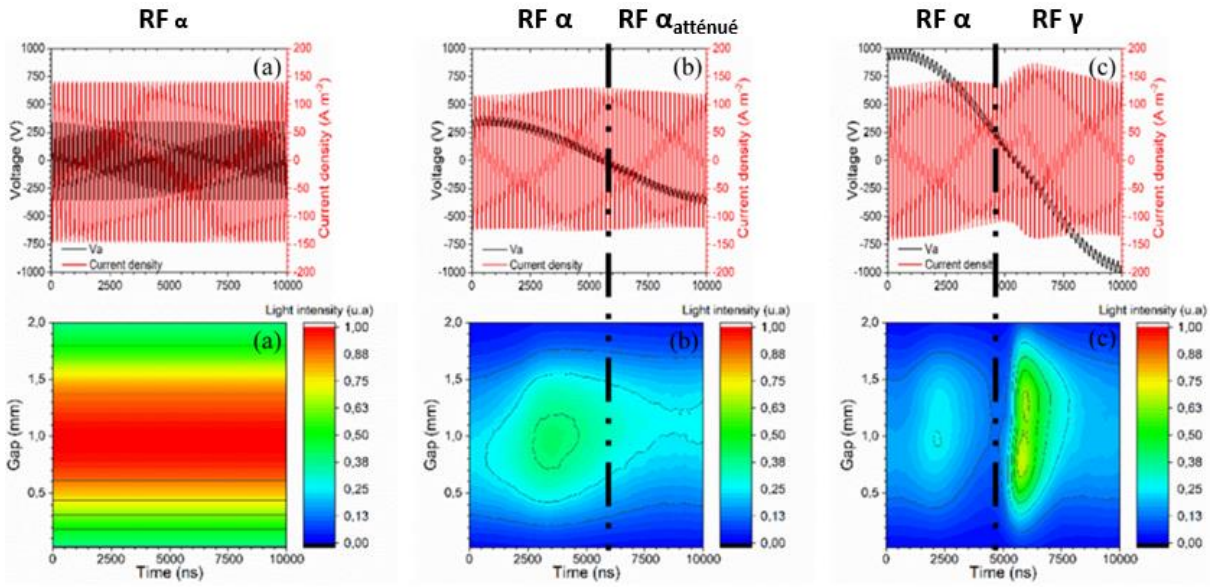

Figure 15. – Densité de courant (en noir), tension appliquée (en rouge) et émission de la décharge résolue dans le temps et l'espace sur une demi période BF pour (a) une RF en régime α, (b) une RF-BF en régime α - α atténué, (c) une RF-BF en mode α - γ [50].

En (c), on retrouve le régime RF **α** lorsque la tension au gaz BF est nulle ou proche de 0. Cependant, lorsque cette tension devient maximum, les ions sont toujours perdus à la paroi, mais le champ électrique de la gaine permet aux électrons secondaires d'engendrer des avalanches électroniques dans la gaine. On atteint alors le critère d'auto-entretien du claquage de Townsend dans la gaine (plutôt que dans le volume du plasma) ; c'est le régime **γ** des plasmas RF. Ce régime est donc une conséquence de l'application simultanée de tension BF et RF lorsque les deux polarités des tensions sont les mêmes, c'est-à-dire quand l'électrode est à la fois cathode pour la basse fréquence et cathode pour la radiofréquence. Ainsi, les électrons secondaires produits par la dérive des ions à la cathode se multiplient suffisamment dans la gaine pour compenser la perte des ions [50]. Selon les données de la Figure 15. – , ce régime a lieu pendant environ 10% du temps de la période BF, ce qui est susceptible de limiter le chauffage du gaz et donc de l'électrode.

Pour résumer, dans les DBDs hybrides produites par des champs électriques de basse et de haute fréquence, le régime RF **α** (ou **Ω**) est contrôlé, par définition, par l'amplitude de la tension RF avec une faible contribution de la BF. Quant aux régimes RF **α** atténué et RF **γ**, ils sont davantage contrôlés par la tension appliquée sur le gaz, cumulée par les deux fréquences. Ainsi, en faisant varier l'amplitude de la tension RF dans cette configuration RF-BF, on peut imaginer qu'il serait possible de jouer sur la contribution respective de ces différents régimes, ce qui offrirait plusieurs possibilités pour les applications. Nous reviendrons sur ces aspects au chapitres 3 et 4. Par ailleurs, il est intéressant de noter que la double fréquence BF-RF permet aussi d'augmenter la stabilité de la DBD en empêchant la transition vers un régime filamentaire via l'allumage constant de la décharge par le signal RF [73]–[75].

Propriétés des décharges homogènes en simple et double fréquence dans les gaz nobles

Cette partie vise à dresser un portrait des propriétés fondamentales des différentes décharges précédemment énoncées pour pouvoir déterminer le ou les régimes de décharges les plus adaptées selon l'application envisagée. Ainsi, après s'être intéressés aux mécanismes de transition entre les régimes de décharge en simple et en double fréquence, on va maintenant se pencher sur les principales grandeurs caractéristiques de ces DBDs. La première partie concerne les décharges homogènes en simple fréquence, la deuxième les décharges en double fréquence.

DBD homogènes simple fréquence

Décharge luminescente ou *glow*

Comme vu précédemment, le premier régime de décharge homogène à être atteint dans un mélanger Penning lorsque la fréquence d'oscillation du champ électrique augmente est la décharge luminescente (*glow*). Cette décharge, obtenue entre 10 et 200 kHz dans les mélanges

Penning Ar/NH_3 et pour un gap de 1 mm [21], est caractérisée par l'apparition d'une chute cathodique permettant de confiner les électrons dans la colonne positive et donc d'assurer une ionisation conséquente. Ainsi, pendant environ un dixième de la période, plusieurs auteurs rapportent des densités de particules chargées maximales dans l'hélium et dans l'argon d'environ 10^{10} à 10^{11} cm^{-3} [19]. Quant aux métastables qui représentent un réservoir d'énergie important pour ces décharges, leur population mesurée par spectroscopie optique d'absorption est elle aussi de l'ordre de 10^{11} cm^{-3} [19]. Cependant, dû au court temps d'allumage de la décharge, la puissance moyenne absorbée et dissipée par les électrons reste relativement faible, de l'ordre de quelques dixièmes de watts par cm^2 au maximum [19]. Ces fortes densités d'électrons sur un temps de décharge relativement court entrainent une densité de courant maximale relativement importante, de l'ordre de 1 à 10 $mA.cm^{-2}$ [19], [41]. Quant à la température des électrons, des mesures de spectroscopie optique d'émission couplées aux prédictions de modèles collisionnel-radiatifs indiquent des valeurs autour de 1 eV lors de l'allumage et d'environ 0.3 eV au maximum du pic de courant dans l'hélium [76], mais aussi dans les mélanges Penning Ar-NH_3 [77]. Ces valeurs de densités et de températures peuvent néanmoins varier en présence d'espèces réactives supplémentaires dans le plasma. Par exemple, en présence d'une forte concentration de N_2 ou de O_2 dans une décharge luminescente d'hélium, on rapporte une baisse importante de la population de métastables et une hausse de la température des électrons [78]. A l'opposé, la présence d'une fraction de gaz moléculaire, induisant un mélange Penning, diminue la température des électrons au claquage, ce qui se répercutera plus globalement sur la décharge [79].

Décharge de Townsend

En augmentant la fréquence, nous avons décrit précédemment la transition du régime *glow* vers un régime similaire a celui des régimes Townsend à basse fréquence. Dans ces conditions, il est généralement admis dans la littérature que l'ionisation devient moins importante, entrainant ainsi des valeurs de densités maximales d'électrons et d'ions plus faibles, respectivement 10^7-10^8 et 10^{10} cm^{-3} (rappelons que $n_i \gg n_e$ dans la décharge de Townsend [37]). La forte différence entre la densité d'électrons et d'ion s'explique par la dérive continue des électrons vers l'anode

puisque le champ est quasi-uniforme sur l'ensemble du gap. Le maximum de la densité d'électron est d'ailleurs observé lorsque la tension est nulle. Les courants de décharge sont aussi plus faibles que ceux observés dans la décharge luminescente, c'est à dire de l'ordre de 0.1 à 5 $mA.cm^{-2}$. Par contre la densité maximale de métastables est, elle, relativement élevée. Celle-ci dépends de la durée de vie des métastables et par exemple dans l'azote, la densité de $N_2(A)$ est de l'ordre de 10^{13} cm^{-3} [19]. La faible densité de particules chargées peut néanmoins laisser penser que la puissance transmise à la décharge est faible. Or, comme elle est allumée pendant un temps plus important que la *glow* (voir Figure 6. – et Figure 8. –) [19], [41], les puissances transmises (de l'ordre de quelques $W.cm^{-2}$) s'avèrent en réalité supérieures [21], [58].

Décharge radiofréquence en régime α (ou Ω)

Pour les applications visées dans ce travail de doctorat, la décharge luminescente à basse fréquence semble ainsi très intéressante, particulièrement pour le dépôt de nanoparticules [28], [30], [31]. Cependant, elle est peu puissante de sorte que les vitesses de dépôt des couches minces demeurent faibles [19], [20]. Un des moyens d'augmenter la vitesse de dépôt est d'augmenter la fréquence du kHz vers le MHz [21]–[25]. En effet, en atteignant le régime RF **α** (ou **Ω**), la Figure 16. – montre que la vitesse de dépôt peut augmenter de manière significative grâce à de plus fortes concentrations de précurseurs et de puissances. De plus, la tension nécessaire au claquage en régime RF est environ 3 fois plus faible que celle requise pour les champs électriques de basse fréquence [21].

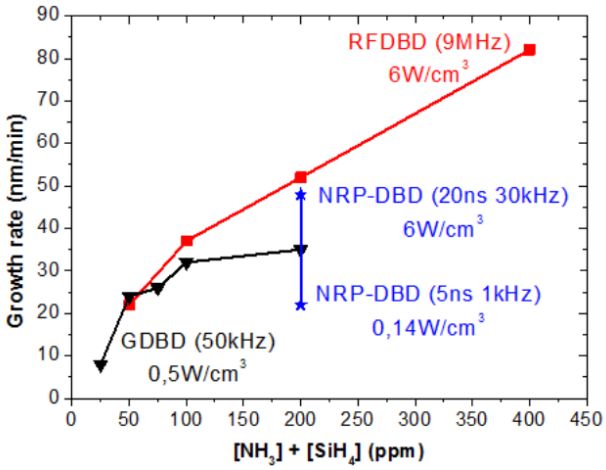

Figure 16. – Vitesse de dépôt du SiN en fonction de la concentration de précurseur totale pour différents régimes de décharge [27].

Le passage de la BF à la RF est accompagné d'une augmentation significative de la densité électronique. Dans ces conditions, plusieurs auteurs ont donc noté l'apparition d'un continuum d'émission attribué à un Bremsstrahlung [80]–[85]. Dans les plasmas faiblement ionisés comme les DBDs, ce continuum, aussi appelé rayonnement de freinage, est principalement issu d'interactions entre les électrons et les particules neutres [82], [85]. De par son intensité et sa distribution spectrale, il permet d'extraire des valeurs de densités et de températures des électrons. Pour les plasmas RF à 13.56 MHz dans l'argon à la pression atmosphérique, les valeurs obtenues sont comprises entre 1.9 et 2.5 eV pour T_e et 3x10^{11} et 6x10^{12} cm^{-3} pour n_e [24], [82], [84]–[86]. Il faut toutefois être prudent avec les valeurs de T_e obtenues des mesures spectroscopiques [87] puisque, selon les conditions opératoires, des études récentes ont montré que la fonction de distribution en énergie des électrons pouvait s'écarter considérablement d'une simple distribution de Maxwell-Boltzmann [88].

Parmi les grandeurs facilement accessibles expérimentalement, il y a la tension efficace appliquée au gaz, $\mathrm{V_{g_{RMS}}}$, et la densité de courant efficace de décharge, $j_{d_{RMS}}$, qui permettent d'estimer des valeurs de densités électroniques moyennes n_e [22]:

$$j_{d_{RMS}} = n_e e \mu_e \frac{V_{g_{RMS}}}{d} \qquad 5$$

où e est la charge élémentaire, μ_e est la mobilité des électrons et d est la distance interélectrodes. Par exemple, la Figure 17. – présente l'effet de la fréquence d'excitation du champ électrique sur la densité d'électrons dans une DBD dans l'hélium [22] et l'argon [84]. Tel qu'attendu, n_e augmente avec la fréquence, i.e. avec la transition vers le régime RF **α** (ou **Ω**) [22]. Sur cette même gamme de fréquences, n_e augmente également avec la puissance transmise à la décharge. Par ailleurs, on note que la puissance augmente de plus d'un facteur 10 entre la BF et la RF pour l'hélium. Des variations similaires ont été observées dans l'argon [84] et les mélanges Penning Ar-NH_3 [21].

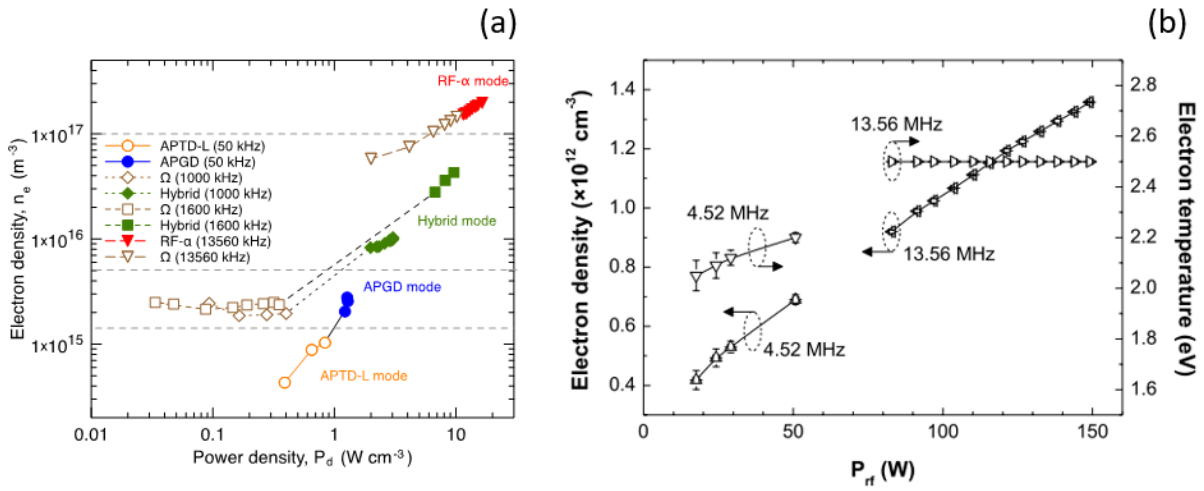

Figure 17. – Corrélation entre la densité d'électrons et la puissance d'une DBD homogène dans l'hélium (a) [22] et dans l'argon (b) pour différentes fréquences d'excitation [84].

Pour fins de comparaisons, en combinant des mesures électriques et les prédictions d'un modèle fluide basé sur l'équation du bilan d'énergie des électrons, Golda et al. [63] arrivent à 9x10^{11} cm^{-3} pour n_e et 1.2 eV pour T_e dans l'argon et 0.8x10^{11} cm^{-3} et 1.9 eV pour n_e et T_e dans

l'hélium. Les valeurs de T_e obtenues des spectres d'émission optique de l'hélium couplés aux prédictions de modèles collisionnels-radiatifs sont toutefois plus faibles [22].

Décharge radiofréquence en régime γ

La Figure 18. – compare la puissance absorbée et dissipée par les électrons pour une décharge RF **α**, la transition de RF **α** vers RF **γ**, ainsi que pour une décharge RF **γ** [89]. En faisant attention à l'échelle des différents graphiques, on se rend compte que la transmission de puissance est bien plus importante dans la gaine que dans le volume en **γ**. De plus, elle est fortement supérieure à celle dans le volume et aux abords de la gaine en **α** [66]. Tel que discuté précédemment, cette transition de **α** à **γ** se traduit par une contribution de l'émission secondaire bien plus importante dans la création d'électrons ; on passe respectivement de 3% à 17% [66]. Ce phénomène s'accompagne évidemment d'une augmentation de la température électronique maximale moyenne dans la gaine, de 4.7 à 10,3 eV [68]. Cependant, une fois le régime **γ** établi, la création d'électrons secondaires affecte uniquement la densité électronique, tandis que la température électronique n'est quasiment pas modifiée [90].

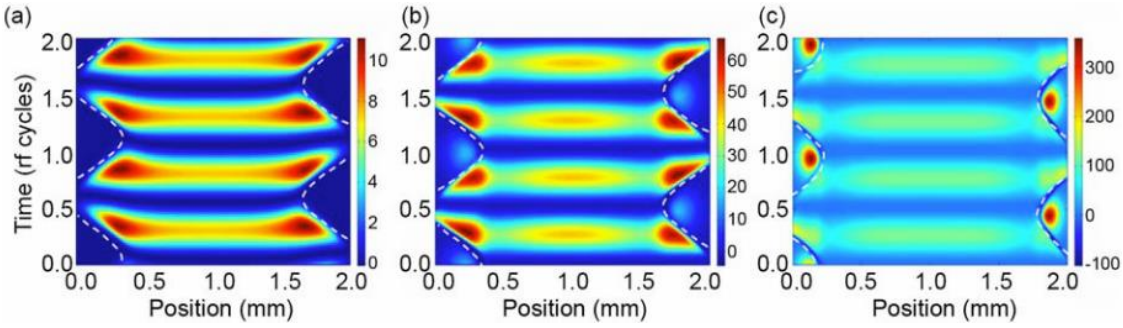

Figure 18. – Puissance absorbée par les électrons (mW.cm^{-3}) calculés à partir de données de simulations, (a) en mode α, (b) pour la transition α-γ, (c) en mode γ. [89]

Cette augmentation de puissance totale fournie à la décharge de plus d'un facteur 20 se manifeste aussi par une augmentation significative de la température du gaz de 340 K (juste avant

la transition) à 530 K (juste après le passage en régime **γ**) [91]. Dans certaines conditions le passage au régime **γ** s'accompagne aussi d'une constriction de la décharge [92], [93].

Pour résumer, la décharges RF **α** se montre fort attrayante par sa densité d'espèces énergétiques assez élevée. Si une application nécessite une densité encore plus importante, la RF **γ** semble toute indiquée. Cependant, on ne pourra pas transiter en **γ** sans risquer d'endommager les substrats à traiter ou les couches à synthétiser du fait de la forte augmentation de la température du gaz. Pour augmenter la densité de puissance fournie à la décharge sans forcément augmenter la température du gaz, il est possible d'ajouter une seconde modulation à une basse fréquence pour exacerber le bombardement ionique.

DBD homogènes en double fréquence

Double fréquence BF-BF

Tel que décrit précédemment, le manque de littérature concernant les décharges en double fréquence BF-BF empêche d'avoir des données chiffrées concernant son utilisation. On est cependant capable de dire, à la vue des éléments précédents, qu'elle sera forcément la moins puissante des décharges double fréquence abordées dans ce travail, donc peu recommandée pour la synthèse de couches minces nanocomposites.

Double fréquence BF-RF

Dans le chapitre précédent (en particulier à la Figure 15. –), on a abordé la physique des DBDs RF-BF et on a identifié différents modes de décharges selon l'amplitude de la tension BF. Il faut cependant faire attention dans l'utilisation des données quantitatives de telles décharges. En effet, ici, la nature des gaz, les tensions (ou puissances) appliquées ou encore les fréquences RF et BF sont amenés à varier suivant les références utilisées. Pour fins de comparaisons, les différents régimes de décharges ont donc été décrits à l'aide de l'influence de l'amplitude d'une

tension BF sur la RF dans les mêmes conditions que celles de la Figure 15. –) ; les données sont rapportées dans le Tableau 1. – [50].

		RF	Régime α - α atténué	Régime α - γ
Electrons ($*10^{10}$ cm^{-3})	**Densité moyenne**	**11**	**6.7**	**16**
	Densité max	**15**	**13**	**63**
Ions Ar_2^+ ($*10^{10}$ cm^{-3})	**Densité moyenne**	**13**	**9.6**	**21**
	Densité max	**16**	**12**	**64**
Métastables ($*10^{10}$ cm^{-3})	**Densité moyenne**	**4.3**	**3.1**	**13**
	Densité max	**23**	**21**	**42**

Tableau 1. – Densité d'électrons, d'ions et de métastables moyennes et maximales obtenues des calculs pour trois modes de décharge en double fréquence, en fonction de l'amplitude de la tension basse fréquence pour une décharge RF 5 MHz – BF 50 kHz [50].

À partir des données du Tableau 1. – , on note que l'ajout d'une tension BF modifie globalement les densités d'espèces de la décharge. Lorsque l'amplitude de la tension demeure faible, on diminue la puissance transmise à la décharge par rapport à une RF seule, ce qui se retrouve sur les densités d'espèces présentes dans la DBD. Lorsque l'amplitude de la tension BF augmente, on passe en mode **α** - **γ**. Cette transition s'accompagne d'une augmentation de la densité moyennes des espèces par rapport à la RF. Par exemple, pour l'exemple présenté, +45% pour la densité d'électrons, +62% pour les ions Ar_2^+ et +200% pour les métastables. Cette augmentation est encore plus importante si on s'intéresse aux densités maximales : le régime γ étant, comme nous l'avons vu à la Figure 18. – , localisé dans l'espace [89]. Il est à noter que la puissance absorbée ou dissipée par électron, elle, diminue avec l'augmentation de la tension BF, cette diminution est encore plus marquée lors du passage **α** – **γ** [94]. Ces résultats sur l'augmentation de la densité des électrons et de la diminution de la puissance absorbée ou dissipée par électron avec l'augmentation de la tension BF sont conformes avec les mesures récentes de n_e et T_e présentées

à la Figure 19. – pour l'argon [84]. Des comportements cohérents ont été rapportés par Zhang et al. [95] par des calculs de la fonction de distribution en énergie des électrons dans des conditions opératoires similaires (Figure 19. –). De ces travaux, on note une distribution de plus en plus maxwellienne avec l'augmentation de la tension BF pour une RF constante, ce qui est cohérent avec une augmentation de n_e.

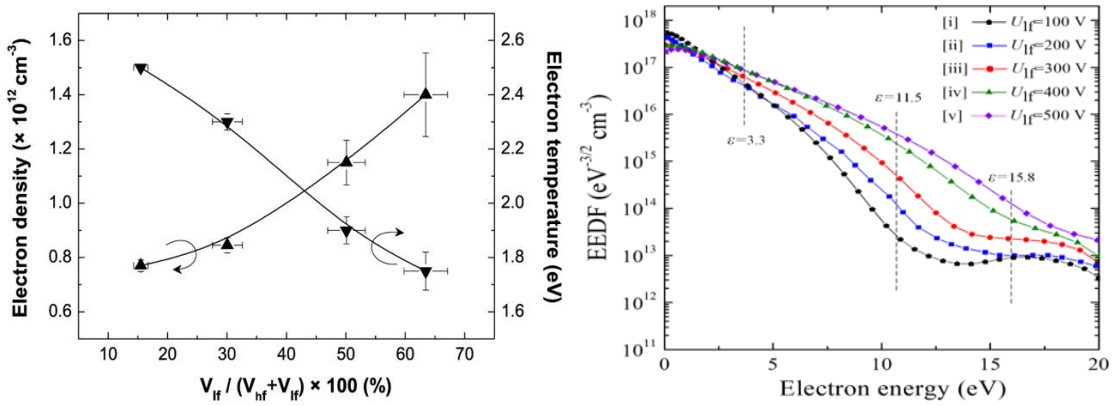

Figure 19. – Influence de la tension BF dans une décharge BF-RF sur la densité et la température des électrons (à gauche) [84] et la fonction de distribution en énergie des électrons (à droite) [95].

Enfin, à partir des travaux de Zhou et al. [96], il est possible de démontrer que la décharge double fréquence RF-BF possède une gamme de fonctionnement bien plus étendue que celle de la BF seule ou de la RF seule. Cette grande souplesse au niveau des propriétés fondamentales de la décharge se manifeste non seulement sur la densité d'électrons (voir Figure 20. –), mais aussi sur la température du gaz (voir Figure 21. –).

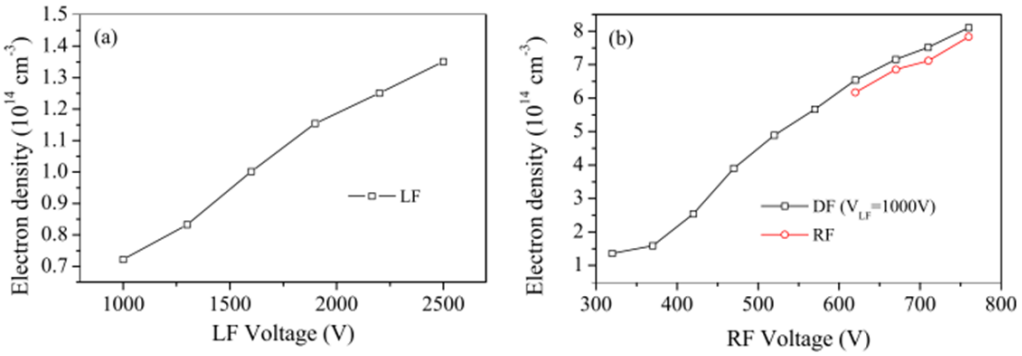

Figure 20. – Variation de la densité électronique avec la tension appliquée : (a) d'une DBD BF en fonction de la tension BF, (b) d'une RF et d'une DBD double fréquence (DF) en fonction de la tension RF [96].

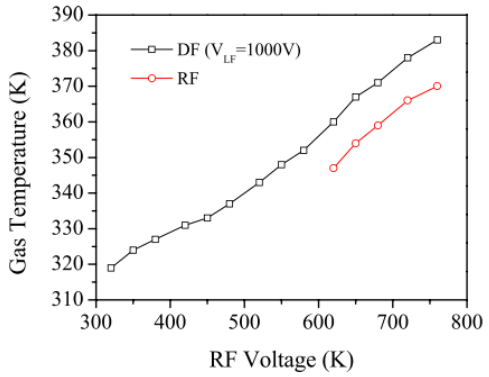

Figure 21. – Température du gaz d'une RF ou DF BF (V_{BF} = 1000 V)- RF, en fonction de la tension RF (en volt) [96].

Outre les propriétés particulières de cette décharge double fréquence BF-RF, il est toutefois primordial de remarquer que la très grande majorité des données présentées dans la littérature sont majoritairement issues de modèles. Il pourrait donc être pertinent d'étudier expérimentalement ces décharges double fréquence afin de pouvoir confronter les résultats de modélisation. Nous reviendrons sur ces points dans les chapitres 2 et 3 en ayant recours à des mesures par spectroscopie optique d'émission et d'absorption résolues dans le temps et dans l'espace couplées à des simulations [50], [94].

Conclusion

En somme, la décharge à barrière diélectrique dans des gaz rares à la pression atmosphérique opérée dans un régime homogène permet d'envisager plusieurs applications, particulièrement en synthèse de couches minces multifonctionnelles. Il faut cependant porter un intérêt tout particulier à la variation de chimie en fonction du temps de résidence et ainsi à la présence de produits de dissociation pouvant interagir avec les couches en formation. Dans ce travail de synthèse, on remarque qu'en variant la fréquence d'excitation du champ électrique ou encore de la puissance fournie à la décharge, différents régimes peuvent être obtenus. En simple fréquence, la puissance absorbée ou dissipée par les électrons dépend directement de la fréquence d'excitation. Cependant, il est nécessaire de prendre en compte l'augmentation de la température du gaz (significative à partir du régime RF **α** ou quand la puissance atteint les 10 $W.cm^{-2}$) dans le choix d'une condition opératoire spécifique selon l'application envisagée. L'intérêt des décharges double fréquence par rapport aux précédentes a aussi été exposé. En particulier, on a relevé que le domaine de fonctionnement devient bien supérieur à ceux des deux décharges prises séparément, et ce, autant d'un point de vue de la température du gaz que de la densité des électrons. De plus, la température électronique maximale et la densité électronique maximale semblent pouvoir être partiellement découplées. Enfin, la décharge RF-BF pourrait permettre de contrôler le transport des ions / radicaux ionisés sur un substrat tout en assurant une puissance transmise à la décharge suffisante pour l'obtention de vitesses de dépôt élevées. Même si ce type de décharge double fréquence semble tout indiqué pour un procédé de synthèse de couches minces [33], il demeure assez peu étudié d'un point de vue fondamental, en particulier au niveau expérimental.

Dans ce contexte, les objectifs de ce travail de doctorat visent justement à mieux comprendre cette DBD double fréquence RF-BF en couplant des diagnostiques électriques et optiques a de la modélisation. De plus, à l'aide de ces même méthodes, appliquées à des mesures en fonction du temps de résidence, il est possible de jeter les bases sur le rôle de la composition chimique sur la physique des DBDs produite dans un mélange Penning.

Chapitre 2 – Cinétique et auto-entretien de décharge à barrières diélectriques BF et RF-BF en présence d'émission induite par des photons VUV

Le chapitre précédent a mis en évidence l'influence de la fréquence d'excitation du champ électrique sur la physique d'une DBD homogène produite dans un mélange Penning à la pression atmosphérique. Suivant la décharge considérée, la localisation de l'ionisation et donc la création d'ions et d'électrons, n'aura pas lieu au même endroit dans le gap. Pour une décharge *glow*, l'ionisation a lieu majoritairement dans la gaine, principalement due à l'importante chute de tension qui y est présente, permettant aux électrons secondaires de créer une avalanche électronique. Dans ce cas de figure, la décharge est contrôlée par des mécanismes aux parois et dans la gaine, c'est-à-dire les deux coefficients de Townsend γ et α. Concernant la décharge RF, en augmentant la fréquence d'excitation du champ électrique, l'excursion des particules chargées et donc leur perte aux parois diminue, réduisant ainsi l'impact de l'émission secondaire et donc du γ sur le fonctionnement de la décharge. La décharge devient donc contrôlée quasiment uniquement par la multiplication électronique dans le *bulk*, i.e. par le premier coefficient de Townsend. Dans une décharge double fréquence RF-BF, on aura donc une alternance entre une décharge contrôlée par des électrons provenant de l'émission secondaire aux surfaces puis une décharge contrôlée par les électrons produits par une avalanche électronique dans le corps du plasma.

Précédemment, on a aussi observé, via l'étude des mélanges Penning, que le premier coefficient de Townsend effectif pouvait être modifié par la chimie du gaz plasmagène et l'intensité du champ électrique. Quant au second coefficient de Townsend, il est davantage contrôlé par la surface (matériau et état de surface) des parois que l'on considère, mais aussi par l'énergie et la

nature des éléments incidents. Or, l'impact des photons énergétiques sur la physique des DBDs homogène est peu documenté dans la littérature. De plus, en théorie, les décharges produites en Ar-NH_3 à la pression atmosphérique émettent de tels photons. Issus de la dissociation de l'excimère Ar_2^*, ces photons ne sont pas réabsorbés par la décharge et peuvent ainsi induire de la photoémission aux parois. Le sujet de ce chapitre est donc d'explorer le rôle possible des photons VUV (ou d'autres photons énergétiques) non réabsorbés dans le gap, sur la physique des DBDs produites dans les mélanges Penning Ar-NH_3. Tel que présenté au chapitre précédent, le critère d'auto-entretien d'une décharge est basé uniquement sur les flux d'ions aux parois. À la lumière de ces résultats, un nouveau critère d'auto–entretien permettant de prendre en compte ce phénomène de transport « instantané » dans le gap est proposé.

Les résultats sont présentés sous la forme d'un article publié dans Plasma Sources Science and Technology « R. Robert, G. Hagelaar, N. Sadeghi, R. Magnan, L. Stafford, and F. Massines, "Role of excimer formation and induced photoemission on the Ar metastable kinetics in atmospheric pressure Ar-NH3 dielectric barrier discharges," *Plasma Sources Sci. Technol.*, vol. 31, no. 6, p. 065010, 2022. »

Role of excimer formation and induced photoemission on the Ar metastable kinetics in atmospheric pressure Ar-NH_3 dielectric barrier discharges

Raphaël Robert[1,2], Gerjan Hagelaar[3], Nader Sadeghi[4], Romain Magnan[1], Luc Stafford[2], Françoise Massines[11]

[1]Laboratoire Procédés Matériaux et Énergie Solaire (PROMES, CNRS, UPR 8521), Rambla de la thermodynamique, 66100 Perpignan, France

[2]Département de physique, Université de Montréal, 1375 ave Thérèse-Lavoie-Roux, Montréal, Québec, H2V 0B3, Canada

[3] Laboratoire Plasma et Conversion d'Énergie (LAPLACE, CNRS, UMR5213), 118 Route de Narbonne, 31077 Toulouse, France

[4]Laboratoire Interdisciplinaire de Physique (LIPhy CNRS, UMR 5588), Laboratoire des Technologies de la Microélectronique (LTM, CNRS, UMR 5129), Université de Grenoble-Alpes, Grenoble, France

Abstract

Tunable diode laser absorption spectroscopy was used to record the space-and time-resolved number density of argon metastable atoms, Ar($1s_3$) (Paschen notation), in plane-to-plane dielectric barrier discharges operated in a Penning Ar-NH_3 mixture at atmospheric pressure. In both low-frequency (LF 650 V, 50 kHz) discharges and dual LF-radiofrequency (RF 190 V, 5 MHz) discharges operated in α-γ mode, the density of Ar($1s_3$) revealed a single peak per half-period of the LF voltage, with rise and decay times in the sub-microsecond time scale. These results were compared to the predictions of a 1D fluid model based on continuity and momentum equations for electrons, argon ions (Ar^+ and Ar_2^+) and excited argon 1s atoms as well electron energy balance equation. Using the scheme commonly reported for Ar-based dielectric barrier discharges in the homogeneous regime, the Ar metastable kinetics exhibited much slower rise and decay times than the ones seen in the experiments. The model was improved by considering the fast creation of Ar_2* excimers through 3-body reactions involving Ar(1s) atoms and the rapid loss of Ar_2* by vacuum ultraviolet light emission. In optically thin media for such photons, they can readily reach the dielectric barriers of the DBD electrodes and induce secondary electron emission. It is shown that Ar_2* and photoemission play a significant role not only on the Ar metastable kinetics, but also on the dominant ionization pathways and possible α-γ transition in dual frequency RF-LF discharges.

Keywords: Dielectric barrier discharges, Tunable laser diode absorption spectroscopy, Dual-frequency discharges, Fluid modeling, Argon excited dimer, Photoemission.

Introduction

The use of dielectric barrier discharges (DBDs) at atmospheric pressure has experienced uninterrupted growth since the 2000s. Their field of applications is widening, ranging from surface engineering [97]–[103], control flow [104], [105], plasma catalyses [106], pollution control [107], or ozone production [108]–[110]. This diversification of applications is accompanied by the development of new DBD regimes [19]. In addition to the filamentary and patterned discharge regimes [111], [112], homogenous discharges in Townsend, glow or RF α and γ modes are also used [21], [22], [93], [113], [114], including for thin film deposition [19], [99]. New excitation waveforms for homogenous discharges have also been proposed, including dual-frequency [50], [71], [84], [115], frequency-shift keying [29], [30] or sawtooth tailored discharges [116]. In low-frequency (LF) plasmas, metastable states play a major role in maintaining the discharge in a homogeneous regime [117]. As a result of their very small diffusion transport, they can remain in the DBD gap from one cycle of the applied voltage to the other. This so-called memory effect can contribute to secondary electron emission at the walls and can induce a pre-ionization of the gas [118], [119]. In a Penning gas mixture, for example He with N_2 or Ar with NH_3, metastable species can also induce excitation and ionization at low applied voltage via stepwise excitation and ionization [6], [11], [41], [58], [77]. For atmospheric-pressure plasmas sustained in noble gases such as Ar, many authors have reported significant vacuum ultraviolet (VUV) emission [120]–[125]. While VUV photons at 104.8 and 106.7 nm emanating from Ar 1s resonant states (Paschen notation) are usually trapped due to high populations of ground-state Ar atoms (optically thick medium) [126], the continuum emission linked to argon excimers at 126 nm is characterized by much longer absorption lengths (optically thin medium) [125], [127]. Such photons can thus induce a number of additional surface and gas phase phenomena, including secondary electron emission [38]. However, the contribution of such mechanism was never explicitly explored for homogeneous DBDs.

In this work, tunable diode laser absorption spectroscopy (TDLAS) is used to record the population of metastable argon $1s_3$ atoms in plane-to-plane DBDs operated in a Penning Ar-NH_3 mixture at atmospheric pressure as a function of time at two locations in the inter-electrode gap for both LF and dual-frequency LF-RF excitations. Through a comparison of TDLAS measurements with the predictions of a 1D fluid model [50], [94], it is found that VUV photons emitted by Ar_2* dimers, created by 3-body reactions involving Ar(1s) species and two ground state Ar atoms, can

induce photoelectron emission at the dielectrics surface of the cathode and can thus play a very significant role on the physics driving Ar-based DBDs.

Experimental setup

The DBD examined in this study relies on two plane-to-plane 50 x 10 mm² metallic electrodes covered by 1 mm-thick 70 x 70 mm² dielectric plates made of alumina and separated by a 2mm gap. The discharge zone is thus fixed to a 50 x 10 x 2 mm^3 volume. The whole DBD cell is contained in an air-tighten chamber. Before each experiment, the chamber was pumped down to 10^{-5} bar and then flushed with Ar + 200 ppm of NH_3 at 3 standard liters per minute (SLM) flow rate. A needle valve between the chamber and the pumping pipe allows fixing the total pressure in the chamber to 1 bar. Considering the dimensions of the gap, the flow is laminar between dielectric plates. As shown in Figure 1, the top electrode is powered by a 50 kHz LF generator, while the bottom electrode is either grounded or powered by a 5 MHz RF generator. Note that, in a DBD, the applied voltage (V_a) is different from the voltage across the gap (V_{gas} – called "gas voltage" in this paper) due to the voltage drop across both top (V_{ds1}) and bottom (V_{ds2}) dielectric plates ($V_a = V_{ds1} + V_{gas} + V_{ds2}$). This voltage drop is caused by charges present in the discharge, collected on the dielectric surfaces, inducing a modification of the gas voltage. Here, LF and RF waveforms are both produced by a single generator (Keysight 33500B Series), which synchronizes their phases. To produce dual-frequency discharges, the LF signal at 50 kHz is brought to the reactor through an audio amplifier (Crest CC4000) connected to a bridged resistance and a step-up voltage transformer (Boige & Vignal). As for the RF signal at 5 MHz, it is sent to a broadband power amplifier (Prana GN500) linked to a custom-made transformer. In this study, the amplitude of the LF and RF voltages are set to 650 V and 190 V, respectively. Current-voltage characteristics are recorded using a current probe and two high-voltage probes (Tektronix P6015A 75 MHz); all signals are visualized on an oscilloscope (Tektronix MSO56).

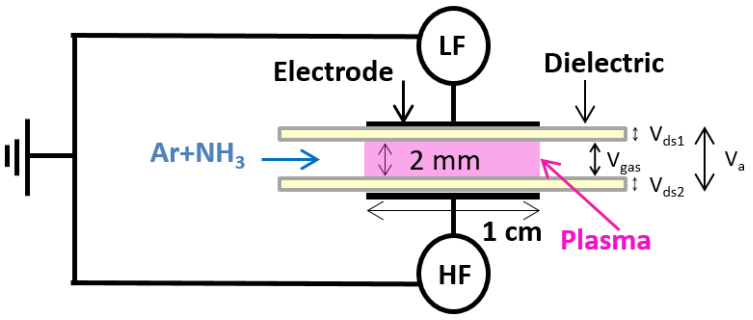

Figure 1. Schematics of the plane-to-plane dielectric barrier discharge with dual-frequency excitation.

Measurement of argon metastable atoms

As shown in Figure 2, a tunable diode laser working around 772 nm (DFB, DL100, Toptica) is used to record the number density of Ar metastable atoms by absorption spectroscopy [44], [128], [129]. In this wavelength range, atoms in the most populated Ar($1s_5$) metastable state can absorb the laser light on $1s_5$-$2p_7$ transition at 772.38 nm and atoms in the other metastable state Ar($1s_3$) can absorb the laser light on $1s_3$-$2p_2$ transition at 772.42 nm.

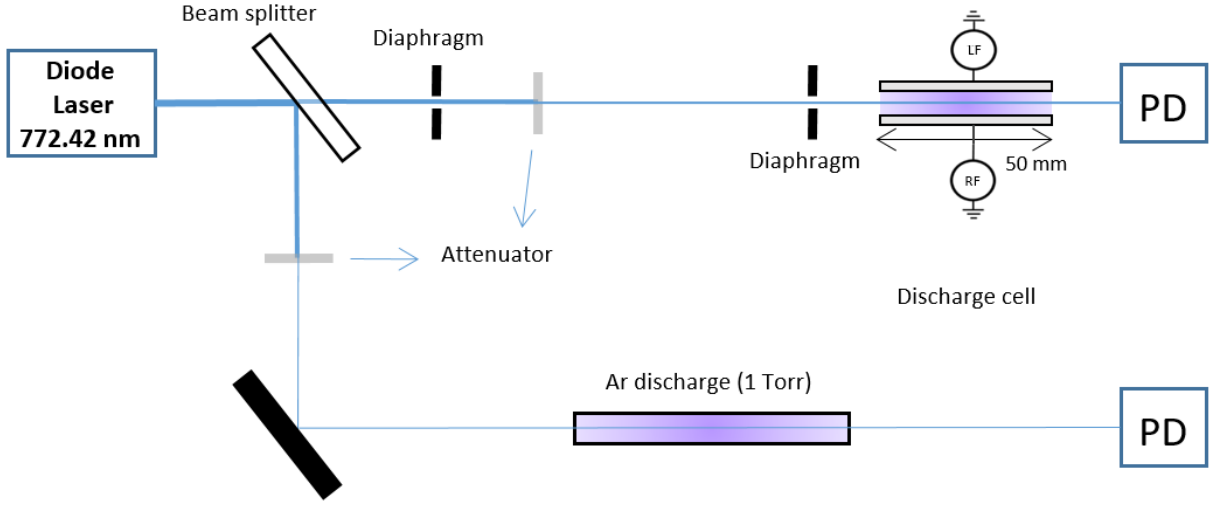

Figure 2. Experimental setup used for determination of the population of Ar $1s_3$ atoms by absorption spectroscopy using a tunable diode laser. PD represents photodiodes.

Figure 3 shows the full absorbance profile when the laser wavelength is scanned around the 772.4 nm range in Ar-based DBDs. Given the closeness of the 772.38 and 772.42 nm transitions, their pressure-broadened absorption profiles overlap under atmospheric pressure conditions. In addition, given the order of magnitude difference in their oscillator strengths (0.0278 and 0.314 for 772.38 and 772.42 nm lines, respectively [130]), the absorption peak intensity of the combined lines is located closer to 772.42 nm. The relative values of the two peak absorbance line profiles and their respective linewidths can be deduced by fitting the experimentally recorded absorbance with two Voigt functions, also shown in Figure 3 by black and red curves. Absolute number densities of metastable argon atoms can be deduced from their respective peak absorbance and width, as described in [128]–[132].

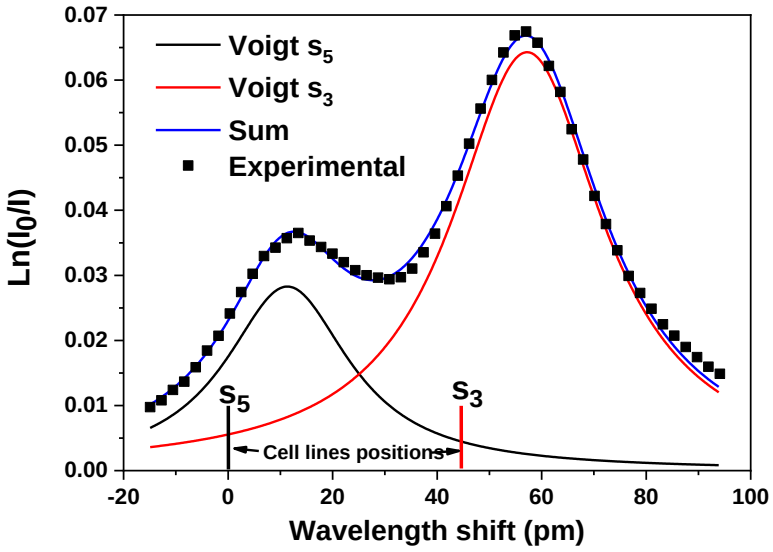

Figure 3. Absorbance profile recorded around 772.4 nm in the Ar-based DBD. Black and red curves are absorbance profiles of 772.38 and 772.42 nm lines, respectively. Positions of these lines in the low-pressure Ar cell are indicated by two *vertical lines (red and black for 772.38 and 772.42 nm lines, respectively).*

Here, the number density of metastable atoms as a function of time and space is obtained by setting the laser wavelength at the peak of the pressure broadened $1s_3$-$2p_2$ transition, which is shifted by about 13 pm from the vacuum wavelength of this line. Note that, the absorption signal from a low-pressure argon discharge cell (see Figure 2) [44], [128] is used to tune the diode laser

at the peak position of the $1s_3$-$2p_2$ transition. For both atmospheric-pressure DBD and low-pressure cell, the absorption signals are acquired with fast photodiodes (3.5 ns rise and fall times) and recorded with digital oscilloscope for data analysis and further data processing. In the DBD, the laser beam crosses the gas flow lines (perpendicular to the plan of Fig. 1) such that the absorption length is fixed to 50 mm (see Figure 2). Diaphragms, placed on the laser path before the discharge zone, reduce the laser beam diameter to about 0.5 mm. Spatially-resolved measurements in the 2 mm gap is obtained by moving simultaneously the laser beam, diaphragms system and detector in the inter-electrode space.

Figure 4 presents time-variation curves of the Ar($1s_3$) density recorded at two positions in the inter-electrode gap of the 50 kHz DBD operated in a homogeneous glow regime. In the first case, the laser beam was placed in the middle of the gap, while for the second one it was close to the upper electrode. Current-voltage characteristics are also shown for comparison. Here, data are presented for one full cycle of the applied LF voltage. In the first half-cycle, the top electrode is the cathode, while in the second one this electrode is the anode. As can be seen in Figure 4, a single discharge current peak appears per half cycle of the applied voltage; this is typical of the homogeneous DBDs operated in a glow discharge regime [6], [11]. Similar behaviors can be seen for both Ar($1s_3$) curves, with rise and decay times in the sub-microsecond time scale. Here, Ar($1s_3$) reaches a maximum value of 1.1 $10^{17}m^{-3}$ close to the cathode with 3.1 $10^{16}m^{-3}$ in the gas bulk. While similar trends and peak values arise in both half-cycles in the middle of the gap, a dissymmetry between the two half-cycles is observed near the upper electrode. More specifically, an order of magnitude larger density is observed when the top electrode is the cathode (first half-cycle), than when it becomes the anode (second half-cycle). Such dissymmetry is in very good agreement with the physics of Ar-based DBDs operated in a glow regime: i) high-energy electrons, needed for the production of excited argon atoms by electron-impact excitation of ground state Ar atoms, are mainly present inside and at the edge of the cathode sheath; ii) at atmospheric pressure, transport of Ar metastable atoms by diffusion is very slow [44], [86], [117], [133] such that their density is directly linked to their local production and destruction rates.

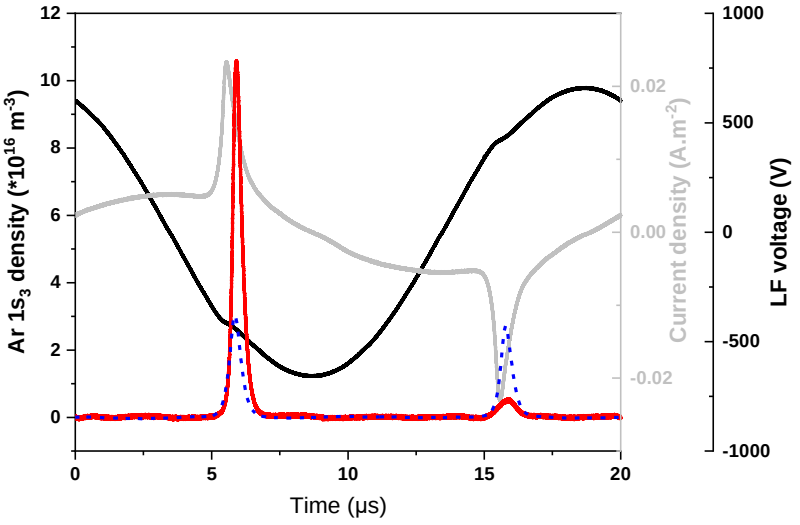

Figure 4. Number density of Ar $1s_3$ atoms close to the upper electrode (solid) and in the middle of the gap (dash) over a complete cycle of the low frequency excitation (LF 650V, 50 kHz). Applied voltage (black) and total current density (grey, discharge + displacement current density) are also shown for comparison. On first half cycle of the applied voltage, the upper electrode is cathode while on the second half-cycle, the lower electrode is cathode.

Figure 4 further shows that in both half-cycles, the maximum of the Ar metastable density near the cathode arises about 350 ns later than the discharge current peak (linked to the electron population), the delay being slightly shorter in the middle of the gap. This delay most likely results from the ~ 100 ns lifetime of Ar metastable atoms at 1 bar [134]. While the metastable and electron densities increase at the same time with the rise of the applied voltage, Ar metastable atoms tend to accumulate for a longer time than charged species (longer effective lifetimes) [117].

Kinetics driving metastable argon atoms

Fluid model from [50]

For a better understanding of the physics driving plane-to-plane Ar-based DBD sustained by either LF or dual frequency excitations, a 1D fluid model was recently developed by Magnan *et al.* [50]. This model solved the continuity and momentum equations for electrons, argon ions (Ar^+ and Ar_2^+) and excited argon 1s atoms as well electron energy balance equation. Here, even if Ar has four Ar 1s levels, Ar($1s_2$), Ar($1s_3$), Ar($1s_4$) and Ar($1s_5$), they are treated as a single Ar(1s) state

[135]–[137] (see additional details below). These above cited equations were coupled to Poisson's equation for the electrical potential and to the standard reaction set displayed in Table 1 for selected collisional and radiative processes in Ar plasmas at atmospheric pressure. Boundary conditions were defined with a secondary electron emission coefficient γ, which describes the probability that an Ar(1s) particle or Ar_2^+ ion creates a secondary electron when interacting with the dielectric surfaces of the DBD cell. In [50], γ was set to 0.1 for ions (Ar^+ and Ar_2^+) and Ar(1s) atoms. It is worth highlighting that in atmospheric-pressure plasmas for which Ar^+ conversion to Ar_2^+ is very fast, the contribution of Ar_2^+ completely dominates the ones of Ar^+ and Ar(1s).

Reaction		Rate coefficient	Ref
R1)	$e + Ar \rightarrow e + Ar(1s)$	f(Te)	[138]
R2)	$e + Ar(1s) \rightarrow 2e + Ar^+$	f(Te)	[138]
R3)	$e + Ar \rightarrow 2e + Ar^+$	f(Te)	[138]
R4)	$e + Ar \rightarrow e + Ar$	f(Te)	[138]
R5)	$e + Ar \rightarrow e + Ar(>1s)$	f(Te)	[138]
R6)	$Ar^+ + 2Ar \rightarrow Ar_2^+ + Ar$	$2.5*10^{-43}$ $m^6.s^{-1}$	[127][47]
R7)	$e + Ar_2^+ \rightarrow Ar(1s) + Ar$	$7.4*10^{-14}*Te^{-0.67}$ $m^3.s^{-1}$	[139]
R8)	$Ar^+ + cathode \rightarrow e + Ar$	$\gamma_{i\ (Ar+)}=0.1$	[50]
R9)	$Ar_2^+ + cathode \rightarrow e + Ar$	$\gamma_{i\ (Ar2+)}=0.1$	[50]
R10)	$Ar(1s) + cathode \rightarrow e + Ar$	$\gamma_{m\ (1s)}=0.1$	[50]
R11)	$Ar(1s) + (NH_3) \rightarrow e + Ar^+ +$ (products)	$4.2*10^{-17}$ $m^3.s^{-1}$	[140]
R12)	$Ar(1s) \rightarrow Ar$	$1.5*10^6$ s^{-1}	[46]

Table 1. Set of gas-phase and surface reactions used in the 1D model of [50]. *Here Te is in K.*

Note that, the contribution of the 200 ppm of NH_3 present in the nominally pure argon gas, which leads to complex Ar-NH_3 interactions, was not explicitly introduced in the fluid model. Instead, two fictive reactions were included in Table 1: reaction R11) accounted for the primary electron production by Penning ionization of NH_3 by Ar(1s) atoms and reaction R12) accounted

for the destruction of Ar(1s) atoms by collisions with Ar atoms and NH_3. The rate coefficients of reaction R11) was taken from [140]. As for the frequency of reaction R12), it was set to the value reported in Table 1 by adjusting the predictions of the model with the measured power, mean and maximal values of the Ar metastable densities [50].

To assess the correctness of this kinetic scheme for time-resolved measurements of Ar metastable atoms, we started by comparing the measured densities of Ar($1s_3$) atoms to the outcome of the model developed in [50]. For such experimental-model comparison, modelling data were integrated over a 0.5 mm circular region to match the laser beam diameter in the experiments. The comparison was realized with data sets recorded close to the upper electrode, although similar findings were found near the lower electrode of the DBD (not shown). Figure 5a presents the values obtained during a complete cycle of the applied voltage at 50 kHz. Clearly, the model [50] predicts much slower kinetics than the one seen in the experiment, both on the rising and falling side. A similar departure between the model and the experiment can be seen in Figure 5b for the dual-frequency DBD (LF 50 kHz, RF 5 MHz) in the α-γ mode [50], [94]. Since reactions R1) to R10) presented in Table 1 are well-established in literature, such disagreement most likely results from the fictive reactions R11) and R12) representing the Penning effect, which are both involving Ar(1s) atoms.

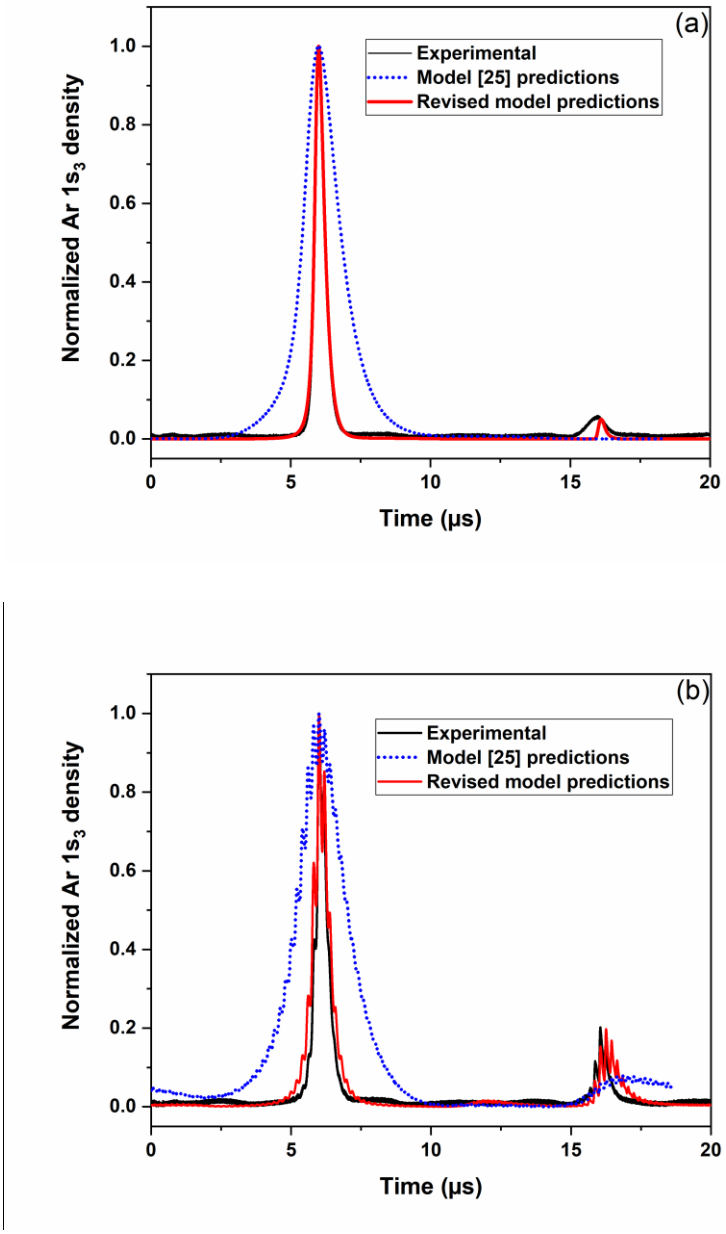

Figure 5. Temporal evolution of the Ar(1s) number density (normalized values): measurements (in black), calculated with the fluid model of [25] (in blue) and with the revised fluid model (in red). The results are shown close to the upper electrode (which was at negative LF voltage in the first half-period and positive in the 2nd one) for (a) 50 kHz LF glow DBD and (b) dual-frequency RF + LF DBD in α-γ mode.

Revised fluid model

In line with the findings of Figure 5, reactions R1) to R10) of Table 1 were maintained and fictive reactions R11) and R12) were reconsidered to more explicitly differentiate the contributions of Penning ionization, Penning dissociation, and 3-body conversion of Ar(1s) states. In addition to the creation of Ar excited dimers through 3-body reactions involving Ar(1s) atoms, the loss of Ar_2* by VUV photons and the VUV-induced secondary electron emission were also added; this yields to the revised kinetic scheme presented in Table 2.

(R13)	Ar(1s) + NH_3 ➔ products + Ar		$5.4*10^{-16}$ $m^3.s^{-1}$	[45]
	(R14)	Ar(1s) + (NH_3) ➔ Ar^+ + e + (products)	$2.3*10^{-16}$ $m^3.s^{-1}$	[45], [46]
	(R15)	Ar(1s) + (NH_3) ➔ Ar + (products)	$3.1*10^{-16}$ $m^3.s^{-1}$	[45], [46]
(R16)	Ar(1s) + 2Ar ➔ Ar_2* + Ar		$1.1*10^{-44}$ $m^6.s^{-1}$	[86]
(R17)	Ar_2* ➔ 2Ar + hν (VUV)		$6.0*10^7$ s^{-1}	[125], [47]
(R18)	hν (VUV) + wall ➔ e + wall		γ_{ph}=0.1	[38]

Table 2. Additional reactions involving excimers and photoemission. (R13) is not explicitly included but introduced through reactions (R14) and (R15), corresponding to Penning ionization and dissociation of NH_3, respectively. Note that, no population kinetics for NH_3 is introduced in the model: there, (R14) and (R15) frequencies are calculated for 40 ppm of NH_3.

Reaction R13) corresponds to the total quenching reaction of Ar($1s_5$) metastable atoms by NH_3. In the revised version of the model, it is decomposed in R14) and R15). Considering the total quenching reaction rate of $5.4x10^{-16}$ $m^3.s^{-1}$ for R13), measured in [45], and the branching ratio of 0.42 for R14), measured in [46], this yields to a reaction rate for Penning ionization of $2.3x10^{-17}$ $m^3.s^{-1}$. Similarly, for NH_3 dissociation by Ar($1s_5$), the branching ratio is 0.58 [46], which yields to a reaction rate for R15) of $3.1x10^{-17}$ $m^3.s^{-1}$. Note that, these measured values differ by about a factor of 5 with respect to the one estimated in [140] and previously used for R11) in [50]. Over the range of experimental conditions investigated in this work, 200 ppm of NH_3 are injected in the nominally pure argon gas. However, upon discharge ignition, many reaction pathways lead to a significant decrease of this concentration [47]. Inspired by typical precursor fragmentation levels along the

gas flow lines of DBD measured in similar conditions by infrared absorption [18] or operated in various discharge modes [19], [20], [27], all data were obtained assuming a concentration fraction of 40 ppm.

Reaction R16) corresponds to the 3-body conversion of Ar(1s) atoms leading to excited argon dimers Ar_2* [141]. This state decays to the dissociative ground state of Ar_2 by producing the VUV continuum emission centered at 126 nm (reaction R17)) [47], [134]. Here, the rate coefficient of R16) corresponds to the one measured for Ar($1s_5$) [86], and was extended to other Ar(1s) levels in agreement with Arakoni [47]. These VUV photons cannot be absorbed by Ar atoms or Ar_2 in its ground state and by the small amount of NH_3 (optically thin medium) [125]; hence, VUV photons have a long mean free path in the DBD cell (typically ~50 cm [127], i.e. 250 times greater than the inter-electrode gap). Consequently, they can rapidly reach the surface of the dielectric walls, inducing secondary electron emission [38]. The yield for such reaction, γ_{ph}, is assumed comparable to the one of ions and Ar(1s) atoms (R17)) in Table 2. Note that, γ_{ph} includes the contributions of both direct, VUV-induced electron emission and VUV-induced desorption of electrons bound to the plasma-exposed dielectrics by weak polarization interactions [142]–[145]. In addition, photons are described with an infinite speed: photoemission is therefore instantaneous after the spontaneous dissociation of Ar_2*. Due to the small inter-electrode gap with respect to the electrode surface, it can be assumed that half of the photons reaches the cathode, the other half goes to the anode [38].

It is worth highlighting that the measurements examine the population of Ar($1s_3$), while the model considers all four Ar(1s) state as a block. To note; when accounting for the about 10 times lower oscillator strength of the 772.38 nm line, compared to the one of the 772.42 nm line, Figure 3 reveals that the number density of metastable atoms is about 5 times lower in the Ar($1s_3$) state than in the Ar($1s_5$) one. This is the ratio between the 2J+1 statistical weights of these states, which have angular momentum J=0 and 2, respectively [130]. A similar rule can be invoked to describe the populations of the resonant Ar($1s_2$) and Ar($1s_4$) states. According to the resonance radiation trapping theory of Holstein [146], [147], extended by Walsh [148], the apparent lifetimes of these states in a 2 mm thick slab of atmospheric-pressure argon gas are 1.2 and 5 μs [126], respectively, which are about 100 times longer than the radiative lifetimes of these states [130]. However, due to the 3-body reaction with two ground state Ar atoms (described by R16)), and to the quenching by NH_3 (described by the sum of R14) and R15)), the effective lifetime of the four Ar(1s) states,

metastable as well as resonance states, decreases by at least one order of magnitude (≈ 100 ns). Considering comparable rate coefficients reported for different Ar(1s) states for R13) in [45] and for R16) in [86], the population densities of these states become proportional to their respective production rates by electron impact excitation, which follow their respective statistical weights 2J+1. Moreover, population transfers between the four Ar(1s) states, induced by collisions with Ar atoms [86], [149] and electrons [135], [136], help for the establishment of this statistical population distribution. Hence, the angular momentum J being 1, 0, 1 and 2 for Ar($1s_2$), Ar($1s_3$), Ar($1s_4$) and Ar($1s_5$) states, respectively [130], their relative population densities should follow 3:1:3:5 ratios. Hence, the total density of excited argon atoms in the four Ar(1s) states calculated by the model corresponds to 12 times the measured density of the Ar($1s_3$) level.

Revised values of the normalized metastable number densities are presented in Figure 5a for the LF discharge (50 kHz) and dual-frequency DBD (LF 50 kHz, RF 5 MHz) operated in the α-γ mode [50], [94]. Clearly, much better agreement is observed with the revised version of the model than with the one originally developed by Magnan *et al.* [50]. Hence, in addition to the higher reaction rates for Penning ionization and dissociation (R14) and R15)), the fast creation of Ar_2* R16) and its rapid radiative decay, leading to VUV emission and secondary electron emission (R17) and R18)), allow a much better description of the time variation of Ar(1s) populations in both LF and LF-RF DBDs, with much more prominent rise and decay times.

A very small peak of Ar(1s) also appears in Figure 5 close to the anode when Ar_2* and photoemission resulting from VUV photons are included in the model. This aspect was examined in more details by plotting the Ar(1s) mapping over time and space. Results are presented in Figure 6a. One can see that the maximum of Ar(1s) is close to the cathode, but the high-density area extends into the gap and reappears close to the anode. Over the range of experimental conditions investigated, Ar(1s) atoms are mainly created by R1), i.e. by high-energy electrons [50], and transport by diffusion is negligible [44], [86], [117], [133]. Spatial variation of the electric field along the gap when the population of Ar(1s) species increases at the anode are presented in Figure 6b with and without chain reactions leading to the photoemission by VUV photons. Compared to [50], the revised kinetic scheme used in the fluid model leads to an increase of the electric field in the gas bulk and near the anode. This necessarily implies a more prominent electron drift from the

cathode to the anode and thus a more important creation of Ar(1s) atoms by high-energy electrons in the anode region.

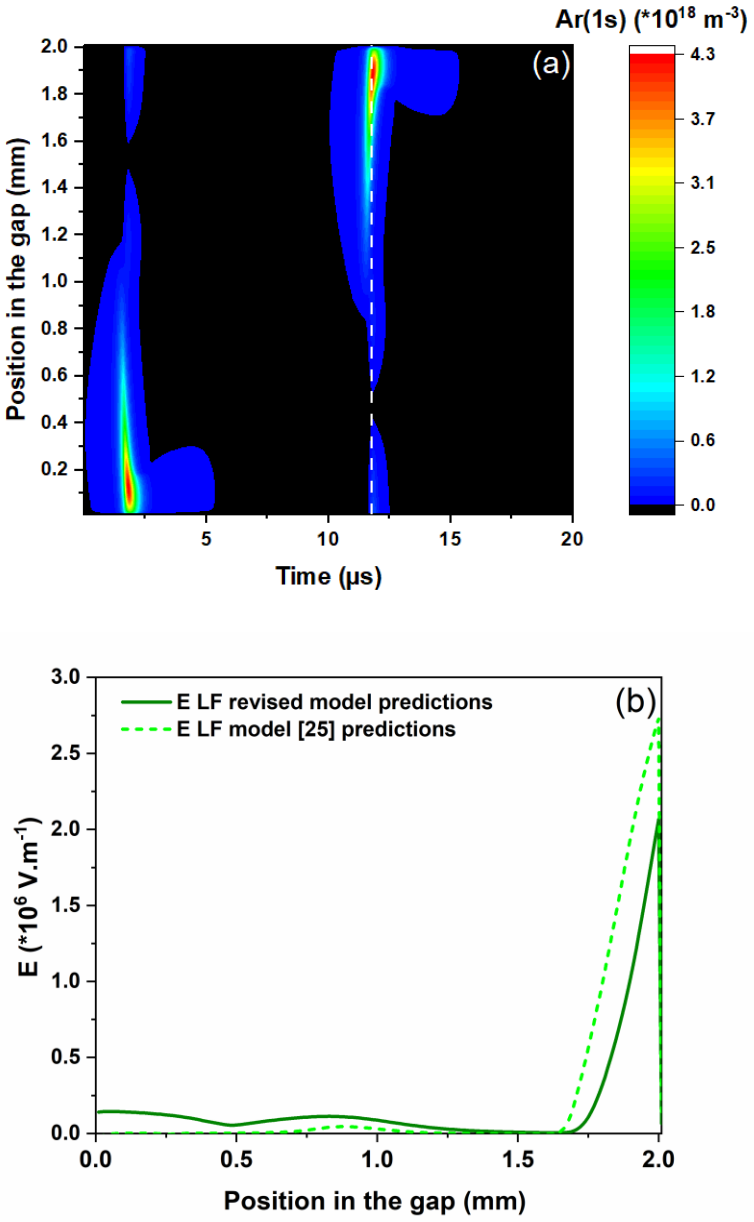

Figure 6. a) Ar(1s) number density evolution over space and time in the LF DBD, b) spatial profile of the electric field along the gap when Ar(1s) is maximum at the anode (vertical line in a). In b), the results for the electric field are shown with the model used in [50] *and with the revised version developed in this work.*

Consequences of excimer formation and photoemission on Ar-based DBDs in LF and LF-RF regimes

Discharge kinetics

The introduction of the population kinetics of Ar_2* (formation through reaction R16) and loss through reaction R17)) and photoemission by VUV photons (reaction R18)) strongly modify the physics driving Ar-based DBDs in both LF and LF-RF DBD regimes.

Table 3 summarizes important modifications on the dominant creation and loss terms of both Ar(1s) atoms and electrons. For Ar(1s), electron-impact excitation represents the dominant creation pathway in both LF and LF-RF regimes. As for the losses, Penning dissociation accounts for 88% of Ar(1s) consumption when using the reaction set provided by Magnan *et al.* [50]. In the revised model, over the range of experimental conditions investigated, the contribution of Penning dissociation decreases, and the dominant loss mechanism becomes the creation of Ar_2*. In the same way, consumption of Ar(1s) states for Penning ionization also reduces. In line with these results, one may think that the more prominent rise and decay times observed for the population of metastable argon atoms in Figure 5a and Figure 5b with the revised model is entirely linked to the Ar_2* kinetics, and not to photoemission. However, if R18) is removed from the model, discharge breakdown no longer occurs, even for very high amplitudes of the LF voltage. This feature is obviously due to the high loss rates of Ar(1s) atoms, which can no longer bring energy to the discharge. It also shows that the creation of Ar(1s) atoms is largely related to photoemission.

		50 kHz LF		50 kHz LF + 5 MHz RF	
		Model of [50]	Revised model	Model of [50]	Revised model
Creation of Ar(1s)	e-Ar_2^+ recombination (%)	4	<0.1	1	<0.1
	Direct excitation (%)	96	100	99	100
Ar (1s) losses	To the walls (%)	<0.1	<0.1	<0.1	<0.1
	Penning ionization (%)	12	3	12	3
	NH_3 dissociation (%)	88	4	88	4
	Creation of the dimer Ar2* (%)	--	93	--	93
Creation of e^-	Penning ionization (%)	79	49	82	52
	Direct ionization (%)	14	30	9	23
	Secondary emission (%)	7	21	9	25
e^- losses	To the walls (%)	76	92	94	98
	e-ion recombination (%)	24	8	6	2

Table 3 Space- and time-averaged contribution of the different mechanisms to the creation and loss of Ar(1s) and electrons for LF 50 kHz 1000 V and dual-frequency 50kHz 750 V + 5MHz 350 V

As for the electrons,

Table 3 shows that while Penning and direct ionization were the dominant ionization pathways in the initial model [50], [94], about 3 times more electrons are now created by photoemission at the walls with the addition of the Ar_2* kinetics and photoemission (R15)). However, the contribution of Penning ionization remains larger than the one of Ar direct ionization. As said previously, even if only 3% of Ar(1s) consumption are involved in Penning ionization, this

reaction remains necessary for the discharge ignition. If Penning ionization is entirely removed from the revised model, the discharge no longer ignites, which fully supports previous experimental findings demonstrating the importance of the NH_3 Penning gas mixture in the physics driving Ar-based, low-frequency DBDs [21], [71]. Experimentally, in dual-frequency DBDs, the γ mode is never reached without NH_3 and thus without Penning ionization contributions. Since direct ionization of NH_3 is fully negligible over the range of experimental conditions investigated [47], this must be linked to Penning ionization contributions.

Table 3 further reveals that the relative contribution of electron losses to the walls increases with respect to recombination processes in the bulk. The explanation is that with addition of the Ar_2* kinetics and photoemission, the contribution of secondary electrons increases, creating more ions and electrons in the sheath. Ions are thus more effectively lost to the cathode surface, while electrons can more easily drift to the anode surface.

RF α ➔ RF α–γ transition criterion in dual frequency RF-LF

In LF-RF Ar-NH_3 DBDs, a transition from α to α-γ can occur with the increase of the LF voltage [50], [94]. Under atmospheric pressure conditions, the first mode is called α or Ω mode, and is characterized by an ohmic heating and electron energy dissipation in the bulk [93], [113]. The second mode is called α-γ mode: during each half cycle of the LF voltage, electron Joule heating and electron energy loss reach a maximum in the sheath region for some μs [90]. This transient γ mode is observed when the gas voltage amplitude reaches a high enough value. Like in a LF DBD, when the γ mode is reached, the gas voltage decreases due to the charge of the dielectrics. Consequently, the maximum of the gas voltage is observed just after the transition from α to γ mode, and the γ mode duration is limited [94], [113]. In this γ mode, the contribution of secondary electrons to the gas ionization becomes large enough to reach the self-sustainment criterion in the cathode sheath [92], [94]:

$$\frac{\gamma_i \langle \Gamma_{i,sheath} \rangle_{RF}}{\langle \Gamma_{SEE} \rangle_{RF}} > 1 , \qquad (1)$$

where $\langle \Gamma_{i,Sheath} \rangle_{RF}$ is the maximum value at a given time of the LF voltage of the total ion flux through electron Joule heating and electron multiplication in the cathode sheath [94]

$$\Gamma_{i,sheath}(t) = \int_{cathode}^{sheath\ edge} S_i(x,t)dx\,, \tag{2}$$

where S_i is the volume production rate of ions. In Equation (2), the integration is realized over the sheath thickness (In practice, this is done by means of a weighting function defined as $W(x) = 1 - ne(x)/ni(x)$, which varies smoothly from ≈1 at the wall to ≈0 in the plasma bulk; the source term S_i is then multiplied by W(x) and then integrated from the electrode to the center of the plasma, as explained in [94]). As for $\langle \Gamma_{SEE} \rangle_{RF}$ in Equation (1), it corresponds to the maximum at a given time of the LF voltage of the secondary electron flux emitted from the cathode wall in the DBD cell. Note that, the criterion given by Equation (1) is obtained with values averaged over one RF cycle because the self-sustainment criterion involving ion transport back to the wall is too slow to react to the RF fluctuations of the electric field in the sheath [94]. Generally, the transition from α to α-γ mode is related to secondary electron emission by ion bombardment only (γ_i); in line with the findings of this work, the secondary electron emission contribution by photons (γ_{ph}) must be added such that the self-sustainment criterion becomes

$$\frac{\gamma_i \langle \Gamma_{i,sheath} \rangle_{RF} + \frac{1}{2}\gamma_{ph}\eta \langle \Gamma_{Ar(1s),sheath} \rangle_{RF}}{\langle \Gamma_{SEE} \rangle_{RF}} > 1, \tag{3}$$

where $\langle \Gamma_{Ar(1s),sheath} \rangle_{RF}$ is the maximum value at a given time of the LF voltage of the Ar(1s) flux in the cathode sheath

$$\Gamma_{Ar(1s),sheath}(t) = \int_{cathode}^{sheath\ edge} S_{Ar(1s)}(x,t)dx\,, \tag{4}$$

where $S_{Ar(1s)}$ is the volume production rate of Ar(1s). In Equation (3), η corresponds to the fraction of the argon metastable atoms in the sheath that lead to the creation of Ar_2* and then to VUV photons. Over the range of experimental conditions investigated, with the reaction set presented in Table 2, η is approximately constant ($\eta \cong 0.926$) due to the constant frequencies of all the dominant conversion processes of Ar(1s). It follows that the maximum photon flux in the sheath is directly proportional to the maximum Ar(1s) flux in the sheath. Since $\eta \langle \Gamma_{Ar(1s),sheath} \rangle_{RF}$ includes photons produced in the cathode sheath but towards both the anode and the cathode, the ½ factor in Equation (3) accounts for the fact that, in optically thin media for VUV photons, only half of the photons reaches the cathode (the other half reaches the anode).

Figure 7 presents the self-sustainment criterion calculated by the Equation (3) as a function of time during a LF period of the dual-frequency discharge. The results are shown for two amplitudes of the LF voltage: in (a), the LF voltage remains below the value required to induce a transition from α to γ mode, while in (b), the LF voltage is such that a transient γ mode occurs. Based on Equation (2), the discharge can transit to the γ mode if the self-sustainment criterion becomes greater than 1 over a given time frame of the LF voltage. In Figure 7 (a), this criterion is never satisfied whereas in Figure 7 (b), it is fulfilled between 3.5 and 5.2 µs. In such conditions, the sheath becomes self-sustained. The presence of the γ mode can be further confirmed by the gas voltage (averaged over one RF cycle) behaviors also displayed in Figure 7. While the gas voltage remains more or less sinusoidal in Figure 7 (a), a rapid gas voltage drop can be seen in Figure 7 (b) due to the corresponding charge of the dielectrics.

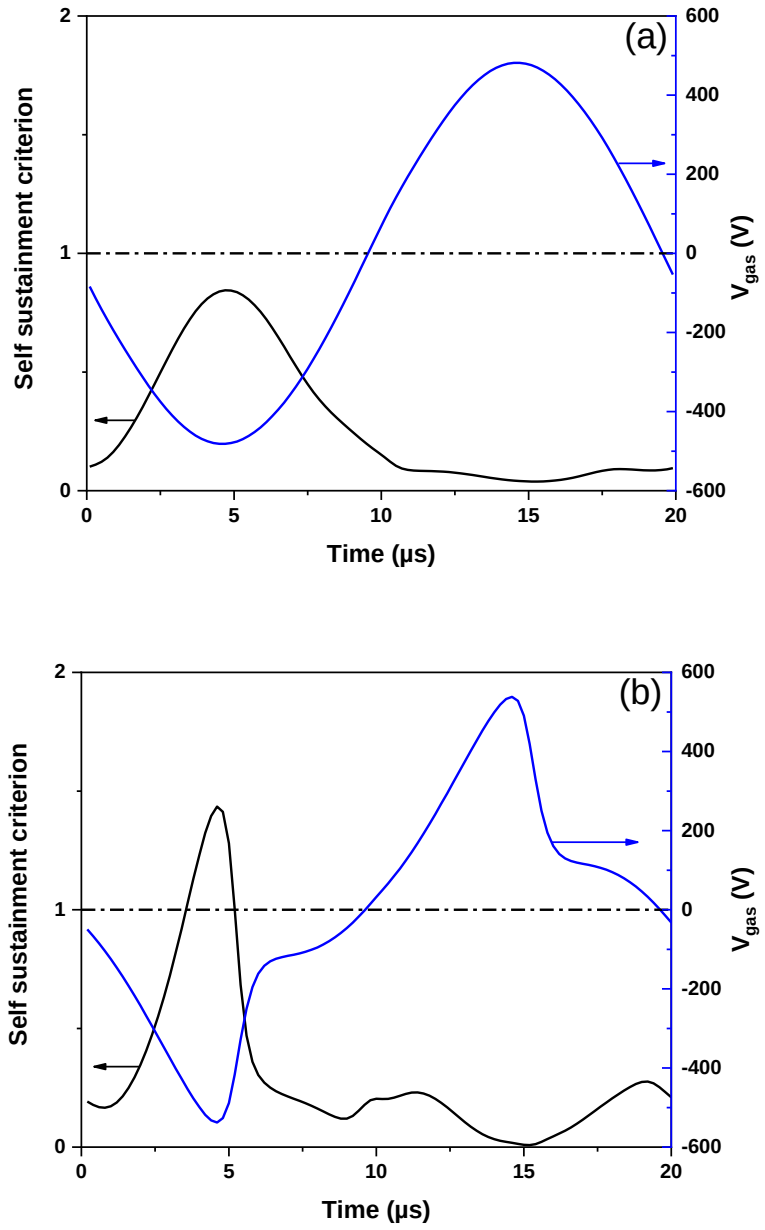

Figure 7. Self-sustainment criterion plot as a function of time during a complete cycle of the LF voltage. Here, the criterion corresponds to left-hand-side of Equation (3) (in black). Gas voltage values are also shown (in blue). Results are presented for a dual frequency LF (50 kHz) – RF (5MHz), V_{RF} = 350 V, (a) V_{LF} = 600 V, (b) V_{LF} = 650 V

In this framework, Figure 8 presents the self-sustainment criterion, at the moment when $|V_{gas}|$ is maximum, calculated by the left-hand-side of Equation (3) as a function of the amplitude of the LF voltage. Again, when the ratio exceeds 1, i.e. when each secondary electron produces

enough ions and Ar(1s) in the sheath to cause the emission of one or more new secondary electrons, the discharge transits to the γ mode, i.e. the sheath becomes self-sustained [50], [94]. As can be seen, the transition occurs for different LF voltage amplitudes depending on the specific set of the chosen γ_i and γ_{ph} values. For γ_i=0.1, the minimum LF voltage required for the α-γ mode transition decreases as γ_{ph} increases. Hence, for a more important electron production through photoemission, a lower LF voltage is sufficient to reach the number of ionizations provided by the self-sustainment criterion. On the other hand, Figure 8 shows that γ_i has only little influence on the value of the LF voltage required for the transition. This is related to the long drift time of ions to the cathode compared to the γ mode duration, which limits the influence of γ_{ions} on the α-γ transition voltage. More precisely, the ions drift from the sheath edge to the cathode lasts about 1 µs, which is the magnitude of the duration of the γ mode. Consequently, ions produced at the sheath edge during the γ mode only have little influence on the γ mode transition.

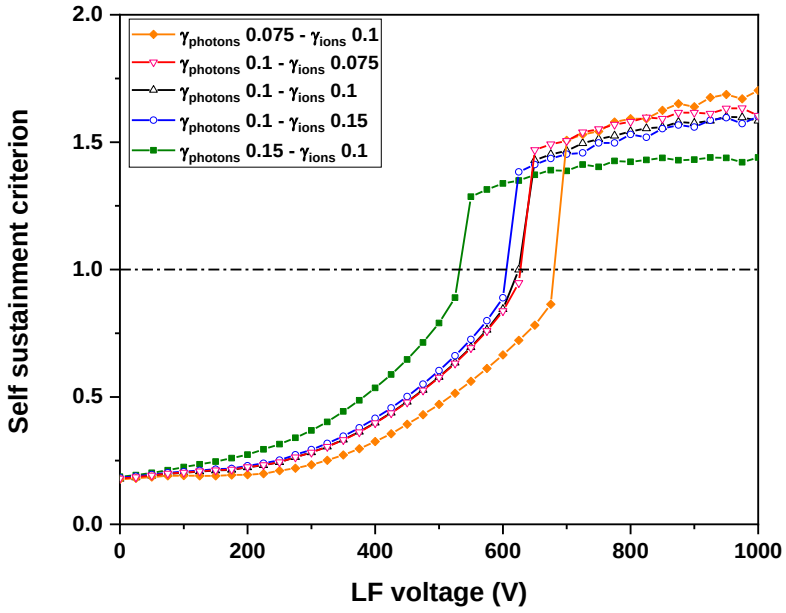

Figure 8. Self-sustainment criterion plot as a function of the amplitude of the LF voltage in dual-frequency LF-RF DBDs. Here, the criterion corresponds to left-hand-side of Equation (3).The results are shown for various γ_i and γ_{ph} values.

Conclusion

Through a comparison between the measured and simulated populations of metastable argon atoms, the objective of this work was to highlight the role of excimer formation, followed by the VUV emission and photoemission on the Ar metastable kinetics in Ar-NH_3 dielectric barrier discharges at atmospheric pressure. The model initially developed to describe Ar-based dual-frequency DBDs [50], [94] was not able to reproduce the time variation of Ar(1s) atoms density characterized by rise and decay times in the microsecond time scale. On the other hand, including Ar_2* formation, Ar_2* spontaneous deexcitation leading to VUV continuum emission, and the induced photoemission at the walls, provided much more accurate Ar metastable kinetics for both low-frequency (50 kHz) and dual frequency (50 kHz - 5 MHz) excitations. In addition, the apparition of a peak in the density of metastable argon atoms at the anode was also better described using photoemission. It was shown that this peak of Ar(1s) atoms density is not directly linked to the consumption-creation balance of Ar(1s) atoms, but rather to the production of an electron beam passing through the discharge during the LF breakdown. Ar_2* and photoemission further played a significant role on the ionization kinetics : while Penning were the truly dominant ionization pathways in the initial model [50], [94], the part of electron's creation by photoemission and direct ionization increases to become of the order of magnitude of that of Penning ionization in the refined version of the model. Photoemission was also demonstrated to influence the transition from α to α-γ mode.

Acknowledgments

The work in France was supported by the Agence Nationale de la Recherche through the Investissement d'avenir program (ANR10LABX2201). As for the one in Canada, it was funded by the National Science and Engineering Research Council (NSERC RGPIN-2018-04550) and by the Fondation Courtois. The "Réseau des Plasmas Froids" of CNRS/MCRT (France) is acknowledged for providing the DFB diode laser and the travel support for Nader Sadeghi. All authors would like to acknowledge the financial support of the CNRS and Université de Montréal through their contributions to the International Research Network on Controlled Multifunctional Nanomaterials.

Chapitre 3 – Influence de la tension RF sur les propriétés spatio-temporelles d'une décharge double fréquence BF-RF

Le chapitre 2 a apporté une meilleure compréhension des processus nécessaire pour transiter vers un régime / claquage gamma en basse fréquence comme en double fréquence.

En ajoutant les photons VUV et la photoémission qu'ils induisent, la cinétique des Ar(1s) de la décharge simulée est quasi identique à celles des Ar(1s) mesurée expérimentalement. Avec cette modification du modèle, on peut donc viser une meilleure compréhension des phénomènes complexes présents dans la décharge double fréquence. Dans leur article, Magnan et al. [50] ont effectué une étude de l'influence de la tension basse fréquence sur une décharge double fréquence, mettant en évidence son rôle dans l'obtention du mode γ dans ces décharges. En se concentrant sur les décharges double fréquence en mode α–γ, on peut se demander quel est l'effet de la tension RF sur ces régimes α et γ.

Un montage expérimental a été mis en place afin d'obtenir des cartographies, résolues dans l'espace inter-électrode (77 µm) et le temps (7 ns sur un cycle de 20 µs), de l'émission lumineuse à certaines longueurs d'ondes, apportant des informations sur les propriétés fondamentales de la décharge. Associé à des mesures de densités d'argon métastables ainsi qu'au modèle fluide 1D précédemment modifié, il est alors possible d'étudier l'effet de l'amplitude de la tension RF. Il ressort qu'une augmentation de tension RF a comme effet d'augmenter l'amplitude des variations de la tension gaz à l'échelle RF et donc la densité d'espèce chargée dans le bulk. Ceci entraine un passage au régime gamma pour une tension appliquée plus faible, et donc une tension gaz maximum plus faible. Ainsi l'augmentation de l'amplitude de la tension RF augmente la densité électronique tout en diminuant la densité des espèces énergétiques, électrons comme métastables. C'est ce qui est démontré plus en détail dans l'article suivant.

Les travaux sont présentés sous la forme d'un article récemment soumis à Plasma Sources Science and Technology (PSST-106025).

Influence of the RF voltage amplitude on the space- and time-resolved properties of RF-LF dielectric barrier discharges in α-γ mode

Raphaël Robert[1,2], Nader Sadeghi[3], Gerjan Hagelaar[4], Luc Stafford[2], Françoise Massines[1]

[1]Laboratoire Procédés Matériaux et Énergie Solaire (PROMES, CNRS, UPR 8521), Rambla de la thermodynamique, 66100 Perpignan, France

[2]Département de physique, Université de Montréal, 1375 ave. Thérèse-Lavoie-Roux, Montréal, Québec, H2V 0B3, Canada

[3]Laboratoire Interdisciplinaire de Physique (LIPhy CNRS, UMR 5588), Université de Grenoble-Alpes, Grenoble, France

[4]Laboratoire Plasma et Conversion d'Énergie (LAPLACE, CNRS, UMR5213), 118 Route de Narbonne, 31077 Toulouse, France

Abstract

This work reports the results of an experimental and modelling study on dual-frequency Ar-NH_3 dielectric barrier discharges (DBD) exhibiting the $\alpha - \gamma$ transition. A combination of space- and time-resolved optical absorption and emission spectroscopy is used to record spatio-temporal mappings of the Ar metastable number density, Ar 750.4 nm line emission intensity, and electron-Ar Bremsstrahlung continuum emission intensity. With the increase of the RF voltage amplitude in a 50 kHz-5 MHz DBD, maximum populations of Ar excited species (1s and 2p states, linked to the population of high-energy electrons) observed in the γ mode decrease and appear earlier in the low-frequency cycle. On the other hand, the density of the bulk electrons, monitored from the continuum emission intensity, increases, with a more prominent rise in the RF-α mode than in the γ regime. Such behaviors are consistent with the predictions of 1D fluid model and results from a decrease of the gas voltage required for self-maintenance of the cathode sheath in the γ breakdown.

Introduction

Since the 1990's, low-pressure dual-frequency plasmas have been developed. First studied for etching processes, the association of a radio frequency (RF) and a microwave voltage [150]–[152], or two RF voltages [153]–[169], is now a common method to tailor the ion energy distribution function (IEDF) on plasma-exposed surfaces, independently of the ion flux [84], [95], [155], [158], [159], [170]. In recent developments of dielectric barrier discharges (DBDs) at atmospheric pressure for a number of applications, in particular for thin-film deposition [71], [72], [74], [171], a RF voltage is often associated with a low frequency (LF) one (between 1 and 500 kHz) [50], [71]–[75], [94], [96], [115], [171]–[173] or with another RF [84], [95], [174]–[178]. In such conditions, dual-frequency discharges increase the power absorbed (and dissipated) by the plasma electrons, while maintaining an homogeneous discharge mode [73]–[75], [96], [172], [173]. Hence, the number densities of charged and reactive species significantly increase [50].

RF-LF dual-frequency discharges operated in Ar-based gases at atmospheric pressure can reveal unique features. In particular, during an LF period, depending on the amplitude of the LF voltage, it is possible to observe an alternation between 2 typical RF discharge conditions: the α regime and the γ regime [50], [72], [94], [171], [175], [177]. On one hand, when the LF voltage applied to the gas is low enough, the discharge exhibits a RF-α behavior, characterized by an ohmic heating of plasma electrons in the bulk [95], [166], [176]. On the other hand, when the amplitude of the LF voltage is almost maximum, and of the same polarity as the RF voltage, the secondary electrons created at the electrode become accelerated by the electric field present in the sheath and a self-sustainment criterion in the sheath is established; this is the γ regime [94]. In recent studies, this so-called α – γ transition was found to depend on a number of operating parameters, including the amplitude of the LF voltage [50], the amplitude of the RF voltage [171], and the relative concentration of NH_3 in Ar-NH_3 Penning gas mixtures [94]. In this work, space- and time-resolved optical emission spectroscopy, combined with tunable diode laser absorption and fluid modeling, are used to examine the influence of the RF voltage amplitude on electron densities, electron temperatures, and populations of Ar metastable atoms in α – γ dual-frequency DBDs operated in Ar-NH_3 Penning gas mixtures. This complete set of data provides new insights into the α – γ transition and highlights the predominant role of dielectrics in DBD conditions.

Experimental setup and diagnostics

DBD reactor

The dual-frequency Ar-based DBD studied in this work is sustained in a plane-to-plane configuration [50]. The gas gap is 2 mm and a 1 mm-alumina-dielectric-layer is placed on each metallic electrode. The DBD cell is located inside an air-tighten chamber, which is first evacuated with a primary vacuum pump down to about 1 mTorr, and is then filled with a Penning mixture of Ar + 200 ppm of NH_3 at a total gas flow rate of 3 SLM (standard liters per minute). A needle valve between the chamber and the pumping system allows fixing the total pressure in the chamber to 760 Torr. Dimensions of the discharge zone are 0.2 x 1 x 5 cm^3. RF and LF voltages are generated by a single-waveform generator (Keysight 33500B Series), allowing their synchronization, and are independently amplified. As in previous studies [50], [94], excitation frequencies are LF 50 kHz and RF 5 MHz. Here, the LF voltage amplitude is set at 650 V, 50 V above the LF breakdown voltage. As for the RF voltage amplitude, it is varied between 0 and 290 V.

Optical emission spectroscopy

The Ar-based DBD is characterized by time- and space-resolved optical emission spectroscopy using the optical system presented in Figure 1. The plasma light is collected with a 10 cm-focal-length lens, placed at 15 cm from the center of the DBD cell. Combined with a set of 3 mirrors (forming a periscope), this lens forms the image of a selected region of the discharge on the entrance slit of a Czerny–Turner monochromator (Jobin-Yvon, 66 cm focal length, 1200 groves/mm grating, slit width 150 µm) located at 30 cm optical distance from the lens. Here, the 3-mirrors set, placed between the lens and the monochromator, rotates the image of the discharge zone by 90°. Considering the dimensions of the DBD and neglecting the edge-effect, the density of the excited species in the plasma volume can be assumed to have only a one dimensional variation along the DBD's gap. Thus, the signal light on the slit represents the intensity of the light emission from the plasma layer at a given distance from the electrodes. The periscope is fixed on a micrometric screw such that its movement along the horizontal axis induces the displacement of the image of the discharge gap on the monochromator's slit and thus offers the possibility to probe light emission from different zones of the plasma gap. Considering the factor 1.95 magnification of the image and the 150 µm width of the entrance slit of the monochromator, the spatial resolution within the gap is 77 µm.

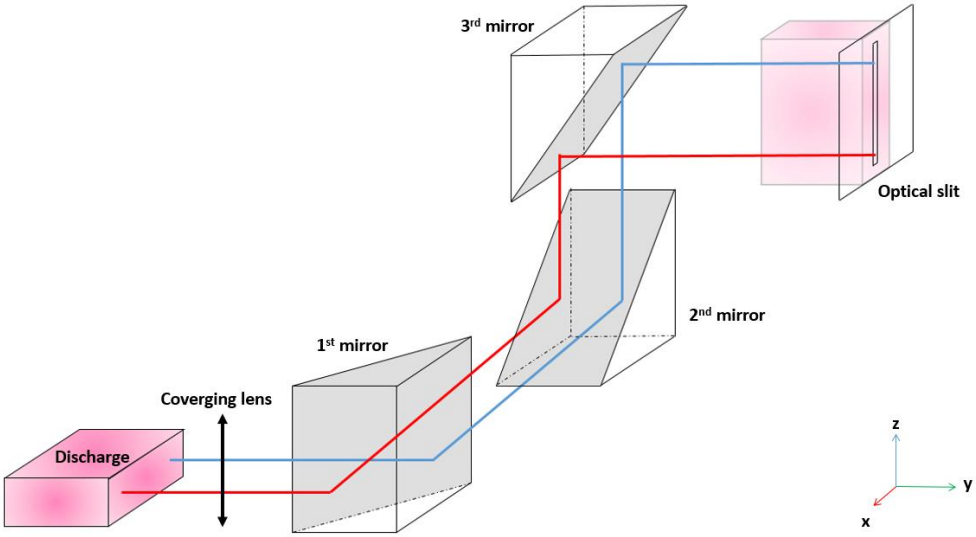

Figure 1. Optical setup used for magnification, rotation, and scanning along the discharge gap of the plasma light emission.

The light at the wavelength selected by the monochromator is detected with a Hamamatsu photomultiplier tube (PMT, H10721-20) operating in photon counting mode. A multichannel photon counter (MSC6A2T8 Fast Comtec) is used to record the time variation of the wavelength-selected light emission intensity over the 20 µs cycle of the LF voltage with a time resolution of 6.4 ns. A TTL signal, in phase with the LF voltage from the waveform generator, triggers the photon counter. The photon pulses from the PMT are counted in different channels of the MCS6A2T8 counter according to their respective arrival time after the triggering signal [71]. Averaging the photon signals over 10^6 LF cycles (20 s total acquisition time) provides an excellent signal-to-noise ratio. Data are transferred to a computer for the storage and further treatment, as shown in Figure 2. This phase-resolved optical signal can further be correlated with the discharge current-voltage characteristics [50] acquired with a digital oscilloscope triggered by the same TTL pulse as the MSC6A2T8 multichannel photon counter.

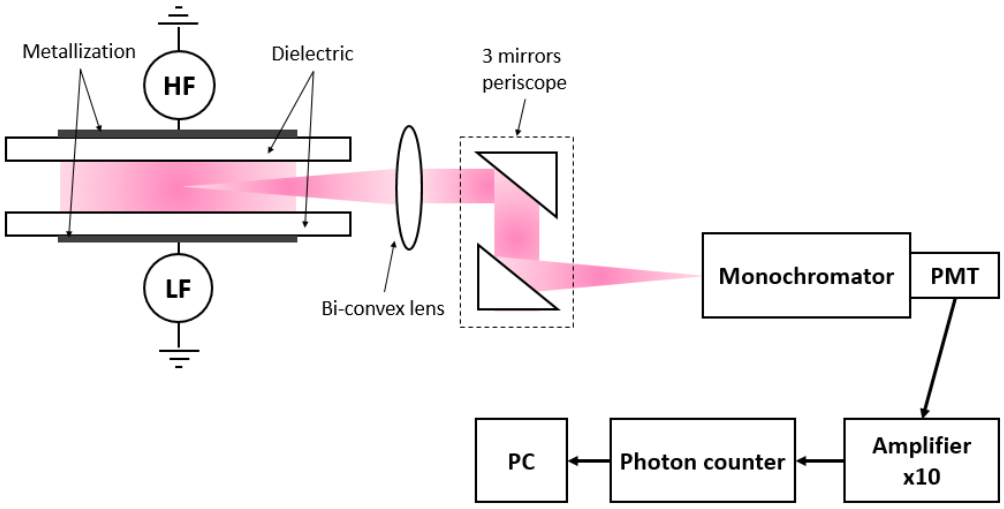

Figure 2. Experimental setup with all optical and electrical components for space- and time-resolved optical emission spectroscopy.

Tunable diode laser absorption spectroscopy

The density of Ar metastable atoms in the Ar-based DBD is measured by tunable diode laser absorption spectroscopy with the same equipment and in the same conditions as [35]. A beam from the tunable diode laser, whose wavelength is tuned around 772.4 nm, crosses the DBD discharge volume along its 5 cm longer arm. Due to the closeness of the Ar transitions 772.38 nm ($2p_7 \leftarrow 1s_5$) and 772.42 nm ($2p_2 \leftarrow 1s_3$), and their pressure broadening at 760 Torr, the laser beam can be absorbed by both Ar($1s_5$) and Ar($1s_3$) metastable atoms (Paschen notations are used, corresponding to $4s[3/2]_2$ and $4s[1/2]_0$ metastable states in Racah notation) [179]. However, as the oscillator strength of the $2p_2 \leftarrow 1s_3$ transition is more than an order of magnitude larger than the one of the $2p_7 \leftarrow 1s_5$ transition [179], by setting the laser wavelength at 772.435 nm, which is the peak position of the pressure-shifted $2p_2 \leftarrow 1s_3$ line [132], the absorption signal represents the density of Ar($1s_3$) atoms [35], [132]. The time-resolved number density of Ar($1s_3$) atoms can be deduced from the time-resolved absorption coefficient at 772.435 nm, using relations reported in [132], [180], [181]. Here, the about 500 µm diameter of the laser beam limits the spatial resolution within the gap but allows to estimate the Ar($1s_3$) atoms density either in the plasma bulk (middle distance from the top and bottom electrodes) or in a zone close to the top electrode, including the sheath edge.

Space and time-resolved optical measurements

Analysis of metastable Ar atoms

Figure 3 shows a typical time variation of the Ar($1s_3$) number density during one LF cycle of the dual-frequency Ar-NH_3 DBD at two positions in the gap: in the bulk at mid-distance between the top and bottom electrodes, and in a zone including the sheath edge, near the top electrode. Applied voltages are V_{LF} = 650 V and V_{RF} = 195 V, and the discharge exhibits the $\alpha - \gamma$ transition [50], [72], [94], [171], [175], [177]. Overall, two main peaks associated to the γ mode can be seen: their duration is a few microseconds and their amplitude is only slightly modulated by the RF voltage. In the signal recorded in the center of the gap, the two peaks of Ar($1s_3$) densities have almost the same amplitude. On the contrary, a strong dissymmetry on the amplitude is observed for measurements done close to the top electrode. This confirms that the maximum population of Ar($1s_3$) states occurs when the discharge is in the γ mode characterized by significant electron heating in the cathode fall and thus significant production of Ar metastable atoms in this region through electron-neutral excitation collisions [35], [50]. In the present 50 kHz – 5 MHz DBD, a typical RF-α mode, characterized by very low populations of high-energy electrons, and thus very low production rates of Ar metastable atoms [35], [50], occurs in between the γ phases [95], [166], [176].

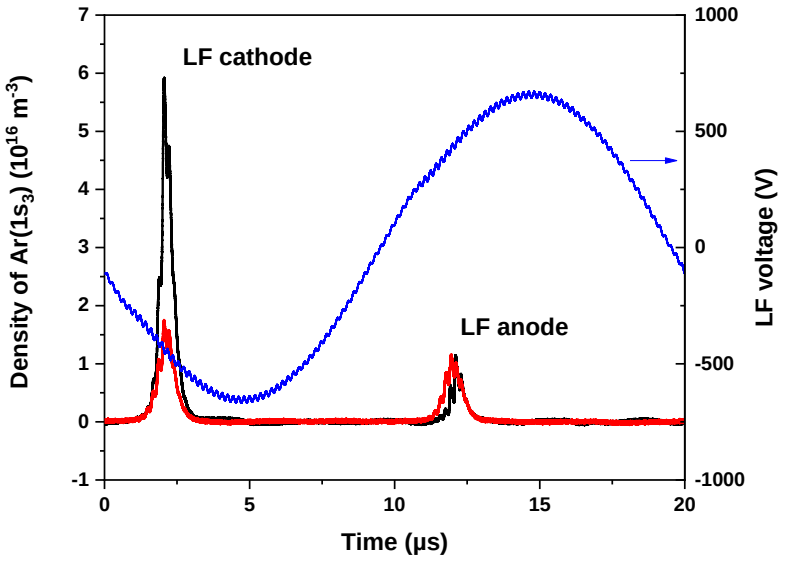

Figure 3. Time variation of the number density of Ar(1s$_3$) atoms, close to the top electrode (in black), and in the center (in red) during a LF period; V_{LF} = 650 V, V_{RF}= 195 V; the LF voltage is applied at the top electrode (in blue)

Ar(1s$_3$) metastable atoms are also measured near the top electrode for different amplitudes of the RF voltage between 0 (LF 650 V only) and 290 V (LF 650 V and RF 290 V). The results are shown in Figure 4 during the half-period of the applied LF voltage in which the γ mode appears at the top electrode (same dissymmetry as in Figure 3 is observed for the other half-period, not shown in Figure 4). Again, the main peak corresponds to the γ mode [35]. With the increase in amplitude of the RF voltage, temporal modulation over the RF cycle appears. In addition, the maximum value of the number density of Ar(1s$_3$) states decreases, and the main peak occurs earlier during the LF cycle, i.e. for a lower value of the applied LF voltage amplitude. Furthermore, the full width at half maximum of the main peak decreases; this result suggests that the γ breakdown lasts longer when the amplitude of the RF voltage increases.

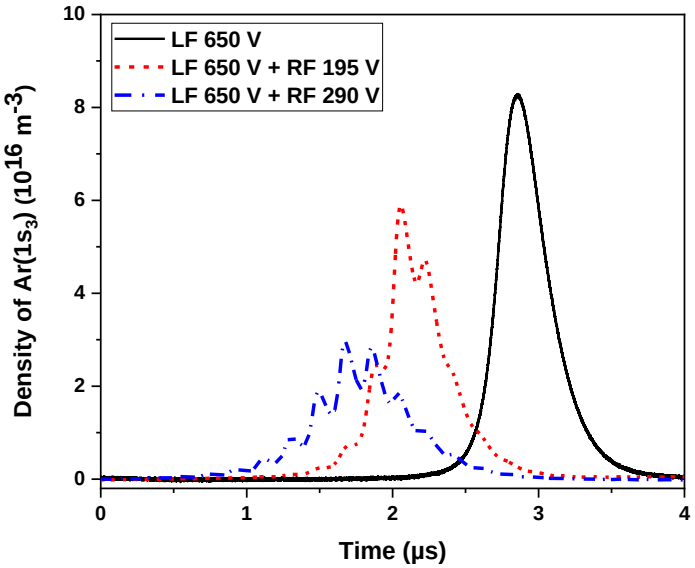

Figure 4. Number density of Ar($1s_3$) atoms recorded close to the top electrode over half-cycle of the applied LF voltage for different amplitudes of the RF voltage.

Analysis of the Ar $2p_1 \rightarrow 1s_2$ line emission intensity

In Ar-based DBD, optical emission spectra show several lines linked to Ar $2p_x \rightarrow 1s_y$ transitions [40]. One of the most important ones occurs at 750.4 nm (Ar $2p_1 \rightarrow 1s_2$). Considering that the Ar $2p_1$ state, at 13.48 eV, is essentially populated by the electron-impact excitation from the ground-state Ar atoms [182], [183], one can conclude that the 750.4 nm line emission intensity characterizes the presence of high-energy electrons. Figure 5 (a)-(c) show the space- and time-resolved mapping of the 750.4 nm line emission intensity during a half-period of the LF signal for the same experimental conditions as in Figure 4. As observed in previous studies of low-frequency DBDs operated in the homogeneous regime [27], [132], [184], the case of LF 650 V and RF 0 V (Figure 5 (a)) reveals a single peak per half cycle of the applied LF voltage, with a maximum value in the cathode fall. In line with the prominent excitation pathway of the Ar $2p_1$ state, the drastic increase of the 750.4 nm line emission intensity in the sheath reveals a significant rise in the population of high-energy electrons in this region. Similar results can be seen in dual-frequency DBD (Figure 5 (b) and Figure 5 (c)), with larger emission intensities in the γ mode than in the RF-α mode [50]. Despite the increase of the RF voltage from 195 to 290 V, Figure 5 (b) and Figure 5

(c) show no significant 750.4 nm emission outside the γ regime. In the case of LF 650 V and RF 195 V, it can be seen in Figure 5 (b) that the discharge is in the γ mode between about 1 and 2.5 μs, and it is in the α mode during the rest of the LF cycle. During the γ regime, the 750.4 nm line emission intensity oscillates with the RF voltage. Furthermore, the intensity first increases at about 500 μm from the cathode, and then gets closer to the cathode during the four following RF cycles. When the Ar $2p_1 \rightarrow 1s_2$ emission reaches a maximum value, it is at about 100 μm from the cathode. The variation of the position of the emission maximum is most likely related to the contraction of the cathode fall occurring with the γ breakdown. During this breakdown, the emission propagates throughout the gap with a decreasing amplitude up to about 300 μm from the anode where it begins to slightly increase. Similar behavior can be seen in Figure 5 (c) for LF 650 V and RF 290 V, with the γ mode occurring earlier during the LF cycle for RF 290 V than for RF 195 V, and being longer. Figure 5 (d) presents the effects of the amplitude of the RF voltage on the 750.4 nm line emission intensity recorded close to the cathode (around 1.75 mm from the bottom electrode, where it reaches a maximum value). Clearly, the 750.4 nm emission decreases with the rise of the RF voltage amplitude. In addition, the temporal width of the Ar $2p_1 \rightarrow 1s_2$ emission is larger when the amplitude of the RF voltage is higher. These results match the ones presented in Figure 4 for Ar($1s_3$) states; we will come back to this point later.

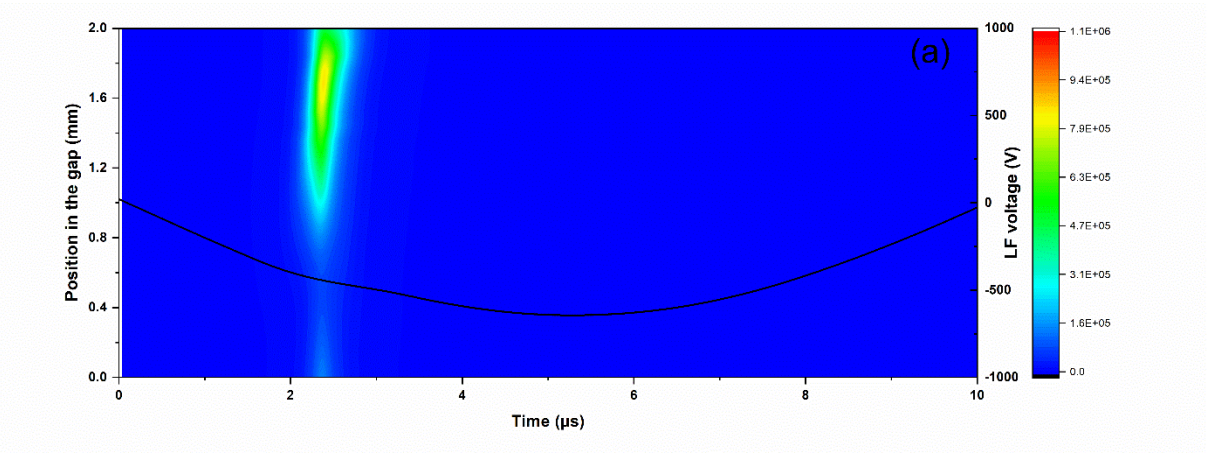
(a)
Position in the gap (mm)
Time (μs)
LF voltage (V)
2.0
1.6
1.2
0.8
0.4
0.0
0
2
4
6
8
10
1000
500
0
-500
-1000
1.1E+06
9.4E+05
7.9E+05
6.3E+05
4.7E+05
3.1E+05
1.6E+05
0.0

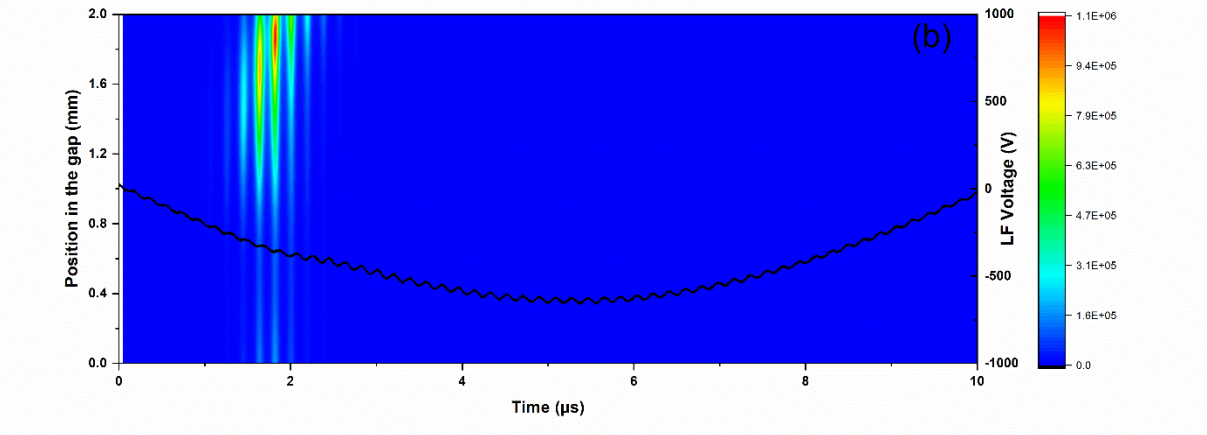
(b)
Position in the gap (mm)
Time (μs)
LF Voltage (V)
2.0
1.6
1.2
0.8
0.4
0.0
0
2
4
6
8
10
1000
500
0
-500
-1000
1.1E+06
9.4E+05
7.9E+05
6.3E+05
4.7E+05
3.1E+05
1.6E+05
0.0

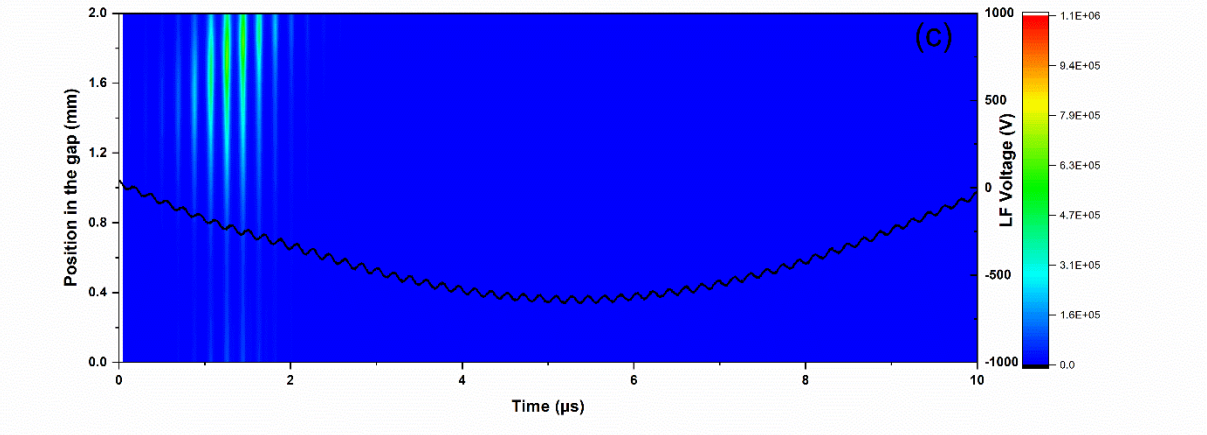
(c)
Position in the gap (mm)
Time (μs)
LF Voltage (V)
2.0
1.6
1.2
0.8
0.4
0.0
0
2
4
6
8
10
1000
500
0
-500
-1000
1.1E+06
9.4E+05
7.9E+05
6.3E+05
4.7E+05
3.1E+05
1.6E+05
0.0

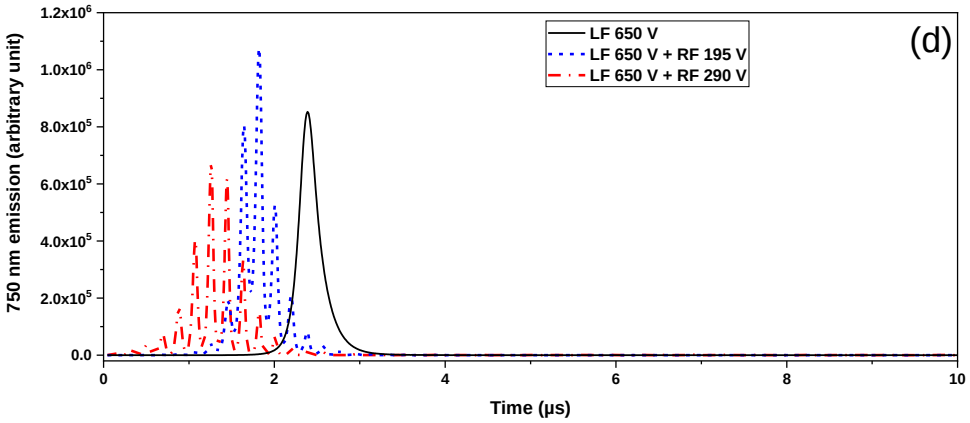

Figure 5. Space- and time-resolved mapping of the Ar 750.4 nm line emission intensity recorded in the dual-frequency Ar-based DBD for different amplitudes of the RF voltage: (a)LF 650 V; RF 0 V, (b) LF 650 V, RF 195 V, and (c) LF 650 V; RF 290 V. In all spatio-temporal mappings, the results are shown for half-cycle of the applied LF voltage, with the top electrode being the LF cathode and the lower one being the LF anode. In (d), the temporal profile of the Ar 750.4 nm emission recorded close to the cathode (at around 1.75 mm i.e. 0.25 mm from the cathode) are shown for RF 0 V, RF 195 V, and RF 290 V.

Analysis of the continuum emission intensity

In Ar-based DBDs sustained by RF excitation, in addition to the Ar $2p_x \rightarrow 1s_y$ transitions, optical emission spectra typically show significant continuum emission between 300 and 650 nm [24]. The origin of this continuum in Ar-NH_3 DBD is not fully determined. However, in weakly-ionized plasmas, it is usually attributed to electron-atom neutral Bremsstrahlung [84], [86], [94]. At a fixed pressure (and thus at a fixed population of neutral atoms), this implies that the continuum emission intensity is related to the electron number density and to the electron average energy (or electron temperature, assuming Maxwellian energy distribution function) [185]. This is in agreement with the fact that it is commonly observed in RF DBD and not in low-frequency DBD characterized by much lower time-averaged electron populations [19]. Furthermore, in RF DBDs, the RF voltage amplitude (or RF power amplitude) has little impact on the electron temperature [84], as confirmed later using the 1D fluid model. Therefore, over the range of experimental conditions investigated, it can be assumed that variations in continuum emission intensity as RF voltage is varied are related to variations in electron densities. Hence, in Ar-based DBD, the 750.4 nm emission mostly probes the population of high-energy electrons, whereas the continuum emission predominantly describes the total number density of electrons [22], [24]. The spatio-temporal mapping of the continuum

emission is also analyzed in the dual-frequency DBD. Here, to avoid perturbation by other emission from Ar $2p_x \rightarrow 1s_y$ transitions, measurements are made at 500 nm.

Figure 6 (a)-(b) show the space- and time-resolved mapping of the 500 nm continuum emission intensity during a half-period of the LF signal for the same experimental conditions as in Figure 5. Here, the case of LF 650 V and RF 0 V is not shown since no continuum was observed. Clearly, the 500 nm emission presented in Figure 6 (a) (LF 650 V and RF 195 V) and Figure 6 (b) (LF 650 V and RF 290 V) behaves quite differently than the emission at 750.4 nm shown in Figure 5 (b) and Figure 5 (c) for the same experimental conditions. First, the continuum emission is present in both γ mode (as for the 750.4 nm emission) and RF-α mode (no emission at 750.4 nm). In both cases, the intensity is RF modulated. Second, the continuum emission appears in the bulk, with maximum intensity occurring towards the LF anode (it is maximum close to the cathode at 750.4 nm). Third, the maxima of the continuum intensity are temporally delayed by about 30 ns with respect to the one at 750.4 nm; such behavior results from the lifetime of $Ar(2p_1)$ state (22 ns) which would delay the argon emission. As mentioned above, the continuum emission being linked to the electron number density, the signal at 500 nm appears when and where the electron population is high, i.e. in the plasma bulk during the γ breakdown and in the RF-α regime. As for the position of the plasma bulk in the gap, it depends on the one of the cathode fall. On one hand, when γ breakdown in the cathode sheath occurs, the bulk is closest to the anode and the continuum emission is more prominent in this region, as seen in Figure 6 (a) and Figure 6 (b). On the other hand, in the RF-α regime, the discharge is centered between the two electrodes and the continuum emission appears near the center of the gap.

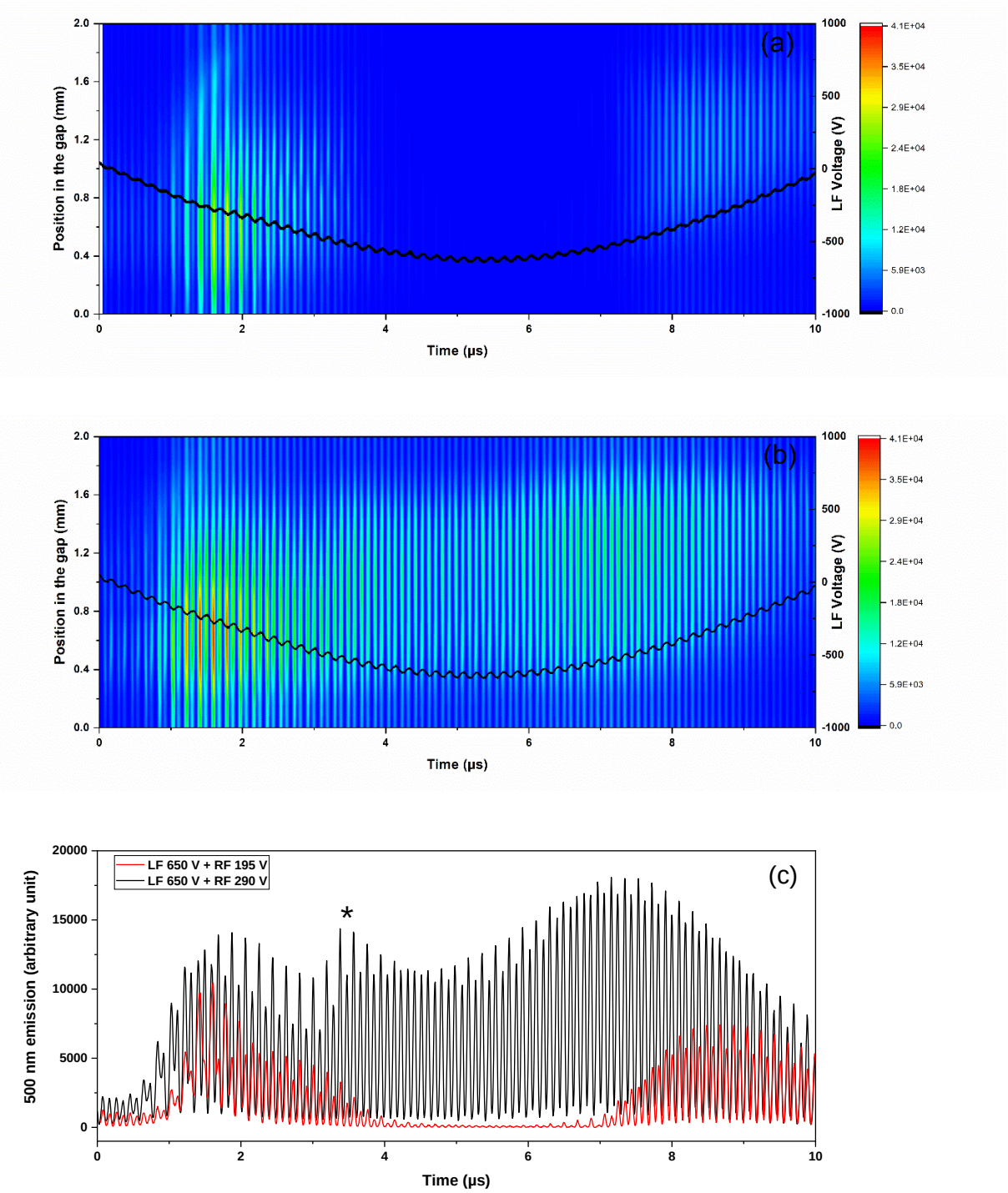

Figure 6. Space- and time-resolved mapping of the 500 nm continuum emission intensity recorded in the dual-frequency Ar-based DBD for different amplitudes of the RF voltage: (a) LF 650 V, RF 195 V and (b) LF 650V; RF 290 V. In both spatio-temporal mappings, the results are shown for half-cycle of the applied LF voltage, with the top electrode being the LF cathode and the lower one being the LF anode. In (c), the temporal profile of the Ar 500 nm emission recorded close to the cathode (at 1.44 mm i.e. 0.56 mm from the anode) are shown for RF 195 V and Rf 290 V.

In line with the results presented in Figure 5 (d) for the 750.4 nm emission, Figure 6 (c) shows the effects of the RF voltage amplitude on the continuum emission intensity recorded close to the cathode (at 1.44 mm). When the amplitude of the RF voltage increases from 190 to 290 V, the continuum emission intensity rises significantly in the RF-α mode, which a much less prominent increase in the γ mode. Between the γ and RF-α modes (between 3 and 7 µs), Figure 6 (c) reveals that the continuum emission intensity strongly depends on the amplitude of the RF voltage. In contrast, the time domain between the RF-α and γ regimes (between 0 and 1 µs) remains very little emissive for both RF 195 V and RF 290 V. Finally, it is worth highlighting that for V_{RF}=290 V, an additional peak appears around 3.5 µs (labeled with a star in Figure 6 (c)). The origin of this peak will be defined later with the understanding of the time variation of the gas voltage.

1D fluid modeling and discussion

As shown in the previous section, the RF voltage amplitude has different effects on the number density of Ar($1s_3$) atoms, measured at two positions in the gas gap (see Figure 3 and Figure 4), on the population of high-energy electrons, deduced from the Ar 750.4 nm line emission intensity (see Figure 5), and on the total number density of electrons, deduced from the intensity of the continuum emission (see Figure 6). On one hand, similar findings are obtained from the measurements of Ar($1s_3$) number densities and 750.4 nm line emission intensity; this results from the fact that Ar($1s_3$) and Ar($2p_1$) levels are mostly populated by electron-impact excitation from the ground state Ar atoms (requiring 11.71, and 13.48 eV for Ar($1s_3$) and Ar($2p_1$), respectively) and their excitation rates therefore reflect the population of high-energy electrons. In both sets of data, the maximum values observed in the γ mode: (i) decrease with the rise of the RF voltage amplitude, (ii) appear earlier in the LF cycle for RF 290 V than for RF 195 V, and (iii) last for a longer time with the rise of the RF voltage amplitude. On the other hand, the continuum emission observed in the bulk, which is related to the number density of electrons, increases significantly between RF 195 V and RF 290 V, with a more prominent rise in the RF-α mode than in the γ regime.

Additional information can be obtained by comparing the space- and time-resolved optical data recorded in this study with the predictions of a 1D fluid model of Ar-based DBD described and validated in a previous work [35]. This model solves the continuity and momentum equations for all species and the energy equation for electrons. It considers 7 species (Ar, Ar^+, Ar_2^+, Ar(1s), Ar_2*, photons and e^-) through 11 reactions. Secondary electron emission from dielectric surfaces, induced by impinging of Ar^+, Ar_2^+, Ar(1s), Ar_2* and VUV photons is also considered. All details on reaction rates and secondary electron emission coefficients are provided in [35]. Of note, Ar has four Ar(1s) levels: Ar($1s_2$), Ar($1s_3$), Ar($1s_4$), and Ar($1s_5$), of which Ar($1s_3$) and Ar($1s_5$) are long-lived metastable states. But due to the resonance radiation trapping of $1s_2 \rightarrow {}^1S_0$ and $1s_4 \rightarrow {}^1S_0$ photons, where ${}^1S_0$ is the Ar ground state, the effective lifetimes of the resonance states Ar($1s_2$) and Ar($1s_4$) become comparable to those of metastable states. Hence, these four states can be considered to be close to their statistical equilibrium, with number density ratios 3:1:3:5 for Ar($1s_2$):Ar($1s_3$):Ar($1s_4$):Ar($1s_5$) states, respectively [130], [132]. Under this assumption, these four states are treated as a single Ar(1s) state, with a total density 12 times higher than the measured density of the Ar($1s_3$) level [35].

As indicated before, experiments are done for a LF voltage amplitude of 650 V, which is 50 V above the LF breakdown for the investigated experimental conditions. In line with this result, calculations are done at V_{LF}=940 V, a value 50 V above the lower LF voltage allowing a LF discharge breakdown in the model. As for the RF voltage amplitude, the first value is set at the lowest value allowing to get a single frequency RF discharge, V_{RF}=350 V. As for the second V_{RF} value, in line with the experiments, it is fixed 100 V above this value, at 450 V. Here, the differences between the experimental and simulated values of the LF and RF breakdown voltages can be partially attributed to the error on the dielectric permittivity of the Al_2O_3 dielectrics placed on top of the metallic electrodes. This permittivity is not measured and is set at 9 in the model [50]. Despite such slight differences in the amplitudes of LF and RF voltages between the simulations and experiment, the agreements are relatively good, as demonstrated below.

Figure 7 shows the Ar(1s) number densities obtained from the model for the two RF voltage amplitudes. In line with the time-resolved tunable diode laser absorption spectroscopy

measurements recorded at two positions in the gas gap (Figure 3), the spatio-temporal mappings displayed in Figure 7 (a) (LF 950 V, RF 350 V) and Figure 7 (b) (LF 950 V, RF 450 V) reveal a significant rise only once per half-period of the applied LF voltage. In addition, such increase appears mostly in the cathode fall in the γ mode. Absolute values of Ar($1s_3$) states predicted by the model (calculated Ar(1s) density divided by 12) are also comparable to the ones recorded experimentally (for V_{RF}=290 V, measured Ar($1s_3$) density is $5.9*10^{16}$ m^{-3}, calculated Ar($1s_3$) density is $1.4*10^{17}$ m^{-3}). As in the experiment (Figure 3), a small increase is also observed in Figure 7 (a) and Figure 7 (b) close to the anode. Of note, the ratio of the maximum at the cathode and the anode is about 5.3 in the calculations and 5.2 in the experiments for the low RF voltage value. At the higher RF voltage, this ratio is 4.8 in the calculations and 4.3 in the model. As for the evolution between RF 350 V and RF 450 V of the Ar(1s) maximum number density integrated over the top 500 µm of the gap near the top electrode, it also follows the same trend as the ones observed experimentally (Figure 4). In particular, the maximum density decreases by 27% following the increase of the RF voltage amplitude by 100 V. These results could be explained by a decrease of the quantity of high-energy electrons when the RF voltage amplitude increases [73]. In addition, the peak density of Ar(1s) atoms appears earlier on the LF cycle (this means for a lower amplitude of the LF voltage), and broadens between RF 350 V and RF 450 V. As shown in Figure 7 (a) and Figure 7 (b), the Ar(1s) population also increases close to the anode, as observed in the experiments (Figure 3).

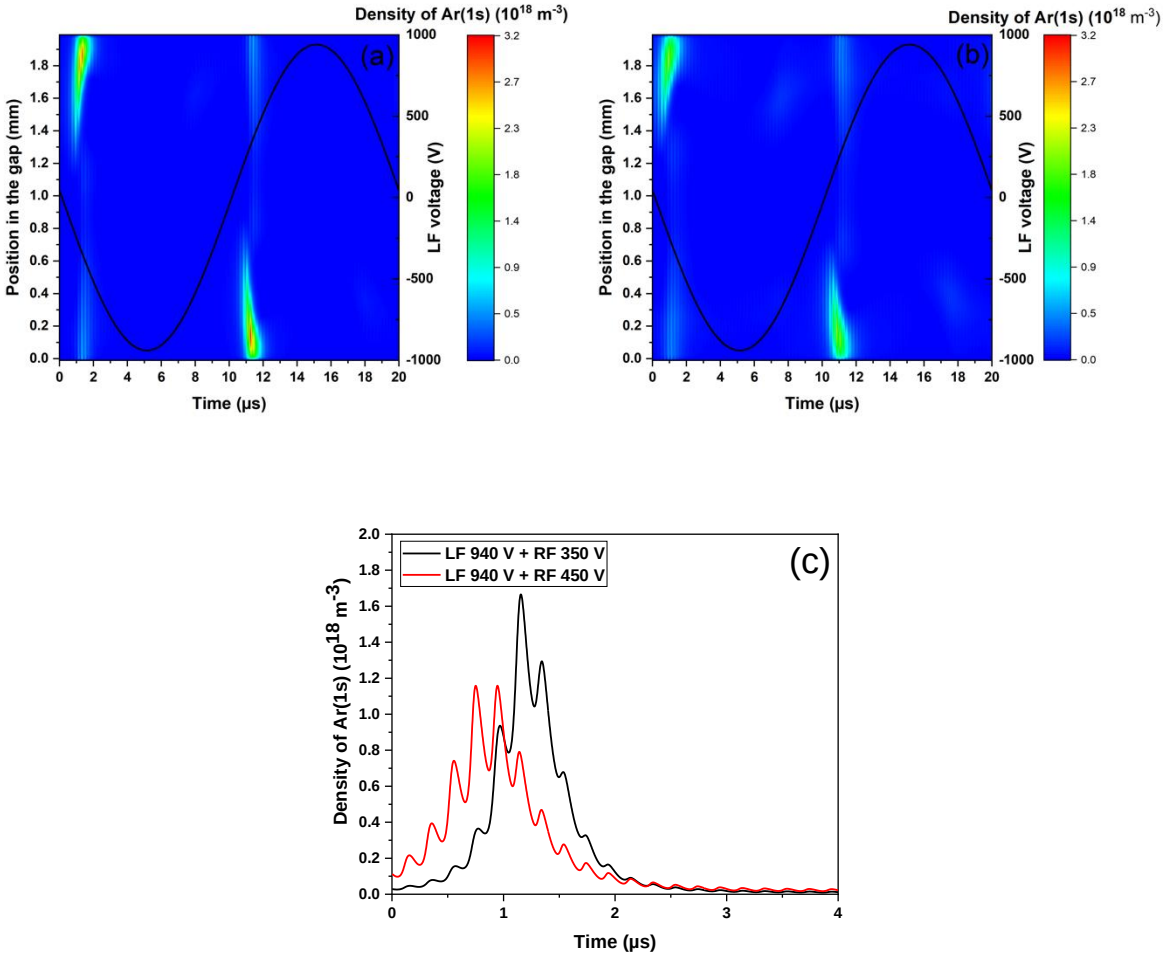

Figure 7. Calculated values of the Ar(1s) number density in the gap as function of time for : (a) LF 940 V and RF 350 V, (b) LF 940 V and RF 450 V. In (c), calculated Ar(1s) number density values integrated over the top 500 μm of the gap near the top electrode (the cathode) between 0 and 4 μs.

Following such validation, the space- and time-resolved optical measurements are further analyzed based on calculated values of n_e (electron number density), n_i (positive ion number density) and T_e (electron temperature). Figure 8 presents spatio-temporal mappings of n_e, n_i and T_e obtained from the model [35] during a LF cycle for the two RF voltage amplitudes. In both, Figure 8 (a) (LF 950 V, RF 350 V) and Figure 8 (b) (LF 950 V, RF 450 V), n_e is high in the bulk and low close to the walls; this defines the sheath region. In addition, there is a local rise close to the anode in the electron density near the γ breakdown. Between RF 350 V and RF 450 V, there is an overall increase in the electron density, with most of this increase occurring in the RF-α regime. Overall,

the space- and time averaged value of n_e rises by 31%. Assuming that the emission at 500 nm is attributed to the electron-atom neutral Bremsstrahlung [84], [94], and is thus mostly linked to n_e (assuming only small variations of T_e, as confirmed below), the increase of n_e deduced from the model in Figure 8 (a) and Figure 8 (b) is consistent with the one seeing in the experiment in Figure 6 (the time and space-integrated continuum emission intensity increases by about factor 2 between RF 195 V and RF 290 V).

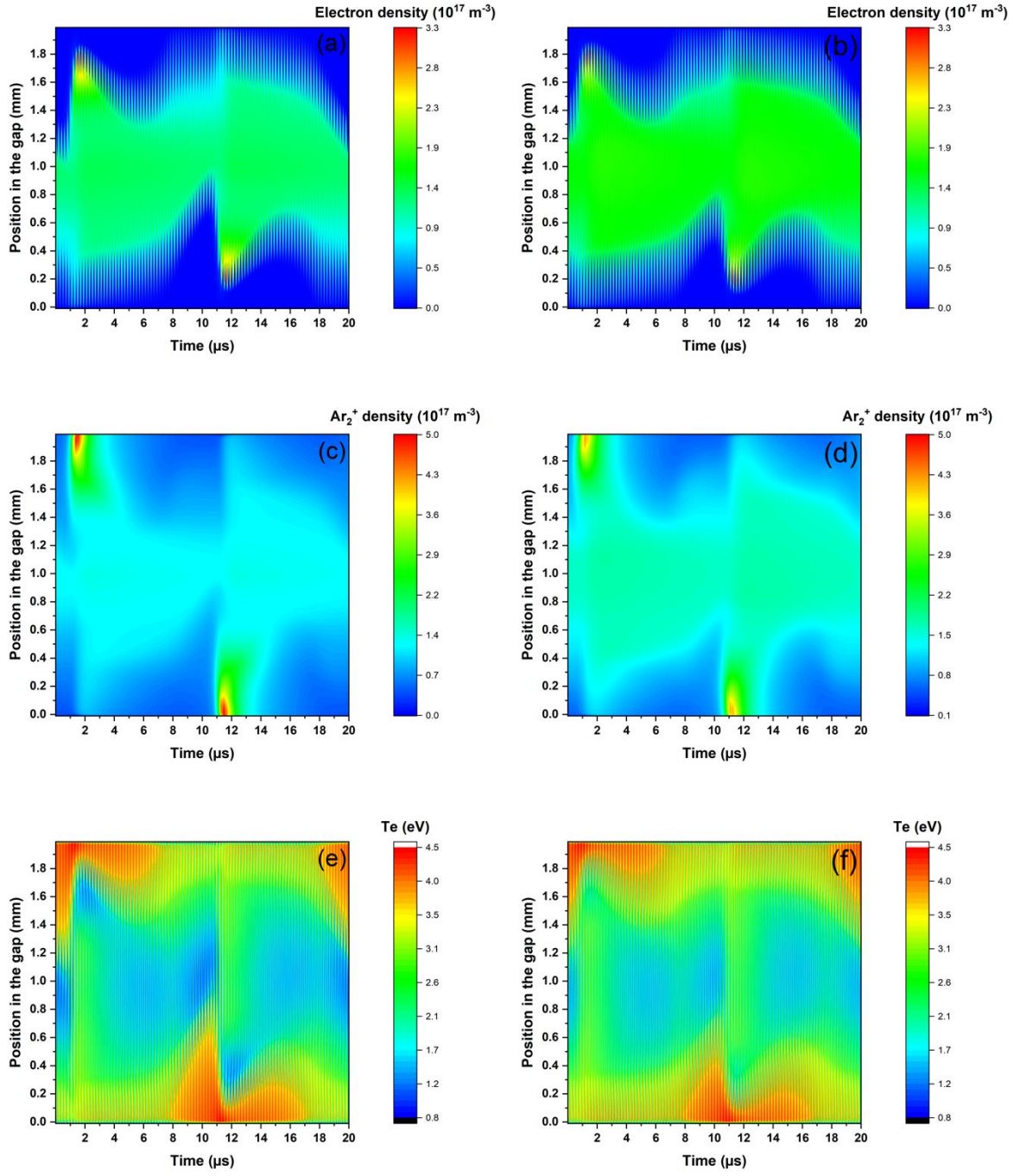

Figure 8. Values of the electron density (a,b), positive ion density (c,d), and electron temperature (e,f) obtained from the model in the gap as function of time for : (a,c,e) LF 940 V and RF 350 V, (b,d,f) LF 940 V and RF 450 V.

Figure 8 (c) and Figure 8 (d) show the spatio-temporal evolution of the Ar_2^+ ions density following the increase of the RF voltage amplitude. In both conditions, the Ar_2^+ density is higher in the bulk

than in the sheaths, except during the γ breakdown. In addition, the temporal evolution of the ions is slow at the RF scale: in contrast to the electron density that evolves at both RF and LF time scales, the population of Ar_2^+ mostly "sees" the LF voltage. Since ionization of Ar by high energy electrons produces Ar^+, which is rapidly converted to Ar_2^+ ions by 3-body reactions with 2 ground-state Ar atoms [35], Ar_2^+ is the dominant positive ion and, at the LF scale, its behavior is expected to follow the one of the high-energy electron population (behavior visible in both the number density of Ar(1s) atoms (Figure 4) and the Ar 750.4 nm line emission intensity (Figure 5)). Here, the space- and time-averaged value of Ar_2^+ increases by 24% between RF 350 V and RF 450 V.

As for the spatio-temporal mapping of the electron temperature presented in Figure 8 (e) and Figure 8 (f), the values are lower in the bulk than in the sheath. As expected, the maxima of T_e appear in the cathode sheath during γ breakdown. At the α - γ transition, one can also see an increase of T_e throughout the gap: this is the consequence of the deformation of electric field in the bulk to evacuate the electrons created in the cathodic sheath in order to maintain the quasi-neutrality in the plasma bulk. Such behavior corroborates the increase from the cathode to the anode observed during γ breakdown in Figure 4 for the Ar(1s) and in Figure 5 for the Ar 750.4 nm line emission intensity. Figure 8 (e) and Figure 8 (f) further show that the space- and time-averaged value of T_e only slightly rises (+5%) between RF 350 V and RF 450 V. Here, this very small increase mostly results from an increase of T_e in the bulk, which is partially compensated by a decrease in the spatio-temporal domain of high T_e values in the γ regime (the cathode sheath is much larger at RF 350 V than at RF 450 V). Such aspect is investigated in more details by examining the behavior of the gas voltage. Here, it is worth recalling that in DBDs, due to the presence of charges on dielectric surfaces, the voltage applied to the gas does not correspond to the voltage applied to the electrodes by the LF and RF generators [186].

Figure 9 (a) and Figure 9 (b) show the gas voltage calculated from the model for the two RF voltage amplitudes. In both cases, the shape is characteristic of a low-frequency DBD operated in a glow regime [58] to which is added a RF voltage. The γ breakdown is recognizable by the fast drop in the gas voltage amplitude just after its maximum value. The RF-α regime occurs between two γ breakdowns, when the gas voltage oscillates around 0 V, i.e. when the LF contribution to the gas

voltage is low. As expected, the RF-α mode is directly linked to the amplitude of the RF voltage: thus, by increasing the RF voltage amplitude, events due to the α regime are reinforced. For the γ mode, Figure 9 (a) and Figure 9 (b) show that the trend is different. The increase from RF 350 V to RF 450 V globally increases n_e and n_i in the bulk, as seen in Figure 8, and this promotes LF breakdown in the γ mode. Here, γ breakdown occurs at a lower gas voltage with increasing RF voltage amplitude (maximum gas voltage is 844 V for the LF + RF 350 V and 787 V for the LF + RF 450 V).

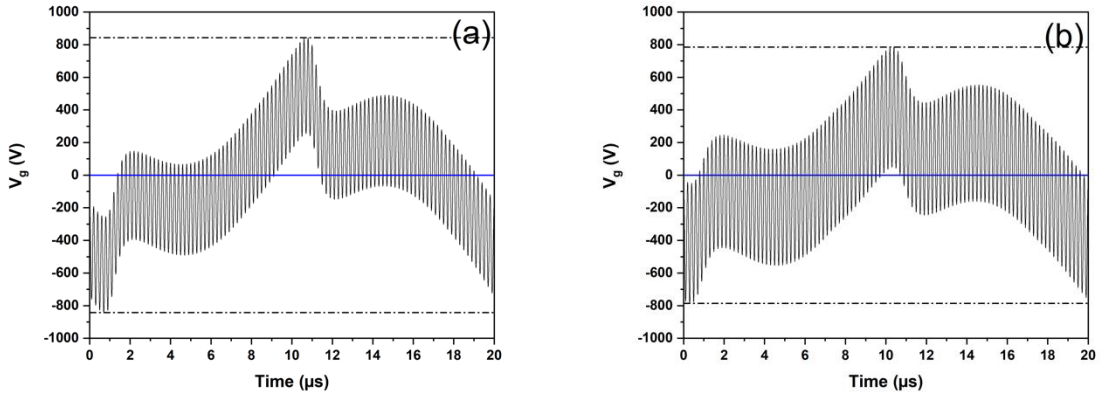

Figure 9. Calculation of the gas voltage during the LF period for (a) LF 940 V and RF 350 V, (b) LF 940 V and RF 450 V.

Figure 10 presents a decomposition between LF (a) and RF (b) contributions of the voltage applied to the gas and the voltage across the dielectrics (V_{ds}) for the same conditions as in Figure 9. Here, the LF contribution corresponds to the RF-smoothed signals of V_g and V_{ds} and the RF contribution corresponds to the amplitude of the RF oscillations on V_g and V_{ds}, calculated from the difference between their upper and lower envelope values. For both RF 350 V and RF 450 V, Figure 10 (a) reveals that the LF gas voltage increases until the γ breakdown, after which it decreases during a short time. The second rise of V_g starts around 2 and 12 µs: this results from the fact that after the γ breakdown, the applied LF voltage is still rising such that V_g follows the same trend. This latter behavior, coupled with the fact that for the LF 940 V + RF 450 V, n_e is greater than for LF 940 V + RF 350 V, also explains the origin of the additional peak of the continuum emission during the γ-to-α transition displayed in Figure 6 (c). By increasing the RF voltage, the γ breakdown appears earlier, i.e. for a lower LF voltage amplitude. In addition, the slope of decrease/increase of V_g due

to dielectric charge after the γ breakdown is lower for LF 940 V + RF 450 V, than for LF 940 V + RF 350 V. Concerning V_{ds}, the main visible change is also linked to the time of the increase/decrease of V_{ds} after the γ breakdown. Since the α - γ transition occurs earlier for higher RF voltage amplitudes, i.e. for a lower LF voltage, the dielectric charges earlier and slower, and this induces the same behavior on V_{ds}. Consequently, the rise in the population of Ar(1s) and Ar(2p) is expected to occur earlier and both peaks are expected to broaden when the RF voltage amplitude rises; such findings are consistent with the experimental results presented in Figure 4 and Figure 5.

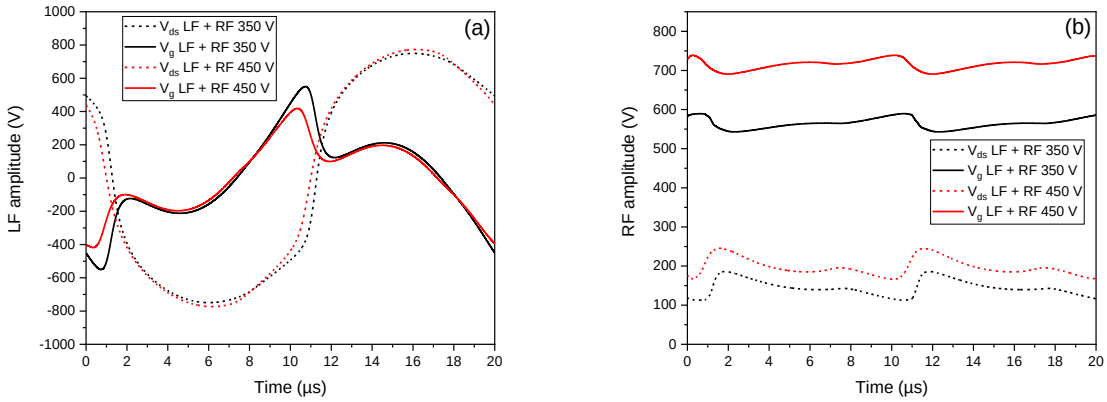

Figure 10. (a) LF contribution to Vg and Vds, (B) RF contribution to Vg and Vds, obtained from the model (LF 940 V and RF 350 V in black, LF 940 V and RF 450 V in red).

As for the RF amplitude, Figure 10 (b), reveals that most of the applied RF voltage is applied to the gas, with only a small drop across dielectrics. When the γ breakdown occurs, charge density increases in the plasma (particularly in the sheath) such that losses and thus charging at the dielectric walls also increase. With such charging of dielectrics, V_{ds} increases, and this leads to a decrease of V_g. Over the range of experimental conditions investigated, Figure 10 (b) further shows that the amplitude of the RF component of V_g increases by only 75 V (averaged over the LF cycle) following the increase between RF 350 V to RF 450 V. Hence, a larger fraction of the applied voltage goes to the dielectrics with increasing amplitude of the RF voltage.

Such analysis of V_g and V_{ds} clearly underlines the importance of dielectrics for a detailed analysis of DBDs exhibiting the α - γ transition. On one hand, as the amplitude of the RF voltage increases, the γ breakdown appears earlier in the LF cycle, a lower maximum gas voltage is distributed in the gap (mainly in the cathode sheath) and this yields to a weaker local electric field. This weaker local electric field accelerates less the electrons in the sheath, inducing a decrease of the spatial and temporal domains of high energy electrons. This results in a decrease in the local production rates of reactions requiring high-energy electrons, for example, excitation and ionization of Ar in the cathode sheath edge. Again, this finding is consistent with the results presented in Figure 4 and Figure 5 showing a decrease of the main Ar(1s) and Ar(2p) peak intensities when V_{RF} is increased from 195 V to 290 V. On the other hand, a rise in the amplitude of the RF voltage increases the power absorbed and dissipated by electrons in the RF-α mode. In line with the spatio-temporal mappings of the continuum emission displayed in Figure 6, this produces higher number densities of charged species in the bulk, which explains the α - γ transition for a lower gas voltage value.

Conclusion

Spatio-temporal mappings of the populations of metastable atoms Ar(1s) and of the emission intensities of Ar(2p) states as well as the continuum emission in Ar-based DBDs exhibiting the α - γ transition were analyzed by space- and time-resolved optical absorption and emission spectroscopy. It was shown that the 50 kHz–5 MHz dual-frequency discharge allows to control the discharge fundamental properties through judicious change of the amplitude of the RF voltage. The higher is the RF voltage amplitude, the higher is the electron density in the bulk and the closer the discharge is to the typical RF-α regime characterized by an ohmic heating of plasma electrons in the bulk. Consequently, in such conditions, the phenomena linked to the γ breakdown (in particular, the production of high-energy electrons in the cathode sheath) have a much lower contribution. It was further shown that increasing the RF voltage amplitude reduces and delays the excitation rate of Ar atoms, thus the maximum values of the Ar(1s) metastable density and of the Ar 750.4 nm line emission intensity, observed in the γ mode. On the other hand, the continuum emission observed in the bulk, which is related to the number density of electrons, increased significantly, with a more prominent rise in the RF-α mode than in the γ regime. Such behaviors, which seemed surprising at first glance, are very well explained by the decrease in the gas voltage necessary to

cause the self-maintenance of the cathode sheath when the electrons and ions densities increase, and leads therefore to the γ breakdown.

Acknowledgments

The work carried out in France was supported by the Agence Nationale de la Recherche through the Investissement d'avenir program (ANR10LABX2201). As for the one done in Canada, it was funded by the National Science and Engineering Research Council (NSERC RGPIN-2018-04550) and by the Fondation Courtois. The 'Réseau des Plasmas Froids' of CNRS/MCRT (France) is acknowledged for providing the DFB diode laser and the travel support for Nader Sadeghi and LPGP, Orsay (France) for lending the MCS6A Multiscaler. All authors would like to acknowledge the financial support of the CNRS and Université de Montréal through their contributions to the International Research Network on Controlled Multifunctional Nanomaterials.

Data availability statement

The data that support the findings of this study are available upon request from the authors.

Chapitre 4 – Influence de la gaine cathodique transitoire sur le transport d'espèces chargées d'une décharge double fréquence BF-RF

Les études, menées dans l'article précédent, concernant la double fréquence soulignent les différences de comportements des régimes α et γ face à une augmentation de tension RF. En s'intéressant plus en détail à la décharge double fréquence, plus spécifiquement autour du régime γ, elles soulèvent aussi de nouvelles questions :

- Quelles sont les origines des dissymétries observées sur le courant mesuré entre les différentes alternances à l'échelle RF ?
- Pourquoi les maximums de densités électroniques sont présents en bordure de gaines lorsque les tensions BF et RF sont opposées ?
- Comment expliquer la différence d'intensité lumineuse du continuum d'émission entre une alternance RF et la suivante ?

L'article suivant se propose de répondre à ces questions à l'aide des mêmes outils que pour l'article précédent c'est-à-dire un diagnostic électrique associé à une cartographie résolue dans l'espace et le temps des émissions à 500 nm et 750 nm ainsi qu'un modèle fluide 1D. Comme énoncé précédemment, cet article se concentre autour du régime γ, pendant un laps de temps de 2.5 µs (soit 1/8 de la période) permettant de mieux appréhender les variations des différentes propriétés fondamentales du régime γ à l'échelle de la RF.

Les travaux sont présentés sous la forme d'un article en préparation finale pour une soumission à Journal of Applied Physics (en attente des corrections des co-auteurs).

Dual frequency sheath oscillations and consequences on the ion and electron transport in dielectric barrier discharges at atmospheric pressure

Raphaël Robert[1,2], Gerjan Hagelaar[3], Nader Sadeghi[4], Luc Stafford[2], Françoise Massines[1]

[1]Laboratoire Procédés Matériaux et Énergie Solaire (PROMES, CNRS, UPR 8521), Rambla de la thermodynamique, 66100 Perpignan, France

[2]Département de physique, Université de Montréal, 1375 ave. Thérèse-Lavoie-Roux, Montréal, Québec, H2V 0B3, Canada

[3] Laboratoire Plasma et Conversion d'Énergie (LAPLACE, CNRS, UMR5213), 118 Route de Narbonne, 31077 Toulouse, France

[4]Laboratoire Interdisciplinaire de Physique (LIPhy CNRS, UMR 5588), Laboratoire des Technologies de la Microélectronique (LTM, CNRS, UMR 5129), Université de Grenoble-Alpes, Grenoble, France

Abstract

Current-voltage characteristics, space- and time-resolved optical emission spectroscopy, and 1D fluid modeling are used to examine the effect of dual-frequency sheath oscillations on the ion and electron transport in dielectric barrier discharges (DBDs) sustained by a combination of low-frequency (LF, 50 kHz, 650 V) and radiofrequency (RF, 5.3 MHz, 195 V) voltages, and exhibiting the α–to–γ mode transition.On one hand, when polarities of the LF and RF voltages are opposite, an electric field near the LF cathode (due to LF cathode sheath) drives the secondary electrons to the plasma bulk and an opposite electric field between the sheath edge and the LF anode attracts the electrons towards the LF cathode (to maintain quasi-neutrality in the plasma bulk). At the sheath edge, electrons become trapped and ions drift towards the cathode and the anode simultaneously according to their position in the gap. On the other hand, when the RF voltage has the same polarity as the LF voltage, the total applied voltage increases and this yields to enhanced production of electrons and ions in the sheath. To maintain quasi neutrality in the bulk, the electric field along the gap exhibits the same polarity as the one in the sheath, allowing electrons created in the sheath to be evacuated towards the LF anode. The behavior of the LF cathode is therefore controlled by the LF sheath, and thus by the LF voltage amplitude, while the behavior in the bulk and at the anode alternates on the time scale of the RF voltage.

Introduction

Over the last 50 years, various configurations leading to stable and diffuse dielectric barrier discharges (DBDs) at atmospheric pressure have been established [6], [8], [9], [52], [54]. Most available studies have been conducted at frequencies of the applied voltage less than 250 kHz, resulting in pulsed discharges whose nature varies depending on the so-called memory effect in which energetic species can be carried from one discharge to the next [41], [119], [131], [187]. This specific behavior is not observed in the radio frequency (RF) range, wherein the discharge is rather continuous, and the time-averaged number density of ions and electrons, partially trapped in the plasma bulk, is much higher than at low frequency (LF) [21], [60]. Moreover, in the RF range, the breakdown voltage is lower than at LF [22], [27], and only a small portion of the applied voltage falls across the solid dielectrics due to rapid voltage oscillations [188]. As a result, the discharge is no longer dominated by the effects of the dielectrics, and the ionization degree is governed by the amplitude of the instantaneous applied voltage [23], [166], [189]. When the power absorbed or dissipated by the plasma electrons is increased, a transition from the RF-α to the RF-γ mode can be reached [50], [72], [94], [171], [175], [177]. This $\alpha - \gamma$ transition induces a significant flux of ions to the cathode and thus the emission of a large number of secondary electrons; hence, there is a strong electron multiplication in the sheath. In this γ mode, a solid dielectric placed on the metallic electrodes is necessary to avoid discharge localization and to improve the discharge stability [93].

More recently, dual-frequency DBDs (DF-DBDs) have emerged as stable, high power DBDs that can be easily implemented in plane-to-plane or jet configurations [89], [96], [171], [190]. In DF-DBDs, one electrode is powered by LF voltage (< 250 kHz), whereas the other one is powered by RF voltage (for example, 5 MHz or 13.56 MHz). The two voltage signals are typically synchronized, and the power supplies have a common ground. So far, many studies have been conducted on DF-DBDs in Ar-based gas mixtures, and various configurations have been examined [50], [71], [84], [89], [94], [96]. In such conditions, it was found that secondary electron emission from the cathode does not only rely on positive ions and Ar metastables irradiation: the VUV photons resulting from the spontaneous de-excitation of the Ar_2^* excimer produced by fast conversion of Ar(1s) metastable states also contribute to secondary electron emission, and thus to electron multiplication in the sheath [35].

In DF-DBDs, two modes can be reached, α or α – γ modes. The α regime in DF-DBDs exhibit the same behavior as in single-frequency RF DBDs characterized by ohmic heating of plasma electrons in the bulk where the electron temperature is quite low [95], [166], [176]. However, the power absorbed or dissipated by the plasma electrons in α DF-DBDs is lower than that of a RF DBD generated at the same RF voltage amplitude [50]. Such variation may be attributed to the effect of the LF voltage in inducing ion loss at the walls, which in turn decreases the plasma density [50]. As for the α – γ DF-DBDs, they alternate between α and γ mode at the LF time scale. γ mode is observed when the electric field established in the sheath is high enough to induce a self-sustained discharge in the LF cathode sheath [50]. Specifically, the high-electric field condition accelerates the flux of secondary electrons across the collisional sheath, thereby promoting electron multiplication and increasing the production of positive ions, VUV photons, and additional secondary electrons in the sheath [35]. The gamma mode is initiated over several RF cycles, each time the LF voltages approaches its maximum (i.e. twice per LF period). In such conditions, since the ions only weakly "see" the RF modulations due to their larger mass than the electrons, they flow continuously towards the cathode. This results in continuous secondary electron emission, which reduces the voltage applied to the gas and thus increases the voltage across the dielectrics. Since the duration of the γ behavior in DF-DBDs is limited by the decrease in gas voltage [188], as in the case of a LF discharge, this mode can last for a few microseconds in the LF cycle (about 10 %), such the α – γ DF-DBD is in α regime most of the time (about 90 %) [50]. Compared to the α mode, this γ regime is characterized by higher time-averaged electron number densities (N_e) and temperatures (T_e) due to increased electron multiplication and enhanced electric field in the cathode fall, respectively [188].

Several studies have been conducted on α and α – γ DF-DBDs operated in Ar-based gas mixtures. Specifically, the α and α – γ modes were compared, and the effects of LF voltage amplitude [50], [84], [95], [96], RF voltage amplitude [96], [188], [190], phase between the two voltage signals [163], [167], [191], and number of harmonics on a fundamental frequency [192], [193] were examined. However, to the best of knowledge, the influence of RF polarity oscillations on the transport properties of charged species in α – γ DF-DBDs has not been reported. In this work, a combination of experimental measurements and simulations is used to examine the effect of dual-

frequency sheath oscillations on the ion and electron transport in an α – γ DF-DBD generated in Ar-NH_3 gas mixtures at atmospheric pressure. For this purpose, the current-voltage characteristics are measured, and the space- and time-resolved optical emission intensities from Ar(2p-1s) lines and bremsstrahlung continuum emission intensities are also recorded. Electrical and optical measurements are further analyzed in combination with the predictions of a 1D fluid model of Ar-based DBDs described and validated in a previous work [35].

Experimental set-up and diagnostics

A full description of the plane-to-plane DBD system used in this study is provided in [35], [188]. Briefly, the setup consists of two metallic electrodes (1 x 5 cm²) covered with a 1-mm-thick layer of alumina dielectric (7 x 7 cm²) and mounted in plane-to-plane configuration at 2 mm gap distance. The DBD cell is housed in a plasma chamber that is first vacuumed down to 1 mTorr and then filled with Ar + 200 ppm of NH_3 at 3 standard liters per minute up to 760 Torr. A needle valve between the chamber and the pumping system allows maintaining the atmospheric pressure condition. The upper electrode is powered by a 50 kHz LF generator, whereas the lower one is connected to a 5.3 MHz RF generator. The LF and RF voltage amplitudes are set to 650 V (50 V above the breakdown voltage of the 50 kHz LF discharge) and 195 V (50 V above the breakdown voltage of the 5.3 MHz RF discharge), respectively. In addition, both waveforms are generated using the same generator (Keysight 33500B series) to ensure adequate synchronization and common ground. Current-voltage characteristics are recorded using a current probe (Lilco 13W5000) and two high-voltage probes (Tektronix P6015A) set on electrodes, and they are visualized on an oscilloscope (Tektronix MSO56).

Space- and time-resolved optical emission spectra of the DF-DBD are recorded using the method described in a previous study [188]. This optical system comprises a lens and a set of 3 mirrors that are used to project the plasma image of the DBD gap on the entrance slit of a Czerny–Turner monochromator (Jobin-Yvon, 66 cm focal length, 1200 groves/mm grating). Herein, the magnification factor and slit opening were fixed at 1.95x and 150 µm, respectively, resulting in a spatial resolution of 77 µm across the 2 mm DBD gap. The system further relies on a

photomultiplier tube module (Hamamatsu H10721-20) operated in photon counting mode and a multichannel photon counter (MSC6A2T8 Fast Comtec), triggered by the LF power supply. Herein, the parameters of the photon counter were set to achieve 6.4 ns time resolution.

Experimental results

Current-voltage characteristics of the α – γ DF-DBDs

Figure 1 (a) and Figure 1 (b) present the current-voltage characteristic of the Ar-based DBD recorded over a single LF cycle. As shown in Figure 1 (a), the current is strongly modulated by the applied RF voltage. In addition, Figure 1 (a) reveals that the current averaged over the RF cycle displays an offset, with either a positive or negative value depending on the amplitude of the LF voltage. These observations remain valid throughout the LF cycle, except around LF current inversion (*i.e.*, at 5.5 and 15.5 µs), when the LF voltage applied to the gas changes polarity (recall that in DBDs operated in a glow regime, the LF voltage applied to the gas (not shown in Figure 1 (b)) does not correspond to the LF voltage applied to the electrodes (shown in Figure 1 (b)) due to the presence of charges on the dielectric surfaces [186]). Moreover, in line with previous studies of RF discharges [194], [195], the currents maxima is delayed by about 48 ns (about a quarter of the RF period, 188 ns at 5.3 MHz) relative to the applied RF voltage. Figure 1 (a) further shows that the current amplitude is enhanced between 1.1 and 2.7 µs, as well as between 11.1 and 12.7 µs. In these time intervals, a drastic increase in the LF current amplitude (averaged over the time scale of the RF cycle) is observed, suggesting that the DBD is in the γ mode. As described above, this regime is characterized by a strong ionization in the cathode sheath such that the discharge becomes self-sustained in this region [35]. Beyond 2.7 µs, the amplitude of RF modulation (and thus the amplitude of the LF current) decreases, and the discharge transits from γ mode to the RF-α mode. This transition is due to the charging of dielectric plates (and thus to the rise of the LF voltage across dielectrics), and the corresponding decrease of the LF voltage applied to the gas [188]. In Section 3.2, optical diagnostics are shown between 0.5 and 3 µs during which the discharge transits to the γ mode. Then, in Section 3.3, simulations are presented in the same time interval for the α – γ DF-DBD. Finally, in Section 3.4, a comparative simulation study is done for the α DF-DBD.

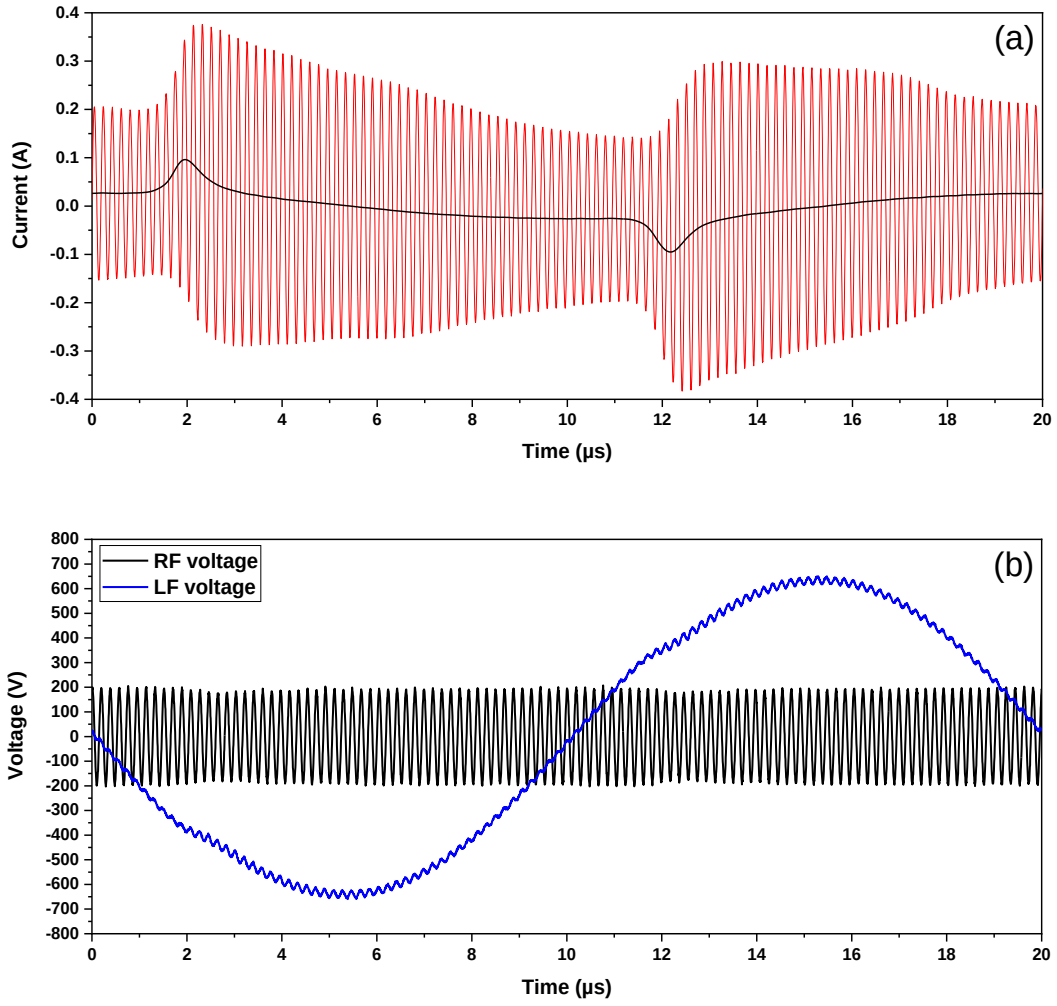

Figure 1. (a) Temporal evolution of the measured current (in red) in the Ar-based DBD for which the upper electrode is powered by a 50 kHz LF generator (period of 20 µs), whereas the lower one is connected to a 5.3 MHz RF generator (period of 188 ns). Here, the LF component of the current (obtained by averaging over the RF period) is also presented (in black). (b) Temporal evolution of the voltage recorded over the top (LF-powered, in black) and bottom (RF-powered, in blue) electrodes (with the same ground). Here, the LF and RF voltage amplitudes are set to 650 and 195 V, respectively. Of note, the polarity of the RF signal was inverted with respect to the one measured to account for the fact that both voltages are not measured on the same electrode of the DBD cell. As expected, small RF modulations are observed in the LF component due to the corresponding rise in current calling for an enhanced power input [196]. *Small variations of the applied RF voltage are also seen throughout the LF cycle, as explained in* [188].

Optical diagnostics of α – γ DF-DBDs

As described in previous studies [188], the main optical signals observed during optical emission spectroscopy of Ar-NH_3 DF-DBDs are continuum emission between 300 and 650 nm attributed to

the electron-neutral bremsstrahlung [84], [94] and Ar lines between 650 and 950 nm linked to Ar $2p_x \rightarrow 1s_y$ transitions [77]. On one hand, in weakly-ionized RF plasmas, for a fixed population of neutral gas atoms, the behavior of the continuum emission intensity can be related to the electron number density and to the average electron energy (or electron temperature, assuming Maxwellian energy distribution function) [24], [94]. On the other hand, in the specific case of the 750.4 nm line (Ar $2p_1 \rightarrow 1s_2$), assuming that the emitting Ar $2p_1$ state is mostly populated by electron-impact excitation from ground-state Ar atoms (this process requires an energy of 13.48 eV) [197], it can be assumed that this line emission intensity characterizes the presence of high-energy electrons [86], [182], [183]. Figure 2 (a) and Figure 2 (b) present the spatio-temporal evolution of the emission intensities of the continuum at 500 nm (to avoid overlap with Ar $2p_x \rightarrow 1s_y$ transitions) and of 750.4 nm (Ar $2p_1 \rightarrow 1s_2$) argon line, both recorded in the same experimental conditions as in Figure 1. Here, in a region focused around the LF positive current peak (Figure 1 (a)), between 0.5 and 3 µs, the LF cathode is the upper electrode.

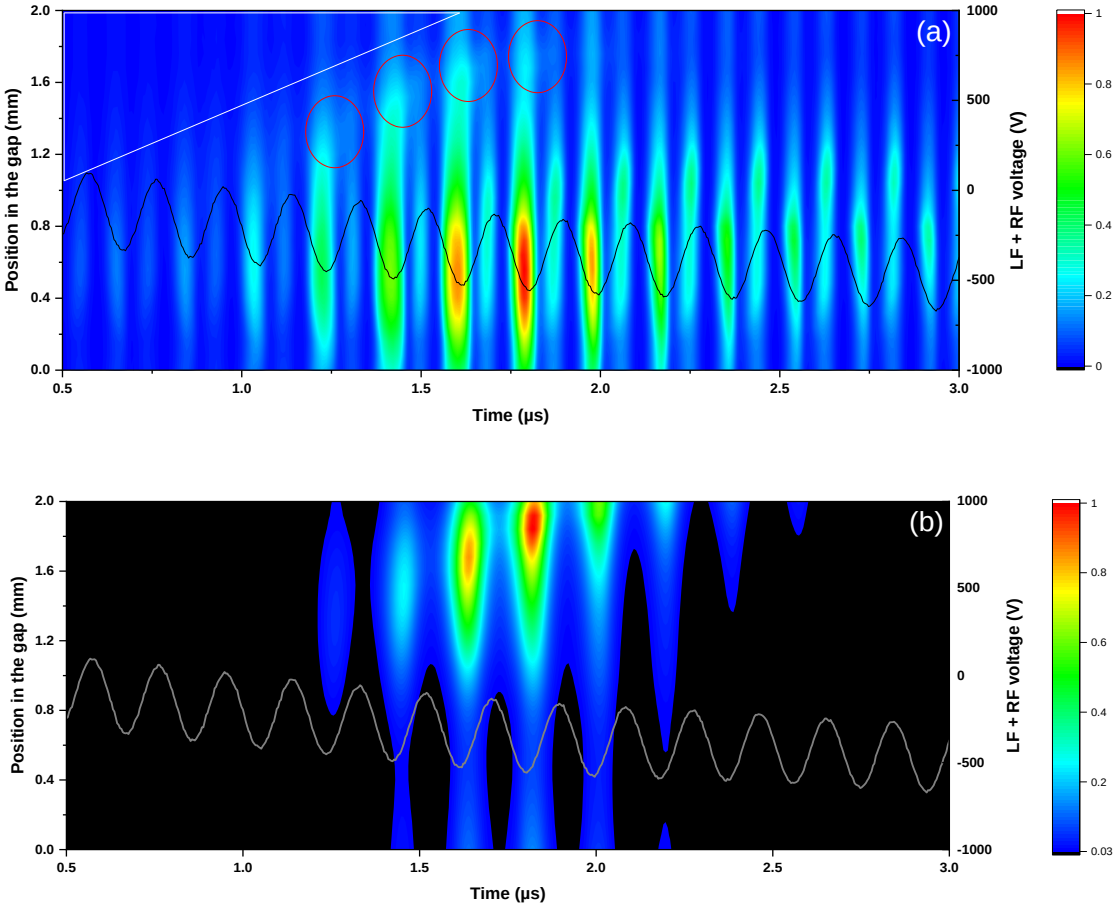

Figure 2. Normalized Spatio-temporal mapping of (a) the Bremsstrahlung continuum emission (500 nm) and (b) the Ar $2p_1 \rightarrow 1s_2$ (750.4 nm) line emission intensity recorded in the inter-electrode gap during γ breakdown of the LF-RF DBD produced at 650 V LF voltage and 195 V RF voltage. The upper electrode is the LF cathode. See text for details on highlighted regions.

In Figure 2 (a), a triangular zone with very weak continuum emission is observed in the top left corner (represented by a white triangle). Such weak emission can be attributed to the reduced electron number density in the cathode sheath, which contrasts with the high electron densities seen in this region during γ breakdown (between 1.25 and 2.25 μs) [188]. Figure 2 (a) further reveals that between 1.2 and 1.8 μs, continuum emission of the two alternances of the RF appear to be joined in the sheath edge zone (see red circles in Figure 2 (a)); however, they are disjointed elsewhere, including at the same position in the gap between the negative and positive RF half cycles. Notably, the junction approaches the cathode with time throughout the LF cycle; this phenomenon is linked to the contraction of the LF sheath in the γ mode (additional details are

provided below). In the bulk, the continuum emission appears twice per RF period, and its amplitude and position depend on the RF polarity. More specifically, maximum intensity is always achieved when a negative RF voltage is applied to the upper electrode (*i.e.*, same as the LF cathode). In terms of position, when the upper electrode is LF cathode with negative RF applied voltage, the maximum is strongly shifted from the middle of the gap towards the LF anode. On the other hand, when the upper electrode is LF cathode with positive RF applied voltage, the maximum occurs closer to the middle of the gap. Considering that the continuum emission is mostly observed in conditions characterized by high electron populations [188], therefore, in the RF plasma bulk, the shift towards the LF anode when the upper electrode is the cathode for both RF and LF signifies a displacement of the plasma bulk along that direction due to the corresponding time evolution of the LF cathode sheath.

In α – γ DF-DBDs, γ breakdown is initiated when the voltage applied to the gas reaches a maximum such that the electric field in the sheath is nearly maximum and electrons become strongly accelerated in this region [188]. In line with the prominent excitation pathway of the $Ar(2p_1)$ state, the 750.4 nm line emission intensity presented in Figure 2 (b) reveals a drastic increase in the cathode sheath linked to the presence of a significant population of high-energy electrons in this region. Figure 2 (b) further shows that, as the sheath contracts during the α–to-γ mode transition, the maximum emission progressively approaches the cathode. Notably, maximum 750.4 nm emission is reached at about 0.6 µs before the maximum in current (Figure 1 (a)) due to the drastic decrease in gas voltage during γ discharge development, as in the case of a low frequency DBD [188]. Compared to the maximum of the continuum emission (Figure 2 (a)), the maximum of the 750.4 nm emission (Figure 2 (b)) is delayed by about 30 ns. Such difference in time between the two maxima can be explained by the lifetime of $Ar(2p_1)$ state (22 ns) which would delay 750.4 nm photon emission. Beyond its maximum intensity in the half-cycle of the applied LF voltage (~1.8 µs), Figure 2 (b) reveals that the 750.4 nm line emission intensity decreases due to the progressive extinction of the γ mode (linked to the charging of the dielectrics, the rise in the voltage across the dielectrics, and thus the corresponding decrease in the gas voltage [188]).

During a RF cycle, it can be seen in Figure 2 (b) that the 750.4 nm emission is maximum shortly after the RF and LF polarities are the same. However, during the γ mode (around 1.4 to 2.3 μs) the emission is always observed near the LF cathode, regardless of RF polarity, but not on the LF anode side. When the emission is highest at the cathode, that is, when the polarities of the two voltages are the same, the discharge crosses the gap and reaches the anode (once every RF cycle). This can be explained by the drift of electrons created in the sheath towards the anode. When the RF applied voltage is negative at the lower electrode, then the 750.4 nm emission is no longer measured in the lower half part of the gap, close to the LF anode. Therefore, there is a difference between the 750.4 nm emission at the LF cathode and the LF anode: near the cathode, the line emission intensity remains high regardless of the RF polarity, but at the anode, the emission is only observed when this electrode is also the powered by a positive RF applied voltage.

Fluid modeling and discussion

α – γ DF-DBDs

Overall, the emission intensities of the continuum and Ar 750.4 nm line, presented in Figure 2 (a) and (b), reveal that the total electron number density and the population of high-energy electrons strongly depend on the position of the plasma bulk relative to the LF sheath. Although different trends are observed for the two optical signals, the behaviors are always related to the polarities of the RF and LF voltages, and thus to dual-frequency sheath oscillations. The aim of this part is to explain the relationship between sheath oscillations, emission intensity and current dissymmetry. In this context, the spatio-temporal evolution of the electron source term, electric field, electron and ion fluxes are analyzed using a 1D fluid model of Ar-based DBDs developed and validated in a previous work [35]. Note that this model solves the continuity and momentum equations for all species and the energy equation for electrons. It considers 7 species (Ar, Ar^+, Ar_2^+, Ar(1s), Ar_2*, photons and e^-) through 11 reactions. Secondary electron emission from dielectric surfaces, induced by impinging of Ar^+, Ar_2^+, Ar(1s), Ar_2* and VUV photons, is also considered. Hence, this model does not account for NH_3 dissociation (and the presence of reaction products such as NH, NH_2, N_2, and H_2 in the gas phase [47]). In addition, the value for the RF frequency selected in the simulations (5 MHz) is slightly less than the one used in the experiments (5.3 MHz); as shown below, this

explains why the time interval during which the DBD is in the γ mode obtained from the model do not exactly coincide with the one seen in the experiments.

Figure 3 depicts the spatio-temporal distribution of the source term in the electron particle balance equation (in $m^{-3}.s^{-1}$) deduced from the model (see details in [50]) in the case wherein the LF cathode is the top electrode and the RF voltage oscillates. Of note, in line with the 750.4 nm emission, this source term can be linked with the population of high-energy electrons [35]. In general, Figure 3 indicates that electrons are mainly produced near the LF cathode, where the continuum emission is low and the 750.4 nm emission is high. Although, in this zone, the electron number density seems to be small (Figure 2 (a)), their average energy is high (Figure 2 (b)), which is consistent with the properties of a cathode sheath. Indeed, the electrons created in the sheath are subjected to a strong electric field, which induces their rapid acceleration towards the bulk. After the γ breakdown, the maximum of the electron source term moves closer to the cathode due to the contraction of the LF sheath. In line with the behavior of 750.4 nm emission presented in Figure 2 (b), the electron source is high at the LF cathode regardless of the RF polarity, whereas at the anode, it is significant only once per RF cycle.

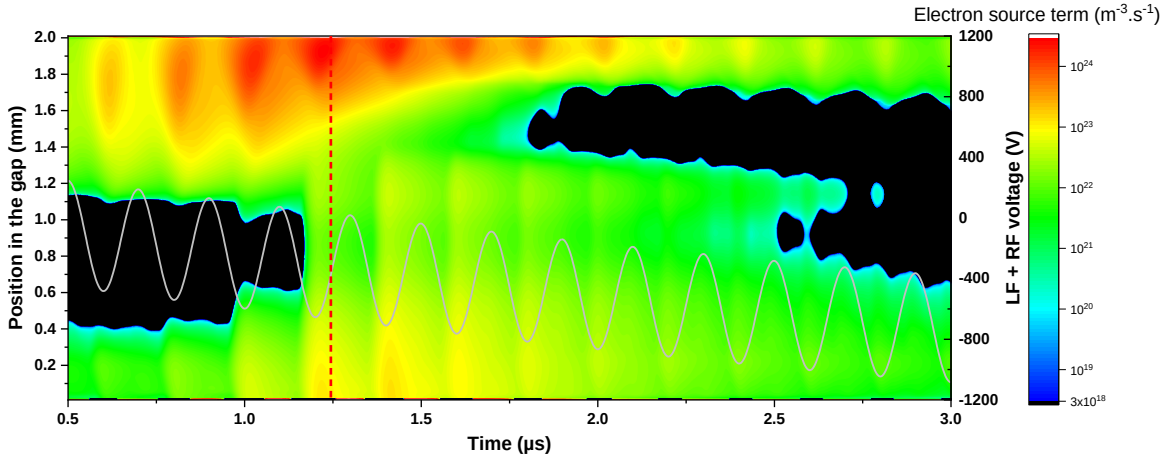

Figure 3. Spatio-temporal distribution of the source term in the electron particle balance equation obtained from the model. The black regions signify negative values or below the threshold of 3.10^{18} $m^{-3}s^{-1}$. The results are shown during γ breakdown of a LF-RF DBD produced at 940 V LF voltage and 350 V RF voltage. Of note, the LF and RF voltage amplitudes used in the model are slightly different from those used in the experiments; additional details are provided in [188]. *The upper electrode is the LF cathode. The dotted line corresponds to an inversion of the RF voltage polarity, and it is shown for the sake of comparison.*

The spatio-temporal mapping of the electric field is shown in Figure 4, wherein positive and negative values are presented in red and blue, respectively, and the solid black line represents 0 electric field. When the electric field is positive, the electrons drift towards the bottom electrode (the LF anode), whereas the ions drift towards the upper electrode (the LF cathode). This trend is reversed when the electric field is negative. Considering that a high positive electric field (corresponding to the cathode sheath) is always present at the upper electrode (recall that the amplitude of the LF voltage is higher than the one of the RF voltage), the electrons created in the sheath always drift to the plasma bulk, and their density is thus rather low in the sheath. Between 0.5 and 1.5 μs, the high electric field zone near the upper electrode contracts due to the ion density increase related to the sudden production of electrons and ions during γ breakdown, and the rapid transport of electrons towards the gas bulk; this is consistent with the contraction of the sheath. In the bulk, the electric field alternates between positive and negative values, according to the RF voltage polarity. When it is positive, the electrons in the gas bulk drift toward the LF anode. However, when it is negative, both, the electrons in the sheath and those in the bulk are accelerated towards the sheath edge. Therefore, the negative electric field achieved in the bulk at opposite RF and LF polarities leads to electron trapping at the sheath edge of the LF cathode sheath. Such trapping results in high electron number density on a local scale (see Figure 5 (b)), especially considering that the trapped electrons cannot escape to the cathode via diffusion. When the polarities of the RF and LF voltages are the same, the accumulated electrons are evacuated towards the LF anode.

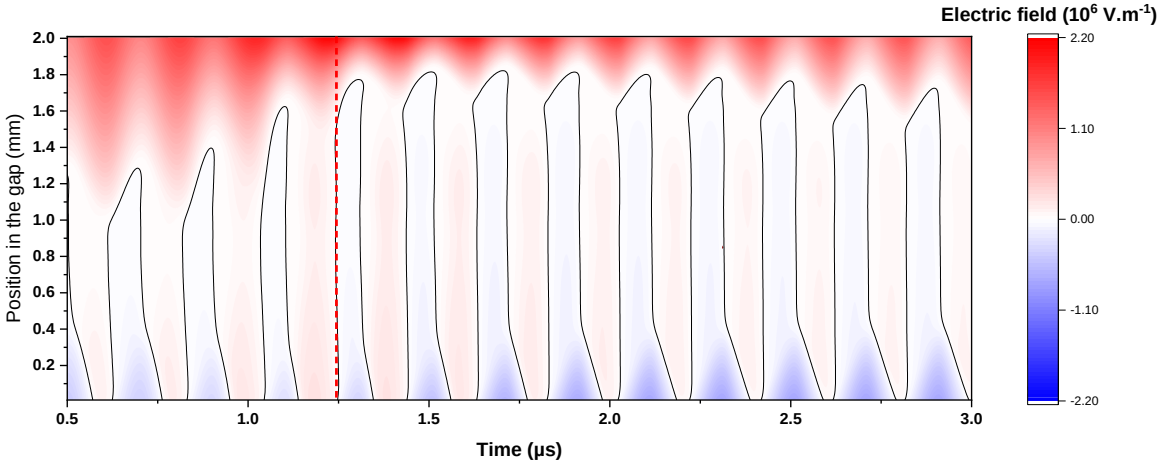

Figure 4. Spatio-temporal distribution of the electric field (positive in red, negative in blue). The simulation conditions are the same as in Figure 3.

The spatio-temporal distribution of the number density of charged species in the α – γ DF-DBDs are presented in Figure 5. In Figure 5 (a), the density of ions is maximum at the cathode during γ breakdown, at around 1.5 µs, as in [188]. At this time, a cathode sheath is present (see Figure 4). The density of ions is also quite high in the bulk center. Notably, the ion density is relatively stable at tens of ns time scale: as expected, despite the electric field oscillations, the ions are only slightly mobile at the RF scale. To examine the spatio-temporal evolution of the cathode sheath length, the mapping of the electron number density in space and time is also analyzed. In Figure 5 (b), the sheath, at LF and RF scales, can be defined by the blue zone corresponding to a low electron number density region. Clearly, the RF oscillations modifies the sheath length on both the LF cathode (top electrode) and the LF anode (bottom electrode). However, the LF cathode sheath oscillates but remains present, regardless of the polarity of the RF voltage while, at the LF anode, the sheath disappears when the bottom electrode is powered by a positive RF applied voltage.

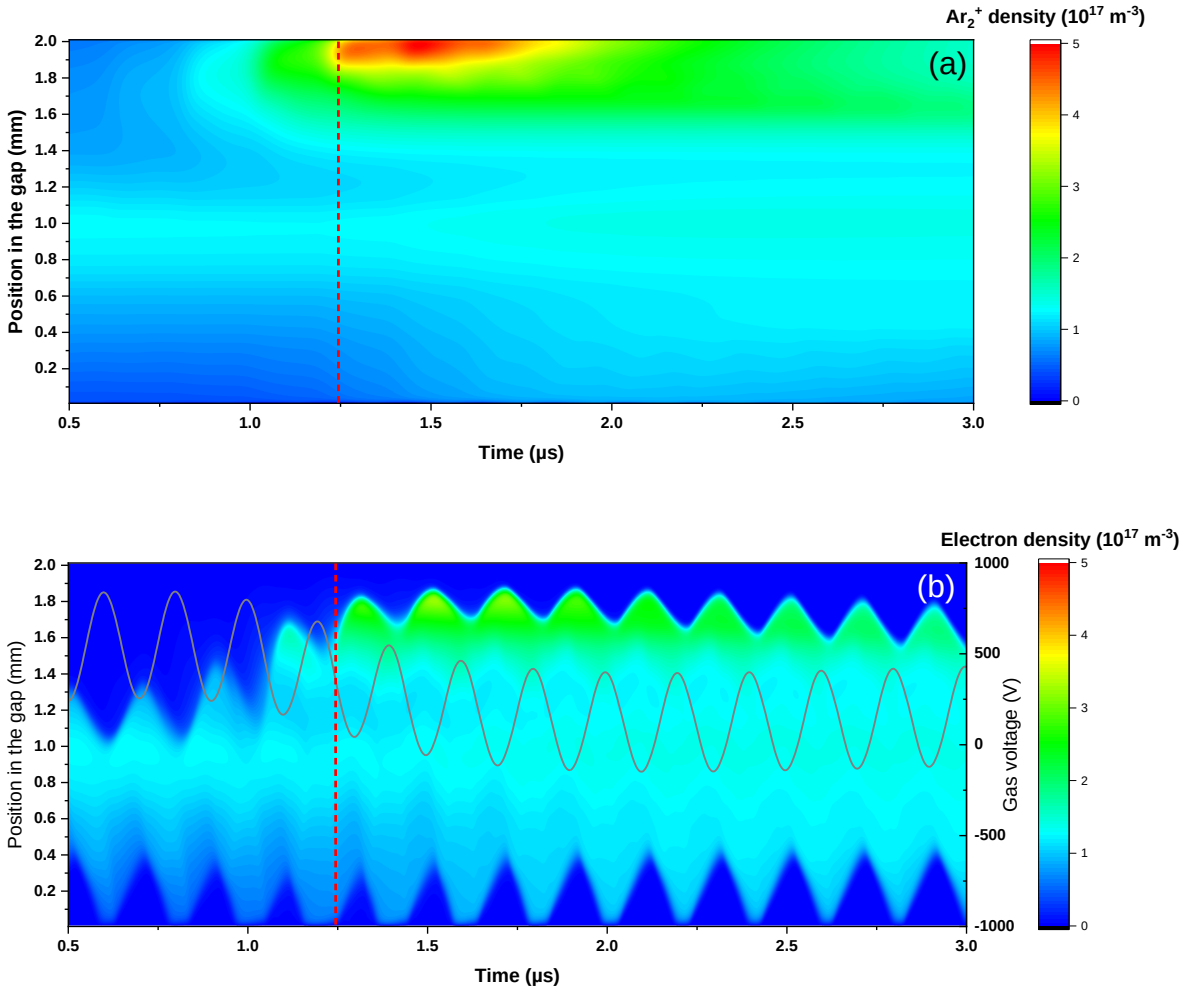

Figure 5. Spatio-temporal distribution of (a) the Ar_2^+ density and (b) the electron number density obtained from the model. In (b), the gas voltage (in black) is also shown. The simulation conditions are the same as in Figure 3.

Between 0.6 and 1.5 μs, Figure 5 (b) further shows that the LF cathode sheath (top electrode) contracts, thereby increasing the plasma bulk length. This agrees well with the spatio-temporal mapping of the continuum emission displayed in Figure 2 (a). However, the zone of high electron number density does never reach the upper electrode (LF cathode). In contrast, at the LF anode (bottom electrode), the electrons only reach the anode when the RF and LF voltage polarities are the same. When the RF and LF voltage polarities are opposite, the RF sheath is thinner and shorter in the γ mode than in the α mode. Hence, in such conditions, the electrons reach the LF anode for a longer time in γ mode than in α mode, in agreement with the continuum emission displayed in Figure 2 (a). At the LF cathode sheath edge, it can also be seen in Figure 5 (b) that the maximum

electron number density appears once per RF period. Specifically, it occurs when the LF cathode sheath is the shortest, *i.e.*, when the polarities of the two applied voltages are opposite inducing the electron accumulation at the sheath border (see the behavior of the gas voltage, white line in Figure 5 (b)). Such trend is observed between 1.3 and 2.1 µs; however, the maximum production is attained at 1.2 µs. This difference indicates that the electron number density is more related to their transport along the electric field rather than to their precise creation zone in the α – γ DF-DBDs.

The electric field distribution presented in Figure 4 can be attributed to variations of applied voltages and of ion and electron number density distributions (space charge electric field). When γ breakdown occurs, ions and electrons are mostly created in the sheath. Considering that the ion source term is strong in the sheath (whatever its length), when the sheath contracts due to the variation in gas voltage, some ions created when the sheath was the longest, will end up in the bulk, near the sheath edge, locally increasing the ion population. To understand the variation of the electric field sign in the bulk, it is necessary to look at the ion density and the electron source term in the sheath, at the time scale of the RF cycle. When the electron source term is the highest in the sheath, the number of electrons created becomes very high. To maintain quasi-neutrality in the bulk, the electric field is deformed to evacuate electrons towards the LF anode. In contrast, when the electron source term is low in the sheath, the number of electrons created is too low to neutralize the high ion density at the sheath edge. As a result, the electric field of the bulk must change sign to restore neutrality by transporting electrons from the bulk and the sheath.

Since the current depends on the total flux of charged species at the walls, the fluxes of electrons and ions at the LF cathode (upper electrode, Figure 6 (a)) and of electrons in the whole gap (Figure 6 (b)) were also analyzed. As shown in Figure 6 (a), the electron and ion fluxes at the cathode are strictly negative and positive, respectively, and they are not significantly affected within the RF time scale to be reduced to 0. Close to the LF cathode, ions flow towards the dielectric, whereas the electrons (secondary electrons emitted from the dielectric by impinging ions and VUV photons [35]) migrate towards the plasma bulk. Notably, significant secondary electron emission is detected between 0.6 and 2 µs, with a significant rise during sheath contraction. Meanwhile, the maximum in the ion flux occurs later in the LF cycle and lasts much longer. The variation between the time intervals of the electron and ion fluxes is attributed to the substantial contribution of VUV photons

from the plasma to secondary electron production (about 95 % calculated from the model, averaged on a LF period) [35]. Indeed, when γ breakdown occurs and the sheath becomes self-sustained, ions and excited Ar and Ar_2 species are produced in the sheath through collisions with high-energy electrons. The average time for (i) the creation of excited Ar_2^* excimer through conversion of atoms in Ar(1s) states by 3-body collisions with 2 ground state Ar atoms, (ii) the de-excitation of Ar_2^* by VUV photon emission, and (iii) the transport of VUV photons towards the wall to induce secondary electron emission, is much shorter than the time it takes for an ion created in the sheath to reach the wall. Thus, due to the contribution of VUV photons in the creation of secondary electrons, the secondary electron flux increases faster than the ion flux arriving at the wall [35].

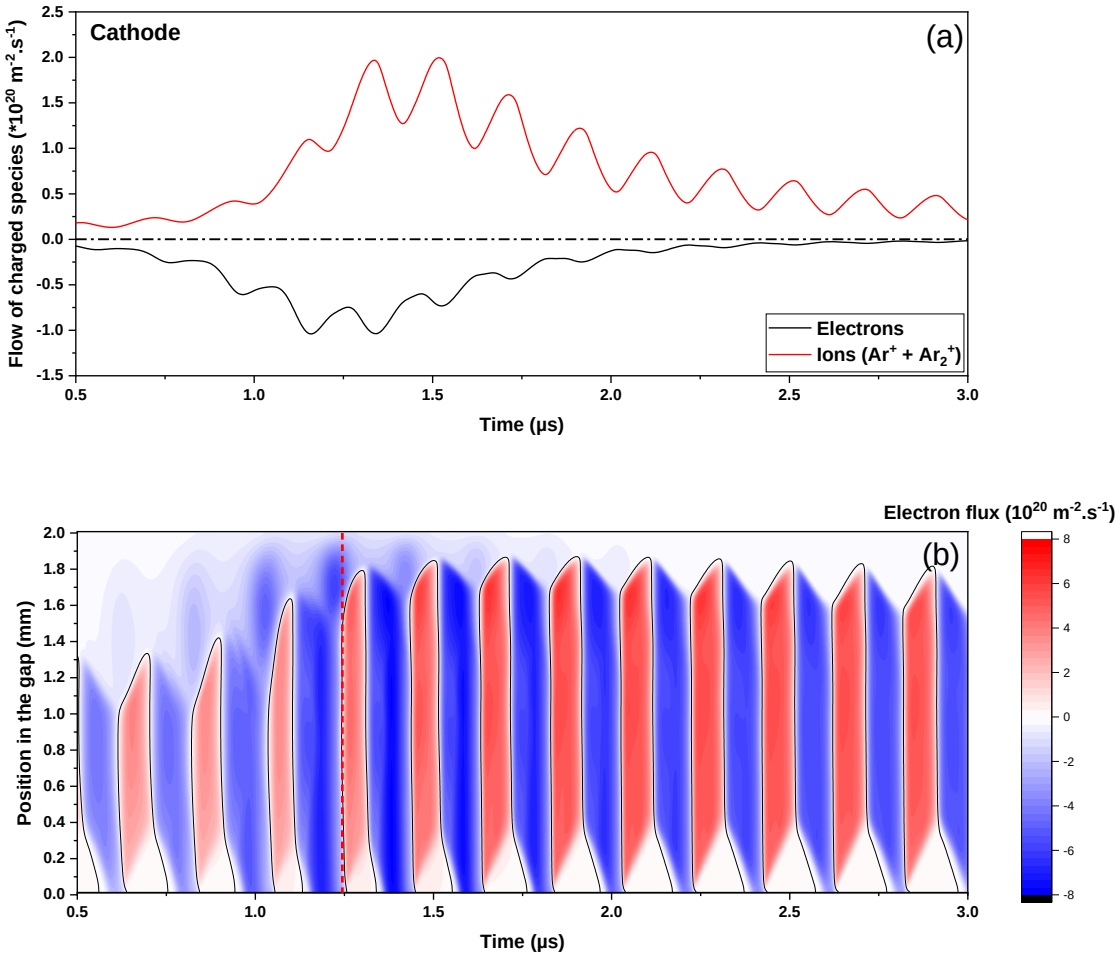

Figure 6. (a) Temporal evolution of the calculated electron and ions fluxes at the LF cathode. (b) Spatio-temporal distribution of the electron flux. A positive flux (in red) is due to electrons moving toward the LF cathode, upper electrode. The white areas depict very small electron flux, and the black line represents the zero values. The simulation conditions are the same as in Figure 3.

In the bulk, Figure 6 (b) shows that the electron flux is alternatively positive, in red, and negative, in blue. On the other hand, near the upper electrode (the LF cathode), it remains negative. Hence, it is controlled by the RF polarity in the gap and by the LF polarity in the LF cathode sheath. The triangular shape discerned at the extremities of positive fluxes at the sheath edge is attributed to its expansion/contraction. This explains the junction of the continuum emission observed in this area in Figure 2. Of note, this junction on the bremsstrahlung continuum emission is related to the contraction of the cathode sheath when polarities of the LF and RF voltages are opposite. This contraction is observed when the high electron negative flux coming from the cathode meets the positive one coming from the bulk. Therefore, the continuum emission is attributed to the high electron populations created from the negative electron flux emanating from the sheath, as well as from the positive electron flux coming from the LF anode to the bulk (this creates a junction in the transition between these two fluxes). Comparatively, when the electron flux is monotonous along the gap, i.e. when polarities of the LF and RF voltages are of the same sign, electrons originating from the sheath are simply dragged towards the anode, decreasing the electron density at the sheath edge. In this configuration, no junction is observed in Figure 2. Furthermore, Figure 6 (b) reveals that during the LF sheath contraction (between 1.13 and 1.25 µs), the negative electron flux at the LF anode lasts longer than anywhere else. At this time, the electron number density at the sheath edge is the highest (see Figure 5 (b)), as electrons cannot be evacuated at the LF cathode. Hence, the electric field is deformed for a longer time to evacuate the electrons towards the anode (see Figure 4).

It is worth highlighting that the behaviors of the electric field seen in Figure 4 and particle flux at the walls shown in Figure 6 can be used to explain the asymmetry between the positive and negative current components reported in Figure 1. As underlined above, and further highlighted in Figure 7, this asymmetry is particularly significant in the 0.5–3 µs time interval, with the positive current component being consistently higher than the negative component (the exact opposite trend is observed during the second γ breakdown in the other LF half-cycle), and it is detected before and during the γ avalanche period (*i.e.*, as soon as the LF sheath is formed). The strong increase in the current amplitude from 1.25 to 2.5 µs emphasizes the asymmetry. The difference between positive

and negative current components during the breakdown is due to the variations in applied voltage and space charge electric field. Because of γ breakdown, strong ionization occurs in the sheath and this causes a strong ion flux to the cathode and an important electron flux to the anode once per RF period [50]. Electrons are accelerated in the LF cathode sheath regardless of the RF polarity, then the electric field in the bulk will accelerate electrons depending on the RF polarity. When the electric field in the bulk is of the same sign as the one in the LF sheath (electrons go towards the anode), the current is the highest (the positive current in Figure 7), but when it is the other way around, the electric field in the bulk and in the sheath are opposite. In this case, mean electron velocities are lower than in the previous case such that the absolute values of the current are also lower.

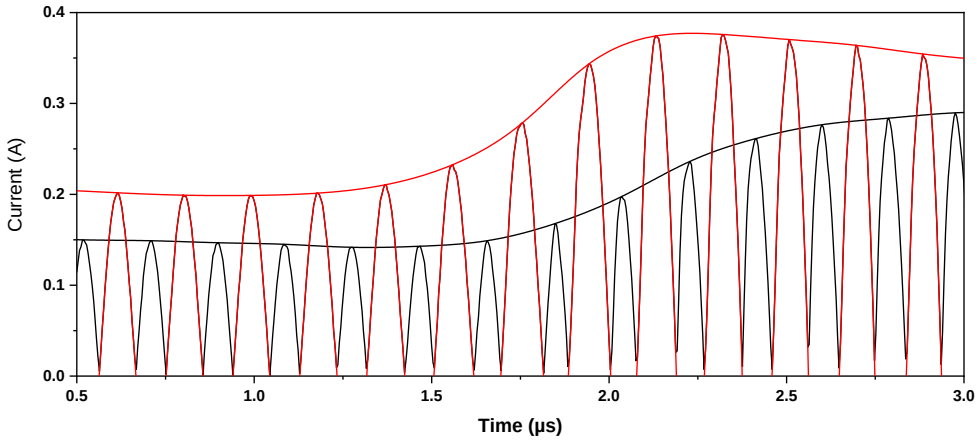

Figure 7. Absolute value of the measured dual frequency current components (positive in red and absolute value of negative in black) and their respective envelopes between 0.5 and 3 μs for LF and RF voltage amplitudes of 650 and 195 V, respectively.

α DF-DBDs

The asymmetry observed in Figure 7 for DF-DBDs exhibiting the α – γ transition is attributed to the production of strong fluxes of charged particles during relatively short periods of time. When the DF-DBD does not allow switching to γ mode (*i.e.*, remaining in RF-α discharge), different results are obtained, as evidenced by the 1D fluid modeling data presented in Figure 8. Here, the α discharge regime is maintained by using a lower amplitude of the applied LF voltage (LF 400 V in Figure 8, instead of LF 940 V in Figure 3 to Figure 6; additional details can be found in [50]). For

LF 400 V, there is no self-sustainment in the cathode sheath, which results in a low creation rate of electrons and ions in the sheath. Consequently, as shown in Figure 8, the electron and ion densities are highest in the bulk, as in the case of RF α discharges [66].

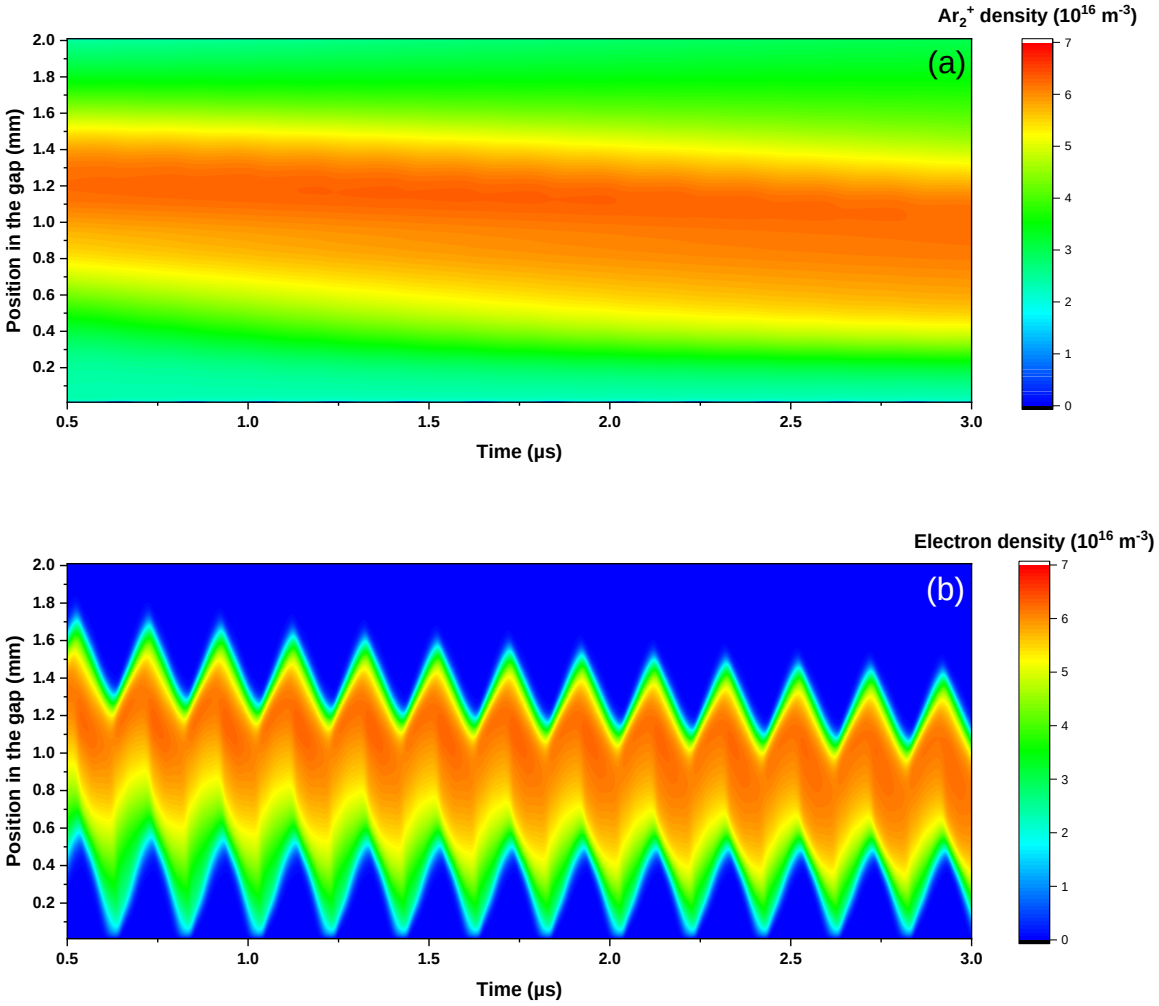

Figure 8. Spatio-temporal distribution of the calculated Ar_2^+ ion density (a) and electron number density (b) running in RF-a mode. The results are shown between 0.5 and 3 μs for LF and RF voltage amplitudes of 400 and 350 V, respectively.

Figure 8 further shows that the ion and electron densities corresponding to the α mode do not present a maximum in the sheath or at the sheath edge. Indeed, both densities are minimum in the sheath, resulting in little sheath contraction and no strong flux to the wall. Therefore, the dielectric voltage does not change suddenly, and the gas and applied voltages remain almost the same (Figure 9 (a)). In this case, the (RF-averaged) sheath lengths changes gradually over the LF period, as seen

in the ion and electron number density distributions. Moreover, as depicted in Figure 9 (b), very little asymmetry in the current density is detected for the α DF-DBDs.

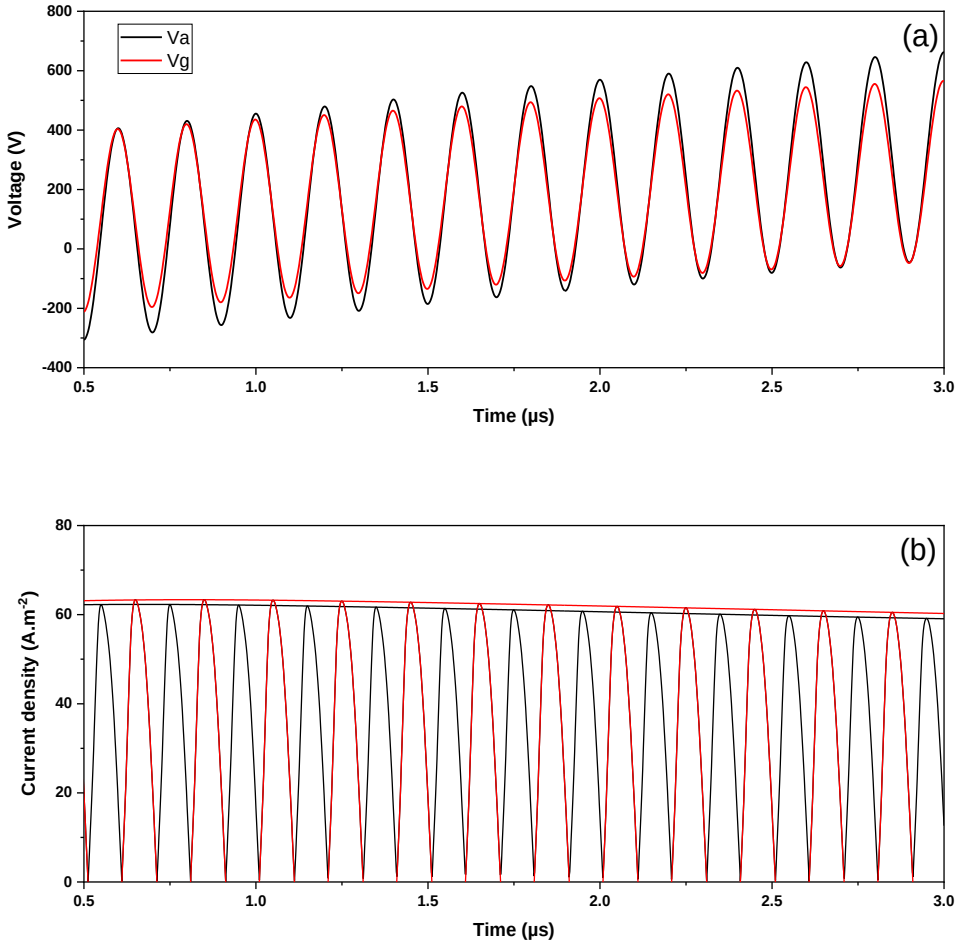

Figure 9. (a) Temporal evolution of the applied voltage (in black) and gas voltage (in red). (b) Current density components (positive in red and negative (absolute value) in black) and their respective envelopes. The results are shown between 0.5 and 3 µs for LF and RF voltage amplitudes of 400 and 350 V, respectively.

Conclusion

This article is focused on the γ mode of a DF-DBD, where the effect of the dual-frequency sheath oscillations is the most important and thus the most visible. It was observed that the presence of a LF sheath influences the functioning of the DF-DBD whatever the discharge mode, as long as a LF component on the applied voltage is present. The set of electrical and optical measurements

reported in this work reveals two different behaviors. First, when the polarities of the LF and RF voltages are opposite, an electric field drives the electrons near the LF cathode sheath towards the plasma bulk and an opposite electric field present from the sheath edge to the LF anode pushes the electrons towards the LF cathode sheath. In such conditions, in the LF cathode sheath, the only modification is the amplitude of the electric field, and the sheath length. However, at the LF sheath edge, electrons become trapped and ions drift towards the cathode and the anode simultaneously according to their position in the gap. A second behavior appears when the RF voltage has the same polarity as the LF voltage. In this case, the electric field along the gap exhibits the same polarity as the one in the sheath, allowing electrons created in the sheath to be evacuated towards the LF anode. The behavior of the LF cathode is therefore controlled by the LF sheath, and thus by the LF voltage, while the one in the bulk and at the anode alternates on the time scale of the RF voltage. This analysis explains the asymmetry between the positive and negative current at the RF scale observed during the γ mode of the DF-DFDs.

Acknowledgments

The work carried out in France was supported by the Agence Nationale de la Recherche through the Investissement d'avenir program (ANR10LABX2201). As for the one done in Canada, it was funded by the National Science and Engineering Research Council (NSERC RGPIN-2018-04550) and by the Fondation Courtois. The 'Réseau des Plasmas Froids' of CNRS/MCRT (France) is acknowledged for providing the DFB diode laser and the travel support for Nader Sadeghi, and LPGP in Orsay (France) for lending the MCS6A Multiscaler. All authors would like to acknowledge the financial support of the CNRS and Université de Montréal through their contributions to the International Research Network on Controlled Multifunctional Nanomaterials (IRN NMC).

Data availability statement

The data that support the findings of this study are available upon request from the authors.

En complément des mesures présentées dans l'article précédent, il est pertinent d'examiner l'émission du continuum à 500 nm calculée à partir du modèle fluide 1D. La présente Figure 22. – cette comparaison entre les valeurs mesurées en (a) et celles mesurées en (b).

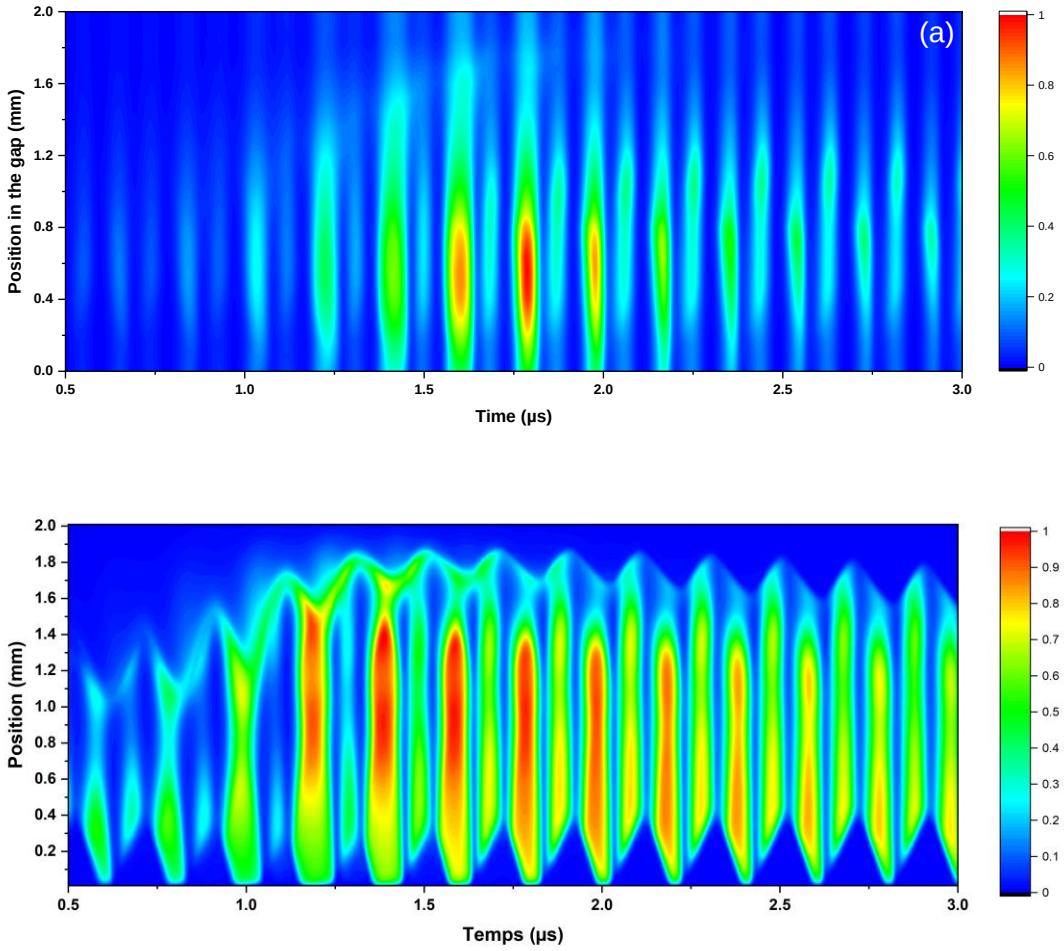

Figure 22. – Emission du bremsstrahlung à 500 nm, mesurée en (a), calculée en (b)

De toute évidence, cette comparaison nous conforte dans la pertinence du modèle fluide utilisé. De nombreuses similitudes apparaissent entre la Figure 22. – (a) et (b), notamment les alternance lumineuses qui présentent des motifs similaires. En particulier la gaine (qui semble de même longueurs) comporte des émissions faibles en sont sein, on voit une claire alternance d'intensité lumineuse de l'émission entre deux alternances RF. Enfin, la jonction décrite dans l'article précédent est aussi visible sur le continuum calculé.

Chapitre 5 – Physico-chimie d'une décharge en mélange Penning

Les articles précédents ont principalement porté sur la DBD double fréquence en mélange Penning Ar-NH_3. Dans ce cadre, l'effet des photons VUV et de l'amplitude de la tension RF ainsi que le transport des particules chargées ont été étudiés. Cependant, dans une décharge en mélange Penning, l'effet de la chimie peut être important. En effet, comme évoqué dans le chapitre 1, un mélange Penning est souvent composé d'un gaz noble auquel est ajouté un gaz moléculaire qui peut être ionisé par transfert d'excitation d'un état métastable du gaz noble. Ce gaz moléculaire peut être dissocié lorsqu'il est plongé dans un milieu énergétique comme un plasma. Plusieurs travaux publiés dans la littérature démontrent que la cinétique de dissociation dépend de la puissance injectée dans le plasma ainsi que du temps de résidence du gaz moléculaire dans la décharge ; ces deux quantités gouvernent l'énergie déposée par molécule de précurseur. De plus, si le flux de gaz est trop faible pour régénérer l'ensemble du gaz entre deux décharges, la chimie du gaz est modifiée en fonction de son éloignement par rapport à l'entrée de la décharge. En effet, si le flux de gaz est trop faible, le temps de résidence du gaz est élevé, i.e. le gaz « voit » de nombreuses décharges le long des électrodes et donc le gaz moléculaire du mélange Penning, ici le NH_3, a de fortes chances d'être dissocié. Ceci engendre une variation de la chimie en fonction de la position le long de la DBD, et, dans notre cas, la création de sous-produits du NH_3, comme du NH, du H_2, du H ou autres [47], [198], [199]. Sous forme de NH_3, d'H_2 ou encore de mélanges, notamment NH_3/H_2, ces espèces présentent un grand intérêt pour plusieurs applications dont l'agriculture [200]–[203], le stockage d'énergie ou encore la combustion, comme source d'énergie « propre » [204]–[210]. Dans ce cadre, il est néanmoins primordial de maitriser les chemins réactionnels menant à la synthèse ou la dissociation de ces espèces.

Pour étudier ces sous-produits et les nouveaux chemins réactionnels qui peuvent en découler sans introduire de difficultés d'interprétation supplémentaire, la DBD *glow* alimentée par une seule tension d'une fréquence de 50 kHz en Ar-NH_3 est choisie comme sujet d'étude. Par rapport aux autres études des DBDs BF dans Ar-NH_3 [24], [49], [77], il a été proposé d'élargir la gamme spectrale de mesures spectroscopique.

Ainsi, à l'aide d'un monochromateur VUV-UV, nous avons pu observer un continuum d'émission attribué à la désexcitation de l'état $H_2(a)$ (autour de 200 nm). Afin de mieux comprendre les implications physiques de cette émission, inspiré par des travaux présentés dans les chapitres précédents, des mesures résolues spectralement et temporellement ont été effectuées. Dans le cas de l'émission issue de $H_2(a)$, une décroissance particulièrement lente a été notée. A la lumière de ces résultats, une réaction faisant intervenir la recombinaison électronique d'un ion NH_3^+ excité vibrationnellement peuplé via un transfert de charge depuis un ion Ar_2^+ est proposée. N'existant pas clairement dans la littérature, ce chemin réactionnel est ajouté et testé dans le modèle fluide précédemment évoqué.

Les travaux sont présentés sous la forme d'un article récemment soumis à Plasma Chemistry and Plasma Processing (068436cc-ef98-4869-b091-5702620ceffc).

Kinetics driving $H_2(a)$ continuum emission in low-frequency Ar-NH_3 dielectric barrier discharges at atmospheric pressure

Raphaël Robert[1,2], Françoise Massines[2], Luc Stafford[1]

[1]Département de physique, Université de Montréal, 1375 ave. Thérèse-Lavoie-Roux, Montréal, Québec, H2V 0B3, Canada

[2]Laboratoire Procédés Matériaux et Énergie Solaire (PROMES, CNRS, UPR 8521), Rambla de la thermodynamique, 66100 Perpignan, France

Abstract

Time-resolved optical emission and absorption spectroscopy was used to analyze a 50 kHz Ar-NH_3 dielectric barrier discharge operated in a homogeneous glow discharge regime at atmospheric pressure. In addition to the typical NH(A-X), N_2(C-B), and Ar(2p-1s) transitions, a continuum emission linked to de-excitation of $H_2\left(a^3\Sigma_g^+\right)$ states was detected between 180 and 250 nm and lasted for a long time after discharge extinction. Over the range of experimental conditions investigated, the emitting $H_2\left(a^3\Sigma_g^+\right)$ states are proposed to be populated by collisions of $H_2\left(X^1\Sigma_g^+\right)$ with Ar(1s) states during discharge, and by dissociative recombination of the vibrationally-excited ammonia ion (NH_3^+(v)) after the discharge. NH_3^+(v) is produced by charge transfer from Ar_2^+ to NH_3, and it breaks into $H_2\left(a^3\Sigma_g^+\right)$ (or $H_2(c^3\Pi_u)$ or $H_2(d^3\Pi_u)$) and NH upon gas phase recombination with a low-energy electron. Based on this proposed mechanism, a 1D fluid model was refined to include these reactions and used to simulate the emission intensity from $H_2\left(a^3\Sigma_g^+\right)$ and revealed good agreement with experimental data.

Introduction

Penning mixtures are often used to obtain diffuse non-equilibrium discharges under atmospheric pressure conditions. In the case of dielectric barrier discharges (DBDs), Penning mixtures (for example, traces of NH_3 in Ar, or traces of N_2 in He) ensures the transition from the typical filamentary regime of DBDs characterized by transient microdischarges randomly distributed in time and space to the homogeneous regime exhibiting a diffuse, non-filamentary appearance, and thus a much higher degree of discharge uniformity [11], [41]. In the case of tubular discharges sustained by high-frequency electric fields, for example surface-wave discharges [211], Penning mixtures (for example traces of Kr or Xe in Ne) fosters the transition from the typical radially-contracted regime to the radially-diffuse regime [212]–[214]. Typically, Penning mixtures are composed of a gas admixture whose ionization energy is less than the metastable excitation energy of the primary noble gas constituent. In such cases, ionization mostly occurs through a two-step process involving: (i) the creation of metastable species from the main plasma gas by electron-impact excitation and (ii) the ionization of the admixture gas by excitation energy transfer from the metastable species [215]. Notably, diffuse discharges are normally obtained for low admixture concentration fractions (between 10^{-5} and 10^{-2} depending on the plasma conditions); above these values, the discharge transits back to the filamentary regime for DBDs [11], [41] and goes back to the radially-contracted regime for tubular high-frequency discharges [216].

When the admixture gas is molecular in nature, it can also be dissociated upon interactions with energetic species, including metastable states from the main plasma gas. For instance, the interaction between Ar(1s) (metastable or resonant state) and NH_3 leads to dissociation of the admixture gas in 58% of cases (in 42% of cases, it yields to Penning ionization) [46]. Notably, the

admixture dissociation produces several by products, which complexifies the discharge physics and chemistry. For example, Fateev *et al.* [198] examined the chemical kinetics in an Ar and 0.1 to 10 % of NH_3 DBDs operated in the filamentary regime. They observed that the microdischarges produced stable species such as N_2, H_2, and N_2H_4. Over the range of experimental conditions investigated by the authors, the leading source of NH_3 dissociation was collisions of NH_3 with Ar metastable species [35], [46]. Other authors have also studied the decomposition of NH_3 by microdischarges for H_2 generation [217]–[220]. Efficiency of conversion of NH_3 to H_2 was found to depend on the power density injected in the discharge as well as the residence time of the gas mixture in the plasma zone, as these properties drive the total energy deposited per NH_3 molecule [48], [198], [199], [221], [222]. While many studies have investigated Ar-NH_3 microdischarges with high NH_3 content (for example, between 10 and 100% [47], [218], [223]), much less analysis was devoted to NH_3 decomposition and by products formation in Penning mixtures relevant for diffuse discharge formation. In such systems, reactive species become much more difficult to assess experimentally as the concentration fractions are only a few tens or hundreds of ppm.

In this work, a combination of optical emission and absorption spectroscopy techniques is used to examine the temporal evolution of selected noble and reactive species produced in a 50 kHz Ar-NH_3 DBD operated in a homogeneous glow discharge regime. With respect to most optical studies of Ar-NH_3 DBDs reported in literature (see, for example, Fateev *et al.* [198], Yao et al. [49], and Bazinette et al. [21]), optical emission spectroscopy measurements are carried out down to 175 nm to highlight the H_2(a) continuum emission [224]–[226]. To understand the different phenomena occurring during and after discharge ignition, reaction pathways involved in the population of H_2(a) states are proposed based on the experimental results, and are implemented in a 1D fluid model of

Ar-based DBDs developed in a previous study [35], [50]. Overall, the set of data reported herein provides insights into the kinetics driving $H_2(a)$ continuum emission in low-frequency DBDs operated in Ar-NH_3 Penning mixtures at atmospheric pressure.

Experimental setup and diagnostics

The discharge examined in this study is a plane-to-plane DBD with a 2 mm gas gap. It is sustained in a square tube with an internal dimension of 0.2*0.2 cm² and a total length of 6 cm. As shown in Figure 1, metallic electrodes with dimensions of 4.7*0.2 cm² (longest dimension is along the gas flow lines) are coated on top and bottom walls made of fused silica. As for the horizontal walls, they are made of MgF_2 (for measurements of UV photons) and have the same dimensions as the top and bottom ones (square tube). During the experiments, the flow rate of Ar + 215 ppm of NH_3 (Praxair ProSpec) is set to 280 SCCM (standard cubic centimeters per minute) using a mass flow controller. As for the pressure in the discharge cell, it is maintained at 745 torr using a throttle valve and vacuum pump located at the outlet of the tube. A function generator (Tektronix AFG 3021B) is used to generate a 50 kHz waveform signal that is first transferred to an audio amplifier connected to a bridged resistance (Crest CC4000), then to a step-up voltage transformer (Atesys-Montoux), and then to the top metallic electrode. The bottom metallic electrode is grounded. The electrical signals are measured using a high voltage probe (Tektronix P6015A) and a current probe (Lilco LTD 13W5000), and they are visualized on an oscilloscope (Teledyne Lecroy HDO6104A).

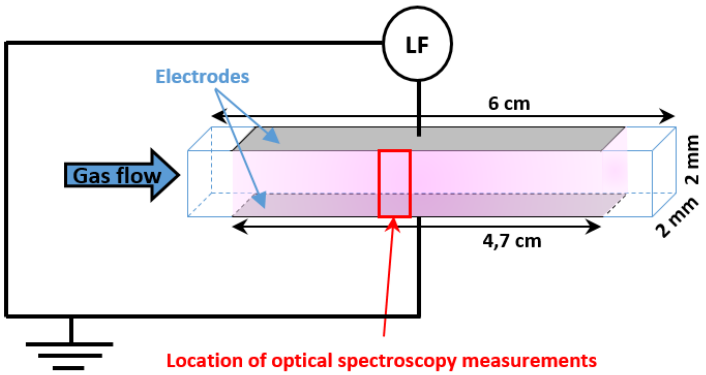

Figure 1. Schematics of the experimental setup for DBD ignition with metallic electrodes coated on the fused silica tube.

To analyze noble and reactive species in the Ar-NH_3 DBD, time-resolved Optical Emission Spectroscopy (OES) measurements are performed at 2.1 cm from the beginning of the plasma zone (see Figure 1) using two different devices. The first one provides optical emission spectra in the UV-visible-NIR range and is composed of a 0.32 m focal length monochromator (Princeton Instruments IsoPlane SCT-320) equipped with 300 and 1200 lines/mm gratings and an intensified charged coupled device (ICCD) camera (Princeton Instruments PI-MAX4 1024*256). The 300 lines/mm grating is used for measurements between 680 and 850 nm, while the 1200 lines/mm grating is used for data between 320 and 345 nm. The second device is used to probe the VUV-UV photons and consists of a 1 m focal length monochromator with a 1200 lines/mm grating, operated under vacuum (Mc Pherson 225). A photomultiplier tube (Hamamatsu R7311) is used to record optical emission at the monochromator exit. To minimize air absorption, the distance between the MgF_2 window of the monochromator and the DBD cell is kept at a minimum value (1.2 cm).

As shown by other authors [35], [46], an important source of NH_3 dissociation in Ar-NH_3 DBDs is collisions of NH_3 with Ar metastable species. The Ar($1s_5$) number density is probed by optical absorption spectroscopy using a tunable laser diode (Sacher Lasertechnik Pilot PZ 500) in Littman/Metcalf configuration (laser linewidth < 100 kHz). The absorption measurements are done perpendicular to the gas flow lines at 2.1 cm from the beginning of the plasma zone (same as the OES measurement position). The laser light intensity signal is recorded on the oscilloscope using a high-speed photodetector (Thorlabs DET36A), and it is measured as a function of time during a 50 kHz period, averaged over 25 000 cycles. The temporal evolution of the absorption coefficient, *A*, is then calculated using the following formula:

$$A(t) = -\ln\left(\frac{I(t)}{I_0}\right) \quad (1)$$

where $I(t)$ is the time-resolved light intensity at a given wavelength. In the kHz range, a glow discharge lasts about 1-2 µs per half-cycle of the applied voltage, and the Ar(1s) lifetime is about 100 ns [35]. Therefore, I_0, in this range, can be assumed to correspond to the laser intensity between two subsequent discharges (assuming that the amount of Ar(1s) remaining in the discharge gap between two discharges is too little to induce significant absorption within the 2 mm optical path). Herein, the temporal evolution of the absorption coefficient is studied at different optical frequencies around the centered value of $3.69312*10^{14}$ Hz (or 811.7542 nm) corresponding to the Ar($1s_5$)-to-Ar($2p_9$) transition. The profiles recorded at 21 frequencies around this centered value allow for the establishment of Lorentzian-fitted profiles corresponding to the evolution of the absorption coefficient as a function of frequency at each probed time. A typical profile is shown in Figure 2.

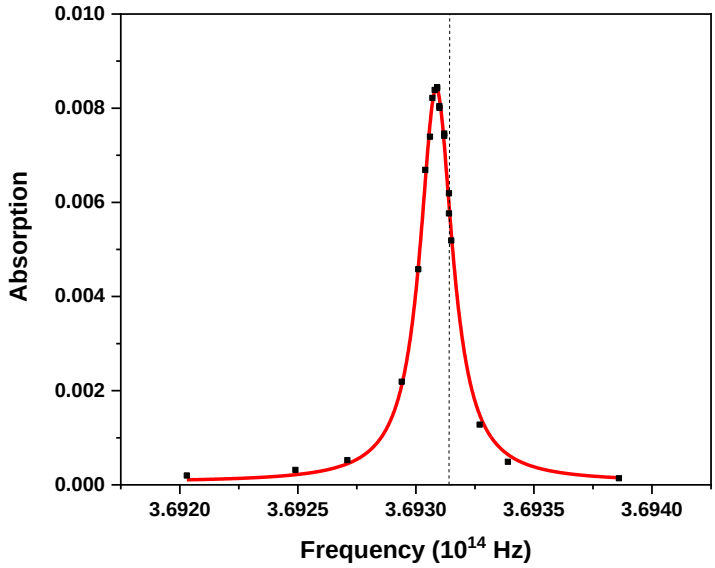

Figure 2. Typical line profile of the absorption coefficient recorded as a function of frequency at a given time in the low-frequency cycle of the 50 kHz Ar-NH_3 DBD. Here, as expected, the central frequency is shifted (Van der Waals pressure shift) with respect to the value of the Ar($1s_5$)-to-Ar($2p_9$) transition in vacuum represented by a dotted line [130]*. The same shift is observed throughout the whole cycle of the applied voltage.*

Finally, the temporal evolution of the Ar($1s_5$) number density is obtained by integrating the Lorentzian line profiles according to the following equation [44]:

$$n_{1s_5}(t) = \frac{8\pi}{A_{2p_9-1s_5}} \frac{g_{1s_5}}{g_{2p_9}} \frac{\nu_0^2}{c^2} \frac{1}{l} \int_{-\infty}^{\infty} A(\nu, t) d\nu \qquad (2)$$

where $A_{2p_9-1s_5}$ is the Einstein coefficient for spontaneous emission of the Ar($2p_9$)-to-Ar($1s_5$) transition, g_{1s_5} and g_{2p_9} are the statistical weights of $1s_5$ and $2p_9$ states, respectively, ν_0 is the central frequency of the transition, c is the speed of light, and l is the plasma length along the optical path (here, 2 mm). A similar method and equation can be used to determine the Ar($1s_3$) number density. For such experiment, the centered value of $3.77080*10^{14}$ Hz (or 795.0362 nm)

corresponding to the Ar($1s_3$)-to-Ar($2p_4$) transition is used, along with the corresponding values of the Einstein coefficient for spontaneous emission, the statistical weights, and the central frequency of the transition in Equation (1).

Experimental measurements

Figure 3 presents the current-voltage characteristics of the low-frequency Ar-NH_3 DBD examined in this work. Of note, the amplitude of the applied voltage is fixed to 2.5 kV peak-to-peak; at this value, and for the selected flow rate of Ar + 215 ppm NH_3 (280 SCCM, corresponding to a gas residence time of 40 ms in the 0.2*0.2 cm² tube), time-resolved analysis of the total light emission pattern (a selected time frame is shown in Figure 3) reveals that the discharge is produced simultaneously over the entire zone covered by the plane-to-plane metallic electrodes. In addition, emission is uniform across the gas flow lines, with a more prominent intensity close to the bottom electrode in the 2 mm gap. Such feature is typical of Ar-NH_3 DBD operated in the glow regime [227]. As can be seen in Figure 3, the current-voltage characteristics confirms the glow discharge regime, with a narrow current peak observed in the voltage rise (absolute value). Before maximum applied voltage is attained, the discharge switches off due to the accumulated charges on the dielectric walls, which decreases the gas voltage (i.e. the voltage applied to the gas) [186]. Considering that discharge behavior in positive and negative alternance of the applied voltage is symmetric, analysis presented below are conducted over a half period, i.e. between 0 and 10 µs.

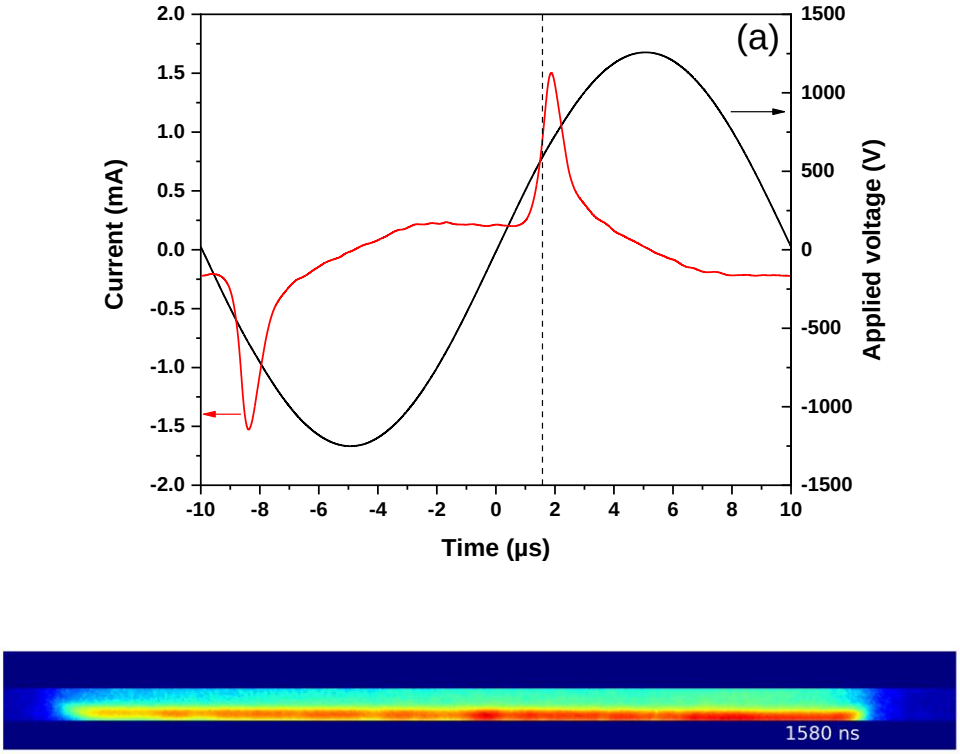

Figure 3. (a) Evolution of the applied voltage (in black) and current as a function of time for a 50 kHz Ar-NH_3 discharge. (b) Optical image of the whole discharge zone recorded over a 20 ns time frame to confirm the glow discharge regime. Here, the time at which the image was taken is indicated by a dotted line in (a). In this image, the bottom electrode is cathode and the gas flows from left to right.

The OES spectrum presented in Figure 4 shows that the Ar-NH_3 glow discharge produces two main optical emission signals. The first one is observed between 650 and 850 nm, and it consists of lines corresponding to the Ar(2p) to Ar(1s) transitions. Over the range of experimental conditions investigated, the Ar(2p) states are mainly populated by direct electron-impact excitation from ground state Ar atoms, by electron-impact excitation from Ar(1s) atoms, and by excitation energy transfer amongst Ar(2p) states [44], [77]. Meanwhile, the second emission is detected in the UV range, between 300 and 400 nm, and it shows bands corresponding to the de-excitation of the

NH(A) and N_2(C) states. Here, these levels can be populated by electron-impact excitation on ground state NH and N_2; in the case of NH(A), excitation can also result from the dissociative excitation involving Ar(1s) and NH_3 [228].

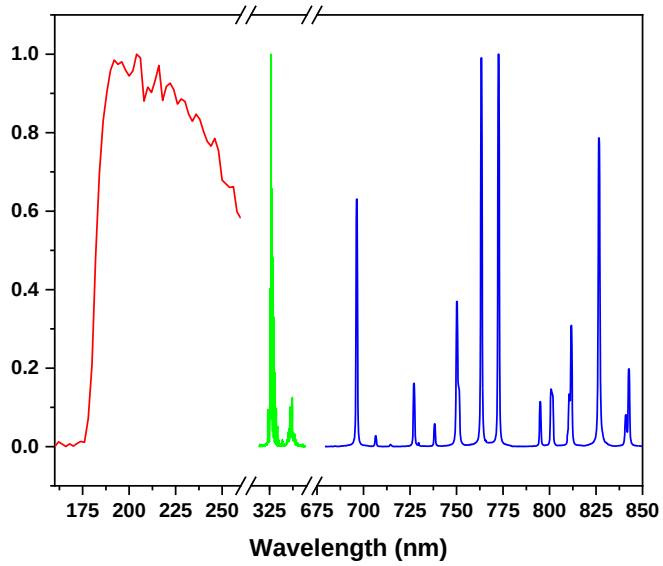

Figure 4. Typical optical emission spectra from an Ar-NH_3 glow DBD measured at 2.1 cm from the entrance of the plasma zone. The main emissions are shown in different colors, and are normalized over each wavelength range of the spectrometers.

In addition to the Ar, NH, and N_2 bands, a continuum emission is detected between 180 and 250 nm. This emission is attributed to the de-excitation of different vibrational levels of the $H_2(a^3\Sigma_g^+)$ excited state to the $H_2(b^3\Sigma_u^+)$ repulsive state [229], [230], creating a continuum emission in the 160 - 600 nm range [231]. The radiative lifetime of the H_2(a) state is about 11 ns [226]. Such H_2 emission has been reported for an atmospheric-pressure RF DBD, and the dominant excitation and de-excitation pathways assumed by the authors are presented below [82]:

$$Ar(1s) + H_2\left(X^1\Sigma_g^+\right) \rightarrow Ar + H_2\left(a^3\Sigma_g^+\right) \quad (3)$$

$$H_2\left(a^3\Sigma_g^+\right) \rightarrow H_2(b^3\Sigma_u^+) + h\nu \quad (4)$$

Figure 5 shows the temporal evolution of the main line and band emission intensities recorded during a half-period of the applied voltage. These intensities increase with increasing current due to higher populations of the excited states induced, in some cases, by direct collision with energetic electrons. Around the current peak, excitation involving high-energy electrons decays, resulting in decreasing emission intensities. Compared to the Ar emission at 763 nm ($2p_6$-$1s_5$ transition), the decrease of NH emission at 326 nm ($c^1\Pi$-$a^1\Delta$ transition) is clearly slower. This is partly attributed to the slower radiative decay time of the NH($c^1\Pi$) excited state, whose radiative lifetime is much longer than that of the Ar($2p_6$) state (respectively 364 vs 41 ns) [130][232]. With a decay time of 2.77 µs, the decrease of the 204 nm emission linked to the excited $H_2\left(a^3\Sigma_g^+\right)$ state is slower than both, the Ar and NH emissions (characteristic decay times of 0.246 and 0.675 µs, respectively). The same trend is observed with other H_2 emission wavelengths of the H_2(a) continuum (not shown in Figure 5).

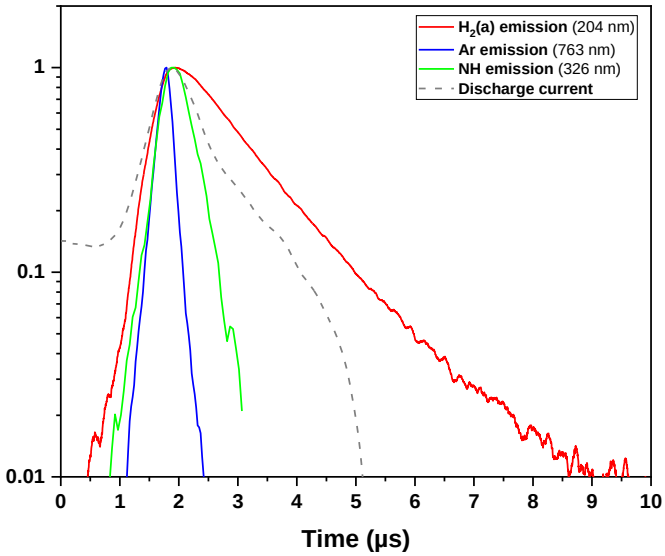

Figure 5. Temporal evolution of the current (discharge and displacement current) and normalized line and band emission intensities measured at 2.1 cm during a half period (Ar 763 nm in blue, NH 326 nm in green, H_2 204 nm in red and discharge current in gray dashed line).

Based on the available literature, the $H_2\left(a^3\Sigma_g^+\right)$ state in hydrogen-containing plasmas is populated by reaction of H_2 with Ar(1s) (see equations 3 and 4), without distinction between the four 1s levels of Ar. As reported in [35], the populations of the four Ar(1s) levels produced by a 50 kHz discharge are statistically distributed, which means that they exhibit similar kinetics. Therefore, the kinetics of $H_2\left(a^3\Sigma_g^+\right)$ formation (equation 3) may be estimated based on the population of a single Ar(1s) level. To verify this hypothesis, the temporal evolution of the Ar($1s_5$) and Ar($1s_3$) population densities was probed; the results are shown in Figure 6 between 0 and 3 µs.

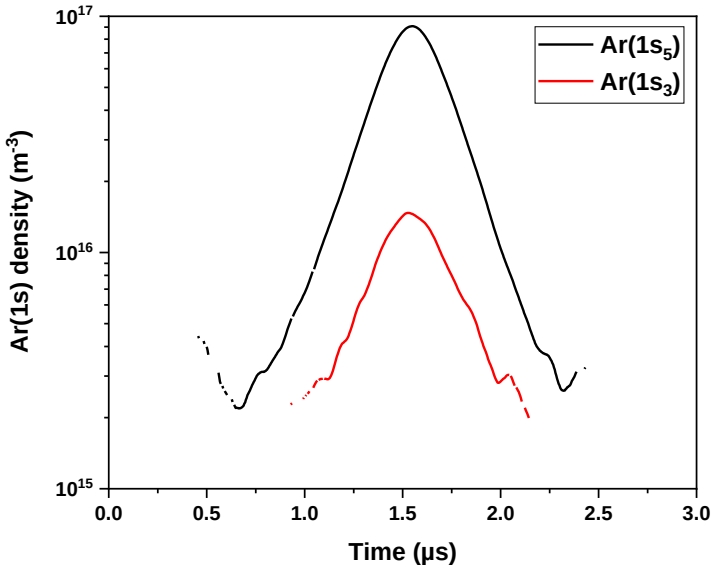

Figure 6. Evolution of the Ar(1s$_5$) and Ar(1s$_3$) number densities as a function of time. The conditions are the same than in Figure 5.

As shown in Figure 6, the two metastable states of Ar during a single discharge present similar time evolution profiles. In addition, the ratio of the maximum Ar(1s$_5$) and Ar(1s$_3$) number densities detected between 0 and 3 µs (9.1 x 10^{16} and 1.5 x 10^{16} m^{-3}, respectively) is 0.17, which is similar to the ratio obtained from the statistical population distribution (0.2). These results suggest that the hypothesis stated above is valid, and that the number density of one Ar(1s) level may be used to probe the kinetics of the whole Ar(1s) state [35], [188].

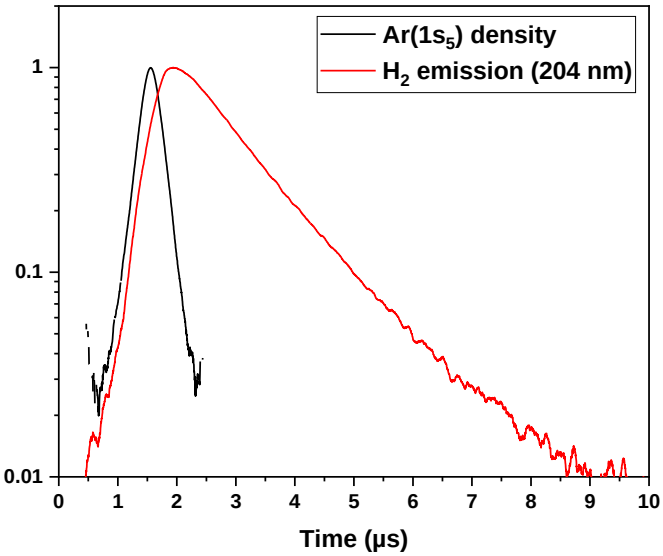

Figure 7. Evolution of Ar(1s$_5$) density and H_2 emission as a function of time during a half period.

To provide further insight into the kinetics driving the H_2(a) continuum emission, Figure 7 compares the profile of the normalized Ar(1s$_5$) density to that of the normalized emission intensity recorded at 204 nm. Over the range of experimental conditions investigated, the maximum relative error is about ± 1% and ± 25% for high and low Ar(1s$_5$) number density values, respectively. As shown in Figure 7, the increase in H_2 emission between 1 and 1.75 µs follows the increase in Ar(1s$_5$) number density. Therefore, the emission of H_2 at the beginning of the discharge seems linked to the pathway described above (i.e. equation (3) and (4)). Beyond 2 µs, however, the Ar(1s$_5$) number density decreases, but the H_2 emission persists for a long time. In fact, the rate of decrease in H_2 emission is about seven times lower than the rate of the Ar(1s$_5$) density decay. Such variation is clearly not associated with the response time of the photomultiplier detector (15 ns for the Hamamatsu R7311) or the radiative lifetime of the $H_2\left(a^3\Sigma_g^+\right)$ state (11 ns), which means that

another mechanism contributes to the formation of the $H_2(a^3\Sigma_g^+)$ state in the post-discharge period (i.e. after the decay of the Ar($1s_5$) number density).

Discussion

To divulge possible other mechanisms involved in the kinetics of H_2(a) states, one must consider that the electronic flux produced between two discharges in low-frequency Ar-NH_3 DBD is very low, resulting in minimal Ar(1s) number density (as seen in Figure 6 and Figure 7) and suppressed $H_2(a^3\Sigma_g^+)$ formation by direct electronic excitation of H_2. Therefore, other energetic species with long lifetimes must be implicated in the formation of the $H_2(a^3\Sigma_g^+)$ state after discharge extinction. Positive ions could be such energetic species, and in the period between two discharges, they are mainly lost by gas phase recombination [41]. In low-frequency Ar-NH_3 DBDs, the main ions produced are Ar_2^+ and NH_3^+ [27], [35], [233]. The former is produced by reaction of Ar^+ with 2 Ar [47], [127], whereas the latter is generated via Penning ionization following collisions involving Ar(1s) states and NH_3 [45], [46], as well as via charge transfer from Ar_2^+ to NH_3 [47]. Of note, the minimal ionization energies of NH_3 and Ar_2 are 10.07 [234] and 14.44 eV [235], respectively.

The dissociative recombination of NH_3^+ with an electron release 10.07 eV, while the creation of H_2(a) requires 11.62 eV, see Figure 8. Thus the NH_3^+ recombination releases too little energy to efficiently create $H_2(a^3\Sigma_g^+)$. However, it is likely that the charge transfer between Ar_2^+ and NH_3 create a NH_3^+ on a high vibrational state (noted NH_3^+(v)). At atmospheric pressure, the vibrational relaxation time of a molecule is much greater than the time between two electron-neutral collisions [236]–[238]; hence, the recombination between an electron and a NH_3^+ on a high vibrational state

is possible and could produce H_2 molecules in excited states. Moreover, three different levels of H_2 could lead to the H_2 emission previously mentioned : $a^3\Sigma_g^+$ (11.62 eV above ground-state) but also $c^3\Pi_u$ (11.61 eV above ground-state) and $d^3\Pi_u$ (13.70 eV above ground-state) [239]–[241], increasing the likelihood of this emission occurring.

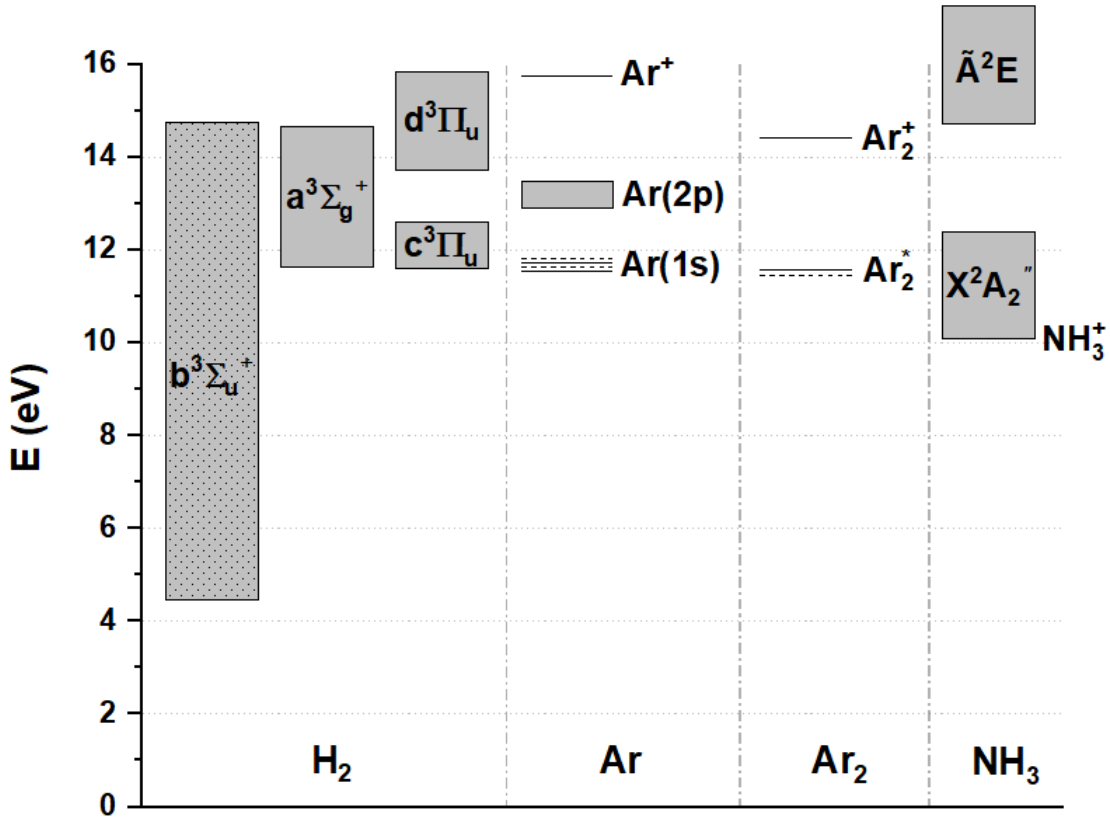

Figure 8. Partial energy level diagram of H_2, Ar, Ar^+, Ar_2^*, Ar_2^+ and NH_3^+. Grey zones represent levels leading to emission lines (or bands) observed in [42], [240], [242]. *Dotted $H_2(b^3\Sigma_u^+)$ state is a repulsive state.*

To better understand the mechanisms underlying $H_2(a)$ creation and emission, simulations were carried out using the one dimensional fluid model of Ar-based DBDs developed and validated in [35]. This model solves the continuity and momentum equations for all species and the energy

equation for electrons. It considers 7 species (Ar, Ar^+, Ar_2^+, Ar(1s), Ar_2*, photons and e^-) through 11 reactions. Electron secondary emission from the walls through collisions with Ar^+, Ar_2^+, Ar(1s), Ar_2* and VUV photons is also considered. All details on reaction rates and secondary electron emission coefficients are provided in [35]. From this model, the only species that reveal a slow decay is the positive ion density [188]. Such decay is attributed to the recombination of Ar_2^+ with electrons at a rate of $7.35*10^{14}*Te^{-0.67}$ $m^3.s^{-1}$ [139]. Like all other recombination processes involving charged species, this reaction is prominent at low electronic temperatures, i.e. when the discharge extinguishes.

It is worth highlighting that the contribution of NH_3 in the Ar-NH_3 DBD, which leads to complex Ar-NH_3 interactions, was not explicitly introduced in the fluid model developed and validated in [35]. Instead, to limit the number of species, NH_3 and NH_3^+ were not explicitly considered. Thus, Penning ionization and dissociation were simulated by reaction 5 and 6 respectively

$$Ar(1s) + NH_3 \rightarrow Ar^+ + e^- + Ar \quad (5)$$

$$Ar(1s) + NH_3 \rightarrow Ar + NH_3(products) \quad (6)$$

Here, equation (5) accounted for the primary electron production by Penning ionization of NH_3 by Ar(1s) atoms while equation (6) accounted for the destruction of Ar(1s) atoms by Penning dissociation of NH_3. However, as discussed in previous studies [35], equation (5) was assumed to produce Ar^+ since NH_3^+ was not considered as an independent specie in the fluid model. Considering that NH_3^+ is the dominant ion in glow-like Ar-NH_3 DBDs operated in a Penning mixture [21], and that recombination processes occurring in the postdischarge must predominantly involve NH_3^+, the model was slightly revised to include NH_3 (with a fixed concentration fraction

of 40 ppm), NH_3^+, $NH_3^+(v)$ and $H_2(a^3\Sigma_g^+)$. To minimize the complexity elicited by such introduction and to conserve the one-dimensional character of the model, it is advisable to evaluate the effect of NH_3 dissociation simply by making the calculation for a fixed estimated NH_3 and by product concentrations, i.e. not directly taking into account NH_3 dissociation.

Table 1 gives the six reactions added to the model, with the first two being only slightly modified with respect to equation (5) and (6). Here, new reactions (1) and (2) accounts for Penning ionization (with the formation of NH_3^+) and Penning dissociation ionization, respectively. As for reaction (3), it considers gas-phase recombination of NH_3^+ with electrons. Meanwhile, reactions (4) and (5) account for the production of $NH_3^+(v)$ by charge transfer from Ar_2^+ to NH_3 and the consumption of $NH_3^+(v)$ by recombination with low-energy electrons, respectively. Notably, there is no clear evidence of the existence of these last two reactions in the literature; however, they were added to the model to determine whether H_2 emission in the post-discharge stage could be attributed to the dissociative recombination of $NH_3^+(v)$ with low-energy electrons. Their rate coefficients were estimated from the ones of similar reactions presented in references [47] and [243]. Since the model is not coupled to a full plasma chemistry model, the NH_3 by-products produced by reactions (2) and (3) were considered as NH_3 with a concentration fraction of 40 ppm (see details in [35]). In addition, the full reaction pathways leading to the creation and destruction of NH and $H_2(b^3\Sigma_u^+)$ species produced by reactions (5) and (6) were not included in the model. The reaction of Ar(1s) with H_2 to produce $H_2(a^3\Sigma_g^+)$ is also not included, as it requires the assumption of a known H_2 number density, and only the dissociative recombination of $NH_3^+(v)$ accounts for this species in Table 1. Therefore, the model cannot simulate the increase in H_2 emission due to H_2 generation

resulting from NH_3 dissociation, and only the H_2(a) emission decay deduced from the model can be compared with the experimental measurements.

Table 4. Additional reactions accounting for directly introduced NH_3 and NH_3^+ species in the model.

	Reaction	Rate coefficient	References
1.	$Ar(1s) + NH_3 \rightarrow NH_3^+ + e^- + Ar$	$k = 2.3 * 10^{-16}\, m^3.s^{-1}$	[45], [46]
2.	$Ar(1s) + NH_3 \rightarrow Ar + NH_3(products)$	$k = 3.1 * 10^{-16}\, m^3.s^{-1}$	[45], [46]
3.	$e^- + NH_3^+ \rightarrow NH_3(products)$	$k = 3.1 * 10^{-13} * \left(\frac{300}{T_e}\right)^{0.5} m^3.s^{-1}$	[243]
4.	$Ar_2^+ + NH_3 \rightarrow NH_3^+(v) + Ar + Ar$	$k = 4.5 * 10^{-16}\, m^3.s^{1}$	
5.	$e^- + NH_3^+(v) \rightarrow H_2\left(a^3\Sigma_g^+\right) + (NH)$	$k = 3.1 * 10^{-13} * \left(\frac{300}{T_e}\right)^{0.5} m^3.s^{-1}$	
6.	$H_2\left(a^3\Sigma_g^+\right) \rightarrow h\nu + \left(H_2(b^3\Sigma_u^+)\right)$	$k = 9.3 * 10^{7}\, s^{-1}$	[226]

Figure 9 compares the time evolution of the measured Ar($1s_5$) number density and H_2 emission intensity, to the calculated contribution of NH_3^+(v) dissociative recombination on H_2 emission intensity and calculated Ar(1s) number density, as deduced from the revised model. Clearly, measured Ar($1s_5$) density and calculated Ar(1s) populations are almost perfectly alike, which validates the reaction set presented in [35] and revised in Table 1. The temporal profiles of H_2 emission are also similar, with both, the measured and calculated profiles showing a slow decay of the emission between 2.5 and 5.5 µs. Such similarity suggests that H_2 emission decay is attributed to the decrease in NH_3^+(v) and/or electron density, which confirms our hypothesis regarding the contribution of NH_3^+(v) dissociative recombination to the creation of H_2(a) in the post-discharge time scale. Notably, important differences are observed between the measured and calculated emission data, particularly in the rising period between 1 and 2.5 µs, i.e. when the Ar(1s) density

is large. In the later time scale, the calculated H_2 emission increases later than the measured one due to the omission of the Ar(1s) + H_2 → $H_2\left(a^3\Sigma_g^+\right)$ reaction from the model and the absence of a full plasma chemistry model accounting for H_2 production in Ar-NH_3 DBDs.

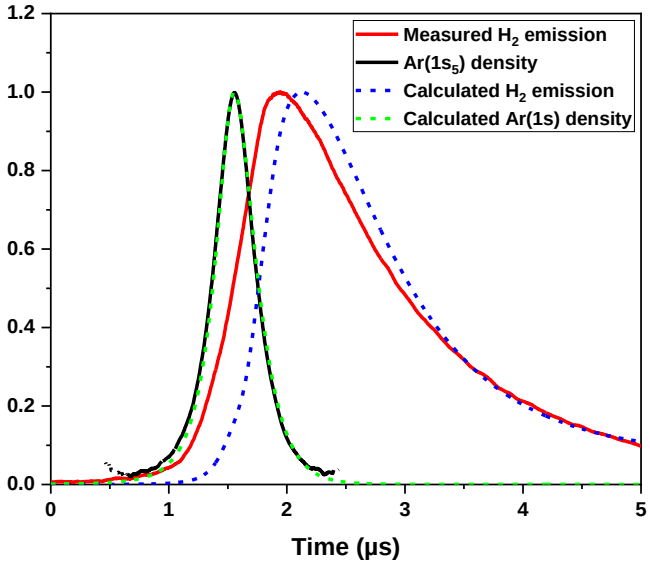

Figure 9. Measured (continuous lines) and calculated (dashed lines) profiles of normalized Ar(1s5) number density (black and green) and H_2 continuum emission intensity (red and blue). For the calculated H_2 continuum emission intensity, only the contribution from NH_3^+(v) dissociative recombination is computed.

Conclusion

A combination of optical emission and absorption spectroscopy was used to examine the temporal evolution of selected noble and reactive species produced in a 50 kHz Ar-NH_3 DBD operated in a homogeneous glow discharge regime. In addition to the typical NH(A-X), N_2(C-B), and Ar(2p-1s) transitions commonly reported in literature, optical emission spectroscopy measurements were carried out down to 175 nm to highlight the H_2(a) continuum emission. It was shown that this H_2 emission remains for a long time after discharge extinction. Over the range of experimental

conditions investigated, the emitting $H_2(a^3\Sigma_g^+)$ states are populated by collisions of $H_2(X^1\Sigma_g^+)$ with Ar(1s) states during discharge, and by dissociative recombination of the vibrationally-excited ammonia ion (NH_3^+(v)) after the discharge. NH_3^+(v) is produced by charge transfer from Ar_2^+ to NH_3, and it breaks into $H_2(a^3\Sigma_g^+)$ (or $H_2(c^3\Pi_u)$ or $H_2(d^3\Pi_u)$) and NH upon gas phase recombination with an electron. When the excited $H_2(a^3\Sigma_g^+)$ state relaxes, it emits VUV-UV photons and produces the $H_2(b^3\Sigma_u^+)$ repulsive state, which later dissociates into two hydrogen atoms. Based on this proposed mechanism, a 1D fluid model was developed and used to simulate the emission intensity from H_2(a) levels. Considering that the calculated temporal profile of the emission is consistent with the measured one, the proposed mechanism seems valid. The importance of this mechanism lies in proving that the ions present in the reaction medium after discharge can bring sufficient energy to produce excited H_2(a) molecules, even in the absence of a significant electron flux.

Acknowledgments

The work carried out in Canada was funded by the National Science and Engineering Research Council (NSERC RGPIN-2018-04550) and by the Fondation Courtois. As for the one in France, it was supported by the Agence Nationale de la Recherche through the Investissement d'avenir program (ANR10LABX2201). All authors would like to acknowledge the financial support of the CNRS and Université de Montréal through their contributions to the International Research Network on Controlled Multifunctional Nanomaterials.

Data availability statement

The data that support the findings of this study are available upon request from the authors.

L'étude de l'émission de H_2, présentée dans l'article précédent, a montré l'importance du transfert de charge entre Ar_2^+ et NH_3, ainsi que la possibilité que la recombinaison du NH_3^+ excité ainsi créé, favorise la production de $H_2(a)$. Ces observations ont aidé à améliorer le modèle (en prenant en compte l'ion NH_3^+ et sa recombinaison en plus de celle de Ar_2^+) et a apporté une réflexion sur les mécanismes de dissociation du NH_3 dans une DBD à basse fréquence produite dans Ar-NH_3. A la lumière de ces résultats, il semble pertinent de s'intéresser à l'effet du temps de résidence du mélange Penning sur la physique de la décharge, rajoutant une dimension spatiale supplémentaire à l'étude.

Dans ce contexte, nous avons eu recours aux mêmes diagnostics optiques que dans l'article précédent ; une caméra ICCD a aussi été utilisée pour avoir une représentation globale de l'émission de l'ensemble de la décharge en fonction du temps. Ces diagnostics ainsi que la caractérisation électrique de la décharge permettent de confronter le comportement global de la décharge avec son évolution locale. On comprend alors que le temps de résidence, impactant la dissociation du NH_3 et la formation des produits de réaction, a un effet vraiment différent que l'on considère la décharge sur l'ensemble des électrodes ou son comportement à une position spécifique. Si la dissociation du NH_3 est assez importante, la décharge s'allume uniquement sur une portion des électrodes et glisse vers la sortie des électrodes à mesure que la tension appliquée augmente. Cependant, a un endroit donné, la physique de la décharge semble peu modifiée par la dissociation du NH_3 et la formation des nouveaux sous-produits. Ce phénomène s'explique par le fait que soit il reste assez de NH_3 pour que l'ionisation Penning joue un rôle soit il n'en reste pas assez et la décharge ne s'allume pas.

Enfin, en comparant les densités d'Ar($1s_5$) mesurées avec les densités d'Ar(1s) calculées par le modèle pour différentes quantités de NH_3, on peut corréler une différence de temps de résidence du gaz avec une différence de quantité de NH_3 dans le mélange Penning. Ce résultat permet d'obtenir un taux de dissociation du NH_3 en fonction du temps de résidence, ou encore de l'énergie nécessaire pour obtenir ce taux de dissociation.

Les travaux sont présentés sous la forme d'un article en préparation finale pour une soumission à Plasma processes and Polymers (en attente des corrections des co-auteurs).

NH_3 dissociation along the gas flow lines of Ar-NH_3 dielectric barrier discharges and its effects on global and local properties

Raphaël Robert[1,2], Françoise Massines[2], Luc Stafford[1]

[1]Département de physique, Université de Montréal, 1375 ave. Thérèse-Lavoie Roux, Montréal, Québec, H2V 0B3, Canada

[2]Laboratoire Procédés Matériaux et Énergie Solaire (PROMES, CNRS, UPR 8521), Rambla de la thermodynamique, 66100 Perpignan, France

Abstract

This paper examines the effects of NH_3 dissociation on the physics driving 50 kHz dielectric barrier discharges operated in Penning Ar-NH_3 gas mixtures. Optical diagnostics in the UV-Vis-NIR range in combination with current-voltage characteristics are used to probe the global (averaged over the whole discharge zone) and local properties as a function of the gas flow rate. When the gas flow is high enough, the dissociation of NH_3 along the gas low lines is too low to significantly impact the discharge; hence, the characteristics are those of a typical glow discharge operated in a Penning mixture along the entire electrode length. When the gas flow is decreased, the gas residence time in the electrode region increases such that NH_3 becomes strongly converted to reaction products other than those leading to Penning ionization. This leads to a glow discharge only over a limited length of the electrode zone, with no further breakdown towards the exit. The perceived effects on the discharge are then significant if the overall behavior is considered, but on a local scale, the populations of Ar($1s_5$), Ar(2p), and H_2(a) states deduced from the optical diagnostics are only weakly modified. Moreover, using Ar($1s_5$) measurements and the predictions of a 1D fluid model, values of the degree of NH_3 dissociation at two gas residence times are obtained. From such analysis, it is highlighted that the discharge can remain in a diffuse mode even when the quantity of NH_3 is much lower than the one in the injected gas mixture.

1. Introduction

Penning mixtures are mixtures of noble and adjuvant (often molecular) gases that are typically used in low-frequency dielectric barrier discharges (DBD) to maintain homogeneous (or diffuse) discharge regime (instead of the most common filamentary discharge regime) [6], [16], [41]. The adjuvant is typically selected such that its ionization energy is less than the metastable excitation energy of the primary noble gas constituent. In such cases, ionization occurs via a two-step process involving first, the creation of the metastable state of the noble gas by electron-impact excitation on ground state atoms, and then, the ionization of the adjuvant gas by excitation energy transfer from the metastable state. Such two-step ionization leads to slower breakdown and lower breakdown voltage than those obtained in discharges produces in noble gases only [215].

In the case of adjuvant gas molecules, they may also undergo dissociation upon interaction with metastable atoms and other energetic species in the plasma [46], [47], [244], [245]. In Ar-NH_3 Penning mixtures, for example, 42% of NH_3 is ionized by interaction with Ar(1s) (metastable state of argon), and 58% is dissociated [46]. Several authors have investigated the decomposition of NH_3 in Ar-NH_3 DBDs operated in the filamentary regime. Indeed, certain applications require effective dissociation of NH_3, which has been recently identified as an H_2 carbon-free energy carrier [204], [246]–[248]. The extent of NH_3 dissociation was found to depend on the power density injected into the discharge and the gas residence time as these properties drive the total energy injected per NH_3 molecule [48], [198], [199], [221], [222], [249]. The effects of other parameters, including the neutral gas temperature [247], and the coupling of the plasma with catalysis or pyrolysis techniques [48], [222], [223], [249]–[254], on the efficiency of NH_3 conversion to H_2 by non-thermal plasmas at atmospheric pressure have also been reported.

Based on such literature, significant change in the neutral gas composition can be expected along the gas flow lines of DBDs, i.e. with increasing position (or gas residence time) from the entrance of the DBD cell. Such plasma chemistry gradient may lead to variations in the discharge physics [119], [187], [255], [256]. For example, in Ar-NH_3 DBDs, the concentration fraction of NH_3 could be high enough close to the entrance to form a Penning mixture and too low near the exit to observe significant excitation energy transfer from Ar(1s) to NH_3. While many studies examined the NH_3 dissociation and the formation of reaction products in the plasma (studies conducted using 0D plasma chemistry models [247], [249], [254]), the resulting changes in fundamental plasma properties during NH_3-to-products conversion are often overlooked.

In this study, we assess the impact of NH_3 dissociation on the physics of a low-frequency DBD operated in Ar-NH_3 Penning mixture and analyze the effect of gas residence time. Global electrical and optical properties are measured over the entire plasma length; however, to gain a better understanding of the DBD physics, the emission and absorption spectra are also probed locally along the gas flow lines. The obtained results confirm that NH_3 dissociation induces significant changes on both global and local discharge properties. Moreover, at low flow rates, when NH_3 becomes strongly converted to products other than those leading to a Penning mixture, the discharge can exhibit a diffuse regime locally without being homogeneous over the entire zone covered by the electrodes.

2. Experimental setup and diagnostics

The discharge was ignited in the 2 mm gap between the top and bottom metal-coated fused silica walls (1 mm thickness, 4.7*0.2 cm² area) of a 0.2*0.2 cm² square-section tube, whose side walls are made of MgF_2 (same dimensions as the fused silica walls), see Figure 10. All details can be found in previous publication [257]. The bottom electrode was grounded, while the top one was connected to a function generator (Tektronix AFG 3021B) producing a 50 kHz, 2.5 kV peak-to-peak sinewave that is amplified by an audio amplifier (Crest CC4000) coupled to a bridged resistor and a step-up voltage transformer (Atesys-Montoux). The electric signals measured by the current (Lilco LTD 13W5000) and voltage probes (Tektronix P6015A) were visualized and recorded on an oscilloscope (Teledyne Lecroy HDO6104A). Prior to an experiment, the tube was pumped down to a few tenth of Torr and then filled with an Ar + 215 ppm NH_3 Penning mixture up to 745 Torr. Different gas flow rates were examined, and the total pressure was maintained near atmospheric pressure for all conditions using a throttle valve located at the exit of the pumping system.

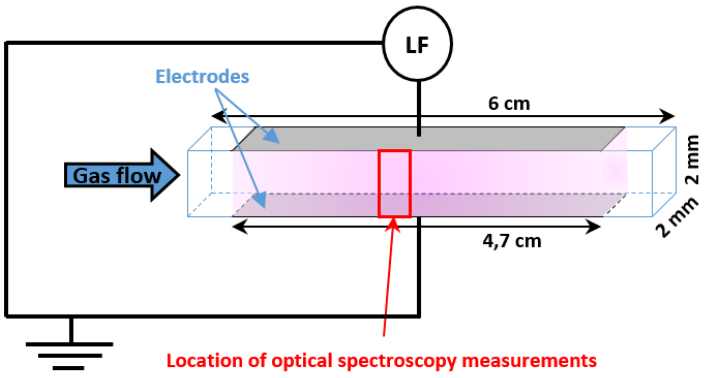

Figure 10. Schematics of the experimental setup for DBD ignition with metallic electrodes coated on the fused silica tube.

The temporal evolution of Ar($1s_5$) number density and H_2(a) emission was monitored as described in [257]. Briefly, the population of the Ar($1s_5$) metastable species was determined based on the absorption of a tunable laser diode (Sacher Lasertechnik Pilot PZ 500), which was measured using a high-speed photodetector (Thorlabs DET36A) operated at different wavelengths around the central wavelength of the Ar $1s_5 \rightarrow 2p_9$ transition. The spectral and time resolution of the photodetector allows for monitoring the Ar($1s_5$) number density during the 50 kHz period of the applied voltage. Meanwhile, the 204 nm continuum emission intensity linked to the $H_2\left(a^3\Sigma_g^+\right) \rightarrow H_2(b^3\Sigma_u^+)$ transition was probed using a vacuum monochromator (Mc Pherson 225) equipped with a 1200 lines/mm grating, and a photomultiplier tube (Hamamatsu R7311). Both, H_2(a) emission and Ar($1s_5$) number density measurements were acquired for various gas flow rates at 2.1 cm from the entrance of the DBD cell.

Space- and time-resolved emission of the discharge integrated over the UV-Vis-NIR range (200 – 900 nm) were also recorded using an ICCD camera (PIMAX-4: 1024 EMB, Princeton Instruments). The camera was positioned perpendicular to the gas flow lines. The emission was collected at the spatial and time resolution of 67 μm and 20 ns, respectively, and it was averaged over 300 cycles of the 50 kHz period of the applied voltage to obtain optimum signal-to-noise ratios.

3. Experimental measurements

3.1. Space integrated measurements: discharge current and light emission

Figure 11 (a) depicts the discharge current profiles recorded during a half period of the applied voltage at various gas flow rates between 70 and 420 SCCM. At these flow rates, the gas flow is laminar, gas particles travel at an average speed of 0.29 to 1.75 $m.s^{-1}$, and thus, they can cross the 4.7 cm discharge distance within 27 to 162 ms. Such transit times are long compared to the discharge duration (a few µs [41]) and the half cycle of the applied voltage (i.e. time between two discharges; 10 µs). Therefore, the gas cannot be completely renewed in the period between two consecutive discharges, and the gas chemistry changes depending on the position of species in the discharge volume along the gas flow lines.

In general, the behavior of a Penning mixture discharge depends on the quantity of adjuvant gas (here NH_3) [6], [50], [198], which in turn varies depending on the gas flow rate and residence time (in a fixed configuration at a specific position). Regardless of the discharge location, the discharge current integrates all charges flowing through the entire electrode surface, and thus, it should be affected by variations in gas flow. Indeed, Figure 11 (a) shows that the current is highly dependent on the Ar + NH_3 flow, with lower current amplitudes and wider peaks (i.e. longer discharge durations) observed at lower flow rates. Moreover, the current maximum is shifted to longer times in the discharge period when the gas flow is decreased, which could mean that the discharge ignites later and/or slower. At high gas flows (420 and 280 SCCM), Figure 11 (a) further shows that the discharge current exhibits characteristics of a typical glow discharge current [58]. However, the

current seems to behave differently at flow rates below 140 SCCM, with shifted current peaks (longer times) and decelerated current decline detected at lower flows.

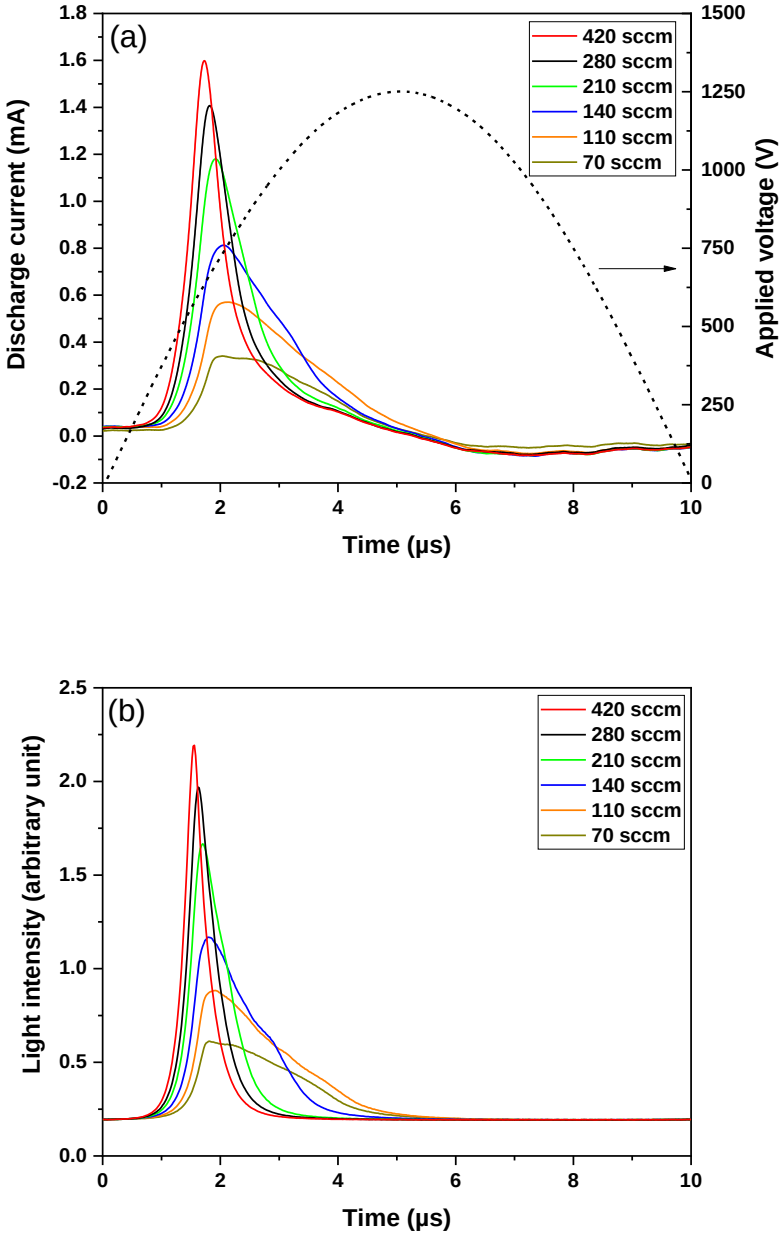

Figure 11. Temporal evolution of the discharge current (a) and temporal evolution of the total light emission (b) as a function of time, at different gas flow rates between 70 and 420 SCCM, during a half period of the applied voltage (dashed line in (a)). Here, the light emission is integrated over the whole discharge volume.

As shown in Figure 11 (b), the temporal profile of the light emission integrated over the whole discharge volume (and recorded using the ICCD camera) exhibit the same variations as the discharge current (Figure 11 (a)), with some slight differences. Compared to the discharge current, the light intensity appears and disappears slightly earlier in the discharge period. Moreover, the full width at half maximum (FWHM) of the light intensity peak is smaller than that of the current peak recorded at the same flow rate (for example, at 420 SCCM, light emission FWHM is 380 ns while that of the current is 576 ns). These aspects are better illustrated in Figure 12 (a) and Figure 12 (b) that compare the discharge current and light emission for two gas flow rates, 110 SCCM (Figure 12 (a)) and 280 SCCM (Figure 12 (b)).

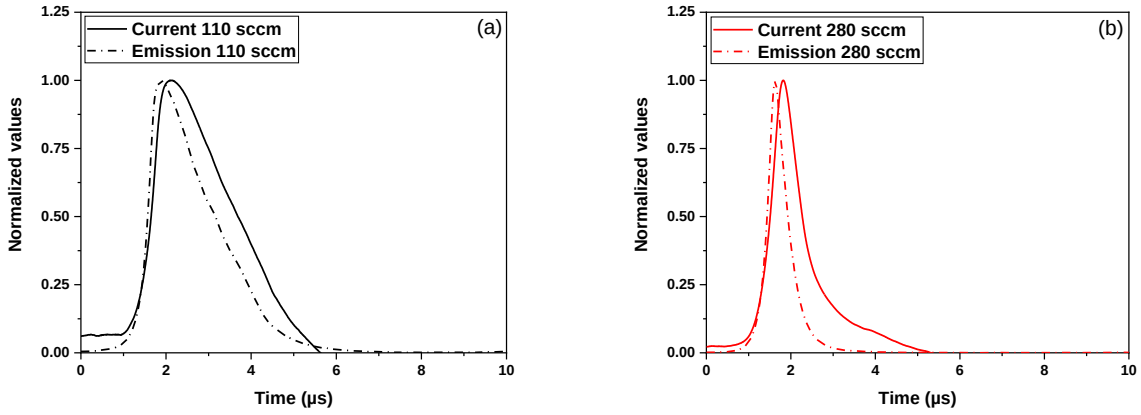

Figure 12. Comparison between the discharge current and the total light emission recorded at (a) 110 SCCM and (b) 280 SCCM.

Over the range of experimental conditions investigated, the discharge emission is mainly observed in the Vis-NIR range, and it is mostly attributed to the $Ar(2p_x) \rightarrow Ar(1s_y)$ transition [49], [256]. Considering that several of the $Ar(2p_x)$ states are primarily populated by electron-impact excitation on ground state Ar atoms, and that such processes require high-energy electrons [44], the emission

profiles presented in Figure 11 and Figure 12 may be regarded as signatures of these electrons. This explains the small differences observed between the current signals, which are mostly correlated with the total electron population, and light intensity signals, which are related to the population of high-energy electrons.

3. 2 Time and space resolved light emission

Figure 11 and Figure 12 do not provide any information regarding the spatial evolution of the discharge properties along the gas flow lines. Such information is needed to better understand the difference between current and light emission variations. The spatially and temporally resolved optical emission data acquired at 280 and 110 SCCM are presented in Figure 13. Here, images of the spectrally-integrated light emission are recorded over the whole discharge area (2 mm gap x 4.7 cm electrode length) at the time of maximum current (Figure 13 (a) and Figure 13 (c)) and at 500 ns after this maximum (Figure 13 (b) and Figure 13 (d)). At maximum current, the 280 SCCM discharge is clearly ignited over the whole electrode volume (Figure 13 (a)), meaning that charges are spread over the entire electrode. The accumulated dielectric charge reduces the voltage applied to the gas [6], thereby simultaneously extinguishing the discharge over almost the entire length of the electrode, as shown in Figure 13 (b)). A small light spot is always observed at the entrance of the discharge. It is probably induced by the reinforced electric field at this location due to the squared electrode shape. At 280 SCCM, the emission intensity increase towards the end of the discharge space shown in Figure 13 (a) and 4 (b)) regardless of the time. Such increase may be related to changes in electron density and electron temperature as a function of the position in the discharge, linked to variations in NH_3 dissociation, as detailed in the discussion.

	At the time of maximum current	500 ns after the current peak
280 SCCM	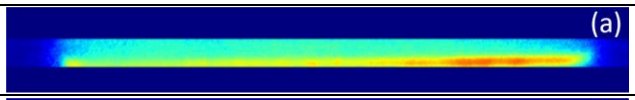	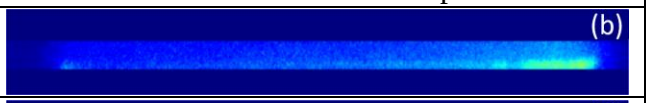
110 SCCM	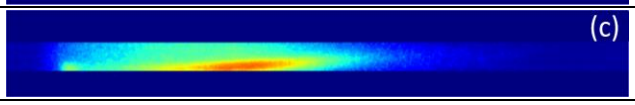	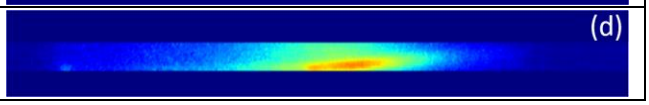

Figure 13. Logarithm of the light intensity emitted from the discharge tube (gas inlet is on the left) at 110 (a and b) and 280 SCCM (c and d). The images shown (a) and (c) were captured at the time of maximum current, whereas those shown in (b) and (d) were captured at 500 ns after maximum current. Gas flow goes from left to right and the cathode is the lower electrode.

Unlike the 280 SCCM discharge, the one produced at 110 SCCM is ignited only up to the middle of the discharge space when the current is maximum (Figure 13 (c)). Beyond the entrance of the space where a small light spot also appears, the emission intensity first increases and then decreases until it disappears around the middle. Comparatively, the emission recorded at 500 ns after maximum current seems to have shifted towards the exit of the inter-electrode space (Figure 13 (d)). This shifting is probably induced by plasma chemistry variations. When the flow rate is reduced, the residence time of the gas increases, resulting in a more significant plasma chemistry gradient along the gas flow lines. At a given applied voltage, the discharge ignites where the quantity of NH_3 is sufficiently high, i.e., at the electrode inlet (Figure 13 (c)). Then, two counter-acting phenomena simultaneously come into play: (i) the locally accumulated dielectric charges extinguish the discharge where it was initially ignited, and (ii) the increasing applied voltage (as a function of time) extends the discharge towards areas of the inter-electrode space where the amount of NH_3 is too low to initially ignite the discharge. At 110 SCCM flow rate, the discharge ignites at ~1 µs and is extinguished at ~5.5 µs (see Figure 11). During this time, the amplitude of the applied voltage increases from 370 V to 1250 V, and the discharge gradually moves toward the exit of the

inter-electrode space. Consequently, the flux of space-integrated electrons towards the walls is prolonged and weakened (the discharge no longer covers the whole electrode zone), resulting in lower current flow and total light emission, as seen in Figure 11.

Figure 13, also show that whatever the conditions, the discharge remains diffuse; there isn't micro discharge and the light is maximum at the cathode.

Figure 14 shows the variation in the light emission intensity integrated over the 2 mm gap as a function of time and position along the discharge length for discharges ignited at 110 and 280 SCCM. The position axis in Figure 14 represents the electrode length, with 0 cm corresponding to the position of gas inlet into the discharge space. At low flow rate (110 SCCM), the discharge ignites at the inlet then gradually propagates towards the outlet over the half-period of 10 µs, while at high flow, the discharge is ignited and extinguished practically at the same time over the entire space. Notably, the discharge does not reach the electrode end (top) at low flow. This effect may be linked to the density of NH_3, which becomes too low for further discharge ignition along the gas low lines.

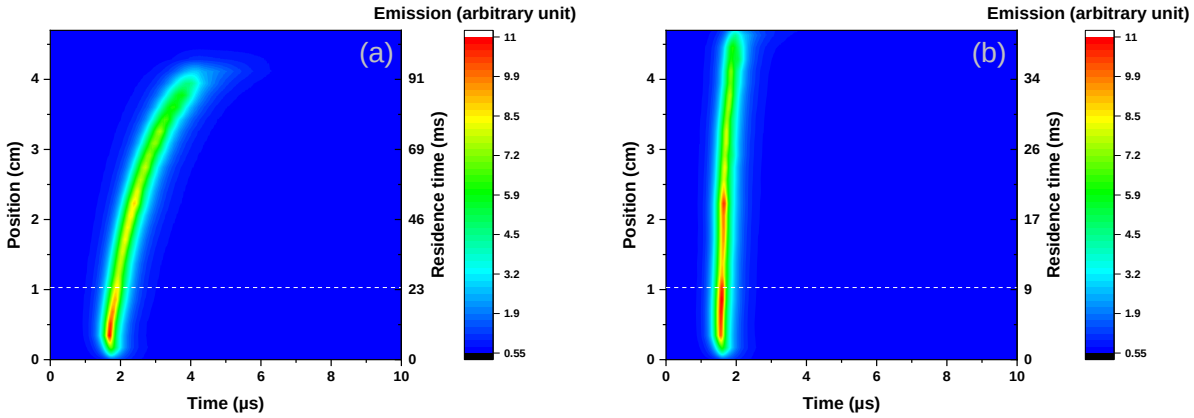

Figure 14. Variation of the light emission intensity (integrated over the 2 mm gap) as a function of position and time at (a) 110 and (b) 280 SCCM. Gas flow is directed from bottom to top. The scale in the position axis corresponds to the full electrode length. White dashed line present in (a) and (b) will be used in the figure 6.

Figure 11, and Figure 13 demonstrate that discharge behavior is highly dependent on the gas flow; however, Figure 14 highlights some common points between the discharges ignited at high and low flows. In both cases, the discharge is initiated at the inlet of the inter-electrode space and at nearly the same time (1.7 µs at 110 SCCM and 1.56 µs at 280 SCCM which corresponds to applied voltage values of 624 V and 578 V respectively). This indicates that for a given NH_3 density (at the discharge inlet, the NH_3 concentration is 215 ppm whatever the flow rate), the discharge ignites at the same value of the applied voltage, regardless of the flow rate The duration of the emission (i.e. duration of the discharge) at each position is also weakly dependent of the gas flow, except for stronger variations observed towards the end of the inter-electrode space. At this position, the emission lasts longer when the flow rate is low. As mentioned earlier, discharge extinction is induced by the locally accumulated dielectric charge on the electrode. When the local current is low, the charge accumulates slowly, resulting in prolonged discharge ignition and emission towards the end of the inter-electrode space at low gas flows. Such behavior may also be attributed to the decreasing applied voltage at this position.

Values of the time full width at half maximum (FWHM) were calculated from the light durations along the gas flow lines. The results are shown in Figure 15, at a given position, for the two examples presented in the Figure 14, in (a), and as a function of the spatial position for different flow rates, in (b). To avoid the complications associated with discharge extinction near the discharge space exit at low flow, the profiles are only analyzed in the range of 0–3 cm. As shown in the figure, the FWHM is larger at the plasma inlet due to the light spot explained previously by the square shape of the electrode. Then, whatever the flow rate a value of 0,35 µs is reached at

0,25cm. From this point the discharge the FWHM slightly increases for all flows, with greater increase observed at lower flow. The maximum difference between FWHM durations of emissions at 110 and 420 SCCM is 160 ns, i.e. an increase of 36 %.

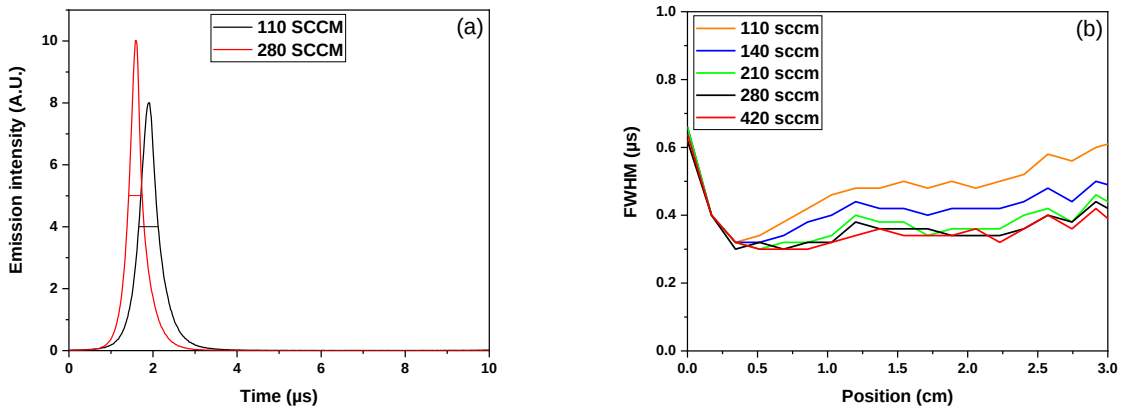

Figure 15. Emission intensity as a function of time at 1.03 cm after the discharge inlet (dashed white lines in figure 5 (a) and (b)), the FWHM is represented by red and black horizontals lines, respectively 319 and 461 ns (a) and values of the full width at half maximum (FWHM) calculated from the light durations along the gas flow lines. The results are shown as a function of position for various gas flow rates.

3.3 Time resolved measurements at a given position: Ar($1s_5$) metastable and H_2 emission

Measurements were made at 2.1 cm from the plasma inlet. The mean gas residence time in the plasma at this position depends on the gas velocity defined by the gas flow; for 110, 140, 210, 280 and 420 SCCM, this corresponds to gas residence times of 46, 36, 24, 18 and 12 ms respectively. The temporal evolution profiles of the Ar($1s_5$) number density and light emission are shown in Figure 16. However, Ar($1s_5$) density peaks slightly before the Ar emission intensities; this is partly

due to the time of spontaneous emission of Ar 2p states (at least a few tens of ns). Notably, greater delay (228 ns compared to 92 ns) between the two profiles is observed at lower gas flow rate. Indeed, when the flow decreases, the residence time of the gas in the discharge before reaching the measurement point increases, the quantity of NH_3 decreases, and thus, news mechanism are involved in the discharge, resulting in a more significant delay between the maxima of Ar($1s_5$) density and Ar emission. In agreement with a discharge breakdown increase when the gas flow decreases, both entities peak later in the discharge period when the flow is reduced from 280 to 110 SCCM. In addition, the maximum Ar($1s_5$) number density increases from $1.6*10^{16}$ to $2.1*10^{16}$ m^{-3}; such increase may be attributed to the decrease in NH_3 concentration due to the increased NH_3 dissociation, which leads to a reduced Ar(1s) consumption by Penning reactions and consequently, higher Ar(1s) populations (as shown previously, Ar($1s_5$) kinetics is representative of Ar(1s) kinetics in this type of discharges [35], [257]). The increased NH_3 dissociation also reduces the Penning contribution in the discharge ignition process, thereby increasing the "breakdown" voltage and delaying ignition. It should be noted that the term "breakdown" is used loosely here, since the discharge propagating through the inter-electrode space is already ignited. Nevertheless, the mechanisms involved in discharge propagation are similar to those implicated in breakdown, except that the medium is pre-ionized.

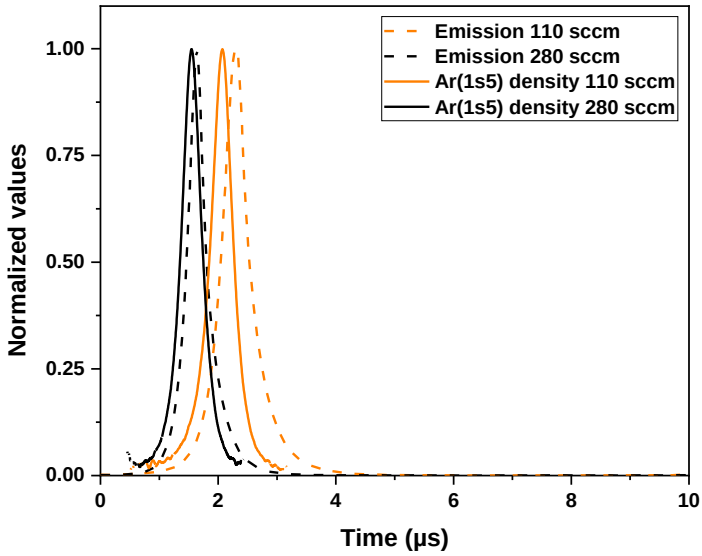

Figure 16. Temporal evolution of the normalized light emission (dotted lines) and Ar(1s5) number density (continuous lines) measured at 2.1 cm from the entrance of the discharge zone at 110 (orange) and 280 SCCM (black).

In line with the results presented in Figure 16, the intensity of the H_2(a) continuum emission is also probed at 2.1 cm from the entrance of the discharge at low and high gas flow rates; the results are presented in Figure 17. During discharge, the $H_2\left(a^3\Sigma_g^+\right)$ excited state responsible for the H_2 continuum emission is mostly populated by reaction of H_2 with Ar(1s) [229], [258]. At later time, as shown in a previous study [257], a more complex reaction pathway involving the recombination of vibrationally excited NH_3^+ with a low-energy electron dominates (the $NH_3^+(v)$ being created by a charge transfer from a Ar_2^+). As seen in Figure 17, when the gas flow is decreased from 280 to 110 SCCM, the intensity of H_2 emission increases, and it appears later in the discharge period. First, this seems consistent with the trend of the Ar($1s_5$) number density discussed above; however, greater increase in H_2 emission is observed. As previously mentioned, the H_2(a) state is populated via two mechanisms. Consequently, the increase of H_2 emission observed is probably the

combination of (i) an increase of Ar(1s) and H_2 density and (ii) an increase of Ar_2^+ or / and electron density. Notably, similar decays in H_2 emission are observed at both gas flows investigated herein, indicating that the decay mechanism remains fairly unchanged.

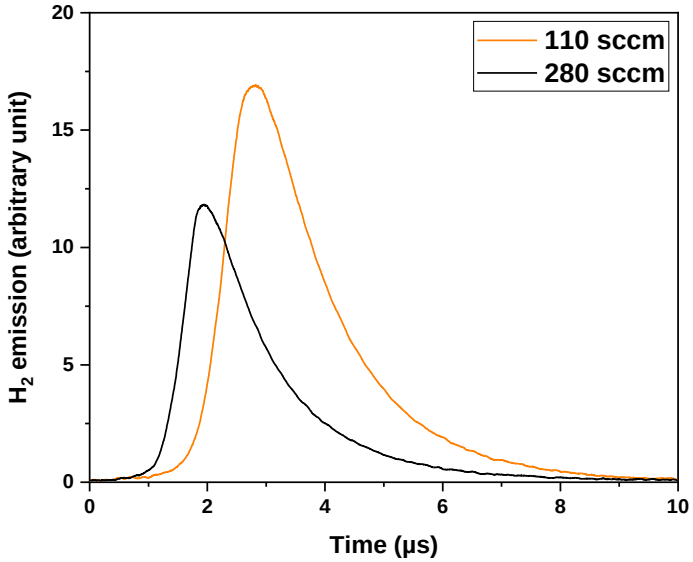

Figure 17. Temporal evolution of the H_2 emission measured at 2.1 cm from the entrance of the discharge space at 110 (orange) and 280 SCCM (black).

4. Discussion

The experimental results obtained in this study clearly demonstrate that the discharge current, Ar emission, Ar($1s_5$) density, and H_2 emission are modified upon changing the gas flow. In global measurements, the current and light emission amplitudes decreases with the gas flow due to a greater "localization" of the discharge near the entrance, with no further breakdown along the gas flow lines as shown by space-averaged optical emission. On a local scale, only small temporal

shifts in the populations of $Ar(1s_5)$, Ar(2p), and $H_2(a)$ states are observed, with values and trends comparable to those seen in the glow regime of low-frequency DBD operated in Penning Ar-NH_3 gas mixtures. For example, for $Ar(1s_5)$ densities, this shift between maximum densities between 280 and 110 sccm is about 520 ns. Numerical modelling was used to determine the correlation between these local variations and the local NH_3 concentration fraction. First, the time and amplitude of the $Ar(1s_5)$ density peaks at 110 and 280 SCCM were determined based on the experimental temporal evolution profiles recorded at these flow rates. Then, the delay and ratio between these peaks were calculated, and they were found to be 520 ns and 1.13, respectively. Knowing that such variation in Ar(1s) density in a Penning mixture is induced by variations in NH_3 fraction in Ar, a 1D fluid model developed and validated in previous studies was used to determine the NH_3 fraction leading 520 ns delay and 1.13 ratio between the Ar(1s) maxima by simulating the temporal evolution of this species at different concentration fractions of NH_3 (15, 20, 30, 40, 60, 80, 120, 150, 200, and 300 ppm). The obtained results reveal that ~520 ns delay is achieved when the ratio between the NH_3 density values is 2. On the other hand, the 1.13 ratio is only attained for the Ar(1s) density maxima produced at 15 and 30 ppm and at 20 and 40 ppm of NH_3. The first set of NH_3 populations (15 and 30 ppm) leads to Ar(1s) peak delay of 454 ns and a maxima ratio of 1.123, whereas the second set (20 and 40 ppm) leads to 476 ns delay and 1.237 ratio. Figure 18 compares the simulated Ar(1s) density profiles obtained at 15 and 30 ppm NH_3 with the experimental profiles measured at 110 and 280 SCCM. For the sake of comparison, the simulated densities are normalized relative to the maximum Ar(1s) density calculated at 30 ppm NH_3, whereas the experimental densities are normalized relative to the maximum density measured at 280 SCCM.

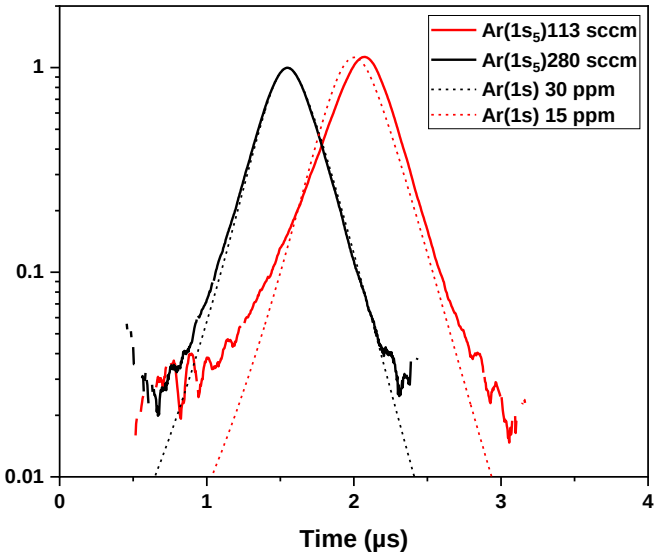

Figure 18. Normalized experimental Ar($1s_5$) density profiles (continuous lines) at 280 (black) and 110 SCCM (red), and normalized theoretical profiles (dashed lines) at 30 (black) and 15 ppm NH_3 (red).

As shown in the figure, the effect of gas flow rate on the population of Ar(1s) states at a specific position along the gas flow lines can be estimated by conducting simulations at different NH_3 densities. As mentioned earlier, the residence time at a given position changes upon adjusting the gas flow rate, leading to variations in NH_3 dissociation and density along the gas flow lines. According to the experimental and modeling results obtained herein, decreasing the NH_3 concentration fraction from 30 to 15 ppm has almost the same effect on Ar($1s_5$) density as increasing the residence time from 18 to 46 ms (values of the mean gas residence time, 2.1 cm after the discharge entrance for 280 and 110 SCCM respectively). However, this effect is not significant and the discharge is always a glow DBD, indicating that unlike discharge chemistry, the discharge physics is always that of a Penning mixture. Analysis of the rate of NH_3 dissociation in the discharge reveals that only 30 ppm of 215 ppm NH_3 initially introduced into the discharge zone

(i.e. 14% of the initial concentration) remain after a residence time of 18 ms. After 46 ms, the amount of NH_3 is reduced to 15 ppm (i.e. 7% of the initial concentration). This is consistent with the 40 ppm NH_3 density value estimated at 10 ms residence time in a previous work [35]. Therefore, the discharge remains in a diffuse regime (i.e. non filamentary discharge), even when as little as 7% of the initial NH_3 density remains in the gap (at 46 ms residence time). This highlights the fact that in a Penning mixture, the physical properties of an ignited discharge do not significantly change upon changing the gas flow rate or residence time. Even with 15 ppm of NH_3, the breakdown voltage of the glow discharge in the Ar-NH_3 Penning mixture is low enough compared to that of a filamentary discharge in Ar, to selectively obtained the diffuse regime. Even if 15 ppm of NH_3 is 7% of the initial concentration of NH_3 and this reduction increases the breakdown voltage, NH_3 density is still 4 order of magnitude larger than the metastable density.

Conclusion

The effect of gas flow rate on the properties of a 4.7-cm-long DBD operated in Ar-NH_3 Penning mixture was analyzed at the LF applied voltage of 1250 V using current-voltage characteristics, optical emission and absorption spectroscopy, as well as a 1D fluid modeling. In the experiments, the gas flowrate was varied between 70 and 420 SCCM, with greater emphasis on the 110 and 280 SCCM cases. At high gas flow, typical behavior of glow DBD at atmospheric pressure is observed, with discharge ignition as well as extinction occurring at the same times over the entire electrode surface. Meanwhile, at low gas flow, discharge breakdown initially occurs at the entrance of the inter-electrode zone only. As the applied voltage increases during the LF period, the discharge gradually extends from the entrance towards the outlet. This extension is slow enough to continue

after the extinction of the initial discharge due to locally accumulated dielectric charges. The discharge current and spatially integrated light emission are strongly affected by this behavior; however, the discharge remains a glow DBD, regardless of the gas flow. Considering that at a given position, the durations of Ar(2p) emission or Ar($1s_5$) number density at different flows are similar, the physical properties of the discharge (at least those associated with high-energy electrons) are only slightly affected by the flow rate. NH_3 consumption at long and short residence times is estimated using a 1D fluid model, based on the delay and ratio between the Ar($1s_5$) density peaks at 110 and 280 SCCM. According to this estimation, 14% of NH_3 remain in the discharge space after 18 ms, and 7% remain after 46 ms. Such decrease in NH_3 population induces an increase of Ar($1s_5$) form 1.6 to 2.1 10^{16} cm^{-3} and an increase of H_2 emission linked to enhanced Ar(1s) and H_2 densities on one hand and Ar_2^+ and electron densities on the other hand. The diffuse discharge is maintained, even when the initial NH_3 concentration is reduced to 7% (or less). Overall, this study demonstrates that the chemistry of a discharge has little impact on the discharge regime and local plasma properties if: (i) the adjuvant gas density at the entrance of the inter-electrode space is sufficiently high to allow for local diffuse breakdown and (ii) the gas flow is large enough to induce discharge propagation along the entire electrode surface during the period of increase in applied voltage.

Acknowledgments

The work carried out in Canada was funded by the National Science and Engineering Research Council (NSERC RGPIN-2018-04550) and by the Fondation Courtois. As for the one in France, it was supported by the Agence Nationale de la Recherche through the Investissement d'avenir

program (ANR10LABX2201). All authors would like to acknowledge the financial support of the CNRS and Université de Montréal through their contributions to the International Research Network on Controlled Multifunctional Nanomaterials.

Data availability statement

The data that support the findings of this study are available upon request from the authors.

Chapitre 6 – Conclusions et perspectives

Ce travail de doctorat visait à avoir une meilleure compréhension des décharges double fréquence RF-BF en mélange Penning Ar-NH_3 à la pression atmosphérique. Dans cette optique, certaines études ont été menées en double fréquence mais aussi en simple fréquence pour mettre en avant des phénomènes complexes à caractériser qu'il pourrait être intéressant d'approfondir dans le cas des décharges double fréquence. L'utilisation de différents moyens de caractérisation (électrique et d'émission ou d'absorption optique, résolue dans l'espace et / ou le temps) ont permis de confronter ces mesures avec les calculs obtenus via un modèle fluide 1D, adapté progressivement pour tenir compte des résultats expérimentaux. Cette conclusion se concentre sur les réalisations majeures de chaque chapitre de la thèse.

L'influence de l'émission secondaire induite par les photons VUV.

Dans un premier temps, des mesures de densités d'Ar($1s_3$) dans une DBD basse fréquence ainsi qu'en double fréquence (à partir d'absorption optique), ont été comparées avec les densités d'Ar(1s) calculées par le modèle fluide 1D utilisé dans [50]. Les résultats de cette comparaison ont révélé une cinétique des Ar(1s) calculée bien plus lente que celle des Ar($1s_3$) mesurée (autant en basse fréquence qu'en double fréquence). La nécessité de mécanismes rapides, (pour augmenter les pentes de croissance ET de décroissance de densité d'Ar(1s)), ainsi que l'étude approfondie du modèle nous ont dirigé vers la prise en compte de la création de photons VUV, issus de la désexcitation des Ar_2^* (formés préalablement par une réaction à trois corps avec un Ar(1s) et non réabsorbés dans la décharge). La création de ces Ar_2^* et l'émission des photons VUV induite, introduit une consommation des Ar(1s) ainsi qu'une production d'électrons secondaires aux parois, augmentant ainsi la vitesse de création et de pertes des Ar(1s). Ces réactions ont été rajoutées dans le modèle, en utilisant les taux de réactions trouvés dans la littérature pour la création des Ar_2^* et pour l'émission spontanée des photons issu de la désexcitation de ce niveau. Les résultats de ces calculs sur la cinétique des Ar(1s) sont vraiment convainquant et permettent

d'approcher la cinétique des Ar($1s_3$) expérimentale que ce soit concernant la décharge basse fréquence ou la double fréquence. Enfin, l'introduction de ces photons VUV amène à redéfinir un critère d'auto-entretien pour prendre en compte l'impact de ces photons sur l'émission secondaire. Ce critère a permis, en outre, de mettre en lumière le rôle prépondérant des photons VUV sur le passage au régime gamma d'une décharge double fréquence, par rapport à celui des ions.

Influence de la tension RF sur les propriétés fondamentales d'une DBD double fréquence

Cette deuxième étude fait suite à l'étude menée par Magnan et al. [50] concernant l'effet de l'amplitude de la tension basse fréquence sur une DBD double fréquence en Ar-NH_3 à la pression atmosphérique. Ici, le sujet est l'influence de la tension RF sur les propriétés spatio-temporelles de la décharge double fréquence en mode α-γ. Pour caractériser ces décharges, des mesures électriques ainsi que des cartographies résolues dans l'espace et le temps à 750 nm (émission liée à la transition Ar $2p_1 \rightarrow 1s_2$) et 500 nm (émission liée au bremsstrahlung), et les densités d'Ar($1s_3$) sont utilisées. Lors de la variation de l'amplitude de la tension RF de la décharge double fréquence, les variations dans l'émission d'Ar à 750 nm et dans les densités d'Ar($1s_3$) sont reliées à des variations de densités d'électrons énergétiques alors que les variations sur l'émission à 500 nm sont liées principalement à une variation de densité électronique. On trouve alors qu'avec une augmentation de la tension RF, l'intensité maximale de l'émission d'Ar 750 nm ainsi que la densité d'Ar($1s_3$) maximale diminuent alors que l'amplitude de l'émission du continuum augmente quasiment en tout points. Ces mesures renseignant sur les variations des propriétés fondamentales du plasma en fonction de la variation de l'amplitude de la tension RF, on utilise le modèle fluide précédemment modifié pour sonder la source de ces variations. On comprend alors qu'une augmentation de la tension RF, conduit à un accroissement des densités d'ions et d'électrons dans le *bulk* du plasma (lié à une augmentation de l'amplitude des variations RF de la tension gaz), expliquant l'augmentation globale de l'intensité de l'émission du continuum. Ceci à pour effet de faciliter la transition vers le régime γ de la double fréquence et donc de diminuer la

tension gaz maximale. Une plus faible tension appliquée induit une zone de fort champ électrique (la gaine cathodique) moins importante entrainant une diminution de la zone spatio-temporelle où les électrons fortement énergétiques sont créés et donc diminue la contribution des réactions nécessitant ces électrons (notamment l'excitation de niveaux tels que $Ar(1s_3)$ ou $Ar(2p_5)$). L'augmentation de l'amplitude de la tension RF entraine donc une augmentation de l'amplitude de la tension gaz, mais une diminution de sa valeur maximale, expliquant les observations sur les émissions à 750 et 500 nm et la densité d'$Ar(1s_3)$.

Rôle de la gaine cathodique basse fréquence sur le transport des particules chargées d'une décharge double fréquence en mode γ

L'objectif ici est de comprendre l'origine de la forte dissymétrie observée sur le courant pendant le régime γ entre les alternances positives et négatives de la tension RF et donc comprendre les différents phénomènes de transport des particules chargées dans le gap d'une décharge double fréquence en présence d'une gaine cathodique basse fréquence. Pour cela, les cartographies spatio-temporelles mises en place pour l'article 2 ainsi que le modèle fluide sont étudiés plus en détails autour de la transition vers le régime γ. Il en ressort, à l'image des émissions à 750 et 500 nm, 2 comportement distinct suivant que l'on s'intéresse à la gaine ou au *bulk*. Les variations temporelles de la gaine cathodique BF sont contrôlées (dans une large mesure) par la tension BF (la tension RF engendrant uniquement de légères variations de longueur de cette gaine) alors que les variations temporelles dans le *bulk* et à l'anode BF, sont contrôlées par la tension RF. Ce comportement s'explique par l'implication de deux phénomènes (i) l'amplitude de la tension BF appliquée est bien plus importante que celle de la tension RF induisant une forte gaine BF (ii) les variations de la longueur de la gaine BF (lié à l'amplitude de la tension RF) induisent une forte densité ionique en bordure de gaine forçant le champ électrique du *bulk* à se déformer (et donc à s'opposer à celui de la gaine) pour maintenir la quasi-neutralité dans l'ensemble du gap (i.e. les électrons du *bulk* et de la gaine sont dérivent vers la bordure de gaine). Dans une double fréquence, le champ électrique dans la gaine est dirigé vers l'anode, alors qu'il y a une alternance du champ électrique dans le reste du gap à l'échelle RF entre un champ électrique

dirigé vers l'anode et vers la cathode. Dans le premier cas, les électrons de la gaine dérivent jusqu'à l'anode et le courant est élevé, dans le deuxième, ils sont piégés en bordure de gaine et le courant est plus faible. L'analyse des mécanismes de transport dans une décharge double fréquence en régime γ explique donc la dissymétrie observée sur le courant ainsi que les comportements des particules chargées pendant cette période.

Physico-chimie dans une décharge glow basse fréquence en mélange Penning Ar-NH_3

La présence d'un mélange Penning induit une dissociation du NH_3 et la présence de ses sous-produits dans une décharge en Ar-NH_3. Dans cette dernière partie, l'étude se porte sur la dissociation du NH_3 et son impact sur la physique de la décharge glow basse fréquence en Ar-NH_3.

Dans un premier temps, l'analyse du spectre d'émission de la décharge souligne une émission d'un continuum d'émission dans les VUV-UV provenant d'une désexcitation d'un état excité de H_2, $H_2(a)$. Cette émission intervient pendant la décharge et se maintient longtemps après l'extinction de la décharge (avec une décroissance bien plus lente que celle des autres émissions). Pour comprendre cette lente décroissance, on doit décrire la population de l'état $H_2(a)$. Un premier mécanisme, majoritairement présent pendant la décharge est dû à l'interaction entre un Ar(1s) et un H_2, créant cet état excité $H_2(a)$. Ce mécanisme, reporté dans la littérature, explique la croissance du continuum en début de décharge mais entraine une décroissance de cet état beaucoup plus rapide que ce qui est mesuré. Il ne permet donc pas d'expliquer la décroissance du continuum en fin de décharge. Pour expliquer la lente décroissance de l'émission, un autre mécanisme, non reporté dans la littérature est proposé : via un transfert de charge de Ar_2^+ vers NH_3, un état excité vibrationnellement de NH_3^+ serait créé ; en se recombinant avec un électron, cet état excité de NH_3^+ pourrait se dissocier, formant potentiellement un état $H_2(a)$. Ce chemin réactionnel hypothétique a été ajouté au modèle fluide précédemment utilisé permettant alors de bien décrire la décroissance de l'émission issue de $H_2(a)$; semblant valider l'hypothèse précédemment proposée. Cette étude concernant le rôle de la dissociation de NH_3 dans l'apparition de sous produits a été menée en un point de la décharge. La seconde étape est de

s'intéresser à l'effet du temps de résidence du gaz dans la décharge, autrement dit s'intéresser au rôle des sous produits de NH_3 sur la décharge le long de l'électrode.

La décharge est donc étudiée en fonction du flux de gaz / du temps de résidence. Lorsque le flux est élevé on obtient un comportement typique d'une décharge glow à la pression atmosphérique. Cependant, en diminuant le flux de gaz, on allonge le temps de résidence du gaz dans la décharge, le NH_3 est alors davantage dissocié. Ce phénomène entraine une localisation de l'allumage de la décharge en entrée d'électrodes (là où la quantité de NH_3 est la plus grande), puis en fonction du temps, avec l'augmentation de la tension appliquée, la décharge « glisse » vers la sortie des électrodes. Ceci est dû à la charge locale des diélectriques, où la décharge s'est initialement allumée qui conduit à l'extinction de la décharge alors que l'augmentation de la tension appliquée sur l'ensemble des électrodes amène à un possible claquage dans des zones avec des quantités plus faible de NH_3. Dans ce cas là, le régime de décharge reste diffus, la physique n'est que peu modifiée mais la décharge n'est pas allumée sur l'ensemble de l'électrode. Via une mesure de densité d'Ar($1s_5$) en fonction du temps à deux temps de résidence connu et au modèle fluide 1D modifié précédemment, il a été possible de calculer le taux de dissociation en fonction du temps (considérant 215 ppm de NH_3 en entrée de décharge, il reste 30 ppm après 18 ms de temps de résidence et 15 ppm après 46 ms) ; Ces résultats sont en accord avec le taux de dissociation estimé, utilisé dans le premier article, c'est-à-dire avec une configuration de décharge et un taux initial de NH_3 différents. Malgré une dissociation importante du NH_3, la physique de la décharge en un point donné est quasiment inchangée, ce qui s'explique par l'allumage en entrée de décharge et la propagation de la décharge diffuse, empêchant des décharges filamentaires d'apparaitre.

Conclusion générale

Cette thèse nous a amené à mettre en place des outils de caractérisation spécifiques comme la mesure du continuum de $H_2(a)$ à 204 nm et la spectroscopie d'émission résolue spatialement à une échelle de 77 µm et temporellement à l'échelle de la RF (7 ns) sur un cycle de 20 µs. Elle nous a aussi amené à raffiner le modèle fluide 1D tout en continuant à minimiser le nombre d'espèces (12) et de réactions (15). Ainsi, nous avons montré l'importance de rajouter la production de photons VUV par désexcitation des excimères et la photoémission induite pour reproduire la cinétique des Ar^*. Nous avons aussi montré l'importance de la recombinaison des ions NH_3^+ comme source d'énergie pendant la post-décharge. Grâce à un fort couplage entre expérience et modélisation, cette thèse apporte une meilleure compréhension des mécanismes à l'œuvre dans une décharge Ar-NH_3, en basse fréquence et double fréquence BF-RF. Il a ainsi été possible de remonter aux propriétés fondamentales de la décharge et d'étudier les chemins réactionnels présents. Outre la forte influence des photons VUV dans les DBD basse fréquence et RF-BF en mode γ en Ar-NH3, elle a permis de comprendre l'effet de l'amplitude de la tension RF sur une décharge double fréquence RF-BF. Lors de l'augmentation de l'amplitude de la tension RF, la densité du plasma croit durant du mode RF α, diminuant la tension gaz nécessaire au passage en mode γ et donc la valeur maximale de la tension gaz. Ainsi, la densité d'électrons augmente, alors que la densité des espèces peuplées par des électrons de haute énergie (Ar(1s) et Ar(2p)) décroit. En s'intéressant plus en détail à l'influence des oscillations RF de la gaine cathodique, on s'aperçoit que ce sont celles-ci qui expliquent la dissymétrie observée sur le courant autour du mode γ. Le champ électrique basse fréquence associé, dicte ainsi le transport des particules chargées dans la gaine alors que ce sont les variations du champ électrique à l'échelle de la RF qui sont responsables du transport dans le bulk. Enfin, la dissociation de NH_3 dans une décharge Ar-NH_3 a été examinée à travers l'étude des sous-produits de NH_3 par spectroscopie d'émission, en particulier une émission due à la désexcitation de $H_2(a)$, observée à 204 nm. Pour expliquer l'évolution de cette émission, un nouveau chemin réactionnel est proposé puis injecté dans le modèle. A l'aide de ce même modèle, le degré de dissociation du NH_3 est estimé et des mesures de l'émission en fonction du temps de résidence amènent une compréhension sur la physique de la propagation de la décharge homogène le long des lignes de flux.

Perspectives concernant les photons VUV :

L'article 1 s'est concentré sur l'effet des photons VUV (notamment à 126 nm) sur la physique des DBDs en Ar-NH_3, notamment sur le rôle de ces photons sur le passage en régime γ. Dans de l'air à la pression atmosphérique, de tels photons sont très rapidement absorbés par le dioxygène présent dans l'air. Malgré de nombreuse tentatives pour s'affranchir de cette absorption, le montage expérimental ne nous a pas permis d'obtenir une atmosphère pleinement contrôlée entre la décharge et le monochromateur VUV utilisé dans les articles 4 et 5. Une mesure de ces photons issus de la désexcitation des Ar2* a pu être tentée en créant une chambre en surpression d'argon autour du tube à décharge et de la fenêtre du monochromateur. Cette chambre, non hermétique, semble réduire le dioxygène présent dans les 1.2 cm séparant la décharge de la fenêtre du monochromateur mais ne supprime pas complètement son absorption. Pour illustrer nos résultats préliminaires, la Figure 23. – montre l'évolution temporelle du signal optique enregistrée par le monochromateur VUV-UV dans les mêmes conditions que celles de l'article 4. Ici, un amplificateur (HP, 8447D) a été placé après le photomultiplicateur pour maximiser le signal. Malgré cela, le rapport signal sur bruit est assez faible.

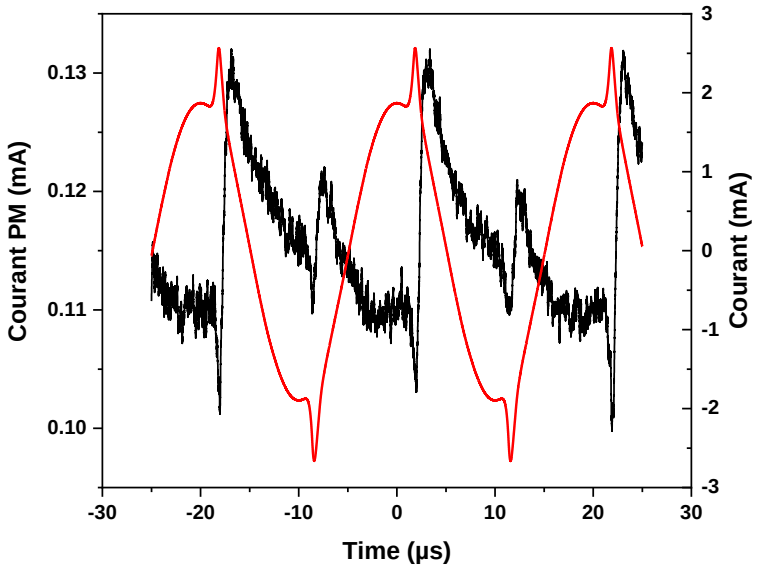

Figure 23. – Émission à 126 nm (en noir) et courant mesuré (en rouge) en fonction du temps (les conditions opératoires sont les même que celles dans l'article 4).

Comme le montre la Figure 23. – , cette mesure apporte une preuve que de tels photons sont effectivement émis par une DBD *glow* BF en Ar-NH_3 ; cependant, leur utilisation pour une quelconque autre interprétation est complexe dû à la qualité de la mesure. En particulier la réponse temporelle du photomultiplicateur semble avoir été augmentée par l'amplificateur. En développant un meilleur système sous vide ou en surpression, et en optimisant le système de détection par exemple en ayant recours au mode de comptage de photons, il devrait être possible de mesurer ces photons avec plus de précision en fonction du temps. De plus, en créant un tube avec les 4 parois en MgF_2 et en le comparant avec celui utilisé dans les études précédentes (parois latérales en MgF_2 et parois horizontales en silice fondue) il devrait être possible de voir l'impact de ces photons VUV sur les caractéristiques électriques et donc sur la physique de la décharge.

Perspectives concernant la caractérisation de décharges émettant un bremsstrahlung :

Dans les articles 2 et 3, les émissions d'Ar (à 750 nm) et du continuum (à 500 nm) résolues dans l'espace inter-électrode et le temps ont été utilisées pour avoir un aperçu des propriétés fondamentales de la décharge double fréquence. Dans ce cadre, les émissions résolues dans l'espace et le temps ont aussi été mesurées pour différentes longueurs d'onde, que ce soit pour les émissions d'Ar (696, 750, 763 et 811 nm) ou pour les émissions du bremsstrahlung (400, 430, 500, 600 et 680 nm). Il est alors pertinent de s'intéresser aux rapport de longueurs d'ondes pour essayer de calculer des propriétés fondamentales du plasma. A cause des différences dans les valeurs du coefficient d'Einstein pour l'émission spontanée des raies d'Ar (entre 22 et 156 ns) et du fait que ces valeurs sont voisines de la période d'oscillation du champ RF (200 ns à 5 MHz), les rapports spatio-temporel de ces raies ne sont pas facilement exploitables (de même pour les rapports d'émission du continuum / émission d'Ar). Les rapports de continuum semblent

néanmoins intéressants pour remonter à la température électronique. En effet, l'émissivité du continuum ϵ_{ea} [24], [82] dépend de la densité du gaz (n_a), de la densité électronique (n_e) et de la température électronique (T_e) à travers la fonction de distribution en énergie des électrons, généralement considérée Maxwellienne [82], [85], [259] :

$$\epsilon_{ea} = C_{ea}\frac{n_e n_a}{\lambda^2}\frac{1}{(kT_e)^{\frac{3}{2}}}\int_{\frac{hc}{\lambda}}^{\infty} Q_{ea}^{mom}(E)\left(1-\frac{hc}{2\lambda E}\right)\times\sqrt{1-\frac{hc}{\lambda E}}\,e^{-\frac{E}{kT_e}}E^2 dE \qquad (1)$$

où

$$C_{ea} = \frac{4\sqrt{2}}{3\pi^{\frac{5}{2}}}\frac{\alpha h}{m_e^{\frac{3}{2}}c} \qquad (2)$$

et

$$Q_{ea}^{mom} = 8.05e^{-28.024E(eV)} + 0.99E(eV)^{1.743}e^{-0.136E(eV)}\ [\text{Å}^2] \qquad (3)$$

Ici, $\frac{hc}{\lambda}$, E, c, λ, k, m_e, α, sont l'énergie du photon émis, l'énergie de l'électron, la vitesse de la lumière, la longueur d'onde du photon, la constante de Boltzmann, la masse de l'électron et la structure fine de l'atome neutre, respectivement [82].

En calculant un rapport de continuum mesuré à deux longueurs d'ondes différentes, on s'affranchit de la dépendance en n_e, en n_{gas} et on obtient une fonction qui ne dépend que de T_e. Comme la fonction de réponse du système optique utilisé pour les mesures n'a pas été déterminé avec précision, le rapport de continuum ne fournit qu'une information sur une variation relative de Te et non sur valeur absolue de la température électronique. La Figure 24. – (a) présente les variations relative de la température électronique autour du mode γ calculée à partir de rapport du continuum à 400 et 500 nm.

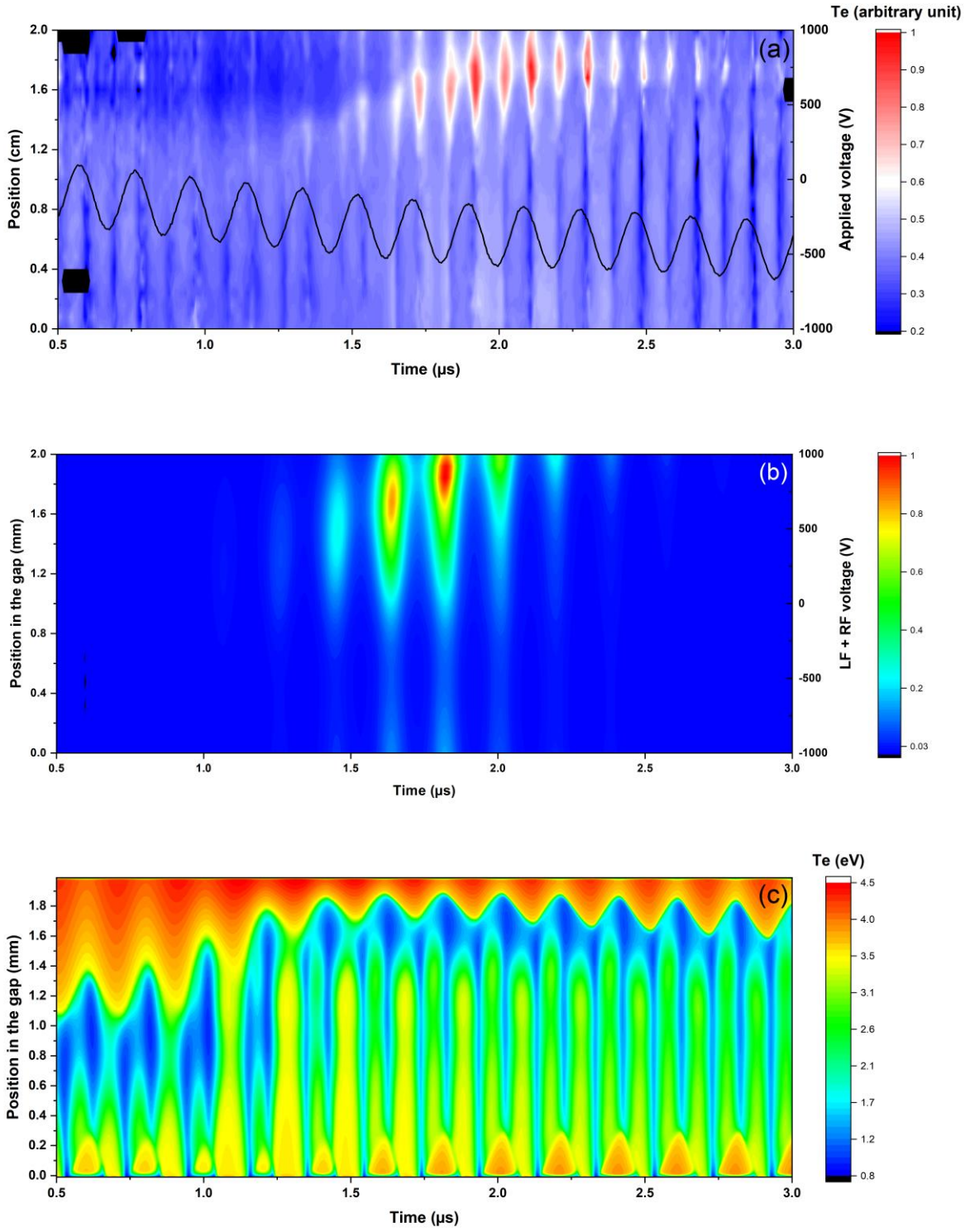
(a)
Te (arbitrary unit)
Position (cm)
Applied voltage (V)
Time (μs)
(b)
Position in the gap (mm)
LF + RF voltage (V)
Time (μs)
(c)
Te (eV)
Position in the gap (mm)
Time (μs)

Figure 24. – Variations relatives de la température électronique calculée entre 0.5 et 3 µs à partir de mesures du continuum enregistrées à 400 et 500 nm (a), émission d'Ar 750 nm (b), température électronique calculée par le modèle fluide (c). Les conditions opératoires sont celles de l'article 3.

Comme le montre la Figure 24. – , les variations spatio-temporelles de la température électronique, obtenues à partir des rapport d'émission du bremsstrahlung, sont très similaires à celles de l'émission d'Ar 750 nm, Figure 24. – (b), liée à la population d'électron énergétiques. On retrouve, comme attendu sur une cartographie de la température électronique, obtenue du modèle fluide Figure 24. – (c), une forte température électronique proche de l'électrode supérieure, i.e. dans la gaine cathodique. La contraction de la gaine cathodique ainsi que l'augmentation de la température électronique une période sur deux à l'anode sont aussi visibles. Malgré ces similarités avec ce qui est observé expérimentalement sur l'émission d'Ar à 750 nm ou avec la température électronique issue du modèle, quelques éléments posent question, par exemple, pourquoi dans la gaine, avant la contraction, la température électronique est faible ? Pourquoi le maximum de T_e à l'anode n'est pas synchronisé avec celui à la cathode ? Ces questions nécessiteraient des études complémentaires sur des rapports de bremsstrahlung qui n'ont pu être réalisées durant cette thèse. Cet outil de caractérisation semble un moyen robuste pour remonter simplement à la température électronique résolue dans l'espace et le temps ; les seuls prérequis sont de poser l'hypothèse d'une distribution maxwellienne, de s'assurer que l'émission aux longueurs d'onde considérées sont uniquement due au bremsstrahlung et que les signaux des différentes longueurs d'onde du bremsstrahlung aux différentes longueurs d'ondes sont correctement synchronisées.

Perspectives concernant la physico-chimie de la décharges glow basse fréquence :

Les articles 4 et 5 ont mis en évidence les variations de physico-chimie via la dissociation du NH_3 dans une décharge en mélange Penning. Dans ce contexte, un modèle fluide 1D a été utilisé pour déterminer le taux de dissociation du NH_3 en fonction du temps de résidence. Cependant, on s'aperçoit rapidement qu'un modèle fluide 1D est assez limité lorsqu'il s'agit de décrire la cinétique chimique dans un réacteur, c'est-à-dire à l'échelle de temps du temps de résidence des espèces moléculaires dans le plasma. Dans le cas du mélange Ar-NH_3, le paramètre ajustable est la quantité de NH_3 que l'on doit fixer pour simuler le comportement de la décharge à un endroit / temps de résidence donné. On néglige alors l'accumulation des sous produits du NH_3 présents dans la décharge. Par exemple, comme énoncé dans l'article 4, à cause de la nécessité d'avoir une densité de H_2 connue, l'émission issue de la désexcitation de $H_2(a)$, formé par collision de Ar^* avec H_2, ne peut être fidèlement reproduite. Il en est de même pour toutes les autres réactions impliquant des sous-produits issus de la dissociation du NH_3. On comprend alors aisément l'intérêt de développer un modèle fluide 2D qui permettrait d'obtenir l'évolution des densités des différentes espèces en fonction du temps de résidence (comme un modèle fluide 0D), mais aussi l'impact de l'évolution de ces densités sur la physique de la décharge. Ceci est d'autant plus intéressant que NH_3 et H_2 sont d'un grand intérêt pour différentes applications notamment en agriculture [200]–[203] ou pour le stockage d'énergie [204]–[210].

De même, Desjardins et al. ont étudié un modèle collisionnel radiatif de l'Argon pour déterminer n_e, T_e et la densité d'Ar(1s) d'une décharge en Ar-NH_3 en un point [77]. A la vue des éléments présentés précédemment, ces valeurs peuvent fluctuer en fonction de la position. Il pourrait alors être intéressant de sonder différents points de la décharge afin de confronter les résultats d'un modèle fluide 2D aux températures et densités électroniques calculées par le modèle collisionnel radiatif.

Cette étude en Ar-NH_3 à basse fréquence, pourrait être menée sur des décharge en régime diffus dans d'autres mélange Penning, afin de vérifier si le comportement décrit dans l'article 5 se généralise à tous les mélange Penning. Plus globalement, l'étude pourrait être étendue à des

décharges avec des précurseurs de dépôt afin de mieux appréhender l'effet de la dissociation du précurseur sur la physique de la décharge.

Enfin, après avoir mis en évidence ce phénomène en décharge glow basse fréquence à la pression atmosphérique, on peut chercher à poursuivre cette étude sur une décharge double fréquence afin de caractériser cette dissociation avec un régime α assez indépendant de la nature du gaz et un régime γ, plus sensible à la chimie.

Références bibliographiques

[1] A. Fridman, A. Chirokov, and A. Gutsol, “Non-thermal atmospheric pressure discharges,” *J. Phys. D. Appl. Phys.*, vol. 38, no. 2, pp. R1–R24, 2005.

[2] N. Gherardi and F. Massines, “Mechanisms controlling the transition from glow silent discharge to streamer discharge in nitrogen,” *IEEE Trans. Plasma Sci.*, vol. 29, no. 3, pp. 536–544, 2001.

[3] L. Bárdos and H. Baránková, “Cold atmospheric plasma: Sources, processes, and applications,” *Thin Solid Films*, vol. 518, no. 23, pp. 6705–6713, 2010.

[4] F. Massines and G. Gouda, “A comparison of polypropylene-surface treatment by filamentary, homogeneous and glow discharges in helium at atmospheric pressure,” *J. Phys. D. Appl. Phys.*, vol. 31, no. 24, pp. 3411–3420, 1998.

[5] W. Siemens, “Ueber die elektrostatische Induction und die Verzogerung des Stroms in Flaschendrahten,” 1857.

[6] F. Massines, A. Rabehi, P. Decomps, R. Ben Gadri, P. Ségur, and C. Mayoux, “Experimental and theoretical study of a glow discharge at atmospheric pressure controlled by dielectric barrier,” *J. Appl. Phys.*, vol. 83, no. 6, pp. 2950–2957, 1998.

[7] V. A. Engel, S. M, and R. Steenbeck, “Über die Glimmentladung bei hohen Drucken,” *Zeitschrift für Phys.*, vol. 144, no. 4, pp. 144–160, 1933.

[8] R. Bartnikas, “Note on ac discharges between metallic-dielectric electrodes in helium,” *J. Appl. Phys.*, vol. 40, no. 4, pp. 1974–1976, 1969.

[9] S. Kanazawa, M. Kogoma, T. Moriwaki, and S. Okazaki, “Stable glow plasma at atmospheric pressure,” *J. Phys. D. Appl. Phys.*, vol. 21, no. 5, pp. 838–840, 1988.

[10] T. Yokoyama, M. Kogoma, T. Moriwaki, and S. Okazaki, “The mechanism of the stabilisation of glow plasma at atmospheric pressure,” *J. Phys. D. Appl. Phys.*, vol. 23, no. 8, pp. 1125–

1128, 1990.

[11] F. Massines, P. Ségur, N. Gherardi, C. Khamphan, and A. Ricard, “Physics and chemistry in a glow dielectric barrier discharge at atmospheric pressure: diagnostics and modelling,” *Surf. Coatings Technol.*, vol. 97, no. 1, pp. 719–722, Sep. 2003.

[12] J. I. Amalvy, M. J. Percy, S. P. Armes, and H. Wiese, “Synthesis and characterization of novel film-forming vinyl polymer/silica colloidal nanocomposites,” *Langmuir*, vol. 17, no. 16, pp. 4770–4778, 2001.

[13] H. M. Xiong, X. Zhao, and J. S. Chen, “New polymer-inorganic nanocomposites: PEO-ZnO and PEO-ZnO-LiClO4 films,” *J. Phys. Chem. B*, vol. 105, no. 42, pp. 10169–10174, 2001.

[14] J. B. Chemin *et al.*, “Transparent anti-fogging and self-cleaning TiO2/SiO2 thin films on polymer substrates using atmospheric plasma,” *Sci. Rep.*, vol. 8, no. 1, pp. 1–8, 2018.

[15] S. Y. Moon, J. Han, and W. Choe, “Control of radio-frequency atmospheric pressure argon plasma characteristics by helium gas mixing,” *Phys. Plasmas*, vol. 13, no. 1, pp. 1–4, 2006.

[16] Y. Matsushita, F. Tochirubo, S. Uchida, and T. Watanabe, “Influence of penning ionization on glowlike dielectric barrier discharge formation in medium-pressure Ar,” *Japanese J. Appl. Physics, Part 1 Regul. Pap. Short Notes Rev. Pap.*, vol. 46, no. 10 A, pp. 6817–6821, 2007.

[17] T. Martens, A. Bogaerts, W. J. M. Brok, and J. V. Dijk, “The dominant role of impurities in the composition of high pressure noble gas plasmas noble gas plasmas,” *Appl. Phys. Lett.*, vol. 041504, no. February 2008, pp. 1–4, 2008.

[18] J. Vallade and F. Massines, “Fourier-transformed infrared absorption spectroscopy: A tool to characterize the chemical composition of Ar-NH3-SiH4 dielectric barrier discharge,” *J. Phys. D. Appl. Phys.*, vol. 46, no. 46, pp. 1–7, 2013.

[19] F. Massines, C. Sarra-Bournet, F. Fanelli, N. Naudé, and N. Gherardi, “Atmospheric pressure low temperature direct plasma technology: Status and challenges for thin film deposition,” *Plasma Process. Polym.*, vol. 9, no. 11–12, pp. 1041–1073, 2012.

[20] I. Enache, H. Caquineau, N. Gherardi, T. Paulmier, L. Maechler, and F. Massines, “Transport phenomena in an atmospheric-pressure townsend discharge fed by N2/N2O/HMDSO mixtures,” *Plasma Process. Polym.*, vol. 4, no. 9, pp. 806–814, Nov. 2007.

[21] R. Bazinette, R. Subileau, J. Paillol, and F. Massines, “Identification of the different diffuse dielectric barrier discharges obtained between 50kHz to 9MHz in Ar/NH3 at atmospheric pressure,” *Plasma Sources Sci. Technol.*, vol. 23, no. 3, p. 035008, 2014.

[22] J. S. Boisvert, L. Stafford, N. Naudé, J. Margot, and F. Massines, “Electron density and temperature in an atmospheric-pressure helium diffuse dielectric barrier discharge from kHz to MHz,” *Plasma Sources Sci. Technol.*, vol. 27, no. 3, p. 035005, 2018.

[23] J. S. Boisvert, J. Margot, and F. Massines, “Transitions between various diffuse discharge modes in atmospheric-pressure helium in the medium-frequency range,” *J. Phys. D. Appl. Phys.*, vol. 49, no. 32, p. 325201, 2016.

[24] R. Bazinette, J. Paillol, and F. Massines, “Optical emission spectroscopy of glow, Townsend-like and radiofrequency DBDs in an Ar/NH3 mixture,” *Plasma Sources Sci. Technol.*, vol. 24, no. 5, p. 55021, 2015.

[25] R. Bazinette, J. Paillol, and F. Massines, “Transition from Townsend to radio-frequency homogeneous dielectric barrier discharge in a roll-to-roll configuration,” *J. Appl. Phys.*, vol. 119, no. 24, p. 243304, Jun. 2016.

[26] F. Massines *et al.*, “Hydrogenated Silicon Nitride SiNx:H Deposited by Dielectric Barrier Discharge for Photovoltaics,” *Plasma Process. Polym.*, vol. 13, no. 1, pp. 170–183, 2016.

[27] R. Bazinette, J. F. Lelièvre, L. Gaudy, and F. Massines, “Influence of the Discharge Mode on the Optical and Passivation Properties of SiNx:H Deposited by PECVD at Atmospheric Pressure,” *Energy Procedia*, vol. 92, pp. 309–316, 2016.

[28] J. Profili *et al.*, “Interaction of atomized colloid with an ac electric field in a dielectric barrier discharge reactor used for deposition of nanocomposite coatings,” *J. Phys. D. Appl. Phys.*, vol. 50, no. 7, p. 075201, Feb. 2017.

[29] P. Brunet, R. Rincón, Z. Matouk, M. Chaker, and F. Massines, “Tailored Waveform of Dielectric Barrier Discharge to Control Composite Thin Film Morphology,” *Langmuir*, vol. 34, no. 5, pp. 1865–1872, 2018.

[30] J. Profili, O. Levasseur, N. Naudé, C. Chaneac, L. Stafford, and N. Gherardi, “Influence of the voltage waveform during nanocomposite layer deposition by aerosol-assisted atmospheric pressure Townsend discharge,” *J. Appl. Phys.*, vol. 120, no. 5, p. 053302, 2016.

[31] P. Brunet *et al.*, “Control of composite thin film made in an Ar/isopropanol/TiO2 nanoparticles dielectric barrier discharge by the excitation frequency,” *Plasma Process. Polym.*, vol. 14, no. 12, 2017.

[32] R. Bazinette, J. Paillol, J. F. Lelièvre, and F. Massines, “Atmospheric Pressure Radio-Frequency DBD Deposition of Dense Silicon Dioxide Thin Film,” *Plasma Process. Polym.*, vol. 13, no. 10, pp. 1015–1024, 2016.

[33] E. Nadal, N. Milaniak, H. Glenat, G. Laroche, and F. Massines, “A new approach for synthesizing plasmonic polymer nanocomposite thin films by combining a gold salt aerosol and an atmospheric pressure low-temperature plasma.,” *Nanotechnology*, vol. 32, no. 17, pp. 1–10, 2021.

[34] J. Vallade, R. Bazinette, L. Gaudy, and F. Massines, “Effect of glow DBD modulation on gas and thin film chemical composition: Case of Ar/SiH4/NH3 mixture,” *J. Phys. D. Appl. Phys.*, vol. 47, no. 22, p. 224006, Jun. 2014.

[35] R. Robert, G. Hagelaar, N. Sadeghi, R. Magnan, L. Stafford, and F. Massines, “Role of excimer formation and induced photoemission on the Ar metastable kinetics in atmospheric pressure Ar-NH3 dielectric barrier discharges,” *Plasma Sources Sci. Technol.*, vol. 31, no. 6, p. 065010, 2022.

[36] S. K. Dhali and P. F. Williams, “Two-dimensional studies of streamers in gases,” *J. Appl. Phys.*, vol. 62, no. 12, pp. 4696–4707, 1987.

[37] Y. P. Raizer, *Gas discharge physics*. Moscow: Springer, 1987.

[38] A. V. Phelps and Z. L. Petrović, “Cold-cathode discharges and breakdown in argon: surface and gas phase production of secondary electrons,” *Plasma Sources Sci. Technol.*, vol. 8, no. 3, p. R21, 1999.

[39] Z. Li, Z. Zhao, and X. Li, “Modeling of plasma chemistry in an atmospheric pressure Ar/NH3 cylindrical dielectric barrier discharge described using the one-dimensional fluid model,” *Phys. Plasmas*, vol. 20, no. 1, p. 013503, 2013.

[40] X. Yuan and L. L. Raja, “Role of trace impurities in large-volume noble gas atmospheric-pressure glow discharges,” vol. 814, no. April 2002, pp. 1–4, 2011.

[41] F. Massines, N. Gherardi, N. Naudé, and P. Ségur, “Recent advances in the understanding of homogeneous dielectric barrier discharges,” *EPJ Appl. Phys.*, vol. 47, no. 2, p. 22805, 2009.

[42] A. Ricard, *Plasmas réactifs*. Société Française du Vide, 1995.

[43] J. L. Delcroix, C. Matos Ferreira, and A. Ricard, *Atomes et molécules métastables dans les gaz ionisés*. 1975.

[44] A. Durocher-Jean, E. Desjardins, and L. Stafford, “Characterization of a microwave argon plasma column at atmospheric pressure by optical emission and absorption spectroscopy coupled with collisional-radiative modelling,” *Phys. Plasmas*, vol. 26, no. 6, p. 063516, 2019.

[45] J. E. Velazco, J. H. Kolts, and D. W. Setser, “Rate constants and quenching mechanisms for the metastable states of argon, krypton, and xenon,” *J. Chem. Phys.*, vol. 69, no. 10, pp. 4357–4373, 1978.

[46] J. Balamuta, M. F. Golde, and Y. Ho, “Product distributions in the reactions of excited noble-gas atoms with halogen-containing compounds,” *J. Chem. Phys.*, vol. 79, no. 6, pp. 2822–2830, 1983.

[47] R. A. Arakoni, A. N. Bhoj, and M. J. Kushner, “H2 generation in Ar/NH3 microdischarges,” *J. Phys. D. Appl. Phys.*, vol. 40, no. 8, pp. 2476–2490, 2007.

[48] M. Akiyama, K. Aihara, T. Sawaguchi, M. Matsukata, and M. Iwamoto, “Ammonia decomposition to clean hydrogen using non-thermal atmospheric-pressure plasma,” *Int. J. Hydrogen Energy*, vol. 43, no. 31, pp. 14493–14497, 2018.

[49] C. Yao *et al.*, “Characteristics of atmospheric Ar/NH3 DBD and its comparison with He/N2 DBD,” *J. Phys. D. Appl. Phys.*, vol. 51, no. 22, p. 225201, 2018.

[50] R. Magnan, G. Hagelaar, M. Chaker, and F. Massines, “Atmospheric pressure dual RF-LF frequency discharge: Influence of LF voltage amplitude on the RF discharge behavior,” *Plasma Sources Sci. Technol.*, vol. 29, no. 3, p. 035009, Feb. 2020.

[51] C. Tendero, C. Tixier, P. Tristant, J. Desmaison, and P. Leprince, “Atmospheric pressure plasmas: A review,” *Spectrochim. Acta - Part B At. Spectrosc.*, vol. 61, no. 1, pp. 2–30, 2006.

[52] S. Kanazawa, M. Kogoma, S. Okazaki, and T. Moriwaki, “Glow plasma treatment at atmospheric pressure for surface modification and film deposition,” *Nucl. Inst. Methods Phys. Res. B*, vol. 37–38, no. C, pp. 842–845, 1989.

[53] J. R. Roth, M. Laroussi, and Chaoyu Liu, “Experimental Generation Of A Steady-state Glow Discharge At Atmospheric Pressure,” in *IEEE International Conference on Plasma, Tampa, FL, USA, 1992*, 2005, pp. 170–171.

[54] C. Liu and J. R. Roth, “Plasma-related characteristics of a steady-state glow discharge at atmospheric pressure,” in *International Conference on Plasma Sciences (ICOPS), Vancouver, BC, Canada, 1993*, 1993, vol. 00226020, no. 3, pp. 1–8.

[55] F. Massines, R. Messaoudi, and C. Mayoux, “Comparison between Air Filamentary and Helium Glow Dielectric Barrier Discharges for the Polypropylene Surface Treatment,” *Plasmas Polym.*, vol. 3, no. 1, pp. 43–59, 1998.

[56] R. Bazinette, “Effet de la forme d’excitation électrique sur une décharge controlée par barrière diélectrique (DBD) à la pression atmosphérique et application au dépot de couche mince,” 2016.

[57] S. Pouliquen, “Etude d’une nouvelle décharge à barrière diélectrique homogène en

mélange Ar/NH3/SiH4 à la pression atmosphérique pour le dépôt en continu de SiNx:H sur cellule photovoltaïque silicium," 2010.

[58] F. Massines, N. Gherardi, N. Naudé, and P. Ségur, "Glow and Townsend dielectric barrier discharge in various atmosphere," *Plasma Phys. Control. Fusion*, vol. 47, no. 12 B, pp. B577–B588, 2005.

[59] P. Kloc, H. E. Wagner, D. Trunec, Z. Navr, Z. Navrátill, and G. Fedoseev, "An investigation of dielectric barrier discharge in Ar and Ar/NH 3 mixture using cross-correlation spectroscopy," *J. Phys. D. Appl. Phys.*, vol. 43, no. 34, p. 345205, 2010.

[60] M. Moravej, X. Yang, M. Barankin, J. Penelon, S. E. Babayan, and R. F. Hicks, "Properties of an atmospheric pressure radio-frequency argon and nitrogen plasma," *Plasma Sources Sci. Technol.*, vol. 15, no. 2, pp. 204–210, 2006.

[61] T. Hemke *et al.*, "Ionization by bulk heating of electrons in capacitive radio frequency atmospheric pressure microplasmas," *Plasma Sources Sci. Technol.*, vol. 22, no. 1, p. 015012, 2013.

[62] L. Bischoff *et al.*, "Experimental and computational investigations of electron dynamics in micro atmospheric pressure radio-frequency plasma jets operated in He/N 2 mixtures," *Plasma Sources Sci. Technol.*, vol. 27, no. 12, p. 125009, 2018.

[63] J. Golda, J. Held, and V. S. Von Der Gathen, "Comparison of electron heating and energy loss mechanisms in an RF plasma jet operated in argon and helium," *Plasma Sources Sci. Technol.*, vol. 29, no. 2, p. 025014, 2020.

[64] Y. P. Raizer, M. N. Shneider, and N. A. Yatsenko, *Radio-Frequency capacitive discharges*. 2017.

[65] M. A. Lieberman, A. J. Lichtenberg, and A. J. L. M. A. Lieberman, *Principles of plasma discharges and materials processing*. 2005.

[66] N. Balcon, G. J. M. Hagelaar, and J. P. Boeuf, "Numerical model of an argon atmospheric pressure RF discharge," *IEEE Trans. Plasma Sci.*, vol. 36, no. 5 SUPPL. 4, pp. 2782–2787,

2008.

[67] K. Ding, M. A. Lieberman, A. J. Lichtenberg, J. J. Shi, and J. Zhang, “Comparison of a hybrid model with experiments in atmospheric pressure helium and argon capacitive rf discharges,” *Plasma Sources Sci. Technol.*, vol. 23, no. 6, p. 065048, 2014.

[68] J. J. Shi and M. G. Kong, “Mechanisms of the α and γ modes in radio-frequency atmospheric glow discharges Mechanisms of the α and γ modes in radio-frequency atmospheric glow discharges,” vol. 023306, pp. 1–7, 2005.

[69] M. Dünnbier *et al.*, “Stability and excitation dynamics of an argon micro-scaled atmospheric pressure plasma jet,” *Plasma Sources Sci. Technol.*, vol. 24, no. 6, 2015.

[70] R. Magnan, “Oxyde transparent conducteur de ZnO:V à partir d’une cible de nanoparticules : De l’ablation par laser pulsé à un procédé de décharge à barrière diélectrique double fréquence à pression atmosphérique,” 2020.

[71] R. Bazinette, N. Sadeghi, and F. Massines, “Dual frequency DBD: Influence of the amplitude and the frequency of applied voltages on glow, Townsend and radiofrequency DBDs,” *Plasma Sources Sci. Technol.*, vol. 29, no. 9, p. 095010, 2020.

[72] F. Massines, R. Bazinette, and J. Paillol, “RF-LF dual frequency uniform dielectric barrier discharge for thin film processing,” *22nd Int. Symp. Plasma Chem.*, p. O-22-3, 2015.

[73] F. R. Kong, Z. L. Zhang, and B. H. Jiang, “Numerical study of the discharge properties of atmospheric dielectric barrier discharge by using 200 kHz/13.56 MHz excitations,” *AIP Adv.*, vol. 8, no. 7, p. 075009, 2018.

[74] Y. Liu, F. M. Elam, E. Zoethout, S. A. Starostin, M. C. M. Van De Sanden, and H. W. De Vries, “Atmospheric-pressure silica-like thin film deposition using 200 kHz/13.56 MHz dual frequency excitation,” *J. Phys. D. Appl. Phys.*, vol. 52, no. 35, pp. 1–11, 2019.

[75] Y. Liu, F. J. J. Peeters, S. A. Starostin, M. C. M. Van De Sanden, and H. W. De Vries, “Improving uniformity of atmospheric-pressure dielectric barrier discharges using dual frequency excitation,” *Plasma Sources Sci. Technol.*, vol. 27, no. 1, pp. 1–5, 2018.

[76] R. K. Gangwar *et al.*, “Determination of the electron temperature in plane-to-plane He dielectric barrier discharges at atmospheric pressure,” *Plasma Sources Sci. Technol.*, vol. 25, no. 1, p. 015011, Feb. 2015.

[77] E. Desjardins *et al.*, “Time-resolved study of the electron temperature and number density of argon metastable atoms in argon-based dielectric barrier discharges,” *Plasma Sources Sci. Technol.*, vol. 27, no. 1, pp. 1–8, 2018.

[78] O. Levasseur, R. Kumar Gangwar, J. Profili, N. Naudé, N. Gherardi, and L. Stafford, “Influence of substrate outgassing on the plasma properties during wood treatment in He dielectric barrier discharges at atmospheric pressure,” *Plasma Process. Polym.*, vol. 14, no. 8, p. 1600172, Aug. 2017.

[79] H. S. Uhm, K. W. Whang, E. H. Choi, and S. S. Kim, “Influence of penning effects on high-pressure discharge in the plasma display panel,” *Phys. Plasmas*, vol. 9, no. 2, p. 706, 2002.

[80] E. Iordanova, N. de Vries, M. Guillemier, and J. J. A. M. van der Mullen, “Absolute measurements of the continuum radiation to determine the electron density in a microwave-induced argon plasma,” *J. Phys. D. Appl. Phys.*, vol. 41, no. 1, p. 015208, Jan. 2008.

[81] L. Taghizadeh, J. van der Mullen, A. Nikiforov, and C. Leys, “Determination of the Electron Density in an Argon Plasma Jet Using Absolute Measurements of Continuum Radiation,” *Plasma Process. Polym.*, vol. 12, no. 8, pp. 799–807, Aug. 2015.

[82] S. Park, W. Choe, S. Youn Moon, and J. Park, “Electron density and temperature measurement by continuum radiation emitted from weakly ionized atmospheric pressure plasmas,” *Appl. Phys. Lett.*, vol. 104, no. 8, p. 084103, 2014.

[83] S. Park, W. Choe, S. Y. Moon, and S. J. Yoo, “Spatio-temporally resolved electron temperature in argon radio-frequency capacitive discharge at atmospheric pressure,” *Plasma Sources Sci. Technol.*, vol. 24, no. 3, p. 032006, Jun. 2015.

[84] S. Park, W. Choe, S. Y. Moon, and J. J. Shi, “Electron Information in Single-And Dual-Frequency Capacitive Discharges at Atmospheric Pressure,” *Sci. Rep.*, vol. 8, no. 1, pp. 1–

10, 2018.

[85] J. Park, I. Henins, H. W. Herrmann, and G. S. Selwyn, “Neutral bremsstrahlung measurement in an atmospheric-pressure radio frequency discharge,” *Phys. Plasmas*, vol. 7, no. 8, pp. 3141–3144, 2000.

[86] G. Nayak, M. Simeni Simeni, J. Rosato, N. Sadeghi, and P. J. Bruggeman, “Characterization of an RF-driven argon plasma at atmospheric pressure using broadband absorption and optical emission spectroscopy,” *J. Appl. Phys.*, vol. 128, no. 24, p. 243302, 2020.

[87] H. Akatsuka, “Optical emission spectroscopic (Oes) analysis for diagnostics of electron density and temperature in non-equilibrium argon plasma based on collisional-radiative model,” *Adv. Phys. X*, vol. 4, no. 1, pp. 1–25, 2019.

[88] J. S. Boisvert, F. Montpetit, F. Vidal, J. Margot, and L. Stafford, “Time and space-resolved experimental investigation of the electron energy distribution function of a helium capacitive discharge at atmospheric pressure,” *J. Phys. D. Appl. Phys.*, vol. 52, no. 24, p. 245202, 2019.

[89] D. W. Liu, F. Iza, and M. G. Kong, “Electron heating in radio-frequency capacitively coupled atmospheric-pressure plasmas,” *Appl. Phys. Lett.*, vol. 93, no. 26, pp. 1–4, 2008.

[90] W. L. Shang *et al.*, “Simulation of radio-frequency atmospheric pressure glow discharge in γ mode,” *Chinese Phys.*, vol. 16, no. 2, pp. 485–492, Feb. 2007.

[91] X. Yang *et al.*, “Comparison of an atmospheric pressure, radio-frequency discharge operating in the α and γ modes,” *Plasma Sources Sci. Technol.*, vol. 14, no. 2, pp. 314–320, 2005.

[92] S. Y. Moon, J. K. Rhee, D. B. Kim, and W. Choe, “A, Γ, and Normal, Abnormal Glow Discharge Modes in Radio-Frequency Capacitively Coupled Discharges At Atmospheric Pressure,” *Phys. Plasmas*, vol. 13, no. 3, pp. 1–7, 2006.

[93] J. J. Shi and M. G. Kong, “Mode transition in radio-frequency atmospheric argon discharges with and without dielectric barriers,” *Appl. Phys. Lett.*, vol. 90, no. 10, p. 101502, 2007.

[94] R. Magnan, G. Hagelaar, M. Chaker, and F. Massines, “Atmospheric pressure dual RF – LF frequency discharge : transition from α to α–γ -mode,” *Plasma Sources Sci. Technol.*, vol. 30, no. 1, p. 015010, Jan. 2021.

[95] Z. L. Zhang, J. W. M. Lim, Q. Y. Nie, X. N. Zhang, and B. H. Jiang, “Electron heating and mode transition in dual frequency atmospheric pressure argon dielectric barrier discharge,” *AIP Adv.*, vol. 7, no. 10, p. 105313, 2017.

[96] Y. J. Zhou, Q. H. Yuan, F. Li, X. M. Wang, G. Q. Yin, and C. Z. Dong, “Nonequilibrium atmospheric pressure plasma jet using a combination of 50 kHz/2 MHz dual-frequency power sources,” *Phys. Plasmas*, vol. 20, no. 11, p. 113502, 2013.

[97] R. Morent *et al.*, “Surface treatment of a polypropylene film with a nitrogen DBD at medium pressure,” in *EPJ Applied Physics*, 2008, vol. 43, no. 3, pp. 289–294.

[98] G. Borcia, C. A. Anderson, and N. M. D. Brown, “Dielectric barrier discharge for surface treatment: Application to selected polymers in film and fibre form,” *Plasma Sources Sci. Technol.*, vol. 12, no. 3, pp. 335–344, 2003.

[99] D. Merche, N. Vandencasteele, and F. Reniers, “Atmospheric plasmas for thin film deposition: A critical review,” *Thin Solid Films*, vol. 520, no. 13, pp. 4219–4236, 2012.

[100] G. Borcia and N. M. D. Brown, “Hydrophobic coatings on selected polymers in an atmospheric pressure dielectric barrier discharge,” *J. Phys. D. Appl. Phys.*, vol. 40, no. 7, pp. 1927–1936, 2007.

[101] J. Profili *et al.*, “Toward More Sustainable Rechargeable Aqueous Batteries Using Plasma-Treated Cellulose-Based Li-Ion Electrodes,” *ACS Sustain. Chem. Eng.*, vol. 8, no. 12, pp. 4728–4733, Mar. 2020.

[102] O. Levasseur *et al.*, “Deposition of hydrophobic functional groups on wood surfaces using atmospheric-pressure dielectric barrier discharge in helium-hexamethyldisiloxane gas mixtures,” *Plasma Process. Polym.*, vol. 9, no. 11–12, pp. 1168–1175, Dec. 2012.

[103] J. Lelièvre *et al.*, “Efficient silicon nitride SiNx:H antireflective and passivation layers

deposited by atmospheric pressure PECVD for silicon solar cells," *Prog. Photovoltaics Res. Appl.*, vol. 27, no. 11, pp. 1007–1019, Nov. 2019.

[104] J. J. Wang, K. S. Choi, L. H. Feng, T. N. Jukes, and R. D. Whalley, "Recent developments in DBD plasma flow control," *Prog. Aerosp. Sci.*, vol. 62, pp. 52–78, 2013.

[105] C. L. Enloe, T. E. McLaughlin, R. D. VanDyken, K. D. Kachner, E. J. Jumper, and T. C. Corke, "Mechanisms and Responses of a Single Dielectric Barrier Plasma Actuator: Plasma Morphology," *AIAA J.*, vol. 42, no. 3, pp. 589–594, Mar. 2004.

[106] I. Michielsen *et al.*, "CO2 dissociation in a packed bed DBD reactor: First steps towards a better understanding of plasma catalysis," *Chem. Eng. J.*, vol. 326, pp. 477–488, Oct. 2017.

[107] R. McAdams, "Prospects for non-thermal atmospheric plasmas for pollution abatement," *J. Phys. D. Appl. Phys.*, vol. 34, no. 18, pp. 2810–2821, 2001.

[108] R. Ono and T. Oda, "Ozone production process in pulsed positive dielectric barrier discharge," *J. Phys. D. Appl. Phys.*, vol. 40, no. 1, pp. 176–182, 2007.

[109] N. Mericam-Bourdet, M. J. Kirkpatrick, F. Tuvache, D. Frochot, and E. Odic, "Effect of voltage waveform on dielectric barrier discharge ozone production efficiency," *Eur. Phys. J. Appl. Phys.*, vol. 57, no. 3, p. 30801, Mar. 2012.

[110] U. Kogelschatz, "Dielectric-barrier discharges: Their History, Discharge Physics, and Industrial Applications," *Plasma Chemistry and Plasma Processing*, vol. 23, no. 1. pp. 1–46, 2003.

[111] U. Kogelschatz, "Filamentary and diffuse barrier discharges," *J. Phys. D Appl. Phys*, vol. 20, p. 1421, 1987.

[112] U. Kogelschatz, "Filamentary, patterned, and diffuse barrier discharges," *IEEE Trans. Plasma Sci.*, vol. 30, no. 4, pp. 1400–1408, Aug. 2002.

[113] J. J. Shi and M. G. Kong, "Mechanisms of the α and γ modes in radio-frequency atmospheric glow discharges," *J. Appl. Phys.*, vol. 97, no. 2, p. 023306, Jan. 2005.

[114] J. L. Walsh, J. J. Shi, and M. G. Kong, “Contrasting characteristics of pulsed and sinusoidal cold atmospheric plasma jets,” *Appl. Phys. Lett.*, vol. 88, no. 17, p. 171501, Apr. 2006.

[115] Y. Liu *et al.*, “Numerical simulation of atmospheric-pressure 200 kHz/13.56 MHz dual-frequency dielectric barrier discharges,” *Plasma Sources Sci. Technol.*, vol. 27, no. 10, p. 105016, 2018.

[116] Z. Zhang, Q. Nie, Z. Wang, and J. W. M. Lim, “Selective modulation of plasma parameters in an atmospheric dielectric barrier discharge driven by sawtooth-type tailored voltage waveforms,” *Phys. Plasmas*, vol. 27, no. 6, p. 063519, 2020.

[117] D. P. Lymberopoulos and D. J. Economou, “Fluid simulations of glow discharges: Effect of metastable atoms in argon,” *J. Appl. Phys.*, vol. 73, no. 8, pp. 3668–3679, Apr. 1993.

[118] G. Dilecce, P. F. Ambrico, S. De Benedictis, S. De Benedictis, and S. De Benedictis, “N2(A3Σ uu density measurement in a dielectric barrier discharge in N2 and N2 with small O2 admixtures,” *Plasma Sources Sci. Technol.*, vol. 16, no. 3, pp. 511–522, Aug. 2007.

[119] C. Tyl *et al.*, “Investigation of memory effect in atmospheric pressure dielectric barrier discharge in nitrogen with small oxygen or nitric oxide addition,” *J. Phys. D. Appl. Phys.*, vol. 51, no. 35, p. 354001, 2018.

[120] M. Moselhy, I. Petzenhauser, K. Frank, and K. H. Schoenbach, “Excimer emission from microhollow cathode argon discharges,” *J. Phys. D. Appl. Phys.*, vol. 36, no. 23, pp. 2922–2927, Dec. 2003.

[121] R. Foest *et al.*, “On the Vacuum Ultraviolet Radiation of a Miniaturized Non-thermal Atmospheric Pressure Plasma Jet,” *Plasma Process. Polym.*, vol. 4, no. S1, pp. S460–S464, Apr. 2007.

[122] H. Lange, R. Foest, J. Schafer, and K.-D. Weltmann, “Vacuum UV Radiation of a Plasma Jet Operated With Rare Gases at Atmospheric Pressure,” *IEEE Trans. Plasma Sci.*, vol. 37, no. 6, pp. 859–865, Jun. 2009.

[123] Y. Andrew, I. Abraham, J. H. Booske, Z. C. Lu, and A. E. Wendt, “Absolute densities of long

lived species in an ionized physical vapor deposition copper-argon plasma," *J. Appl. Phys.*, vol. 88, no. 6, pp. 3208–3219, 2000.

[124] F. Liu, L. Nie, X. Lu, J. Stephens, and K. Ostrikov, "Atmospheric plasma VUV photon emission," *Plasma Sources Sci. Technol.*, vol. 29, no. 6, p. 065001, Jun. 2020.

[125] B. Gellert and U. Kogelschatz, "Generation of excimer emission in dielectric barrier discharges," *Appl. Phys. B Photophysics Laser Chem.*, vol. 52, no. 1, pp. 14–21, 1991.

[126] J. B. Boffard *et al.*, "Comparison of surface vacuum ultraviolet emissions with resonance level number densities. I. Argon plasmas," *J. Vac. Sci. Technol. A Vacuum, Surfaces, Film.*, vol. 32, no. 2, p. 021304, Mar. 2014.

[127] S. K. Lam, D. Zheng, A. Lo, A. Dem'yanov, and A. P. Napartovich, "Kinetics of Ar2* in high-pressure pure argon," *J. Phys. D. Appl. Phys.*, vol. 33, no. 3, pp. 242–251, 2000.

[128] S. Hübner, N. Sadeghi, E. A. D. Carbone, and J. J. A. M. Van Der Mullen, "Density of atoms in Ar*(3p(5)4s) states and gas temperatures in an argon surfatron plasma measured by tunable laser spectroscopy," *J. Appl. Phys.*, vol. 113, no. 14, p. 143306, 2013.

[129] B. Niermann, M. Böke, N. Sadeghi, and J. Winter, "Space resolved density measurements of argon and helium metastable atoms in radio-frequency generated He-Ar micro-plasmas," *Eur. Phys. J. D*, vol. 60, no. 3, pp. 489–495, 2010.

[130] E. P.J. Linstrom and W.G. Mallard, "NIST Chemistry WebBook, NIST Standard Reference Database Number 69, National Institute of Standards and Technology, Gaithersburg MD, 20899," *NIST Chem. Webb.*

[131] C. Douat, I. Kacem, N. Sadeghi, G. Bauville, M. Fleury, and V. Puech, "Space-time resolved density of helium metastable atoms in a nanosecond pulsed plasma jet: Influence of high voltage and pulse frequency," *J. Phys. D. Appl. Phys.*, vol. 49, no. 28, p. 285204, 2016.

[132] N. Sadeghi, R. Magnan, and F. Massines, "Pressure broadening of 772.376 and 772.421 nm argon lines and kinetics of argon metastable atoms," *J. Quant. Spectrosc. Radiat. Transf.*, vol. 288, p. 108264, 2022.

[133] S. G. Belostotskiy, V. M. Donnelly, D. J. Economou, and N. Sadeghi, “Spatially resolved measurements of argon metastable (1s5) density in a high pressure microdischarge using diode laser absorption spectroscopy,” *IEEE Trans. Plasma Sci.*, vol. 37, no. 6 PART 1, pp. 852–858, Jun. 2009.

[134] J. H. Kolts and D. W. Setser, “Decay rates of Ar(4s,3P2), Ar(4s’, 3P0), Kr(5s,3P2), and Xe(6s, 3P2) atoms in argon,” *J. Chem. Phys.*, vol. 68, no. 11, pp. 4848–4859, 1978.

[135] E. Carbone, E. Van Veldhuizen, G. Kroesen, and N. Sadeghi, “Electron impact transfer rates between metastable and resonant states of argon investigated by laser pump-probe technique,” *J. Phys. D. Appl. Phys.*, vol. 48, no. 42, p. 425201, 2015.

[136] E. Carbone, S. Hübner, J. J. A. M. Van Der Mullen, G. M. W. Kroesen, and N. Sadeghi, “Determination of electron-impact transfer rate coefficients between argon 1s2 and 1s3 states by laser pump-probe technique,” *J. Phys. D. Appl. Phys.*, vol. 46, no. 41, p. 415202, 2013.

[137] E. Carbone *et al.*, “Spatio-temporal dynamics of a pulsed microwave argon plasma: Ignition and afterglow,” *Plasma Sources Sci. Technol.*, vol. 24, no. 1, p. 015015, 2015.

[138] G. J. M. Hagelaar and L. C. Pitchford, “Solving the Boltzmann equation to obtain electron transport coefficients and rate coefficients for fluid models,” *Plasma Sources Sci. Technol.*, vol. 14, no. 4, pp. 722–733, 2005.

[139] F. J. Mehr and M. A. Biondi, “Electron-temperature dependence of electron-ion recombination in Argon,” *Phys. Rev.*, vol. 176, no. 1, pp. 322–326, 1968.

[140] M. J. Kushner, “Simulation of the gas-phase processes in remote-plasma-activated chemical-vapor deposition of silicon dielectrics using rare gas-silane-ammonia mixtures,” *J. Appl. Phys.*, vol. 71, no. 9, pp. 4173–4189, 1992.

[141] W. Wieme and J. Lenaerts, “Excimer formation in argon, krypton, and xenon discharge afterglows between 200 and 400 K,” *J. Chem. Phys.*, vol. 74, no. 1, pp. 483–493, 1981.

[142] R. Tschiersch, S. Nemschokmichal, and J. Meichsner, “Influence of released surface

electrons on the pre-ionization of helium barrier discharges: Laser photodesorption experiment and 1D fluid simulation," *Plasma Sources Sci. Technol.*, vol. 26, no. 7, p. 075006, 2017.

[143] R. Tschiersch, M. Bogaczyk, and H. E. Wagner, "Systematic investigation of the barrier discharge operation in helium, nitrogen, and mixtures: Discharge development, formation and decay of surface charges," *J. Phys. D. Appl. Phys.*, vol. 47, no. 36, p. 365204, 2014.

[144] M. Li, C. Li, H. Zhan, J. Xu, and X. Wang, "Effect of surface charge trapping on dielectric barrier discharge," *Appl. Phys. Lett.*, vol. 92, no. 3, p. 031503, 2008.

[145] O. Guaitella, I. Marinov, and A. Rousseau, "Role of charge photodesorption in self-synchronized breakdown of surface streamers in air at atmospheric pressure," *Appl. Phys. Lett.*, vol. 98, no. 7, p. 071502, 2011.

[146] H. T., "Imprisonment of Resonance Radiation in Gases T.," *Phys. Rev.*, vol. 72, no. 12, p. 1212, 1947.

[147] T. Holstein, "Imprisonment of Resonance Radiation in Gases. II," *Phys. Rev.*, vol. 83, no. 6, p. 1159, 1951.

[148] P. J. Walsh, "Effect of Simultaneous Doppler and Collision Broadening and of Hyperfine Structure on the Imprisonment of Resonance Radiation," *Phys. Rev.*, vol. 116, no. 3, pp. 511–515, 1959.

[149] E. Ellis and N. D. Twiddy, "Time-resolved optical absorption measurements of excited-atom concentrations in the argon afterglow," *J. Phys. B At. Mol. Phys.*, vol. 2, no. 12, pp. 1366–1377, 1969.

[150] A. Raveh, L. Martinu, H. M. Hawthorne, and M. R. Wertheimer, "Mechanical and tribological properties of dual-frequency plasma-deposited diamond-like carbon," *Surf. Coatings Technol.*, vol. 58, no. 1, pp. 45–55, 1993.

[151] A. S. da Silva Sobrinho, M. Latrèche, G. Czeremuszkin, J. E. Klemberg-Sapieha, and M. R. Wertheimer, "Transparent barrier coatings on polyethylene terephthalate by single- and

dual-frequency plasma-enhanced chemical vapor deposition," *J. Vac. Sci. Technol. A Vacuum, Surfaces, Film.*, vol. 16, no. 6, pp. 3190–3198, 1998.

[152] J. E. Klemberg-Sapieha, O. M. Küttel, L. Martinu, and M. R. Wertheimer, "Dual-frequency N2 and NH3 plasma modification of polyethylene and polyimide," *J. Vac. Sci. Technol. A Vacuum, Surfaces, Film.*, vol. 9, no. 6, pp. 2975–2981, 1991.

[153] E. Kawamura, M. A. Lieberman, and D. B. Graves, "Fast 2D fluid-analytical simulation of ion energy distributions and electromagnetic effects in multi-frequency capacitive discharges," *Plasma Sources Sci. Technol.*, vol. 23, no. 6, pp. 1–12, 2014.

[154] J. P. Booth, G. Curley, D. Marić, and P. Chabert, "Dual-frequency capacitive radiofrequency discharges: Effect of low-frequency power on electron density and ion flux," *Plasma Sources Sci. Technol.*, vol. 19, no. 1, pp. 1–7, 2010.

[155] V. Georgieva, A. Bogaerts, and R. Gijbels, "Numerical investigation of ion-energy-distribution functions in single and dual frequency capacitively coupled plasma reactors," *Phys. Rev. E - Stat. Nonlinear, Soft Matter Phys.*, vol. 69, no. 2 2, pp. 1–11, 2004.

[156] J. Schulze, T. Gans, D. O'Connell, U. Czarnetzki, A. R. Ellingboe, and M. M. Turner, "Space and phase resolved plasma parameters in an industrial dual-frequency capacitively coupled radio-frequency discharge," *J. Phys. D. Appl. Phys.*, vol. 40, no. 22, pp. 7008–7018, 2007.

[157] E. Semmler, P. Awakowicz, and A. Von Keudell, "Heating of a dual frequency capacitively coupled plasma via the plasma series resonance," *Plasma Sources Sci. Technol.*, vol. 16, no. 4, pp. 839–848, 2007.

[158] P. C. Boyle, A. R. Ellingboe, and M. M. Turner, "Electrostatic modelling of dual frequency rf plasma discharges," *Plasma Sources Sci. Technol.*, vol. 13, no. 3, pp. 493–503, 2004.

[159] P. C. Boyle, A. R. Ellingboe, and M. M. Turner, "Independent control of ion current and ion impact energy onto electrodes in dual frequency plasma devices," *J. Phys. D. Appl. Phys.*, vol. 37, no. 5, pp. 697–701, 2004.

[160] J. K. Lee, O. V. Manuilenko, N. Y. Babaeva, H. C. Kim, and J. W. Shon, "Ion energy distribution

control in single and dual frequency capacitive plasma sources," *Plasma Sources Sci. Technol.*, vol. 14, no. 1, pp. 89–97, 2005.

[161] K. N. Kim, J. H. Lim, G. Y. Yeom, S. H. Lee, and J. K. Lee, "Effect of dual frequency on the plasma characteristics in an internal linear inductively coupled plasma source," *Appl. Phys. Lett.*, vol. 89, no. 25, pp. 3–5, 2006.

[162] E. Kawamura, M. A. Lieberman, and A. J. Lichtenberg, "Stochastic heating in single and dual frequency capacitive discharges," *Phys. Plasmas*, vol. 13, no. 5, p. 053506, 2006.

[163] T. Gans, D. O'Connell, V. Schulz-Von Der Gathen, and J. Waskoenig, "The challenge of revealing and tailoring the dynamics of radio-frequency plasmas," *Plasma Sources Sci. Technol.*, vol. 19, no. 3, p. 034010, 2010.

[164] X. S. Li *et al.*, "Modulating effects of the low-frequency source on ion energy distributions in a dual frequency capacitively coupled plasma," *Appl. Phys. Lett.*, vol. 93, no. 3, p. 031504, 2008.

[165] B. B. Sahu and J. G. Han, "Electron heating mode transition induced by mixing radio frequency and ultrahigh frequency dual frequency powers in capacitive discharges," *Phys. Plasmas*, vol. 23, no. 5, pp. 1–10, 2016.

[166] M. M. Turner and P. Chabert, "Electron heating mode transitions in dual frequency capacitive discharges," *Appl. Phys. Lett.*, vol. 89, no. 23, pp. 9–11, 2006.

[167] D. O'Connell, T. Gans, E. Semmler, and P. Awakowicz, "The role of the relative voltage and phase for frequency coupling in a dual-frequency capacitively coupled plasma," *Appl. Phys. Lett.*, vol. 93, no. 8, pp. 1–3, 2008.

[168] W. Tsai, G. Mueller, R. Lindquist, B. Frazier, and V. Vahedi, "High selectivity plasma etching of silicon dioxide with a dual frequency 27/2 MHz capacitive radio frequency discharge," *J. Vac. Sci. Technol. B Microelectron. Nanom. Struct.*, vol. 14, no. 5, p. 3276, 1996.

[169] V. Georgieva and A. Bogaerts, "Numerical simulation of dual frequency etching reactors: Influence of the external process parameters on the plasma characteristics," *J. Appl. Phys.*,

vol. 98, no. 2, pp. 1–13, 2005.

[170] T. H. Kim *et al.*, “Plasma characteristics of inductively coupled plasma using dual-frequency antennas,” *Jpn. J. Appl. Phys.*, vol. 52, no. 5 PART 3, pp. 1–5, 2013.

[171] Y. Liu, S. A. Starostin, F. J. J. Peeters, M. C. M. Van De Sanden, and H. W. De Vries, “Atmospheric-pressure diffuse dielectric barrier discharges in Ar/O2 gas mixture using 200 kHz/13.56 MHz dual frequency excitation,” *J. Phys. D. Appl. Phys.*, vol. 51, no. 11, p. 114002, 2018.

[172] D. B. Kim, J. K. Rhee, B. Gweon, S. Y. Moon, and W. Choe, “Comparative study of atmospheric pressure low and radio frequency microjet plasmas produced in a single electrode configuration,” *Appl. Phys. Lett.*, vol. 91, no. 15, pp. 2005–2008, 2007.

[173] E. P. van de Ven, I.-W. Connick, and A. S. Harrus, “Advantages of dual frequency PECVD for deposition of ILD and passivation films,” in *Seventh International IEEE Conference on VLSI Multilevel Interconnection*, 1990, pp. 194–201.

[174] V. Georgieva, A. Bogaerts, and R. Gijbels, “Numerical study of Ar/CF4/N2 discharges in single- and dual-frequency capacitively coupled plasma reactors,” *J. Appl. Phys.*, vol. 94, no. 6, pp. 3748–3756, 2003.

[175] D. Liu, A. Yang, X. Wang, C. Chen, M. Rong, and M. G. Kong, “Electron heating and particle fluxes in dual frequency atmospheric-pressure helium capacitive discharge,” *J. Phys. D. Appl. Phys.*, vol. 49, no. 49, pp. 1–7, 2016.

[176] C. Oneill, J. Waskoenig, and T. Gans, “Tailoring electron energy distribution functions through energy confinement in dual radio-frequency driven atmospheric pressure plasmas,” *Appl. Phys. Lett.*, vol. 101, no. 15, pp. 1–5, 2012.

[177] J. Waskoenig and T. Gans, “Nonlinear frequency coupling in dual radio-frequency driven atmospheric pressure plasmas,” *Appl. Phys. Lett.*, vol. 96, no. 18, pp. 3–6, 2010.

[178] Z. L. Zhang *et al.*, “Numerical studies of independent control of electron density and gas temperature via nonlinear coupling in dual-frequency atmospheric pressure dielectric

barrier discharge plasmas," *Phys. Plasmas*, vol. 23, no. 7, p. 073501, 2016.

[179] W. L. Wiese, J. W. Brault, K. Danzmann, V. Helbig, and M. Kock, "Unified set of atomic transition probabilities for neutral argon," *Phys. Rev. A*, vol. 39, no. 5, pp. 2461–2471, 1989.

[180] Á. Martín Ortega, A. Lacoste, S. Béchu, A. Bès, and N. Sadeghi, "Characterization of X-ray gas attenuator plasmas by optical emission and tunable laser absorption spectroscopies," *J. Synchrotron Radiat.*, vol. 24, no. 6, pp. 1195–1208, 2017.

[181] L. Latrasse, N. Sadeghi, A. Lacoste, A. Bès, and J. Pelletier, "Characterization of high density matrix microwave argon plasmas by laser absorption and electric probe diagnostics," *J. Phys. D. Appl. Phys.*, vol. 40, no. 17, pp. 5177–5186, 2007.

[182] J. B. Boffard, G. A. Piech, M. F. Gehrke, L. W. Anderson, and C. C. Lin, "Measurement of electron-impact excitation cross sections out of metastable levels of argon and comparison with ground-state excitation," *Phys. Rev. A - At. Mol. Opt. Phys.*, vol. 59, no. 4, pp. 2749–2763, 1999.

[183] Y. K. Lee, S. Y. Moon, S. J. Oh, and C. W. Chung, "Determination of metastable level densities in a low-pressure inductively coupled argon plasma by the line-ratio method of optical emission spectroscopy," *J. Phys. D. Appl. Phys.*, vol. 44, no. 28, p. 285203, 2011.

[184] J. S. Boisvert, J. Margot, and F. Massines, "Transitions of an atmospheric-pressure diffuse dielectric barrier discharge in helium for frequencies increasing from kHz to MHz," *Plasma Sources Sci. Technol.*, vol. 26, no. 3, p. 035004, 2017.

[185] A. Y. Nikiforov, E. R. Ionita, G. Dinescu, and C. Leys, "Characterization of a planar 8 mm atmospheric pressure wide radiofrequency plasma source by spectroscopy techniques," *Plasma Phys. Control. Fusion*, vol. 58, no. 1, p. 014013, 2015.

[186] A. V. Pipa, J. Koskulics, R. Brandenburg, and T. Hoder, "The simplest equivalent circuit of a pulsed dielectric barrier discharge and the determination of the gas gap charge transfer," *Rev. Sci. Instrum.*, vol. 83, no. 11, p. 115112, 2012.

[187] X. Lin, C. Tyl, N. Naudé, N. Gherardi, N. A. Popov, and S. Dap, "The role of associative

ionization reactions in the memory effect of atmospheric pressure Townsend discharges in N2 with a small O2 addition," *J. Phys. D. Appl. Phys.*, vol. 53, no. 20, p. 205201, 2020.

[188] R. Robert, G. Hagelaar, N. Sadeghi, L. Stafford, and F. Massines, "Influence of the RF voltage amplitude on the space- and time-resolved properties of RF-LF dielectric barrier discharges in α–γ mode," *Work Submitt. Publ.*

[189] V. A. Godyak and R. B. Piejak, "Abnormally low electron energy and heating-mode transition in a low-pressure argon rf discharge at 13.56 MHz," *Phys. Rev. Lett.*, vol. 65, no. 8, pp. 996–999, 1990.

[190] Y. Sun, Z. Zhang, and J. W. M. Lim, "Enhancement of discharge properties of atmospheric pressure plasma systems through trace radio-frequency oscillation control," *Plasma Sources Sci. Technol.*, vol. 30, no. 7, p. 075018, 2021.

[191] D. Ziegler *et al.*, "The influence of the relative phase between the driving voltages on electron heating in asymmetric dual frequency capacitive discharges," *Plasma Sources Sci. Technol.*, vol. 19, no. 4, p. 045001, 2010.

[192] B. Bruneau, T. Novikova, T. Lafleur, J. P. Booth, and E. V. Johnson, "Ion flux asymmetry in radiofrequency capacitively-coupled plasmas excited by sawtooth-like waveforms," *Plasma Sources Sci. Technol.*, vol. 23, no. 6, p. 065010, 2014.

[193] B. Bruneau, T. Gans, D. O'Connell, A. Greb, E. V. Johnson, and J. P. Booth, "Strong ionization asymmetry in a geometrically symmetric radio frequency capacitively coupled plasma induced by sawtooth voltage waveforms," *Phys. Rev. Lett.*, vol. 114, no. 12, pp. 1–5, 2015.

[194] P. Belenguer and J. P. Boeuf, "Transition between different regimes of rf glow discharges," *Phys. Rev. A*, vol. 41, no. 8, pp. 4447–4459, 1990.

[195] I. Y. Baranov, "Low-current moderate-pressure RF discharge with secondary electron photoemission," *Plasma Phys. Reports*, vol. 28, no. 1, pp. 71–77, 2002.

[196] S. S. Ivković, B. M. Obradović, N. Cvetanović, M. M. Kuraica, and J. Purić, "Measurement of electric field development in dielectric barrier discharge in helium," *J. Phys. D. Appl. Phys.*,

vol. 42, no. 22, p. 225206, 2009.

[197] M. Schulze, A. Yanguas-Gil, A. Von Keudell, and P. Awakowicz, “A robust method to measure metastable and resonant state densities from emission spectra in argon and argon-diluted low pressure plasmas,” *J. Phys. D. Appl. Phys.*, vol. 41, no. 6, p. 065206, 2008.

[198] A. Fateev, F. Leipold, Y. Kusano, B. Stenum, E. Tsakadze, and H. Bindslev, “Plasma chemistry in an atmospheric pressure Ar/NH3 dielectric barrier discharge,” *Plasma Process. Polym.*, vol. 2, no. 3, pp. 193–200, 2005.

[199] J. A. Andersen *et al.*, “Ammonia decomposition in a dielectric barrier discharge plasma: Insights from experiments and kinetic modeling,” *Chem. Eng. Sci.*, vol. 271, p. 118550, 2023.

[200] E. Buijsman, H. F. M. Maas, and W. A. H. Asman, “Anthropogenic NH3 emissions in europe,” *Atmos. Environ.*, vol. 21, no. 5, pp. 1009–1022, 1987.

[201] S. V. Krupa, “Effects of atmospheric ammonia (NH3) on terrestrial vegetation: A review,” *Environ. Pollut.*, vol. 124, no. 2, pp. 179–221, 2003.

[202] C. Emmerling, A. Krein, and J. Junk, “Meta-analysis of strategies to reduce NH3 emissions from slurries in European agriculture and consequences for greenhouse gas emissions,” *Agronomy*, vol. 10, no. 11, p. 1633, 2020.

[203] A. F. Bouwman, L. J. M. Boumans, and N. H. Batjes, “Estimation of global NH3 volatilization loss from synthetic fertilizers and animal manure applied to arable lands and grasslands,” *Global Biogeochem. Cycles*, vol. 16, no. 2, p. 1024, 2002.

[204] S. Wu, N. Salmon, M. M. J. Li, R. Bañares-Alcántara, and S. C. E. Tsang, “Energy Decarbonization via Green H2 or NH3?,” *ACS Energy Lett.*, vol. 7, no. 3, pp. 1021–1033, 2022.

[205] S. Verhelst and T. Wallner, “Hydrogen-fueled internal combustion engines,” *Prog. Energy Combust. Sci.*, vol. 35, no. 6, pp. 490–527, 2009.

[206] M. K. Singla, P. Nijhawan, and A. S. Oberoi, “Hydrogen fuel and fuel cell technology for

cleaner future: a review," *Environ. Sci. Pollut. Res.*, vol. 28, no. 13, pp. 15607–15626, 2021.

[207] N. Armaroli and V. Balzani, "The hydrogen issue," *ChemSusChem*, vol. 4, no. 1, pp. 21–36, 2011.

[208] H. Li, H. Xiao, and J. Sun, "Laminar burning velocity, Markstein length, and cellular instability of spherically propagating NH3/H2/Air premixed flames at moderate pressures," *Combust. Flame*, vol. 241, p. 112079, 2022.

[209] M. V. Manna, P. Sabia, G. Sorrentino, T. Viola, R. Ragucci, and M. de Joannon, "New insight into NH3-H2 mutual inhibiting effects and dynamic regimes at low-intermediate temperatures," *Combust. Flame*, vol. 243, p. 111957, 2022.

[210] P. Kumar and T. R. Meyer, "Experimental and modeling study of chemical-kinetics mechanisms for H 2-NH3-air mixtures in laminar premixed jet flames," *Fuel*, vol. 108, pp. 166–176, 2013.

[211] M. Moisan and H. Nowakowska, "Contribution of surface-wave (SW) sustained plasma columns to the modeling of RF and microwave discharges with new insight into some of their features. A survey of other types of SW discharges," *Plasma Sources Sci. Technol.*, vol. 27, no. 7, p. 073001, 2018.

[212] Y. Kabouzi, M. D. Calzada, M. Moisan, K. C. Tran, and C. Trassy, "Radial contraction of microwave-sustained plasma columns at atmospheric pressure," *J. Appl. Phys.*, vol. 91, no. 3, pp. 1008–1019, 2002.

[213] E. Castãos-Martínez, M. Moisan, and Y. Kabouzi, "Achieving non-contracted and non-filamentary rare-gas tubular discharges at atmospheric pressure," *J. Phys. D. Appl. Phys.*, vol. 42, no. 1, p. 012003, 2009.

[214] E. Castaños Martinez, Y. Kabouzi, K. Makasheva, and M. Moisan, "Modeling of microwave-sustained plasmas at atmospheric pressure with application to discharge contraction," *Phys. Rev. E - Stat. Physics, Plasmas, Fluids, Relat. Interdiscip. Top.*, vol. 70, no. 6, p. 12, 2004.

[215] M. J. Druyvesteyn and F. M. Penning, “The mechanism of electrical discharges in gases of low pressure,” *Rev. Mod. Phys.*, vol. 12, no. 2, pp. 87–174, 1940.

[216] E. Castanos-Martinez and M. Moisan, “Expansion/homogenization of contracted/filamentary microwave discharges at atmospheric pressure,” *IEEE Trans. Plasma Sci.*, vol. 39, no. 11 PART 1, pp. 2192–2193, 2011.

[217] D. D. Hsu and D. B. Graves, “Microhollow cathode discharge reactor chemistry,” *Plasma Chem. Plasma Process.*, vol. 25, no. 1, pp. 1–17, 2005.

[218] H. Qiu, K. Martus, W. Y. Lee, and K. Becker, “Hydrogen generation in a microhollow cathode discharge in high-pressure ammonia-argon gas mixtures,” *Int. J. Mass Spectrom.*, vol. 233, no. 1–3, pp. 19–24, 2004.

[219] P. J. Van Den Oever *et al.*, “Density and production of NH and NH 2 in an Ar-NH 3 expanding plasma jet,” *J. Appl. Phys.*, vol. 98, no. 9, p. 093301, 2005.

[220] P. J. Van Den Oever *et al.*, “Downstream ion and radical densities in an Ar-NH3 plasma generated by the expanding thermal plasma technique,” *Plasma Sources Sci. Technol.*, vol. 15, no. 3, pp. 546–555, 2006.

[221] K. Van’t Veer, Y. Engelmann, F. Reniers, and A. Bogaerts, “Plasma-Catalytic Ammonia Synthesis in a DBD Plasma: Role of Microdischarges and Their Afterglows,” *J. Phys. Chem. C*, vol. 124, no. 42, pp. 22871–22883, 2020.

[222] M. El-Shafie, S. Kambara, and Y. Hayakawa, “Energy and exergy analysis of hydrogen production from ammonia decomposition systems using non-thermal plasma,” *Int. J. Hydrogen Energy*, vol. 46, no. 57, pp. 29361–29375, 2021.

[223] J. A. Andersen, J. M. Christensen, M. Østberg, A. Bogaerts, and A. D. Jensen, “Plasma-catalytic ammonia decomposition using a packed-bed dielectric barrier discharge reactor,” *Int. J. Hydrogen Energy*, vol. 47, no. 75, pp. 32081–32091, 2022.

[224] D. Brand and C. Ottinger, “H2(ag+3 bu+3) continuum emission excited by low-energy rare-gas ion collisions,” *Phys. Rev. A*, vol. 19, no. 1, pp. 219–230, 1979.

[225] J. M. Ajello and D. E. Shemansky, “electron excitation of the H2 (a=>b) continuum in the vacuum ultraviolet,” *Astrophys. J.*, vol. 407, pp. 820–825, 1993.

[226] J. Bretagne, J. Godart, and V. Puech, “Time-resolved study of the H2 continuum at low pressures,” *J. Phys. B At. Mol. Phys.*, vol. 14, no. 23, pp. L761–L765, 1981.

[227] F. Massines, P. Ségur, N. Gherardi, C. Khamphan, and A. Ricard, “Physics and chemistry in a glow dielectric barrier discharge at atmospheric pressure: Diagnostics and modelling,” *Surf. Coatings Technol.*, vol. 174–175, pp. 8–14, Sep. 2003.

[228] D. H. Stedman, “Reactions of Ar, Kr, and Xe metastables with simple NH-containing compounds,” *J. Chem. Phys.*, vol. 52, no. 8, pp. 3966–3970, 1970.

[229] U. Fantz, B. Schalk, and K. Behringer, “Calculation and interpretation of the continuum radiation of hydrogen molecules,” *New J. Phys.*, vol. 2, no. 7, pp. 1–15, 2000.

[230] A. J. Palmer, “Stimulated emission of the H2 continuum,” *J. Appl. Phys.*, vol. 41, no. 1, pp. 438–439, 1970.

[231] J. Godart and V. Puech, “Kinetic studies of the H2(a3Σ+g→ b2Σ+u) continuum emission of an ArH2 mixture pumped by e-beam,” *Chem. Phys.*, vol. 46, no. 1–2, pp. 23–29, 1980.

[232] D. Cvejanovic, A. Adams, and G. C. King, “Radiative lifetime measurements of NH and CH using the electron-photon delayed coincidence method,” *J. Phys. B At. Mol. Phys.*, vol. 11, no. 9, pp. 1653–1662, 1978.

[233] Z. Li, Z. Zhao, and X. Li, “Numerical model of an Ar/NH 3 atmospheric pressure direct current discharge in parallel plate geometry,” *Phys. Plasmas*, vol. 19, no. 3, p. 033510, 2012.

[234] R. Locht, B. Leyh, W. Denzer, G. Hagenow, and H. Baumgärtel, “The photoionization of ammonia revisited. The vibrational autoionization of NH3 and its three isotopomers in the 10-12 eV photon energy range,” *Chem. Phys.*, vol. 155, no. 3, pp. 407–422, 1991.

[235] J. T. Moseley, R. P. Saxon, B. A. Huber, P. C. Cosby, R. Abouaf, and M. Tadjeddine, “Photofragment spectroscopy and potential curves of Ar2+,” *J. Chem. Phys.*, vol. 67, no. 4,

pp. 1659–1668, 1977.

[236] V. Blackman, “Vibrational relaxation in oxygen and nitrogen,” *J. Fluid Mech.*, vol. 1, no. 1, pp. 61–85, 1956.

[237] O. Eichwald, M. Yousfi, A. Hennad, and M. D. Benabdessadok, “Coupling of chemical kinetics, gas dynamics, and charged particle kinetics models for the analysis of NO reduction from flue gases,” *J. Appl. Phys.*, vol. 82, no. 10, pp. 4781–4794, 1997.

[238] M. Laroussi, “Interaction of microwaves with atmospheric pressure plasmas,” *Int. J. Infrared Millimeter Waves*, vol. 16, no. 12, pp. 2069–2083, 1995.

[239] M. Capitelli, R. Celibertoc, A. Eletskii, and A. Laricchiutaa, “Electron-molecule dissociation cross-sections of H2, N2 and O2 in different vibrational levels,” *At. Plasma Mater. Interact. Data Fusion*, vol. 9, pp. 47–64, 2001.

[240] T. E. Sharp, “Potential-energy curves for molecular hydrogen and its ions,” *At. Data Nucl. Data Tables*, vol. 2, no. C, pp. 119–169, 1970.

[241] R. L. Day, R. J. Anderson, and F. A. Sharpton, “Radiative decay constants of the H2 Fulcher bands,” *J. Chem. Phys.*, vol. 69, no. 12, pp. 5518–5520, 1978.

[242] D. Edvardsson *et al.*, “A photoabsorption, photodissociation and photoelectron spectroscopy study of NH3 and ND3,” *J. Phys. B At. Mol. Opt. Phys.*, vol. 32, no. 11, pp. 2583–2609, 1999.

[243] J. Brian and A. Mitchell, “The dissociative recombination of molecular ions,” *Phys. Rep.*, vol. 186, no. 5, pp. 215–248, 1990.

[244] M. Abrar *et al.*, “Effect of helium mixing on excitation temperature and nitrogen dissociation in inductively coupled plasma,” *Curr. Appl. Phys.*, vol. 13, no. 6, pp. 969–974, 2013.

[245] D. Loffhagen, M. M. Becker, A. K. Czerny, and C. P. Klages, “Modeling of Atmospheric-Pressure Dielectric Barrier Discharges in Argon with Small Admixtures of Tetramethylsilane,” *Plasma Chem. Plasma Process.*, vol. 41, no. 1, pp. 289–334, 2021.

[246] E. Spatolisano, L. A. Pellegrini, A. R. de Angelis, S. Cattaneo, and E. Roccaro, “Ammonia as a Carbon-Free Energy Carrier: NH3 Cracking to H2,” *Ind. Eng. Chem. Res.*, vol. 62, pp. 10813–10827, 2023.

[247] S. Bang, R. Snoeckx, and M. S. Cha, “Kinetic Study for Plasma Assisted Cracking of NH3: Approaches and Challenges,” *J. Phys. Chem. A*, vol. 127, no. 5, pp. 1271–1282, 2023.

[248] J. Guo and P. Chen, “Catalyst: NH3 as an Energy Carrier,” *Chem*, vol. 3, no. 5, pp. 709–712, 2017.

[249] J. A. Andersen, K. van ’t Veer, J. M. Christensen, M. Østberg, A. Bogaerts, and A. D. Jensen, “Ammonia decomposition in a dielectric barrier discharge plasma: Insights from experiments and kinetic modeling,” *Chem. Eng. Sci.*, vol. 271, p. 118550, 2023.

[250] L. Wang, Y. H. Yi, H. C. Guo, X. M. Du, B. Zhu, and Y. M. Zhu, “Highly dispersed co nanoparticles prepared by an improved method for plasma-driven NH3 decomposition to produce H2,” *Catalysts*, vol. 9, no. 2, pp. 1–13, 2019.

[251] M. El-Shafie, S. Kambara, and Y. Hayakawa, “Plasma-enhanced catalytic ammonia decomposition over ruthenium (Ru/Al2O3) and soda glass (SiO2) materials,” *J. Energy Inst.*, vol. 99, no. August, pp. 145–153, 2021.

[252] L. Wang, Y. Yi, Y. Guo, Y. Zhao, J. Zhang, and H. Guo, “Synergy of DBD plasma and Fe-based catalyst in NH3 decomposition: Plasma enhancing adsorption step,” *Plasma Process. Polym.*, vol. 14, no. 6, p. 1600111, 2017.

[253] Y. Yi, L. Wang, Y. Guo, S. Sun, and H. Guo, “Plasma-assisted ammonia decomposition over Fe–Ni alloy catalysts for COx-Free hydrogen,” *AIChe J.*, vol. 65, no. 2, pp. 691–701, 2019.

[254] M. Zhang, Q. Chen, G. Zhou, J. Sun, and H. Lin, “Low-temperature chemistry in plasma-driven ammonia oxidative pyrolysis,” *Green Energy Environ.*, vol. Articles i, 2023.

[255] C. Tyl *et al.*, “New local electrical diagnostic tool for dielectric barrier discharge (DBD),” *Rev. Sci. Instrum.*, vol. 92, no. 5, p. 053552, 2021.

[256] Z. S. Chang, C. W. Yao, S. Le Chen, and G. J. Zhang, “Electrical and optical properties of

Ar/NH3 atmospheric pressure plasma jet," *Phys. Plasmas*, vol. 23, no. 9, p. 093503, 2016.

[257] R. Robert, F. Massines, and L. Stafford, "Kinetics driving H2(a) continuum emission in low-frequency Ar-NH3 dielectric barrier discharges at atmospheric pressure," *Work Submitt. Publ.*

[258] V. D. Hodoroaba, E. B. M. Steers, V. Hoffmann, and K. Wetzig, "Effect of small quantities of hydrogen on a glow discharge in neon. Comparison with the argon case," *J. Anal. At. Spectrom.*, vol. 16, no. 1, pp. 43–49, 2001.

[259] C. Goldbach, G. Nollez, and P. Plomdeur, "Measurements of the argon plasma continuum: High-pressure peculiarities," *J. Phys. B At. Mol. Phys.*, vol. 10, no. 6, pp. 1181–1189, 1977.

[260] J. P. Boeuf and L. C. Pitchford, "Two-dimensional model of a capacitively coupled rf discharge and comparisons with experiments in the Gaseous Electronics Conference reference reactor," *Phys. Rev. E*, vol. 51, no. 2, pp. 1376–1390, 1995.

[261] S. Pancheshnyi *et al.*, "The LXCat project: Electron scattering cross sections and swarm parameters for low temperature plasma modeling," *Chem. Phys.*, vol. 398, no. 1, pp. 148–153, 2012.

[262] L. C. Pitchford *et al.*, "LXCat: an Open-Access, Web-Based Platform for Data Needed for Modeling Low Temperature Plasmas," *Plasma Processes and Polymers*, vol. 14, no. 1–2. 2017.

[263] E. Carbone *et al.*, "Data needs for modeling low-temperature non-equilibrium plasmas: The LXCat project, history, perspectives and a tutorial," *Atoms*, vol. 9, no. 1, pp. 1–40, 2021.

[264] A. V. Phelps, "https://lxcat.laplace.univ-tlse.fr," *database, retrieved June 4, 2013.* .

[265] H. W. Ellis, R. Y. Pai, E. W. McDaniel, E. A. Mason, and L. A. Viehland, "Transport properties of gaseous ions over a wide energy range. Part II*," *At. Data Nucl. Data Tables*, vol. 17, no. 3, pp. 177–210, 1976.

[266] H. W. Ellis, M. G. Thackston, E. W. McDaniel, and E. A. Mason, "Transport properties of gaseous ions over a wide energy range. Part III*," *At. Data Nucl. Data Tables*, vol. 31, no.

1, pp. 113–151, 1984.

[267] G. J. M. Hagelaar, G. Fubiani, and J. P. Boeuf, “Model of an inductively coupled negative ion source: I. General model description,” *Plasma Sources Sci. Technol.*, vol. 20, no. 1, 2011.

[268] J. Gregório, X. Aubert, G. J. M. Hagelaar, V. Puech, and L. C. Pitchford, “Nanosecond-pulsed dielectric barrier discharges in Kr/Cl2 for production of ultraviolet radiation,” *Plasma Sources Sci. Technol.*, vol. 23, no. 1, 2014.

Annexe

Dans l'ensemble de ce travail de thèse, un modèle fluide 1D est utilisé et adapté graduellement pour répondre aux besoins rencontrés dans chacune des études. Celui-ci décrit le comportement d'une décharge à barrière diélectrique en configuration plan-plan en prenant en compte des grandeurs macroscopiques (intégrées sur toute la fonction de distribution en vitesse et énergie) décrivant les populations d'électrons, d'ions et de particules neutres en fonction de la position dans l'espace inter-électrodes et du temps. Pour l'ensemble des particules, le modèle résout l'équation de conservation des particules (équation dite de continuité) ainsi que l'équation de conservation de la quantité de mouvement sous l'approximation de dérive-diffusion :

$$\frac{\partial n_j}{\partial t} + \nabla.\left(\boldsymbol{\Gamma_j}\right) = S_j \tag{1}$$

$$\boldsymbol{\Gamma}_j = \pm\mu_j n_j \boldsymbol{E} - D_j \nabla n_j \tag{2}$$

où j représente l'espèce de particule considérée, n_j est la densité de particules j, $\boldsymbol{\Gamma_j}$ est le flux de particules j, S_j correspond au terme source net de particules j dû à la chimie plasma, μ_j et D_j sont respectivement les coefficients de mobilité et de diffusion de la particule j (avec $\mu = 0$ pour les particules neutres). Le terme source net est une somme sur les différents processus collisionnels ou chimiques k menant à la production ou la perte de particules j :

$$S_j = \sum_k M_{k,j} K_k \prod_l n_{l,k}$$

où $M_{k,j}$ est le nombre de particules j produites dans une seule collision/réaction de type k (négatif en cas de perte), K_k est le coefficient de réaction et $\prod_l n_{l,k}$ est le produit des densités des espèces réactants. Quant au vecteur champ électrique, $\boldsymbol{E}$, il est calculé à l'aide du potentiel électrostatique ϕ via l'équation de Poisson :

$$\varepsilon_0 \nabla \cdot \boldsymbol{E} = -\varepsilon_0 \nabla^2 \phi = -e n_e + \sum_i q_i n_i \tag{3}$$

où ε_0 est la permittivité du vide, e est la valeur absolue de la charge élémentaire et q_i est la charge de l'ion *i*. Ici, la somme s'effectue sur l'ensemble des espèces ioniques du plasma.

Pour les ions et les particules neutres, les équations de conservation de l'énergie ne sont pas résolues. Les valeurs de températures des particules neutres représentent des paramètres ajustables dans le modèle ; ici, elles sont supposées égales à 0.026 eV, soit 302 K. Quant aux électrons, l'équation de conservation de l'énergie est résolue en considérant le chauffage lié à la présence du champ électrique $\boldsymbol{E}$, le transport d'énergie lié à la présence de gradients de densité électronique et de température électronique, ainsi que les gains et les pertes d'énergie des électrons associées aux processus collisionnels (ici, nous avons des termes représentant la pertes d'énergie via les collisions élastiques (transfert de quantité de mouvement) et inélastiques (processus d'ionisation et d'excitation)).

$$\frac{3e}{2}\frac{\partial n_e T_e}{\partial t} + \frac{5e}{2}\nabla \cdot (\boldsymbol{\Gamma}_e T_e - n_e T_e \mu_e \nabla T_e) = e\boldsymbol{\Gamma}_e \cdot \nabla\phi + \Pi_e \qquad (4)$$

où T_e est la température électronique en eV, $\boldsymbol{\Gamma}_e$ est le flux électronique, Π_e est la densité de puissance nette perdue dans les collisions élastiques et inélastiques.

Dans ce travail, nous faisons l'approximation de l'énergie moyenne locale pour les électrons [260]. Plus précisément, nous supposons que les coefficients de transport électronique μ_e et D_e et les coefficients de réaction K_k des processus collisionnels impliquant les électrons sont paramétrisés en fonction de le température électronique T_e, définie comme 2/3 de l'énergie électronique moyenne. La fonction de distribution en énergie des électrons n'est cependant pas supposée être Maxwellienne, mais sa forme est calculée à partir de l'équation de Boltzmann homogène et un ensemble complet de sections efficaces électron-neutre tiré de la plateforme de données LXCat [261]–[264]. Ce calcul est fait à l'aide du logiciel BOLSIG+, qui ensuite génère des tables de μ_e, D_e et K_k en fonction de l'énergie électronique moyenne, utilisables comme données d'entrée pour le modèle fluide. En revanche, pour les mobilités ioniques (μ_i), nous utilisons des données expérimentales en fonction du champ électrique réduit [265], [266].

Quant à l'émission d'électrons secondaires, elle est considérée sur les surfaces diélectriques recouvrant les deux électrodes métalliques de la décharge à barrière diélectrique avec un

coefficient d'émission secondaire γ de 0.1 pour les ions, les particules neutres métastables et les photons VUV.

Les conditions aux frontières sur la continuité des particules sont imposées sur les flux de particules aux parois tel que le flux net normal à une paroi est la différence entre le flux de particules issus de la décharge en direction de la paroi auquel est retranché le flux issu de la paroi vers la décharge (i.e. le flux d'électrons secondaires, nul pour les particules autres que les électrons).

$$\boldsymbol{\Gamma}_e \cdot \mathbf{n} = n_e v_{w,e} - \sum_i \gamma_i n_i v_{w,i} - \gamma_{VUV} \boldsymbol{\Gamma}_{VUV} \cdot \mathbf{n} \tag{5}$$

$$\boldsymbol{\Gamma}_i \cdot \mathbf{n} = n_i v_{w,i} \tag{6}$$

où $\mathbf{n}$ est le vecteur normal pointant vers la paroi et v_w est la vitesse effective de la particule considérée à la paroi. Dans l'expression pour le flux d'électrons secondaires, le flux de photons VUV impactant la paroi est obtenu comme la moitié de l'intégral du terme source de photons VUV sur l'espace inter-électrodes :

$$\boldsymbol{\Gamma}_{VUV} \cdot \mathbf{n} = \frac{1}{2} \int S_{VUV} dx \tag{7}$$

Pour les conditions aux frontières concernant l'énergie électronique, elles sont basées sur le même principe, prenant en compte le flux d'énergie de chaque particule du plasma vers la paroi et le flux d'énergie des particules des parois vers le plasma pour les électrons secondaires et les particules neutres.

Enfin, la tension (BF et RF) appliquée aux électrodes est la condition aux limites pour l'équation de Poisson qui est résolue en utilisant la densité de charge surfacique calculée à l'aide de la densité de courant (elle-même calculée à une électrode).

Les différentes études ayant lieu à pression atmosphérique, la densité du gaz est fixée à $2.45*10^{25}$ m^{-3} et la densité initiale d'ions et d'électrons pour lancer les simulations est fixée à $1*10^{16}$ m^{-3}. En imposant une condition initiale sur les densités des espèces chargées, il devient possible de

modéliser des phénomènes transitoires avant d'atteindre un état stationnaire entre deux périodes de tension appliquée.

Le modèle décrit est résolu numériquement à l'aide d'un code FORTRAN sur un ordinateur de bureau. Les espèces, collisions, réactions, la géométrie ainsi que les conditions d'opérations sont des paramètres d'entrée. Les méthodes numériques utilisées pour résoudre les équations sont, pour la majorité, relativement classiques (voir [267], [268] pour plus de détails). Enfin, les équations sont discrétisées sur un maillage uniforme le long du gap de 400 points et traitées avec des méthodes implicites et semi-implicites, permettant de s'affranchir de la contrainte sur le pas de temps reliée au Courant–Friedrich–Levy (CFL) et celle liée au couplage entre l'équation de conservation des particules chargées et l'équation de Poisson.